



THESIS APPROVAL

GRADUATE SCHOOL, KASETSART UNIVERSITY

Doctor of Engineering (Electrical Engineering)

DEGREE

Electrical Engineering

Electrical Engineering

FIELD

DEPARTMENT

TITLE: Implementation of Perfectly Matched Layer (PML)
in the Finite Difference Time Domain (FDTD)
Simulation of a Mobile Phone Operating near a Metal Wall

NAME: Mr. Terapass Jariyanorawiss

THIS THESIS HAS BEEN ACCEPTED BY

THESIS ADVISOR

(Associate Professor Nuttaka Homsup, Ph.D.)

COMMITTEE MEMBER

(Professor Wiroj Homsup, Ph.D.)

COMMITTEE MEMBER

(Assistant Professor Wachira Chongburee, Ph.D.)

COMMITTEE MEMBER

(Assistant Professor Waroth Kuhirun, Ph.D.)

DEPARTMENT HEAD

(Associate Professor Mongkol Raksapatcharawon, Ph.D.)

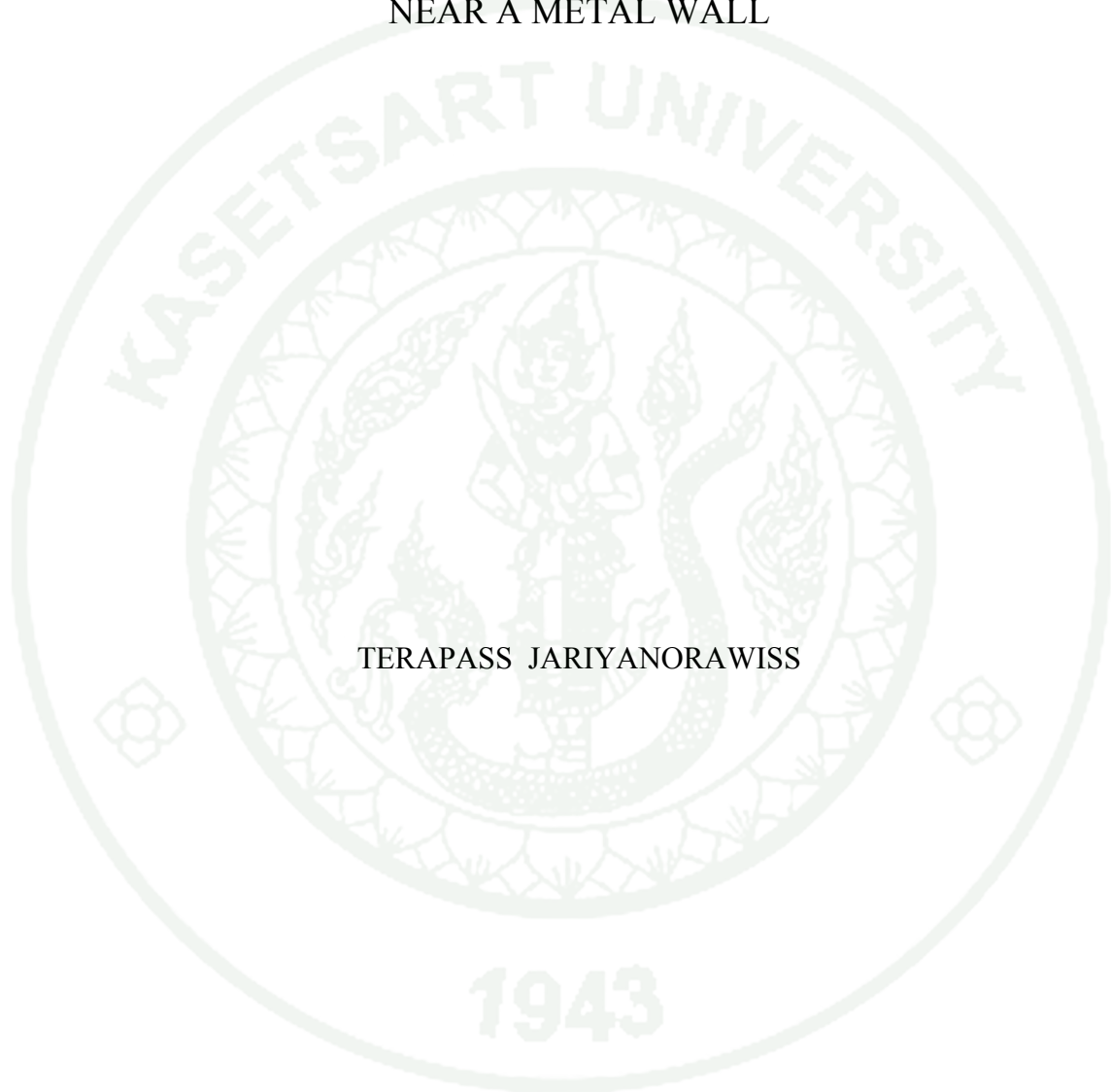
APPROVED BY THE GRADUATE SCHOOL ON _____

DEAN

(Associate Professor Gunjana Theeragool, D.Agr.)

THESIS

IMPLEMENTATION OF
PERFECTLY MATCHED LAYER (PML)
IN THE FINITE DIFFERENCE TIME DOMAIN (FDTD)
SIMULATION OF A MOBILE PHONE OPERATING
NEAR A METAL WALL



TERAPASS JARIYANORAWISS

A Thesis Submitted in Partial Fulfillment of
the Requirements for the Degree of
Doctor of Engineering (Electrical Engineering)
Graduate School, Kasetsart University
2010

Terapass Jariyanorawiss 2010: Implementation of Perfectly Matched Layer (PML) in the Finite Difference Time Domain (FDTD) Simulation of a Mobile Phone Operating near a Metal Wall. Doctor of Engineering (Electrical Engineering), Major Field: Electrical Engineering, Department of Electrical Engineering. Thesis Advisor: Associate Professor Nuttaka Homsup, Ph.D. 231 pages.

In recent years, the Finite Difference Time Domain (FDTD) is the most often used method for evaluating of electromagnetic fields in human tissue. This research presents a study of heating effects resulted from using a mobile phone operating near a Metal Wall. Apparently, the FDTD is suitable for this model because the FDTD technique allows the users to specify any material at all points within the computational physical domain and the absorbing layer. The simulated physical domain consists of a mobile phone, an artificial human head and a Metal Wall. Obviously, the dipole antenna is presented as a mobile phone and it operates on 900 MHz and 1.8 GHz. In this case, the absorbing boundary condition is implemented using Perfectly Matched Layer (PML). The Specific Absorption Rate (SAR) is computed and averaged on a tissue mass of one gram and ten grams which are specified as SAR 1-g and SAR 10-g, respectively. The main purpose of this research is to compare SAR resulted from a mobile phone operated at two different frequencies, 900 MHz and 1.8 GHz, in the close proximity to a Metal Wall. Correspondingly, the average power (P_{avg}) absorbed in various human tissues is computed with a distance between an antenna and a Metal Wall as a varying parameter (Δl). In this case, results from the simulation show that the computed SAR 1-g and SAR 10-g are not exceed the limitation value established by various standard institutes, 1.6 watts per kilogram, but it is dramatically decreasing as the distance get shorter. Last but not least, the average power absorbed in all tissue models with a mobile phone operated at 1.8 GHz has an average power lower than those operated at 900 MHz except for the average power absorbed in muscle ($6 < \Delta l < 8$ cm) and eye ($6 < \Delta l < 10$ cm).

Student's signature

Thesis Advisor's signature

ACKNOWLEDGEMENTS

First and foremost, I would like to thank Associate Professor Dr. Nuttaka Homsup and Professor Dr. Wiroj Homsup. They introduced me into the theories and experimental aspects of the Finite Difference Time Domain (FDTD). Also, a special thank goes to my committee members, Assistant Professor Dr. Wachira Chongburee and Assistant Professor Dr. Waroth Kuhirun. They helped me complete writing this Ph.D. thesis. A thousand thanks for my English teacher, Dr. Issariya Thaveesilpa, who taught me how to write academic papers. Besides, I take this opportunity with much pleasure to thank my MATLAB's teacher, Mr. Sane Tangsatit. I am also greatly indebted to my math teachers: Miss Sasiprapa Thanharuk and Mr. Wiwat Roongkaew.

I would like dedicate all my works to my parents: Mr. Siew-Leng Sae-Ju, Mrs. Oui-Siew Sae-Ju, Mrs. Thorn Lumsmuth, Mr. Jaroong Jariyanorwich, Mrs. Tamtong Jariyanorwich, Mrs. Supeewong Pavasopon, Mrs. Tabtim Ampornpong and Mr. Pooris Saipet. Mrs. Tamtong Jariyanorwich had trained me with the smart technique "How to take notice any objects at first glance and instantaneously keep them in our memory" so I can apply this method for my study and daily life until now. Besides, special sincere thank goes to Mrs. Tabtim Ampornpong, who had adopted me for her son.

I wish to thank the Abbot of Wat Parinayok Worawihan, Phra Amorn Metajarn Sukon Papragaro, for his hospitality before I was settled to a permanent residence in Bangkok. Besides, I wish to acknowledge the supports of my friends: Mr. Komgrich Opasnawakun, Dr. Sittipong Jareernprasert, Dr. Orraya Porniammongkol, Mr. Pitipong Promla, Mr. Somsak Limvipas, Mr. Suphavut Udomthanakornkul, Mr. Sapon Deesomsak, Mr. Aekapol Hirunyaaekapap, Mr. Sirichai Sasataradol (Sae-Wong), Mr. Nipon Pimpuch, Mr. Meta Polpasee, Mr. Piranat Virunha, Mr. Songkran Pisanupoj and Mr. Vuttichai Kesornpatumanun. During the completion of my Ph.D. thesis, they shared their experiences in international conferences with me.

Terapass Jariyanorawiss
June, 2010

TABLE OF CONTENTS

	Page
TABLE OF CONTENTS	i
LIST OF TABLES	ii
LIST OF FIGURES	v
LIST OF ABBREVIATIONS	xvii
INTRODUCTION	1
OBJECTIVES	4
LITERATURE REVIEW	5
MATERIALS AND METHODS	149
Materials	149
Methods	149
RESULTS AND DISCUSSION	180
Results	180
Discussion	209
CONCLUSION AND RECOMMENDATIONS	210
Conclusion	210
Recommendations	210
LITERATURE CITED	212
APPENDIX	221
Appendix A The diagram of the electromagnetic simulation software	222
CURRICULUM VITAE	228

LIST OF TABLES

Table		Page
1	The % of the absolute error between the Exact Solution and MoM (N = 512)	59
2	The % of the absolute error between the Exact Solution and MoM (N = 128)	59
3	The % of the absolute error between the Exact Solution and MoM (N = 32)	59
4	The % of the absolute error between the Exact Solution and MoM (a = 1 / 2048)	68
5	The % of the absolute error between the Exact Solution and MoM (a = 1 / 1024)	68
6	The % of the absolute error between the Exact Solution and MoM (a = 1 / 512)	68
7	The % of the absolute error between the Exact Solution and MoM (a = 1 / 256)	69
8	The iteration rounds in the Gauss-Seidel method depending on $\ RE\ _{\infty}$	74
9	The comparison of iteration rounds between the Gauss-Seidel method and the Multigrid method depending on $\ RE\ _{\infty}$	76
10	The comparison of iteration rounds between the Gauss-Seidel method and the Multigrid method with an expandable basis depending on $\ RE\ _{\infty}$	80
11	The comparison of iteration rounds between the Gauss-Seidel method and the Multigrid method with a compensatory basis depending on $\ RE\ _{\infty}$	84
12	The iteration rounds in the Gauss-Seidel method depending on $\ RLE\ _{\infty}$	86

LIST OF TABLES (Continued)

Table		Page
13	The comparison of iteration rounds between the Gauss-Seidel method and the Multigrid methods depending on $\ RLE\ _{\infty}$	89
14	The relation between Gray scale and types of cell in human head	130
15	Electromagnetic parameter values in human head for 900 MHz (f_c)	132
16	Electromagnetic parameter values in human head for 1.8 GHz (f_c)	133
17	The comparison table of the spatial-average SAR _{Cell-1} 1-g, SAR _{Cell-2} 1-g and SAR _{Cell-3} 1-g in the reference model	142
18	The comparison table of the spatial-average SAR _{Cell-1} 1-g, SAR _{Cell-1} 10-g, and the average power absorbed by a human head in the reference model	143
19	The comparison table of the average power absorbed by any material in a human head between 900 MHz and 1.8 GHz in the reference model	144
20	Sample of parameters for simulate feeding-gap of the dipole antenna, $\frac{l}{\Delta} = 41$	184
21	Comparison of SAR between reference model and compact model at 900 MHz	192
22	Comparison of SAR between reference model and compact model at 1.8 GHz	193
23	The comparison table of SAR 1-g, SAR 10-g and the average power absorbed (P_{avg}) by a human head respecting to Δl , frequency = 900 MHz	197
24	The comparison table of SAR 1-g, SAR 10-g and the average power absorbed (P_{avg}) by a human head respecting to Δl , frequency = 1.8 GHz	201

LIST OF TABLES (Continued)

Table		Page
25	The comparison table of the average power absorbed (P_{avg}) by materials in the human head respecting to Δl , frequency = 900 MHz	203
26	The comparison table of the average power absorbed (P_{avg}) by materials in the human head respecting to Δl , frequency = 1.8 GHz	204

LIST OF FIGURES

Figure		Page
1	The commercial dipole antenna	5
2	Formation of electric field lines for a dipole antenna	6
3	The stationary wave current for various center-fed dipoles	7
4	The input impedance of a dipole antenna	8
5	The impedance matching	8
6	The current maximum does not occur at the input terminal	10
7	The comparison graph between the radiation impedance and the input impedance, radius of a dipole $(a) = l / 128 \lambda$	12
8	The comparison graph between the radiation impedance and the input impedance, radius of a dipole $(a) = l / 256 \lambda$	13
9	The comparison graph between the radiation impedance and the input impedance, radius of a dipole $(a) = l / 512 \lambda$	14
10	The comparison graph between the radiation impedance and the input impedance, radius of a dipole $(a) = 0.00001 \lambda$	15
11	Local and global basis	21
12	A set of pulse basis functions	22
13	Geometry for the calculation of potentials	29
14	Thin wire dipole of length l and radius a	31
15	The incident electric field	34
16	The delta-gap or the infinitesimal gap model	36
17	Behavior of the vector potential function A_z in the vicinity of the input region of the antenna	37
18	The segmentation of dipole antenna	41
19	Relative current magnitude of a dipole antenna, $l = \frac{\lambda}{4}$, $N = 512$ and $a = l / 1024$	45

LIST OF FIGURES (Continued)

Figure		Page
20	Relative current phase of a dipole antenna, $l = \frac{\lambda}{4}$, $N = 512$ and $a = l/1024$	45
21	Relative current magnitude of a dipole antenna, $l = \frac{\lambda}{2}$, $N = 512$ and $a = l/1024$	46
22	Relative current phase of a dipole antenna, $l = \frac{\lambda}{2}$, $N = 512$ and $a = l/1024$	46
23	Relative current magnitude of a dipole antenna, $l = \lambda$, $N = 512$ and $a = l/1024$	47
24	Relative current phase of a dipole antenna, $l = \lambda$, $N = 512$ and $a = l/1024$	47
25	Relative current magnitude of a dipole antenna, $l = \frac{3}{2}\lambda$, $N = 512$ and $a = l/1024$	48
26	Relative current phase of a dipole antenna, $l = \frac{3}{2}\lambda$, $N = 512$ and $a = l/1024$	48
27	Relative current magnitude of a dipole antenna, $l = 2\lambda$, $N = 512$ and $a = l/1024$	49
28	Relative current phase of a dipole antenna, $l = 2\lambda$, $N = 512$ and $a = l/1024$	49
29	The comparison graph of relative current distribution on a dipole antenna, $l = 0.25, 0.50, 1.00, 1.50$ and 2.00λ , $N = 512$ and $a = l/1024$	50
30	The input impedance of a dipole antenna, $N = 512$ and $a = l/1024$	51

LIST OF FIGURES (Continued)

Figure		Page
31	The comparison graph of the antenna input resistance between the Exact Solution ($a = 0.00001 \lambda$) and MoM ($N = 512$)	52
32	The comparison graph of the antenna input reactance between the Exact Solution ($a = 0.00001 \lambda$) and MoM ($N = 512$)	53
33	The comparison graph of the antenna input resistance between the Exact Solution ($a = 0.00001 \lambda$) and MoM ($N = 128$)	54
34	The comparison graph of the antenna input reactance between the Exact Solution ($a = 0.00001 \lambda$) and MoM ($N = 128$)	55
35	The comparison graph of the antenna input resistance between the Exact Solution ($a = 0.00001 \lambda$) and MoM ($N = 32$)	56
36	The comparison graph of the antenna input reactance between the Exact Solution ($a = 0.00001 \lambda$) and MoM ($N = 32$)	57
37	The illustration of the absolute error between the Exact Solution and MoM	58
38	The comparison graph of the antenna input resistance between the Exact Solution ($a = 0.00001 \lambda$) and MoM ($a = l / 2048 \lambda$)	60
39	The comparison graph of the antenna input reactance between the Exact Solution ($a = 0.00001 \lambda$) and MoM ($a = l / 2048 \lambda$)	61
40	The comparison graph of the antenna input resistance between the Exact Solution ($a = 0.00001 \lambda$) and MoM ($a = l / 1024 \lambda$)	62
41	The comparison graph of the antenna input reactance between the Exact Solution ($a = 0.00001 \lambda$) and MoM ($a = l / 1024 \lambda$)	63

LIST OF FIGURES (Continued)

Figure		Page
42	The comparison graph of the antenna input resistance between the Exact Solution ($a = 0.00001 \lambda$) and MoM ($a = l / 512 \lambda$)	64
43	The comparison graph of the antenna input reactance between the Exact Solution ($a = 0.00001 \lambda$) and MoM ($a = l / 512 \lambda$)	65
44	The comparison graph of the antenna input resistance between the Exact Solution ($a = 0.00001 \lambda$) and MoM ($a = l / 256 \lambda$)	66
45	The comparison graph of the antenna input reactance between the Exact Solution ($a = 0.00001 \lambda$) and MoM ($a = l / 256 \lambda$)	67
46	The flow chart of Gauss-Seidel method using $\ RE\ _{\infty}$	73
47	$\ RE\ _{\infty}$ computed by the Gauss-Seidel method	74
48	The flowchart of Multigrid method using $\ RE\ _{\infty}$	75
49	The cover area of using basis in the Multigrid method	76
50	$\ RE\ _{\infty}$ computed by the Multigrid method, $N = 100$	77
51	$\ RE\ _{\infty}$ computed by the Multigrid method, $N = 512$	77
52	$\ RE\ _{\infty}$ computed by the Multigrid method, $N = 1,024$	78
53	The cover area of using basis in the Multigrid method with an expandable basis	79
54	$\ RE\ _{\infty}$ computed by the Multigrid method with an expandable basis, $N = 100$	80
55	$\ RE\ _{\infty}$ computed by the Multigrid method with an expandable basis, $N = 512$	81
56	$\ RE\ _{\infty}$ computed by the Multigrid method with an expandable basis, $N = 1,024$	81

LIST OF FIGURES (Continued)

Figure		Page
57	The cover area of using basis in Multigrid method with a compensatory basis	83
58	$\ RE\ _{\infty}$ computed by the Multigrid method with a compensatory basis, N = 100	85
59	$\ RE\ _{\infty}$ computed by the Multigrid method with a compensatory basis, N = 512	85
60	$\ RE\ _{\infty}$ computed by the Multigrid method with a compensatory basis, N = 1,024	86
61	$\ RLE\ _{\infty}$ computed by the Gauss-Seidel method	87
62	The flowchart of Multigrid method using $\ RLE\ _{\infty}$	88
63	$\ RLE\ _{\infty}$ computed by the Gauss-Seidel method and the Multigrid methods, N = 100	90
64	$\ RLE\ _{\infty}$ computed by the Gauss-Seidel method and the Multigrid methods, N = 512	90
65	$\ RLE\ _{\infty}$ computed by the Gauss-Seidel method and the Multigrid methods, N = 1,024	91
66	The V-Shape algorithm of the Multigrid methods	91
67	The central difference scheme	94
68	The Yee's cell model	96
69	The physical Yee's cell model	96
70	The model of the incorrect boundary layer	101
71	Cross-section of the applied incorrect boundary layer (Timestep = 50)	101
72	Cross-section of the applied incorrect boundary layer (Timestep = 100)	102
73	Cross-section of the applied incorrect boundary layer (Timestep = 300)	102
74	Illustration of complex coordinates stretching	104
75	Illustration of anisotropic material and isotropic material	105

LIST OF FIGURES (Continued)

Figure		Page
76	The spatial conductivity of PML in x-axis	112
77	The spatial conductivity of PML in y-axis	112
78	The spatial conductivity of PML in z-axis	112
79	The intersection of spatial conductivity in x,y,z-axis	113
80	The relationship of spatial conductivity with Maxwell's equations in both Equation (154) and Equation (155)	114
81	Cross-section of the applied absorbing boundary layer (PML) to the computational domain (Timestep = 50)	116
82	Cross-section of the applied absorbing boundary layer (PML) to the computational domain (Timestep = 100)	116
83	Cross-section of the applied absorbing boundary layer (PML) to the computational domain (Timestep = 300)	117
84	Cross-section of the applied absorbing boundary layer (PML) to the computational domain (Timestep = 1000)	117
85	Comparison cross-section of the applied incorrect boundary layer and the applied absorbing boundary layer (PML) at timestep = 300	118
86	Global error illustration	121
87	Comparison between Global error and PML layers	122
88	Comparison between Global error and maximum conductivity	122
89	The quaternary H - field around the narrow feeding gap	124
90	The one-cell gap model of a thin-wire dipole antenna	124
91	Geometry for the reference model	128
92	MRI Images of PD, T1 and T2 at layer 26 th	129
93	MRI machine	130
94	Artificial human head cross-section at layer 26 th created by computer	131
95	Artificial human head side view created by computer	131
96	Cell surface with in inhomogeneous medium	134
97	E_x, E_y and E_z field components	136

LIST OF FIGURES (Continued)

Figure		Page
98	Sample figure of the spatial-average SAR 1-g, located at the position closed to dipole feeding gap	138
99	Sample figure of the spatial-average SAR 10-g, located at the position closed to dipole feeding gap	139
100	Sample figure of the spatial-average SAR _{Cell-1} 1-g, SAR _{Cell-2} 1-g, and so on located by the incremental n	140
101	The comparison graph of the normalized spatial-average SAR _{Cell n} 1-g at various distances in a human head between the method of using averaged dielectric constant in a human head and the simple method	141
102	The comparison bar of the spatial-average SAR _{Cell-1} 1-g, SAR _{Cell-2} 1-g and SAR _{Cell-3} 1-g in the reference model	142
103	The comparison bar of the spatial-average SAR _{Cell-1} 1-g and SAR _{Cell-1} 10-g between 900 MHz and 1.8 GHz in the reference model	143
104	The comparison bar of the average power absorbed by any material in a human head between 900 MHz and 1.8 GHz in the reference model	144
105	The simulation of a mobile phone located at 1 cm from a human head and a mobile phone operated at 900 MHz (the reference model). The simulation start from 0 and end with 1000Δt	146
106	The simulation of a mobile phone located at 1 cm from a human head and a mobile phone operated at 1.8 GHz (the reference model). The simulation start from 0 and end with 1000Δt	147
107	The quaternary <i>H</i> - field around the one-cell gap model	149
108	Guideline for the formulation of the one-cell gap model	150
109	Field locations and geometry for thin wire	151
110	Field locations of the improved one-cell gap model	153
111	Field locations of the infinitesimal gap model	155
112	The improved one-cell gap model is the infinitesimal gap model	157

LIST OF FIGURES (Continued)

Figure		Page
113	The summary of the improved one-cell gap model or the infinitesimal gap model	158
114	The H - field component no.1	159
115	Spatial field locations for H - field component no.1	160
116	The summary of the finite gap model no.1	162
117	Spatial field locations for H - field component no.2	163
118	The summary of the finite gap model no.2	165
119	Spatial field locations for H - field component no.3	166
120	The summary of the finite gap model no.3	168
121	Spatial field locations for H - field component no.4	169
122	The summary of the finite gap model no.4	171
123	Spatial E_z - field locations surround the dipole	174
124	The two general forms of the dipole feeding gap	176
125	The Electromagnetic Cycle (EM-Cycle)	177
126	Geometry for the simulated dipole feeding gap	178
127	Geometry for the reduced domain	178
128	Geometry for the FDTD simulation of a mobile phone operating near a Metal Wall	179
129	Sample of the feeding signal for the one-cell gap model, the infinitesimal gap model and the finite gap model, $\frac{l}{\Delta} = 21$	180
130	Comparison of the electromagnetic field (E_{Total} , dB) simulated by the one-cell gap model, the infinitesimal gap model and the finite gap model $\frac{\Delta z_0}{\Delta z} = 0.85$, respectively, at timestep = 100	181

LIST OF FIGURES (Continued)

Figure		Page
131	Comparison of the electromagnetic field (E_{Total} , dB) simulated by the one-cell gap model, the infinitesimal gap model and the finite gap model $\frac{\Delta z_0}{\Delta z} = 0.85$, respectively, at timestep = 200	182
132	Sample of the feeding signal for the one-cell gap model, the infinitesimal gap model and the finite gap model, $\frac{l}{\Delta} = 41$, Timestep = 4096	183
133	The input impedance simulated by the commercial software, XFDTD	185
134	The input impedance simulated by MoM and the FDTD programming	185
135	Comparison the input impedance simulated by MoM, $N = 128$, and the one-cell gap model, $l/r_0 = 256$	186
136	Comparison the return loss simulated by MoM, $N = 128$, and the one-cell gap model, $l/r_0 = 256$, $Z_S = 50 \Omega$	186
137	Comparison the return loss simulated by MoM, $N = 128$, and the one-cell gap model, $l/r_0 = 256$, $Z_S = 75 \Omega$	187
138	Comparison the return loss simulated by MoM, $N = 128$, and the one-cell gap model, $l/r_0 = 256$, $Z_S = 73 + j42.5 \Omega$	187
139	Comparison the input impedance simulated by MoM, $N = 128$, and the infinitesimal gap model, $l/r_0 = 256$	188
140	Comparison the return loss simulated by MoM, $N = 128$, and the infinitesimal gap model, $l/r_0 = 256$, $Z_S = 50 \Omega$	188
141	Comparison the return loss simulated by MoM, $N = 128$, and the infinitesimal gap model, $l/r_0 = 256$, $Z_S = 75 \Omega$	189
142	Comparison the return loss simulated by MoM, $N = 128$, and the infinitesimal gap model, $l/r_0 = 256$, $Z_S = 73 + j42.5 \Omega$	189

LIST OF FIGURES (Continued)

Figure		Page
143	Comparison the input impedance simulated by MoM, $N = 128$, the infinitesimal gap and the finite gap model, $l / r_0 = 256$	190
144	Comparison the return loss simulated by MoM, $N = 128$, the infinitesimal gap and the finite gap model, $l / r_0 = 256$, $Z_S = 50 \Omega$	190
145	Comparison the return loss simulated by MoM, $N = 128$, the infinitesimal gap and the finite gap model, $l / r_0 = 256$, $Z_S = 75 \Omega$	191
146	Comparison the return loss simulated by MoM, $N = 128$, the infinitesimal gap and the finite gap model, $l / r_0 = 256$, $Z_S = 73 + j42.5 \Omega$	191
147	The simulation of a mobile phone located at 1 cm from a human head with a truncated domain and a mobile phone operated at 900 MHz. The simulation start from 0 and end with $1000\Delta t$	192
148	The simulation of a mobile phone located at 1 cm from a human head with a truncated domain and a mobile phone operated at 1.8 GHz. The simulation start from 0 and end with $1000\Delta t$	193
149	Top view of E_t in the simulated physical domain (Operating frequency = 900 MHz and $\Delta l = 1$ cm.)	194
150	Top view of E_t in the simulated physical domain (Operating frequency = 900 MHz and $\Delta l = 5$ cm.)	194
151	Top view of E_t in the simulated physical domain (Operating frequency = 900 MHz and $\Delta l = 10$ cm.)	195
152	Top view of E_t in the simulated physical domain (Operating frequency = 900 MHz and $\Delta l = 15$ cm.)	195

LIST OF FIGURES (Continued)

Figure		Page
153	Top view of E_t in the simulated physical domain (Operating frequency = 900 MHz and $\Delta l = 20$ cm.)	196
154	Top view of E_t in the simulated physical domain (Operating frequency = 1.8 GHz and $\Delta l = 1$ cm.)	198
155	Top view of E_t in the simulated physical domain (Operating frequency = 1.8 GHz and $\Delta l = 5$ cm.)	198
156	Top view of E_t in the simulated physical domain (Operating frequency = 1.8 GHz and $\Delta l = 10$ cm.)	199
157	Top view of E_t in the simulated physical domain (Operating frequency = 1.8 GHz and $\Delta l = 15$ cm.)	199
158	Top view of E_t in the simulated physical domain (Operating frequency = 1.8 GHz and $\Delta l = 20$ cm.)	200
159	Spatial- average SAR 1-g respecting to the distance between the Metal Wall and the antenna, Δl	202
160	Spatial- average SAR 10-g respecting to the distance between the Metal Wall and the antenna, Δl	202
161	Total average power absorbed in human head respecting to the distance between the Metal Wall and the antenna, Δl	205
162	The average power absorbed (P_{avg}) in Skin respecting to the distance between the Metal Wall and the antenna, Δl	205
163	The average power absorbed (P_{avg}) in Bone respecting to the distance between the Metal Wall and the antenna, Δl	206
164	The average power absorbed (P_{avg}) in Muscle respecting to the distance between the Metal Wall and the antenna, Δl	206
165	The average power absorbed (P_{avg}) in Fat respecting to the distance between the Metal Wall and the antenna, Δl	207

LIST OF FIGURES (Continued)

Figure	Page
166	The average power absorbed (P_{avg}) in Eye respecting to the distance between the Metal Wall and the antenna, Δl
207	
167	The average power absorbed (P_{avg}) in Brain respecting to the distance between the Metal Wall and the antenna, Δl
208	
168	The average power absorbed (P_{avg}) in Blood respecting to the distance between the Metal Wall and the antenna, Δl
208	
169	The practical dipole
210	
170	How to insert interested material to the EM-Cycle
211	
Appendix Figure	
A1	The diagram of how to verify the electromagnetic simulation software
223	
A2	The diagram of the reference model
224	
A3	The diagram of the dipole feeding gap model
225	
A4	The diagram of the proposed model
226	
A5	The diagram of the electromagnetic simulation software
227	

LIST OF ABBREVIATIONS

ANSI	=	American National Standards Institute
CST [®]	=	Computer Simulation Technology
EM-Cycle	=	Electromagnetic Cycle
EMC	=	Electromagnetic Compatibility
EMI	=	Electromagnetic Interference
FCC	=	Federal Communications Commission
FDA	=	Food and Drug Administration
FDTD	=	Finite Difference Time Domain
IEEE	=	Institute of Electrical and Electronics Engineers
LAN	=	Local Area Network
MATLAB [®]	=	Matrix Laboratory
MoM	=	Method of Moments, Moment Methods
MRI	=	Magnetic Resonance Imaging
NCRP	=	National Council on Radiation Protection and Measurements
P_{avg}	=	Average Power
PEC	=	Perfect Electric Conductor
PML	=	Perfectly Matched Layer
RE	=	Round Error
RECAPE	=	Research Center of Applied Electromagnetic
RF	=	Radio Frequency
RLE	=	Relative Error
SAR	=	Specific Absorption Rate
XFDTD [®]	=	3D Electromagnetic Simulation Software

IMPLEMENTATION OF PERFECTLY MATCHED LAYER (PML) IN THE FINITE DIFFERENCE TIME DOMAIN (FDTD) SIMULATION OF A MOBILE PHONE OPERATING NEAR A METAL WALL

INTRODUCTION

In recent years wireless communication has gained popularity because of its mobile capability. In other words, the users can access to the communication network without hooking up to a communication outlet. Mobile phone, for example, is commonly used wireless communication equipment that allows the users to be free from the telephone outlet. The mobile capability is achieved by the radiation. All mobile phones have an antenna which plays a key role in the radiation. The antenna produces electromagnetic wave to carry the information from the transmitter to the remote receiver. Dipole is one of the simplest antennas, which is usually integrated with commercial wireless communication devices such as a mobile phones, Local Area Network (LAN), routers and etc. The dipole is made from a two metal wire with a center fed. In theory, the feeding gap must be infinitesimal gap. However, in practical, it does have a physical dimension.

It is believed that the invisible electromagnetic wave generated by the continuous power fed to the antenna is harmful to the human, especially to the operating user. Although, there is no strong scientific evidence to prove that the using mobile phone can lead to health hazards—memory loss, headache, tumor and cancer, however, the Food and Drug Administration (FDA) has been continued to monitor the updated scientific research reports on these topic. Correspondingly, the Federal Communications Commission (FCC) has released guidelines specifying the limits for the human exposure to the radio frequency (RF) emissions from the hand-held mobile phones in terms of the Specific Absorption Rate (SAR). SAR is a measure of the rate of absorption of the RF energy by the human body. The limit of SAR is 1.6 watts per kilogram (1.6 W/kg), which is averaged over one gram mass of tissues. It is known as “SAR 1-g”. The commercial mobile phone is required to meet this specification.

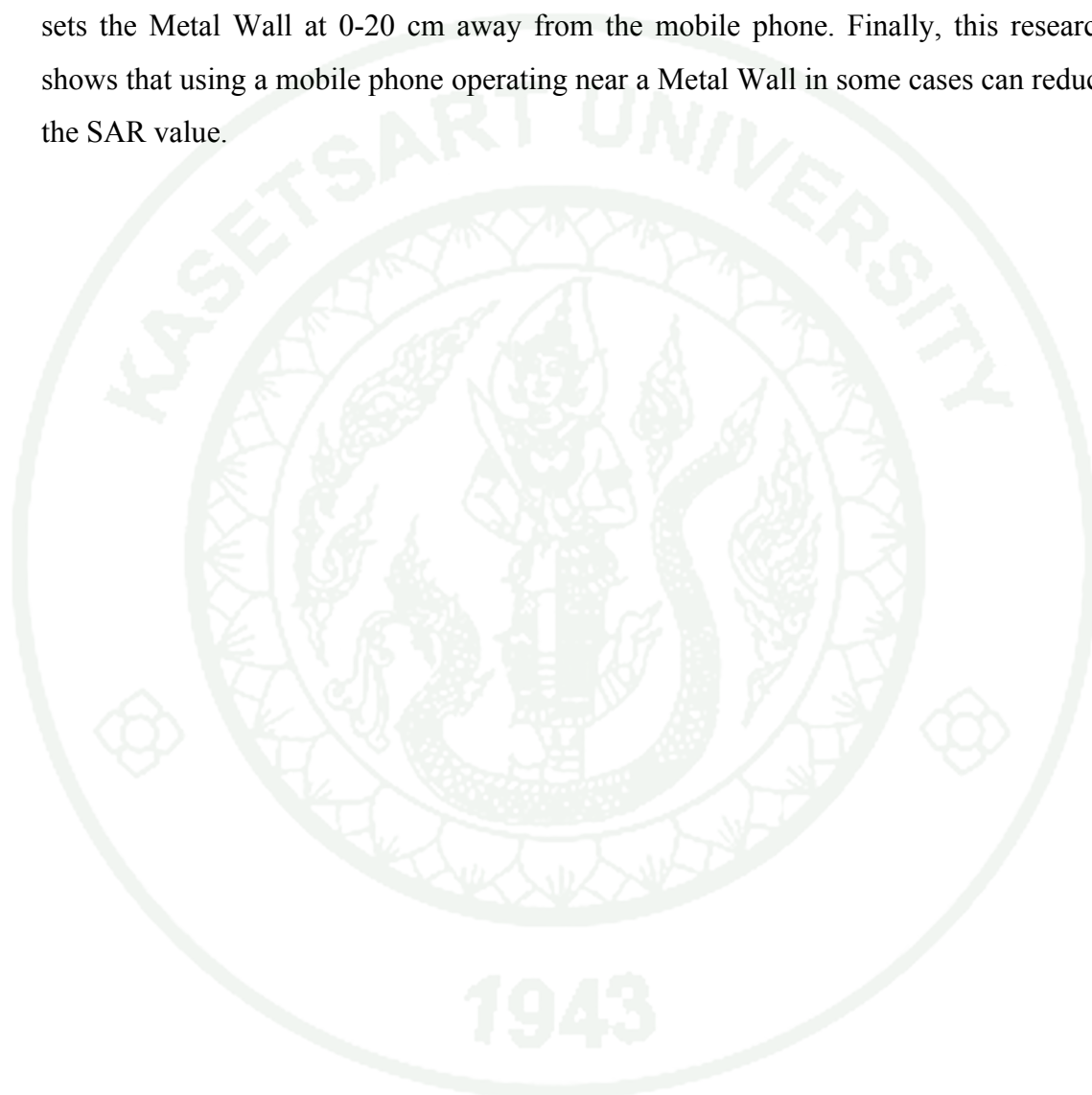
SAR determination can be implemented by either experimental based measurement or computer simulation. In order to setup the experimental measurement, an artificial human head is to be built. Typically, the dimension is based on a size of a large adult male head. The human head model is then filled with a type of liquid that has the same dielectric properties as a human head tissue. A scientific probe is inserted to measure the SAR. The probe establishes a reference point in the phantom closed to the mobile phone.

Computer simulation is much cheaper than the first technique. The researchers usually create a dipole antenna as well as the wireless mobile phone in the computer model. Fortunately, dipole antennas are easy to be model on the computer. Specially, the dipole model acts as electromagnetic source. Meanwhile, a realistic human head can be modeled by a technique of Magnetic Resonance Imaging (MRI). Also, the absorbing boundary condition is implemented using an absorbing boundary layer.

Both experiment and simulation, in practice, focus on the frequency bands of 900 MHz and 1.8 GHz, which are the bands assigned for commercial mobile phone. It is obvious that the SAR increases as the transmit power increases. Many researches draw the same conclusion that SAR is frequency dependent; the absorption at 1.8 GHz is lower than at 900 MHz. Both parameters, in practice, cannot be adjusted. The interest then goes to the answer of the question “Is there any other way to reduce the SAR value?”

This research covers theoretical development on generalization of feeding gap models for dipole antenna, invention of generally-used the Finite Difference Time Domain (FDTD) simulation tools and investigation of a method to reduce the SAR. The one-cell gap model, the infinitesimal gap model and the finite gap model are generalized. It is shown that the improved one-cell feeding gap of FDTD simulation is similar to the infinitesimal gap model. Correspondingly, the advantage of the finite gap model is that it represents a good model of the practical dipole antenna. Furthermore, the finite gap's equations are compatible with the Electromagnetic Cycle (EM-Cycle). An FDTD computer program is developed and verified by comparing both the input

impedance and the return loss with known values from the Exact Solution and the Moment Methods (MoM). In this case, Perfectly Matched Layer (PML) is used as the absorbing boundary layer through the investigation. In addition, PML acts as an electromagnetic fields absorbing layer and is backed by a Perfect Electric Conductor (PEC). The simulation sets a mobile phone at 1 cm from the artificial human head and sets the Metal Wall at 0-20 cm away from the mobile phone. Finally, this research shows that using a mobile phone operating near a Metal Wall in some cases can reduce the SAR value.



OBJECTIVES

1. This research proposes how to verify the Finite Difference Time Domain (FDTD) programming. The FDTD programming was verified by comparison of the input impedance and the return loss to the Method of Moments (MoM).
2. This research generalizes the Hallen's Integral Equation in order to compute the antenna input impedance and return loss by MoM. It is implemented in the FDTD programming.
3. This research proposes the Multigrid methods so as to improve the rate of convergence of Gauss-Seidel method.
4. This research improves FDTD model for the feeding gap of a dipole antenna. Also, this research compares the input impedance and the return loss among the one-cell gap model, the infinitesimal gap model and the finite gap model.
5. This research proposes that the simulation domain can be greatly reduced in order to save both computer simulation time and storage memory.
6. This research studies the heating effect from a Metal Wall.
7. In some cases, the simulation results show that SAR 1-g and SAR 10-g values are reduced when a mobile phone operating near a Metal Wall.

LITERATURE REVIEW

The Verification of the Electromagnetic Simulation Software

All too commonly in the first section is about the verification of the electromagnetic simulation software (Appendix Figure A1), there are three important schemes: the Analytical Approach (the Exact Solution), the Moment Methods (MoM) and the Finite Difference Time Domain (FDTD), in order to simulate a dipole antenna. First of all, the Exact Solution is derived by Constantine A. Balanis (Balanis, 2005). Second, the MoM calculation is derived from Hallen's Integral Equation and it has been generalized by Mei (Mei, 1965; Lan *et al.*, 1999). Last but not least, the FDTD calculation is the time domain method; its solution covers a wide frequency range with a single simulation run. In conclusion, the FDTD calculation is the most popular field computational technique. The results are as the following aspects:

1. The Analytical Approach (The Exact Solution)

1.1 A dipole antenna

An antenna is defined by Oxford Advanced Learner's Dictionary as "a piece of equipment made of wire or long straight pieces of metal for receiving or sending radio and television signals". There are seven types of antennas: Wire Antennas, Aperture Antennas, Microstrip Antennas, Array Antennas, Reflector Antennas, Lens Antennas and Nano Antennas. Generally, a dipole antenna is a wire antenna; simplest and cheapest antenna, as shown in Figure 1. It should be noted that this section only simulates a dipole antenna.



Figure 1 The commercial dipole antenna.

There are three types of dipole antennas: an infinitesimal dipole, a small dipole and a finite length dipole. First, the infinitesimal dipole is the infinitesimal linear wire ($l \ll \lambda$). Unfortunately, it is impractical due to its dimension. Next, the small dipole is bigger than the infinitesimal dipole ($\lambda/50 < l \leq \lambda/10$). Its current distribution is set to be constant so a constant current distribution is not realizable. Last, the finite length dipole is very thin dipole ($\lambda/2 \leq l < \lambda, a \approx 0$). In other words, the finite length dipole has a negligible diameter.

1.2 Current distribution

In general, the electric lines of force are detached from a dipole antenna to form the Free-Space waves because two opposite charges (+, -) are moving between the ends of the dipole antenna. The opposite charge leads to a displacement current density ($j\omega\epsilon\bar{E}$). Then, the displacement current density gives rise and fall to electromagnetic wave propagating outward from the dipole antenna, as shown in Figure 2. After that, this process is repeated itself. In addition, the moving charges is required to excite the fields but is not needs to sustain them and may exist in its absence.

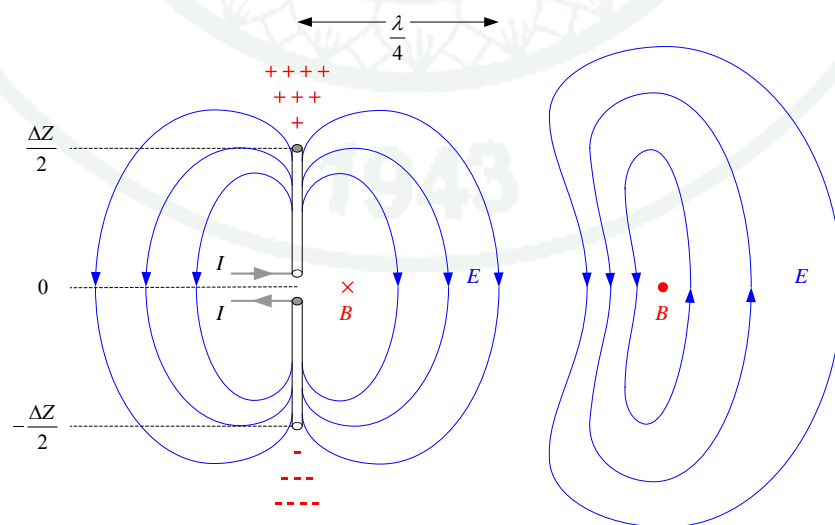


Figure 2 Formation of electric field lines for a dipole antenna.

It is apparent that the movement of two charges produces a stationary wave current, also known as current distribution. It is a wave current that remains in a constant position. In addition, it can arise in a dipole antenna as a result of interference between two charges traveling in opposite direction. In this case, current distribution is assumed to sinusoidal so that the dipole antenna is center-fed and the current vanishes at the end points ($Z/2, -Z/2$), as shown in Figure 3.

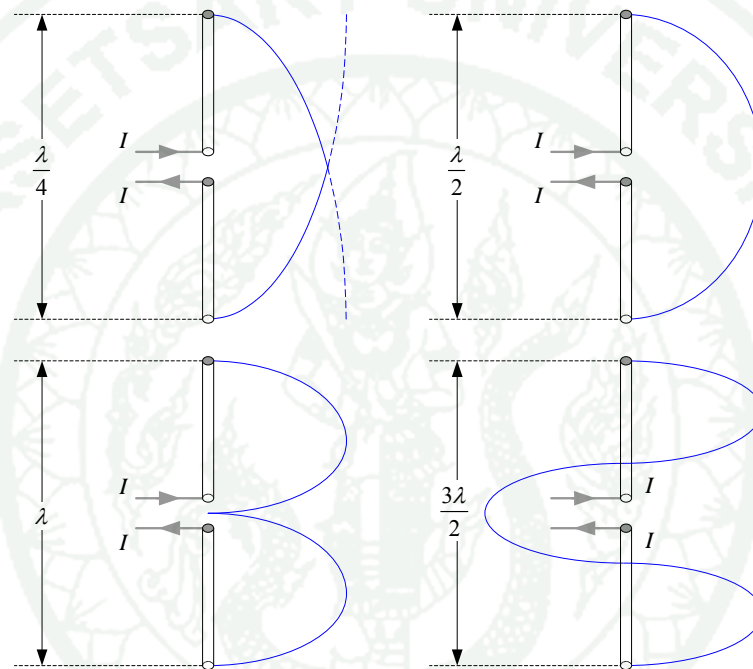


Figure 3 The stationary wave current for various center-fed dipoles.

1.3 Input impedance

Generally, the input impedance of an antenna is defined as the ratio of the voltage to current at its terminals, with no load attached. It is important that the input impedance always occurs at a pair of terminals of a dipole antenna. Besides, the dipole antenna is assumed isolated. The input impedance is consisted of real and imaginary parts ($Z_i(f) = R_i + jX_i$), as shown in Figure 4. The former, the input resistance R_i represents power dissipation, which dissipated power in two ways: antenna heating and the radiation, respectively. The latter, the input reactance X_i represents power

stored in the near field of the antenna. Its behavior is a bit like the way a capacitor or inductor can store electrical energy and release it, returning to the generator.

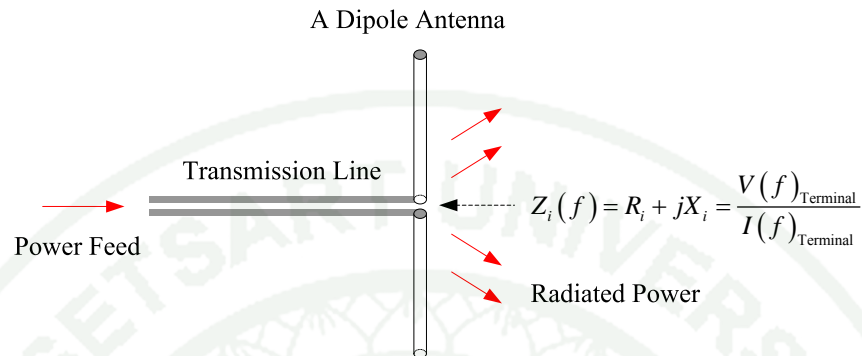


Figure 4 The input impedance of a dipole antenna.

The input impedance of an ideal dipole antenna always matches the impedance of the signal generator, as shown in Figure 5, in order that an ideal dipole antenna will accept all the power sent to it from a generator and radiate it away into Free-Space— Maximum power transfer. Matching is obtained when $R_i = R_g$.

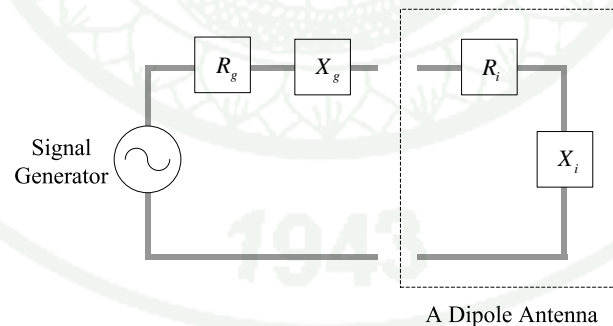


Figure 5 The impedance matching.

1.4 Radiation impedance

The radiation impedance of an antenna is defined as the ratio of the voltage to the maximum current, because some dipole: $L = \lambda, 2\lambda$, etc., has zero current magnitude at input terminals. However, the radiation impedance is similar to the input impedance because it is consisted of real and imaginary parts ($Z_r(f) = R_r + jX_r$). This generalized impedance has a real part R_r representing a radiation resistance, and an imaginary part X_r representing a radiation reactance. The radiation impedance is shown as follow (Balanis, 2005)

$$R_r = \frac{\eta}{2\pi} \left\{ C + \ln(kl) - C_i(kl) + \frac{1}{2} \sin(kl) [S_i(2kl) - 2S_i(kl)] \right. \\ \left. + \frac{1}{2} \cos(kl) \left[C + \ln\left(\frac{kl}{2}\right) + C_i(2kl) - 2C_i(kl) \right] \right\} \quad (1)$$

$$X_r = \frac{\eta}{4\pi} \left\{ 2S_i(kl) + \cos(kl) [2S_i(kl) - S_i(2kl)] \right. \\ \left. - \sin(kl) \left[2C_i(kl) - C_i(2kl) - C_i\left(\frac{2ka^2}{l}\right) \right] \right\} \quad (2)$$

R_r = Radiation resistance.

X_r = Radiation reactance.

$C = 0.5772$ (Euler's constant).

C_i = The cosine integrals.

S_i = The sine integrals.

k = Wavenumber $\left(\frac{2\pi}{\lambda}\right)$, Wavelength per unit distance.

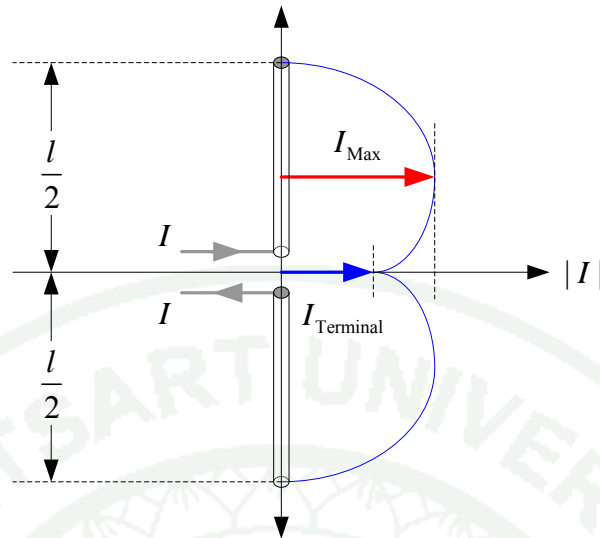


Figure 6 The current maximum does not occur at the input terminal.

For a dipole antenna of length l , the current at input terminal is related to the current maximum as the following equation

$$I_{\text{Terminal}} = I_{\text{Max}} \sin\left(k \frac{l}{2}\right) \quad (3)$$

Clearly, the input resistance (R_i) can be derived from the radiation resistance (R_r). The antenna itself assumed to be lossless so the power at the input terminal is equal to the power at the current maximum.

$$P_{I,\text{Terminal}} = P_{I,\text{Max}}$$

$$\left| \frac{I_{\text{Terminal}}}{\sqrt{2}} \right|^2 R_i = \left| \frac{I_{\text{Max}}}{\sqrt{2}} \right|^2 R_r$$

$$R_i = \left| \frac{I_{\text{Max}}}{I_{\text{Terminal}}} \right|^2 R_r \quad (4)$$

Replacing Equation (3) in Equation (4), thus the input resistance can be written as

$$R_i = \frac{R_r}{\sin^2\left(k\frac{l}{2}\right)} \quad (5)$$

Correspondingly, the input reactance (X_i) can be derived from Equation (2), with the same manner. Finally, the input reactance can be expressed as the following equation

$$X_i = \frac{X_r}{\sin^2\left(k\frac{l}{2}\right)} \quad (6)$$

The comparison graph between the radiation impedance and the input impedance is plotted by vary dipole length per wavelength (l/λ).

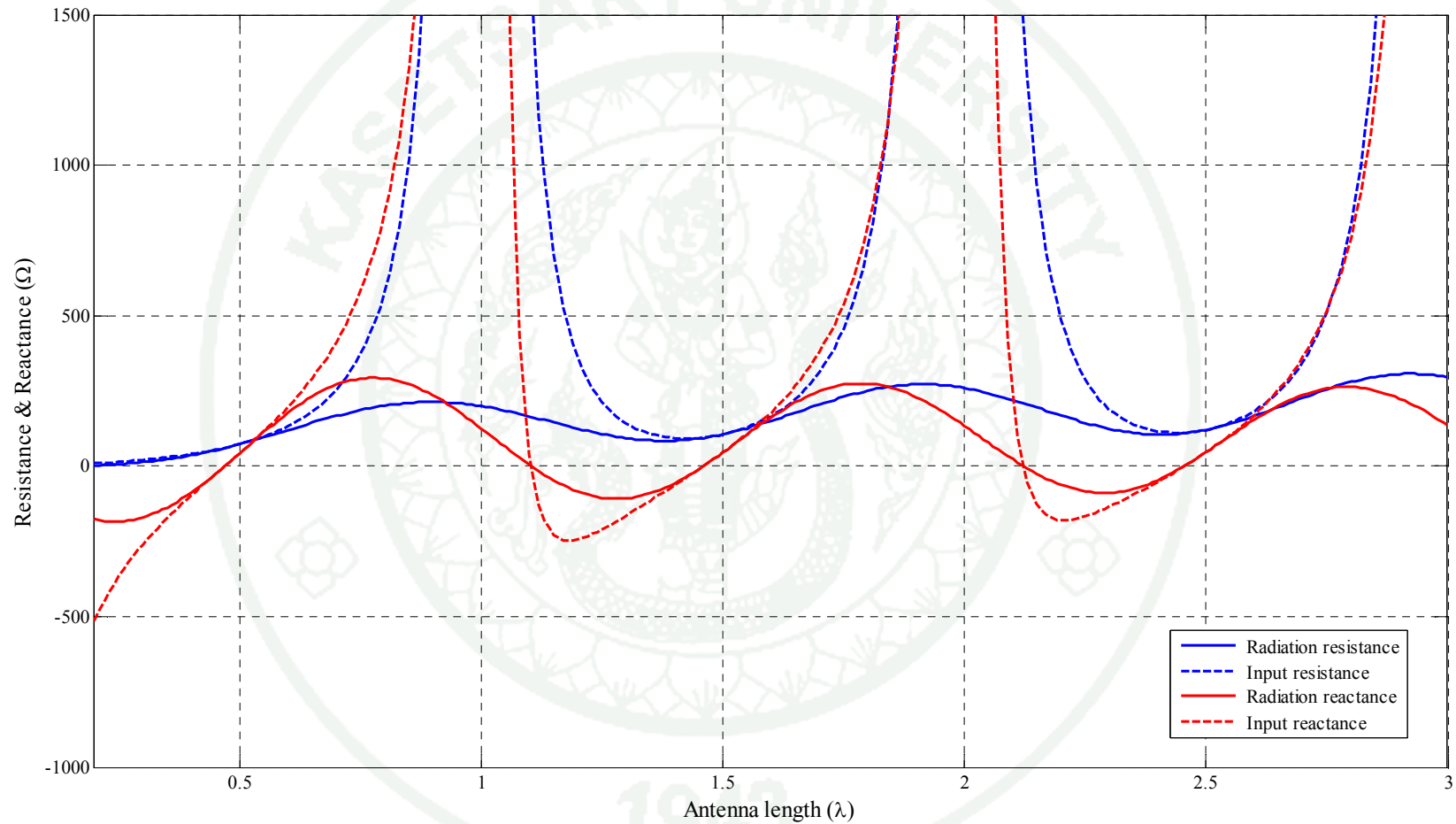


Figure 7 The comparison graph between the radiation impedance and the input impedance, radius of a dipole (a) = $l / 128 \lambda$.

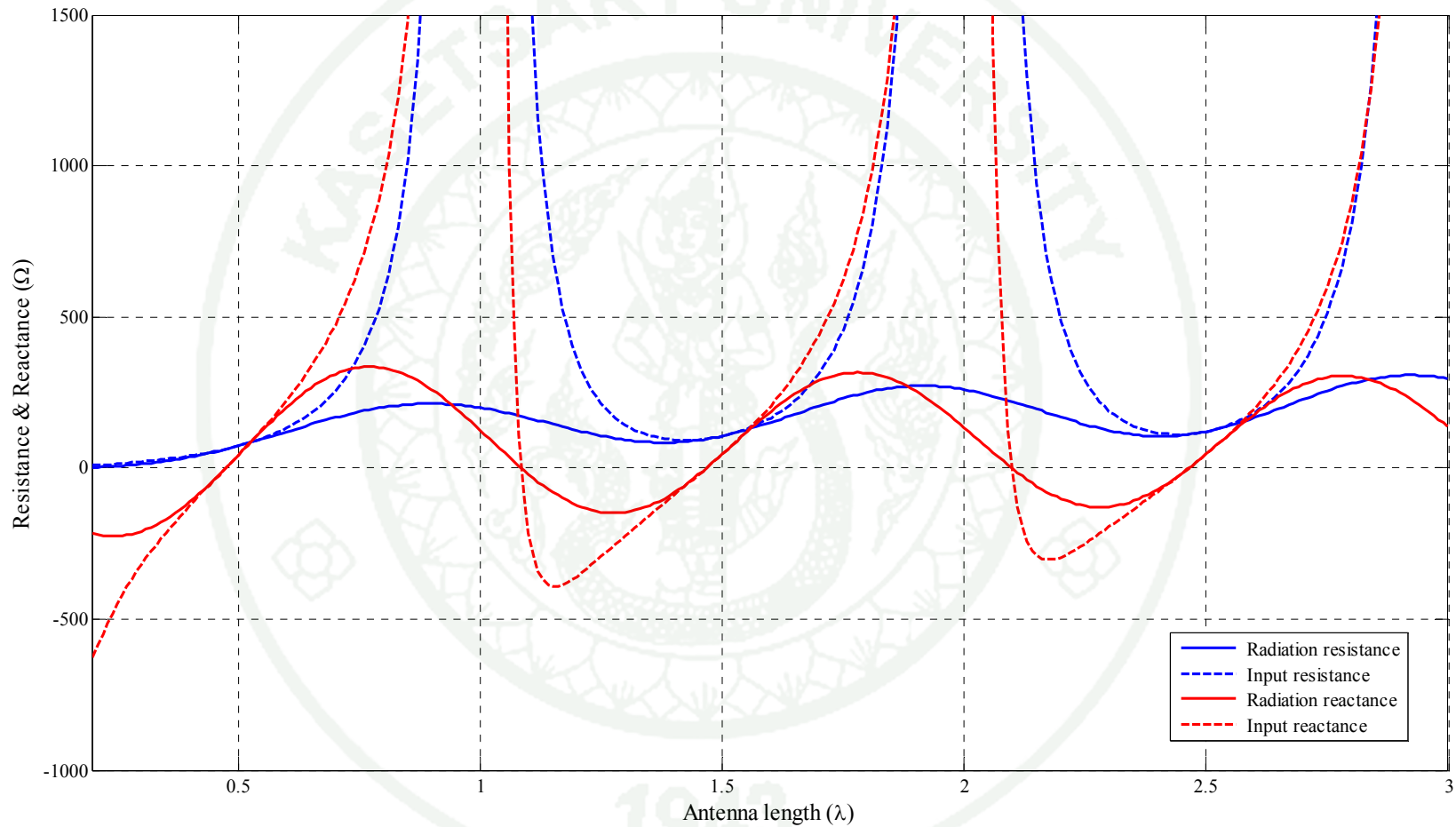


Figure 8 The comparison graph between the radiation impedance and the input impedance, radius of a dipole (a) = $l/256\lambda$.

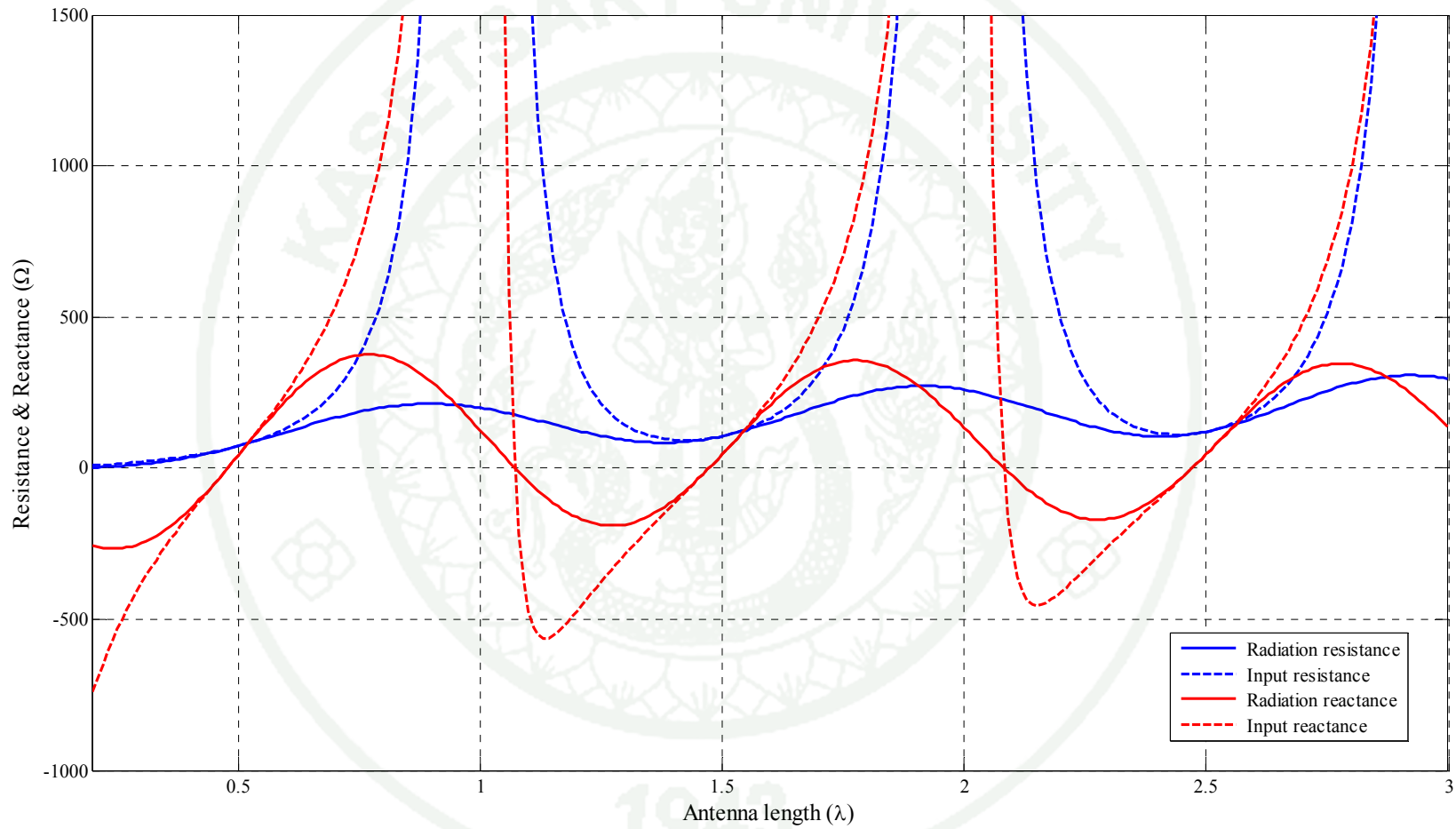


Figure 9 The comparison graph between the radiation impedance and the input impedance, radius of a dipole (a) = $l / 512 \lambda$.

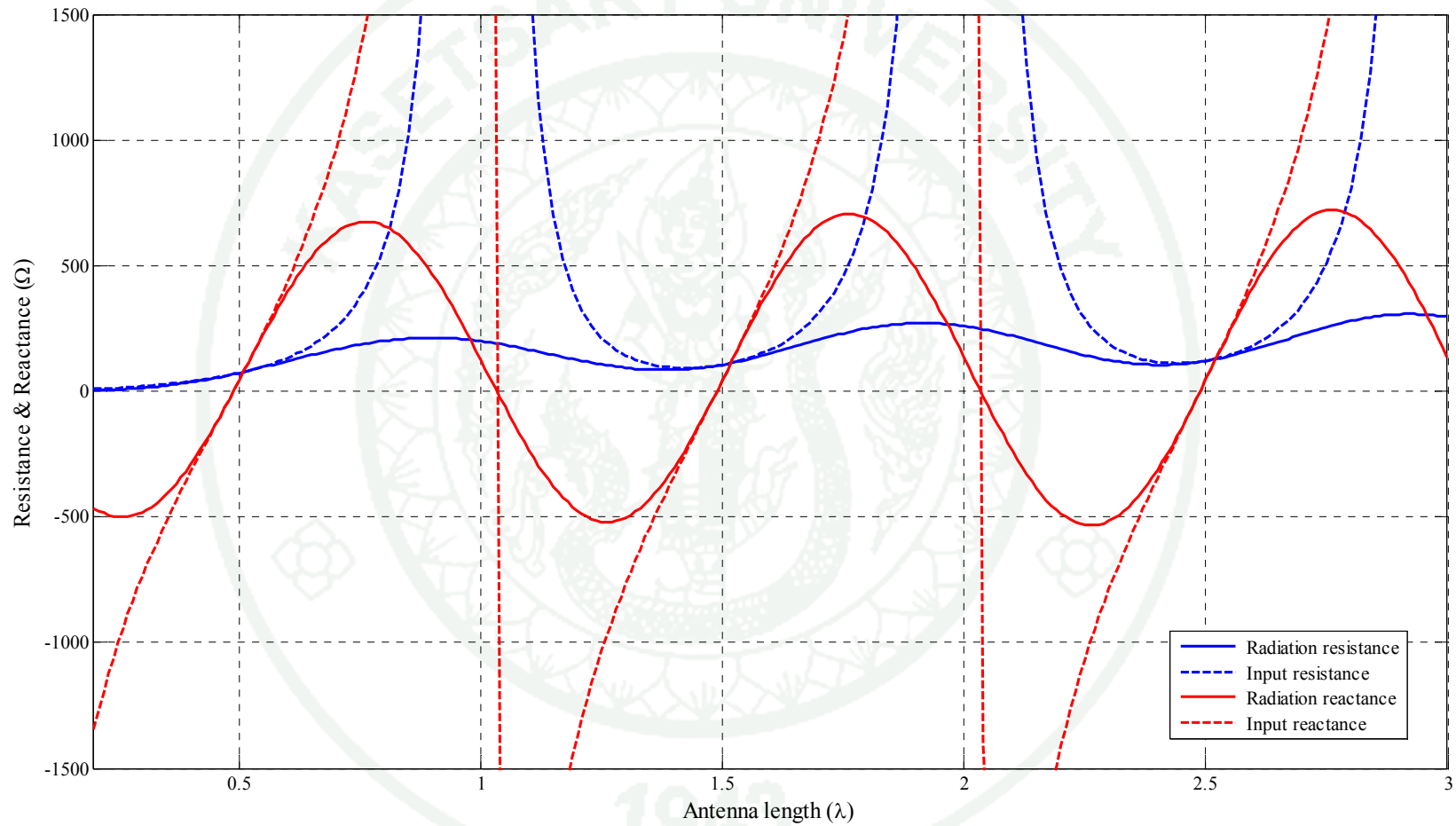


Figure 10 The comparison graph between the radiation impedance and the input impedance, radius of a dipole $(a) = 0.00001 \lambda$.

2. The Method of Moments (MoM)

2.1 Inner product spaces

An inner product (or scalar product) on a complex vector space V is a mapping $\langle \cdot, \cdot \rangle: V \times V \rightarrow \mathbb{C}$ such that, for all $x, y, z \in V$ and all $\lambda \in \mathbb{C}$, (Young, 1988)

2.1.1 $\langle x, y \rangle = \overline{\langle y, x \rangle}$ is called Conjugate Symmetry.

2.1.2 $\langle \lambda x, y \rangle = \lambda \langle x, y \rangle$ is called Linearity.

2.1.3 $\langle x + y, z \rangle = \langle x, z \rangle + \langle y, z \rangle$ is called Linearity.

2.1.4 $\langle x, x \rangle > 0$ when $x \neq 0$ is called Positive-definiteness.

An inner product space (or pre-Hilbert space) is a pair $\langle V, \langle \cdot, \cdot \rangle \rangle$ where V is a complex vector space and $\langle \cdot, \cdot \rangle$ is an inner product on V . The property of an inner product space V is the following aspects

2.1.5 $\langle x, y + z \rangle = \langle x, y \rangle + \langle x, z \rangle$.

$$\begin{aligned} \langle x, y + z \rangle &= \overline{\langle y + z, x \rangle} \\ &= \overline{\langle y, x \rangle + \langle z, x \rangle} \\ &= \overline{\langle y, x \rangle} + \overline{\langle z, x \rangle} \\ &= \langle x, y \rangle + \langle x, z \rangle. \end{aligned}$$

2.1.6 $\langle x, \lambda y \rangle = \bar{\lambda} \langle x, y \rangle$.

$$\langle x, \lambda y \rangle = \overline{\langle \lambda y, x \rangle} = \bar{\lambda} \overline{\langle y, x \rangle} = \bar{\lambda} \langle x, y \rangle.$$

2.1.7 $\langle x, 0 \rangle = 0 = \langle 0, x \rangle$.

2.1.8 If $\langle x, z \rangle = \langle y, z \rangle$ for all $z \in V$ then $x = y$.

$$\begin{aligned} \text{If } \langle x, z \rangle &= \langle y, z \rangle \text{ then } 0 = \langle x, z \rangle + (-1) \langle y, z \rangle \\ &= \langle x, z \rangle + \langle -y, z \rangle = \langle x - y, z \rangle = \langle 0, z \rangle. \quad \therefore x = y. \end{aligned}$$

2.2 Linear operators

In computational electromagnetics or some important metric notions such as length, angle and the energy of physical systems can be expressed in terms of the inner product. Also, MoM is based on linear operator (L) and an inner product $\langle f, g \rangle$. An inner product $\langle f, g \rangle$ on a complex linear space is a complex-valued scalar satisfying (Pan, 2003)

$$\langle f, g \rangle = \overline{\langle g, f \rangle} \quad (7)$$

$$\langle \alpha f + \beta g, h \rangle = \overline{\alpha} \langle f, h \rangle + \overline{\beta} \langle g, h \rangle \quad (8)$$

$$\langle f, f \rangle = \|f\|^2 \begin{cases} > 0 & \text{if } f \neq 0 \\ = 0 & \text{if } f = 0 \end{cases} \quad (9)$$

Where the over bar denotes the complex conjugate. Corresponding, almost all of the mathematical equations can be expressed as (Young, 1988)

$$Lf = g \quad (10)$$

Here L is linear operator, g is given excitation and f is unknown function. The inverse operator of L is denoted as L^{-1} . For instance, the typical solution is

$$f = L^{-1}g \quad (11)$$

In computational electromagnetics, a linear operator is represented by a matrix. Moreover, the unknown function $f(x)$ can be expanded in terms of the basis functions $f_n(x)$ with unknown coefficients α_n namely

$$f = \sum_{n=1}^N \alpha_n f_n \quad (12)$$

$$L \sum_{n=1}^N \alpha_n f_n = g \quad (13)$$

Multiplying both side of Equation (13) by the weighting (testing) function (W_m) and taking the inner product $\langle \cdot, \cdot \rangle$ then

$$\sum_{n=1}^N \alpha_n \langle W_m, Lf_n \rangle = \langle W_m, g \rangle \quad (14)$$

This equation can be rewritten in matrix form as

$$[l_{mn}] |\alpha\rangle = |g\rangle, \quad (15)$$

It appears as

$$[l_{mn}] = \begin{bmatrix} \langle W_1, Lf_1 \rangle & \cdots & \langle W_1, Lf_N \rangle \\ \vdots & \ddots & \vdots \\ \langle W_N, Lf_1 \rangle & \cdots & \langle W_N, Lf_N \rangle \end{bmatrix}_{N \times N} \leftarrow \text{Evaluated,}$$

$$|\alpha\rangle = \begin{bmatrix} \alpha_1 \\ \alpha_2 \\ \vdots \\ \alpha_N \end{bmatrix}_{N \times 1} \leftarrow \text{Unknown,}$$

$$|g\rangle = \begin{bmatrix} \langle W_1, g \rangle \\ \langle W_2, g \rangle \\ \vdots \\ \langle W_N, g \rangle \end{bmatrix}_{N \times 1}$$

Finally, this formal equation is solved to yield (Pan, 2003)

$$|\alpha\rangle = [l_{mn}]^{-1} |g\rangle \quad (16)$$

2.3 The methods of weighted residual

Methods of weighted residual are useful to obtain approximate solutions to a differential governing equation. In order to explain the methods, we consider the following classical problem (Kwon and Bang, 1996)

$$f(x) = \frac{d^2U(x)}{dx^2} - U(x) = -x, \quad (0 < x < 1)$$

and boundary conditions are

$$\text{boundary condition } \begin{cases} U(0) = 0 \\ U(1) = 0 \end{cases}$$

First, we assume the trial function, $\tilde{U}(x) = ax(1-x)$, is selected as an approximate to $U(x)$. Also, the trial function is chosen here such that it satisfies the boundary conditions a $\tilde{U}(0) = 0$ and $\tilde{U}(1) = 0$, and it has one unknown coefficient a to be determined. Once a trial function is selected, residual is computed by substituting the trial function into the differential equation. That is, the residual $R(x)$ becomes.

$$\begin{aligned} R(x) &= \left(d^2\tilde{U}(x) / dx^2 - \tilde{U}(x) \right) - (-x) \\ &= \frac{d^2(ax - ax^2)}{dx^2} - (ax - ax^2) + x \\ &= ax^2 + (1-a)x - 2a \end{aligned}$$

Because $\tilde{U}(x)$ is different from the Exact Solution, the residual does not vanish for all values of x within the domain. The next step is to determine the unknown constant a such that the chosen test function best approximates the Exact Solution. In this case, the weighting function $W(x)$ is selected and the weighted average of the residual over the problem domain is set to zero. That is

$$\int_0^1 W(x)R(x)dx = ax^2 + (1-a)x - 2a = 0$$

In this research, we use Collocation method, which uses the Dirac delta function, $\delta(x-x_i)$. Its definition is $\delta(x) \begin{cases} \infty & x=0 \\ 0 & x \neq 0 \end{cases}$. Also its properties are

$$\int_{-\infty}^{\infty} \delta(x)dx = 1 \quad \text{and} \quad \int_{x_i-\delta}^{x_i+\delta} f(x)\delta(x-x_i)dz = f(x_i).$$

The sampling point x_i must be within the domain, ($0 < x_i < 1$). In other words, $W_i(x) = \delta(x-x_i)$. Let $x_i = 0.5$ and we substitute the test function into the weighted residual then $a = 0.2222$. The approximate solution becomes $\tilde{U}(x) = 0.2222x(1-x)$ and $f_{\text{Collocation}}(0.5) = 0.0556$. In order to improve the approximation solution, we use trial function as $\tilde{U}(x) = a_1x(1-x) + a_2x^2(1-x)$. This trial function has two unknown constants to be determined. Computation of the residual using the present trial function yields

$$R(x) = a_2x^3 + (a_1 - a_2)x^2 - (a_1 + 6a_2 - 1)x - 2(a_1 - a_2)$$

It is apparent that we need the same number of test functions as that of unknown constants, a_1 and a_2 , in order that the constants can be determined properly. For instance, $W_1(x) = \delta(x-x_1)$ and $W_2(x) = \delta(x-x_2)$.

2.4 The generalized integral function

Let's consider a single function $K(z)$, whose expected value is

$$K(z) = \int_a^b U(z, \xi) d\xi \quad (17)$$

$K(z)$ = Known function.

$U(z, \xi)$ = Unknown function of two variables.

In this case, the unknown function is current distribution. The solution of $K(z)$ is approximated by a linear combination of known basis function $u_i(z, \xi)$ and unknown coefficients c_i , so called degrees of freedom (Harrington, 1993).

$$U(z, \xi) \approx \sum_{i=1}^N c_i u_i(z, \xi) \quad (18)$$

The basis functions are chosen to reasonable model the expected behavior of the unknown function throughout its domain. In numerical mathematic, a mixture of the basis functions builds interpolating function. If the basis functions have a local support in the domain, they are called local or sub-domain basis function. Local basis functions are defined on all the region of interests ($a \rightarrow b$) but each of them is non zero only on a sub-region of the intervals of interests. For example, the unit pulse function is the local basis. If their support spans the entire-domain, they are called global or entire-domain basis functions. For example, the Fourier expansion represents typical entire-domain approximation. If basis functions are normalized then coefficients c_i have got the meaning of sample values of the approximated functions. The application of sub-domain approximations is usually simpler than the application of entire-domain functions, and sub-domain basis functions have been favored by the most author ever since.

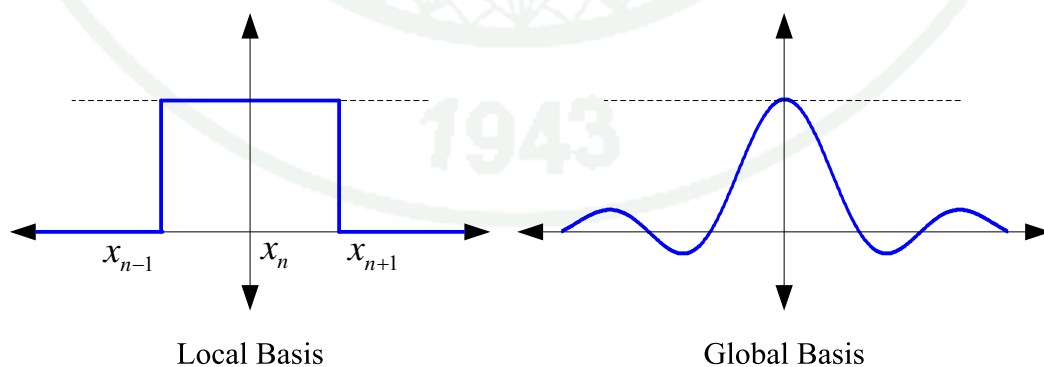


Figure 11 Local and global basis.

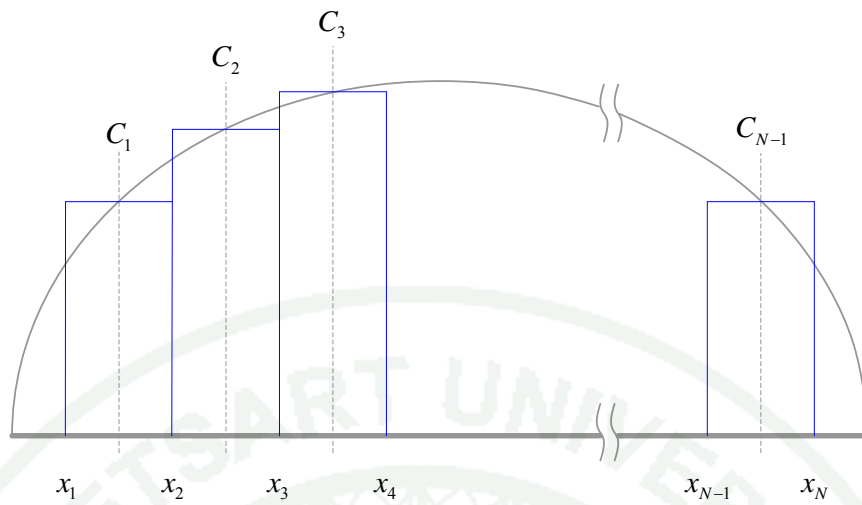


Figure 12 A set of pulse basis functions.

A set of pulse basis functions is illustrated in Figure 12. Where the domain has been divided into N points with $N-1$ subsegments/pulse. Every one of the segments has equal lengths. The pulse function is defined as

$$f_n(x) \begin{cases} 1 & x_n \leq x \leq x_{n+1} \\ 0 & \text{elsewhere} \end{cases} \quad (19)$$

Pulse functions comprise a simple and crude approximation to the solution over each segment, but they can greatly simplify the evaluation of MoM matrix elements (Gibson, 2007).

Substitution Equation (18) to Equation (17), the summation and the integration are swapped, then

$$K(z) = \sum_{i=1}^n c_i \int_a^b u_i(z, \xi) d\xi + R(z)$$

$$R(z) = K(z) - \sum_{i=1}^n c_i \int_a^b u_i(z, \xi) d\xi \quad (20)$$

$R(z)$ = Residual of approximation $U(z, \xi)$.

A residual is an observable estimate of the function. If a residual is removing, the approximation function is very accurate. In order to solve for the unknown coefficients c_i , Equation (20) is multiplying by weighting functions $W_j(z)$ and integrating both sides.

$$\int_a^b W_j(z) R(z) dz = \int_a^b W_j(z) \left(K(z) - \sum_{i=1}^n c_i \int_a^b u_i(z, \xi) d\xi \right)$$

Corresponding to the method of weighted residual, then

$$\int_a^b W_j(z) R(z) dz = 0, \quad i = 0, 1, \dots, N \quad (21)$$

$$\int_a^b W_j(z) K(z) dz = \int_a^b W_j(z) dz \sum_{i=1}^n c_i \int_a^b u_i(z, \xi) d\xi \quad (22)$$

This research uses Point matching method (Collocation method), which is easy to grasp and straightforward to implement, may not yield an optimal convergence. In addition, Point matching method uses Dirac delta functions, which are place to points where the values of unknown coefficients are computed, as weighting functions.

$$\delta(z) \begin{cases} \infty & z = 0 \\ 0 & z \neq 0 \end{cases} \text{ and its properties } \int_{-\infty}^{\infty} \delta(z) dz = 1, \quad \int_{a-\delta}^{a+\delta} f(z) \delta(z-a) dz = f(a) \quad (23)$$

$$W_j(z) = \delta(z - z_j) \quad (24)$$

Due to the filtering property of Dirac delta function, the first integration is eliminated on both sides. Then, Equation (22) becomes (Raida, 2001)

$$K(z_j) = \sum_{i=1}^n c_i \int_a^b u_i(z_j, \xi) d\xi \quad (25)$$

2.5 Maxwell equations and potentials

$$\nabla \times \bar{E} = -\frac{\partial \bar{B}}{\partial t} - \bar{J}_m \quad (26)$$

$$\nabla \times \bar{H} = \frac{\partial \bar{D}}{\partial t} + \bar{J}_e \quad (27)$$

$$\nabla \cdot \bar{D} = \rho \quad (28)$$

$$\nabla \cdot \bar{B} = 0 \quad (29)$$

Generally, these equations have a complete set of equations that govern electromagnetics. The consolidation of this set of equations, including the concept of displacement current density, was primarily due to J. C. Maxwell. Therefore, this set of equations bears his name. Maxwell's first equation gives us a relation between electric and magnetic fields Ampere's law, or Maxwell's second equation for magnetostatics. Equation (28) essentially states that charge density is a source (or sink) of electric flux lines. Note that we can no longer say that all electric flux begins and terminates on charge, because the point form of Faraday's law, Equation (26), shows that E , and hence D , may have circulation if a changing magnetic field is present. Thus the lines of electric flux may form closed loops. However, the converse is still true, and every coulomb of charge must have one coulomb of electric flux diverging from it. Equation (29) acknowledges the fact that "magnetic charges", or poles, are not known to exist. Magnetic flux is always found in closed loops and never diverges from a point source. It is emphasized once again, that the magnetic flux density is solenoidal; having no source or sink. In addition to Maxwell's equations, there are four medium-dependent equations $\bar{D} = \epsilon \bar{E}$, $\bar{B} = \mu \bar{H}$, $\bar{J}_e = \sigma \bar{E}$ and $\bar{J}_m = \sigma^* \bar{M}$. It is important that $\bar{J}_m = \sigma^* \bar{M}$ is the magnetic conductive current density (volts/meter²) and σ^* is the magnetic resistivity (ohms/meter). These are called constitutive relations for the medium in which the Maxwellian fields exist; single valued, bounded and continuous functions of space and time with continuous derivatives. In conclusion, one may accurately state that if we study of Maxwell's equations, we study of electromagnetic field theory (Hayt, 1989).

In electrostatics and magnetostatics, it is often convenient to use auxiliary functions in analyzing an EM field. These auxiliary functions are the scalar electric potential V and vector magnetic potential \bar{A} . The desired field quantity \bar{E} or \bar{B} , could be found from the potential by differentiation. Although two potential functions are arbitrary, they are required to satisfy Maxwell's equations. Their derivation is based on two fundamental vector identities

$$\nabla \cdot \nabla \times \bar{A} \equiv 0 \quad (30)$$

$$\nabla \times \nabla V \equiv 0 \quad (31)$$

Equation (30), the divergence of the curl of any vector is identically zero. So, Equation (29) ($\nabla \cdot \bar{B} = 0$) is satisfied if we define \bar{A} such that

$$\bar{B} = \nabla \times \bar{A} \quad (32)$$

Substitution Equation (32) into Equation (26) gives

$$\nabla \times \bar{E} = -\frac{\partial}{\partial t}(\nabla \times \bar{A})$$

$$\nabla \times \bar{E} = -\nabla \times \frac{\partial \bar{A}}{\partial t}$$

$$0 = -\nabla \times \left(\bar{E} + \frac{\partial \bar{A}}{\partial t} \right) \quad (33)$$

This means that $\bar{E} + \frac{\partial \bar{A}}{\partial t}$ is a conservative (zero curl) field and therefore a

scalar V exists such that $\bar{E} + \frac{\partial \bar{A}}{\partial t} = -\nabla V$

$$\bar{E} = -\frac{\partial \bar{A}}{\partial t} - \nabla V \quad (34)$$

Thus, if we have the potential function V and \bar{A} , we can find the fields \bar{E} and \bar{B} from Equation (34) and Equation (32), respectively. The phasor representation allows us to replace the time derivations $\frac{\partial}{\partial t}$ by $j\omega$ since $\frac{\partial e^{j\omega t}}{\partial t} = j\omega e^{j\omega t}$. It means that the complex exponential is the eigenfunction ($\mathbf{A}\mathbf{x} = \lambda\mathbf{x}$) of the derivative operation.

$$\bar{E} = -j\omega\bar{A} - \nabla V \quad (35)$$

Equation (32) and Equation (34) do not completely define \bar{A} . Moreover, Equation (34) is not exactly inviting for determining \bar{E} because it contains both scalar and a vector potential. A pair of coupled equations for V and \bar{A} may be obtained in the following way. First, as we have seen before, the vector identity is

$$\nabla^2 \bar{A} \equiv \nabla(\nabla \cdot \bar{A}) - \nabla \times \nabla \times \bar{A} \quad (36)$$

$$\nabla^2 \bar{A} = a_x \nabla^2 A_x + a_y \nabla^2 A_y + a_z \nabla^2 A_z \quad (37)$$

Laplacian of a vector ($\nabla^2 \bar{A}$) is occurring only in rectangular coordinates. In other coordinate systems, a result as simple as this equation does not occur. This point should be kept in mind. Substituting one of four medium-dependent equations $\bar{B} = \mu \bar{H}$ into Equation (32) gives

$$\bar{H} = \frac{1}{\mu} (\nabla \times \bar{A}) \quad (38)$$

μ = Permeability (H/m).

Substituting Equation (38) into Equation (27) and $\bar{D} = \varepsilon \bar{E}$

$$\nabla \times \nabla \times \bar{A} = \mu \varepsilon \frac{\partial}{\partial t} \bar{E} + \mu \bar{J} \quad (39)$$

ε = Permittivity (F/m).

Also, substituting Equation (34) into Equation (39) and assuming a linear, homogeneous medium,

$$\begin{aligned}\nabla \times \nabla \times \bar{A} &= \mu \varepsilon \frac{\partial}{\partial t} \left(-\frac{\partial \bar{A}}{\partial t} - \nabla V \right) + \mu \bar{J} \\ -\nabla \times \nabla \times \bar{A} &= \mu \varepsilon \frac{\partial^2 \bar{A}}{\partial t^2} + \mu \varepsilon \frac{\partial}{\partial t} \nabla V - \mu \bar{J}\end{aligned}\quad (40)$$

Applying the vector identity

$$\nabla^2 \bar{A} - \nabla (\nabla \cdot \bar{A}) = \mu \varepsilon \frac{\partial^2 \bar{A}}{\partial t^2} + \mu \varepsilon \frac{\partial}{\partial t} \nabla V - \mu \bar{J}\quad (41)$$

Second, substituting one of four medium-dependent equations $\bar{D} = \varepsilon \bar{E}$ into Equation (28)

$$\nabla \cdot \bar{E} = \frac{\rho}{\varepsilon}\quad (42)$$

Substituting Equation (34) into Equation (42) gives

$$\begin{aligned}\nabla \cdot \left(-\frac{\partial \bar{A}}{\partial t} - \nabla V \right) &= \frac{\rho}{\varepsilon} \\ \nabla^2 V + \frac{\partial}{\partial t} (\nabla \cdot \bar{A}) &= -\frac{\rho}{\varepsilon}\end{aligned}\quad (43)$$

Equation (41) can be rewritten as

$$\nabla^2 \bar{A} - \nabla \left(\nabla \cdot \bar{A} + \mu \varepsilon \frac{\partial}{\partial t} V \right) - \mu \varepsilon \frac{\partial^2 \bar{A}}{\partial t^2} = -\mu \bar{J}\quad (44)$$

In the area of vector calculus, Helmholtz's theorem, also known as the vector theorem of calculus, states that any sufficiently smooth, rapidly decaying vector

field in three dimensions can be resolved into the sum of an irrotational (curl-free) vector field and a solenoidal (divergence-free) vector field. The term ‘‘Helmholtz’s theorem’’ can also refer to the following. Let \mathbf{C} be a vector field and d is a scalar field on \mathbf{R}^3 which are sufficiently smooth and which vanish faster than $1/r^2$ at infinity. Then there exists a vector field \mathbf{F} such that $\nabla \cdot \mathbf{F} = d$ and $\nabla \times \mathbf{F} = \mathbf{C}$ if additionally the vector field \mathbf{F} vanishes as $r \rightarrow \infty$, then \mathbf{F} is unique. In other words, a vector field can be constructed with both a specified divergence and a specified curl, and if it also vanishes at infinity, it is uniquely specified by its divergence and curl. Now, we have already specified the curl of $\bar{\mathbf{A}}$ in Equation (32). In order to completely define $\bar{\mathbf{A}}$, we must also specify its convergence. Equation (43) and Equation (44) suggest very strongly that we choose

$$\nabla \cdot \bar{\mathbf{A}} = -\mu\epsilon \frac{\partial}{\partial t} V \quad (45)$$

Equation (45) is called Lorentz condition. If this is done, then $\bar{\mathbf{A}}$ is said to be unique in the Lorentz gauge and Equation (43) and Equation (44) are uncoupled, for then we have

$$\nabla^2 V - \mu\epsilon \frac{\partial^2}{\partial t^2} V = -\frac{\rho_v}{\epsilon} \quad (46)$$

$$\nabla^2 \bar{\mathbf{A}} - \mu\epsilon \frac{\partial^2}{\partial t^2} \bar{\mathbf{A}} = -\mu \bar{\mathbf{J}} \quad (47)$$

These are called the inhomogeneous scalar and vector Helmholtz wave equations, respectively. Thus Maxwell’s equations in term of the potentials V and $\bar{\mathbf{A}}$ reduce to the three equations, Equation (45) to Equation (47). In other words, the three equations are equivalent to the ordinary form of Maxwell’s equations in that potentials satisfying these equations always lead to a solution of Maxwell’s equations for $\bar{\mathbf{E}}$ and $\bar{\mathbf{B}}$ when used with Equation (32) and Equation (34). Integral solutions to Equation (46) and Equation (47) are the so-called retarded potentials.

$$V(\vec{r}, t) = \frac{1}{4\pi\epsilon} \iiint_{\text{vol}'} \frac{\rho_v(\vec{r}', t - R\sqrt{\mu\epsilon})}{R} dv' \quad (48)$$

$$\vec{A}(\vec{r}, t) = \frac{\mu}{4\pi} \iiint_{\text{vol}'} \frac{\vec{J}(\vec{r}', t - R\sqrt{\mu\epsilon})}{R} dv' \quad (49)$$

The potentials given by Equation (48) and Equation (49) are called retarded potentials. In other words, a change in the source cannot be observed at the field point until a later time. It is apparent that the effect propagates at a velocity given by speed of light ($1/\sqrt{\mu\epsilon}$). If the region of interest does not include the source, then Equation (48) and Equation (49) are solutions to the homogeneous differential equations (wave equations).

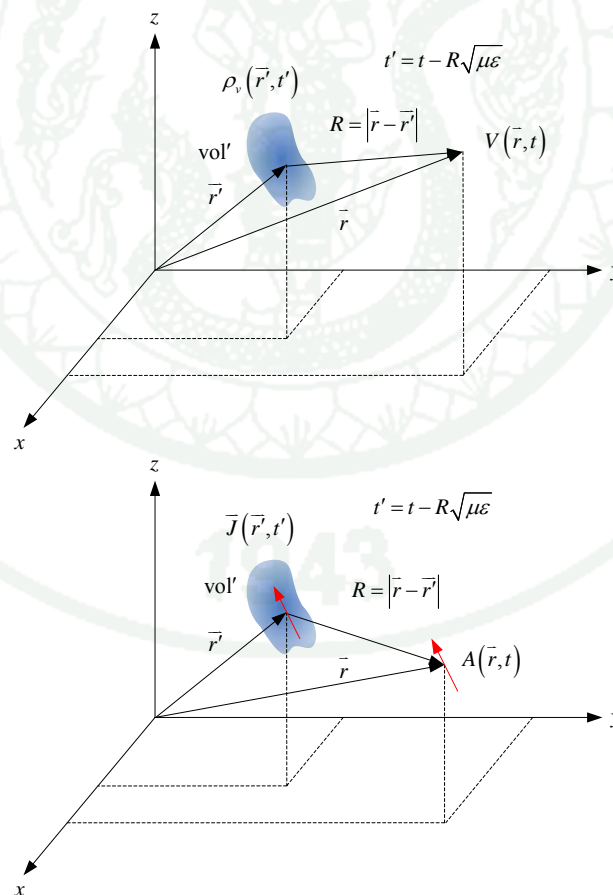


Figure 13 Geometry for the calculation of potentials.

That is, to evaluate V at \vec{r} and time t , the value of ρ_v at \vec{r}' and time $t' = t - R\sqrt{\mu\epsilon}$, or retarded time, should be used in the integrand. In the same way, to evaluate \vec{A} at \vec{r} and time t , the value of \vec{J} at \vec{r}' and $t - R\sqrt{\mu\epsilon}$ should be used. In addition, R is the distance from any point in the source point to the observation point (Neff, 1987).

It is simpler to show Equation (49) in phasor form. There is no loss in generality in this approach because if the response to a general sinusoidal (phasor) excitation is known, then the response to any excitation can be found by Fourier methods of Equation (49). Additionally, a phase shifts in the frequency domain because a time shifts in the time domain. Therefore, the phasor form is

$$\begin{aligned}\bar{A}(\vec{r}, \omega) &= \mu \iiint_{\text{vol}'} \bar{J}(\vec{r}', \omega) \frac{e^{-j\omega\sqrt{\mu\epsilon}R}}{4\pi R} dv' \\ \bar{A}(\vec{r}, \omega) &= \mu \iiint_{\text{vol}'} \bar{J}(\vec{r}', \omega) \frac{e^{-jkR}}{4\pi R} dv'\end{aligned}\quad (50)$$

k = Wave number, Phase change constant (radians/meter, m^{-1}).

$$k = \frac{2\pi}{\lambda}.$$

$$k = \omega\sqrt{\mu\epsilon}, \quad k^2 = \omega^2\mu\epsilon.$$

R = The distance from any point in the source point to the observation point.

$$R = \frac{\lambda}{2\pi} \rightarrow kR = 1 \text{ is referred to radian distance.}$$

which satisfies the phasor form of Equation (47) ; namely,

$$\nabla^2 \bar{A} + \omega^2 \mu\epsilon \bar{A} = -\mu \bar{J} \quad (51)$$

2.6 Hallen's Integral Equation

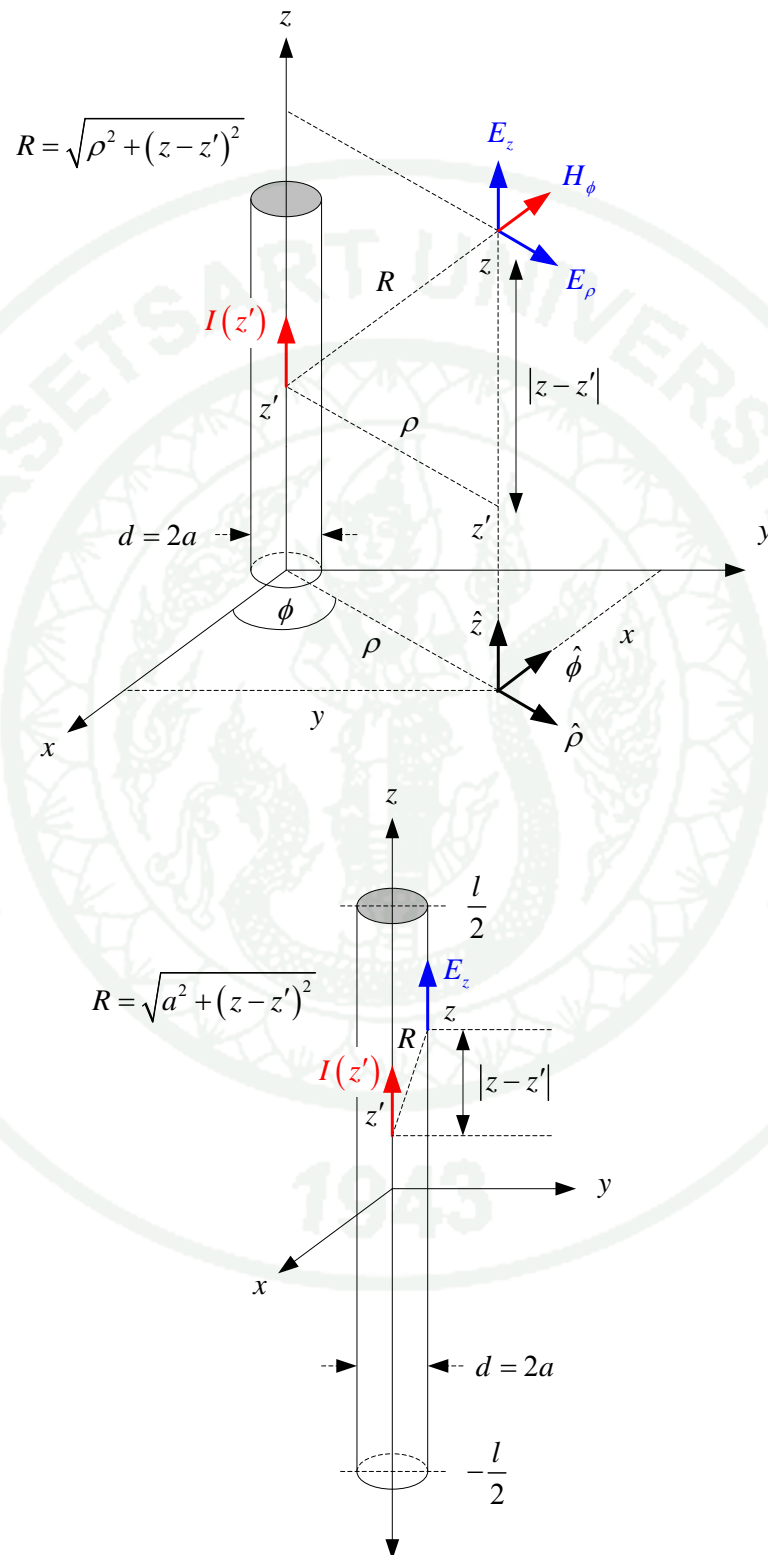


Figure 14 Thin wire dipole of length l and radius a .

This section simplify considerably in the special case of linear wire antenna, which is a thin cylindrical antenna. In addition, a perfectly conducting cylindrical antenna has radius a , extending between $-l/2 \leq z \leq l/2$. Let the antenna be located in a lossless homogeneous dielectric medium ($\sigma = 0$). We assume a z-directed current on the cylinder, only axial electric field E_z is produced due to axial symmetry. Then Equation (35) becomes

$$E_z = -j\omega A_z - \frac{\partial}{\partial z} V \quad (52)$$

Also, Equation (45) becomes

$$\begin{aligned} \frac{\partial}{\partial z} A_z &= -j\omega\mu\epsilon V \\ V &= \frac{j}{\omega\mu\epsilon} \frac{\partial}{\partial z} A_z \end{aligned} \quad (53)$$

Substituting Equation (53) into Equation (52) gives

$$\begin{aligned} E_z &= -j\omega A_z - \frac{j\omega}{\omega^2 \mu\epsilon} \frac{\partial^2}{\partial z^2} A_z \\ E_z &= -j\omega \left(1 + \frac{1}{k^2} \frac{\partial^2}{\partial z^2} \right) A_z \end{aligned} \quad (54)$$

According to Equation (50), $k^2 = \omega^2 \sqrt{\mu\epsilon}$ and ω is the angular frequency of the suppressed harmonic time variation $e^{j\omega t}$. In this case, Figure 14, the current sources are filamentary line currents along z-axis, $I(z')$. The assumption that the radius of the wire is much smaller than its length means effectively that the current density $\vec{J}(\vec{r}', \omega)$ will be z-directed and confined to zero transverse dimensions, that is

$\bar{J}(\bar{r}', \omega) = I(z') \delta(x') \delta(y') \hat{z}$. Inserting $\bar{J}(\bar{r}', \omega)$ into Equation (50), it follows that the vector potential will be z-directed and cylindrically symmetric (Orfanidis, 2008).

$$\begin{aligned}\bar{A}(\bar{r}, \omega) &= \mu \iiint_{\text{vol}'} I(z') \delta(x') \delta(y') \hat{z} \frac{e^{-jkR}}{4\pi R} dv' \hat{z} \\ \bar{A}(\bar{r}, \omega) &= \mu \iiint_{\text{vol}'} I(z') \delta(x') \delta(y') \hat{z} \frac{e^{-jkR}}{4\pi R} dx' dy' dz' \hat{z} \\ \bar{A}(\bar{r}, \omega) &= \mu \int_{-l/2}^{l/2} I(z') \frac{e^{-jkR}}{4\pi R} dz' \hat{z}\end{aligned}$$

where $R = \sqrt{\rho^2 + (z - z')^2}$, as shown in Figure 14. The z' -integration is over the finite length of the antenna. Thus, $\bar{A}(\bar{r}, \omega) = \hat{z} A_z(\rho, z)$, so that

$$A_z(\rho = a, z) = A_z(a, z) = \mu \int_{-l/2}^{l/2} I(z') \frac{e^{-jkR}}{4\pi R} dz' \quad (55)$$

R = Distance between source point and observation point.

$$R = \sqrt{\rho^2 + (z - z')^2} = \sqrt{a^2 + (z - z')^2}.$$

Source point is located at z' .

Observation point is located at z .

Apparently, $G(z, z') = \frac{e^{-jkR}}{4\pi R}$ is the Free-Space Green's function so that

Equation (55) can be represented as

$$A_z = \mu \int_{-l/2}^{l/2} I(z') G(z, z') dz' \quad (56)$$

Substituting Equation (56) into Equation (54) gives

$$E_z^{sct} = -j\omega\mu \left(1 + \frac{1}{k^2} \frac{\partial^2}{\partial z^2} \right) \int_{-l/2}^{l/2} I(z') G(z, z') dz' \quad (57)$$

A thin wire dipole can be either receiving or transmitting antenna. Actually in both case, it is always driven by an external source. In receiving mode, it is done by an incident electric field (typically, a uniform plane wave if it is arriving from far distances). In transmitting mode, a thin wire dipole is receiving a power from a generator voltage applied to its input terminals. In conclusion, a source of thin wire dipole antenna is always referred to the external source field as the “Incident electric field (E_z^{inc})” (Orfanidis, 2008).

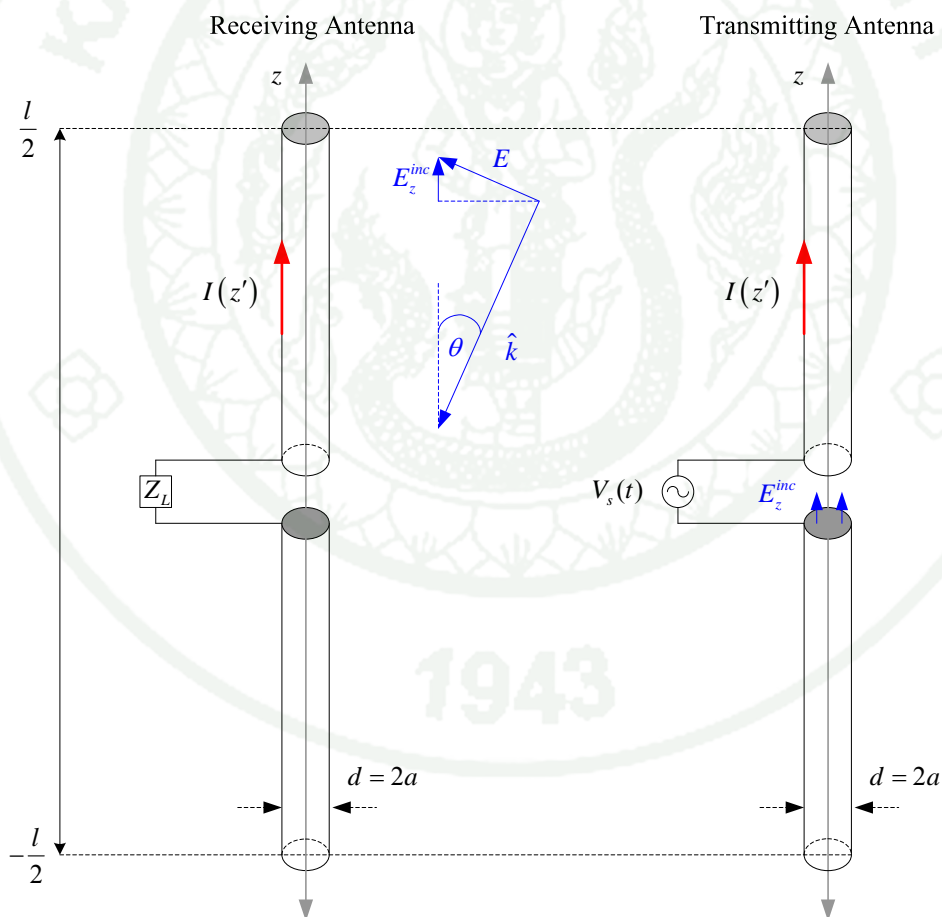


Figure 15 The incident electric field.

Source: Orfanidis (2008)

The incident electric field induces a current on the thin wire dipole. Then the induced current produces its own total electric field (E_z^{total}). Furthermore, the total electric field in the vicinity of the cylinder can be expressed as a sum of the incident and scattered electric field, respectively (Poljak, 2007). The equation is

$$E_z^{total} = E_z^{inc} + E_z^{sct} \quad (58)$$

Assuming a perfectly conducting cylinder (PEC), the boundary conditions are the condition at the surface of a conductor whereby the tangential electric fields are zero ($E_z^{total} = 0$) and the normal electric flux density is equal to the surface charge density on the conductor. Then, these boundary conditions are enough to determine the current distribution induced on the thin wire dipole ($E_z^{inc} = -E_z^{sct}$). To summarize, given an incident electric field (E_z^{inc}), Equation (57) can be solved for the current distribution ($I(z')$). Equation (57) can be rewritten as

$$E_z^{inc} = \frac{j\omega}{k^2} \left(\frac{\partial^2}{\partial z^2} + k^2 \right) \mu \int_{-l/2}^{l/2} I(z') G(z, z') dz', \quad k^2 = \omega^2 \mu \epsilon$$

$$\left(\frac{\partial^2}{\partial z^2} + k^2 \right) \mu \int_{-l/2}^{l/2} I(z') G(z, z') dz' = -j\omega \mu \epsilon E_z^{inc} \quad (59)$$

Equation (59) is a second-order linear ordinary differential equation. This integral equation was first derived by Pocklington in 1897 (Stutzman and Thiele, 1998). A modification of this equation was introduced by Hallen in 1938 (Hallen, 1938) and is simpler to deal with from a numerical-computation point of. Furthermore, this equation has been generalized by Mei (Mei, 1965; Lan *et al.*, 1999) to perfectly conducting wires of arbitrary shape. Hallen's Integral Equation is computationally convenient since its kernel contains only l/r term. Equation (59) can be rewritten in a compact form as

$$\left(\frac{\partial^2}{\partial z^2} + k^2 \right) A_z = -j\omega\mu\epsilon E_z^{inc} \quad (60)$$

Although the external source field E_z^{inc} can be specified arbitrarily, there are two special model of practical importance. First model is delta-gap model, which imitates the way a transmitting thin wire dipole is fed by a transmission line. The other is an incident electric field, which is generally called uniform plane wave. In either model, the applied voltage V_s can be thought of as arising from an incident electric field (E_z^{inc}), which exists only within the infinitesimal gap (Orfanidis, 2008).

$$V_s = \int_{-l/2}^{l/2} E_z^{inc} dz \quad (61)$$

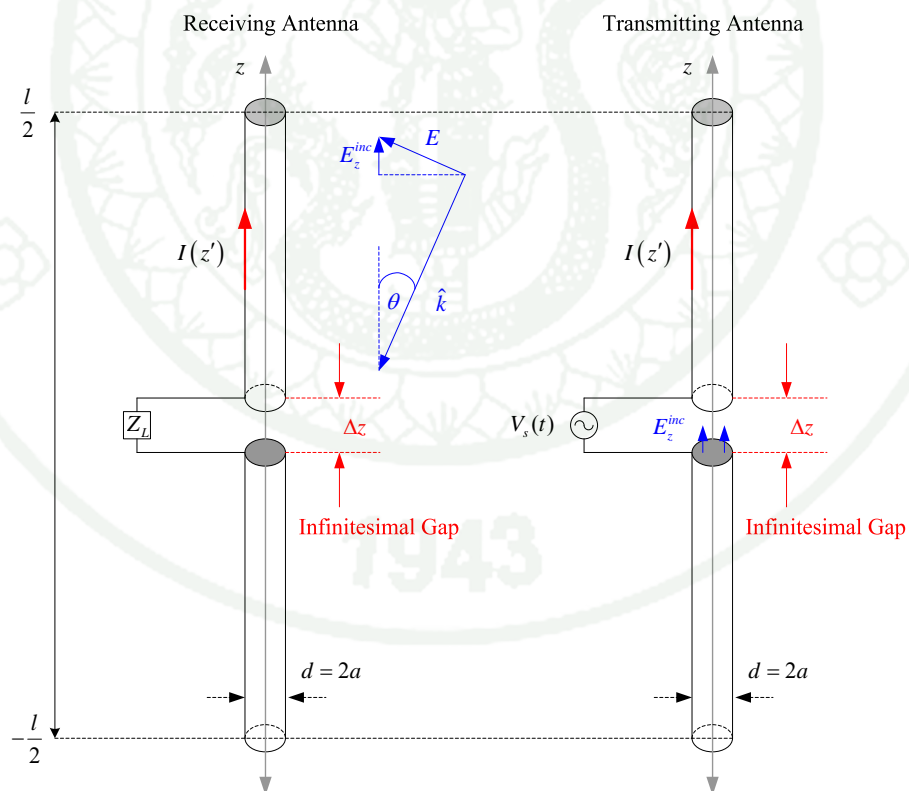


Figure 16 The delta-gap or the infinitesimal gap model.

Source: Orfanidis (2008)

If the limit $\Delta z \rightarrow 0$, then $V_s = E_z^{inc} \Delta z$ or $E_z^{inc} = V_s / \Delta z$. So as to maintain a finite value of V_s in the left-hand side of Equation (61) then E_z^{inc} must become proportionately large. This means that in this limit

$$E_z^{inc} = V_s \delta(z') \quad (62)$$

In this case $\delta(z)$ is Dirac delta function, which has the properties in Equation (23). The delta function used here is the same as that used in circuit theory, except the argument is z instead of the time. Substituting Equation (62) into Equation (60) gives

$$\left(\frac{\partial^2}{\partial z^2} + k^2 \right) A_z = -j\omega\mu\epsilon V_s \delta(z') \quad (63)$$

The potential A_z in Equation (63), must be continuous, and the first derivative of A_z , namely, dA_z/dz , should have a step change of amount $-j\omega\mu\epsilon V_s \delta(z')$ at $z = 0$, so that the second derivative will have an impulse of the same strength. The behavior of A_z in the vicinity of $z = 0$ is shown in the following picture (Collin, 1985).

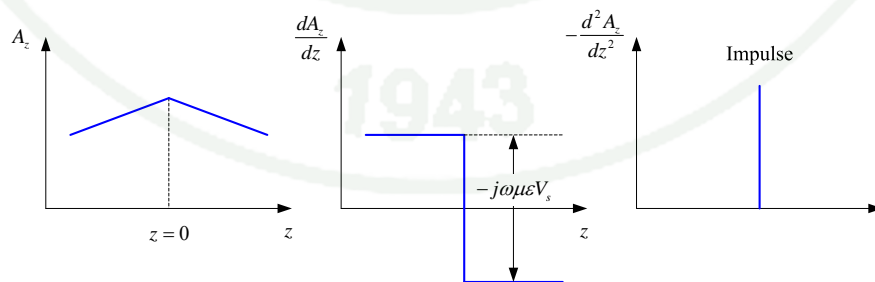


Figure 17 Behavior of the vector potential function A_z in the vicinity of the input region of the antenna.

Source: Collin (1985)

Equation (63), the general solution over the interval $-l/2 \leq z \leq l/2$ can be expressed as (Elliott, 2003).

$$A_z = C_1 \cos kz + C_2 \sin kz, \quad z \rightarrow 0^+ \quad (64)$$

$$A_z = C_3 \cos kz + C_4 \sin kz, \quad z \rightarrow 0^- \quad (65)$$

with C_1, C_2, C_3 and C_4 are constants. One can match these solutions across $z = 0$ by noting from Equation (60) that, if A_z is to be finite everywhere, the singularity in V_s at $z = 0$ must be matched by a singularity in $dA_z/dz = 0$, since it cannot be accommodated by $k^2 A_z(0)$. In order that A_z will be continuous at $z = 0$ Equation (64) and Equation (65) indicate that $C_1 = C_3$. The derivative of A_z evaluated between $z \rightarrow 0^-$ and $z \rightarrow 0^+$ is

$$\int_{0-\delta}^{0+\delta} \frac{d^2 A_z}{dz^2} = \frac{dA_z}{dz} \Big|_{0-\delta}^{0+\delta} = (-kC_1 \sin k(0^+) + kC_2 \cos k(0^+)) - (-kC_3 \sin k(0^-) + kC_4 \cos k(0^-))$$

$$\frac{dA_z}{dz} \Big|_{0-\delta}^{0+\delta} = kC_2 - kC_4 = -j\omega\mu\epsilon V_s \quad (66)$$

Since the antenna is assumed symmetrical at $z = 0$, both A_z and E_z will be even function of z , $f(z) = f(-z)$, hence

$$C_2 = -C_4 \quad (67)$$

and then we find that Equation (67) becomes

$$C_2 = -\frac{j\omega\mu\epsilon V_s}{2k} = -\frac{j\sqrt{\mu\epsilon}}{2} V_s = -\frac{j\mu}{2\eta} V_s \quad (68)$$

$\eta = \sqrt{\mu/\epsilon}$, The characteristic or intrinsic wave impedance.

$\eta_0 = \sqrt{\mu_0/\epsilon_0} \approx 377 \Omega \approx 120\pi$, The characteristic impedance of Free-Space.

Substituting Equation (67) and Equation (68) into Equation (64) and Equation (65), respectively, gives the solution for A_z along the dipole antenna surface (King, 1953, 1956, 1959, 1967; King and Harrison, 1943; Fikioris and Wu, 2001).

$$A_z = \mu \int_{-l/2}^{l/2} I(z') G(z, z') dz' = C_1 \cos kz - \frac{j\mu}{2\eta} V_s \sin k|z|$$

$$\int_{-l/2}^{l/2} I(z') G(z, z') dz' = -\frac{j}{\eta} \left(A \cos kz + \frac{V_s}{2} \sin k|z| \right) \quad (69)$$

which is a Fredholm Integral Equation of the first kind. If we let

$$I(z') = \sum_{n=1}^N I_n u_n(z') \quad (70)$$

Substituting Equation (70) into Equation (69) gives

$$\int_{-l/2}^{l/2} \sum_{n=1}^N I_n u_n(z') G(z, z') dz' + R(z') = D(z) \quad (71)$$

$$D(z) = -\frac{j}{\eta} \left(A \cos kz + \frac{V_s}{2} \sin k|z| \right) \quad (72)$$

$$R(z') = D(z) - \int_{-l/2}^{l/2} \sum_{n=1}^N I_n u_n(z') G(z, z') dz' \quad (73)$$

$R(z')$ = Residual of approximation $I(z')$.

Taking the inner products (moments) by multiplying either side of Equation (77) with a weighting function $W_m(z)$ and integrating both side.

$$\int_{-l/2}^{l/2} R(z') W_m(z) dz = \int_{-l/2}^{l/2} D(z) W_m(z) dz - \int_{-l/2}^{l/2} \int_{-l/2}^{l/2} \sum_{n=1}^N I_n u_n(z') G(z, z') dz' W_m(z) dz$$

According to Equation (21), the residual must be removed. By reversing the order of the summation and integration,

$$0 = \int_{-1/2}^{1/2} D(z)W_m(z)dz - \sum_{n=1}^N I_n \int_{-1/2}^{1/2} u_n(z') \int_{-1/2}^{1/2} G(z, z')W_m(z)dzdz'$$

$$\sum_{n=1}^N I_n \int_{-1/2}^{1/2} u_n(z') \int_{-1/2}^{1/2} G(z, z')W_m(z)dzdz' = \int_{-1/2}^{1/2} D(z)W_m(z)dz \quad (74)$$

By method of weighted residual, the integration on either side of Equation (74) can be carried out numerically or analytically if possible. If we use the Point matching method by selecting the weighting function as Dirac delta function, $W_m(z) = \delta(z - z_m)$, and its property, $\int_{z_m - \delta}^{z_m + \delta} f(z)\delta(z - z_m)dz = f(z_m)$. In addition, Equation (23) shows the integral of any function multiplied by $\delta(z - z_m)$ gives the value of function at z_m . Then, Equation (74) becomes

$$\sum_{n=1}^N I_n \int_{-1/2}^{1/2} u_n(z')G(z_m, z')dz' = D(z_m) \quad (75)$$

Also, we choose pulse functions as the expansion function,

$$u_n(z') \begin{cases} 1, & z_n - \frac{\Delta z}{2} < z_n < z_n + \frac{\Delta z}{2} \\ 0, & \text{elsewhere,} \end{cases} \quad (76)$$

Equation (76) yields

$$\sum_{n=1}^N I_n \int_{z_n - \frac{\Delta z}{2}}^{z_n + \frac{\Delta z}{2}} G(z_m, z')dz' = D(z_m) \quad (77)$$

Substituting Equation (72) into Equation (77) gives

$$\sum_{n=1}^N I_n \int_{z_n - \frac{\Delta z}{2}}^{z_n + \frac{\Delta z}{2}} \frac{e^{-jkR_m}}{4\pi R_m} dz' = -\frac{j}{\eta} \left(A \cos kz_m + \frac{V_s}{2} \sin k|z_m| \right) \quad (78)$$

Equation (78) will contain N unknown variables, I_n , and the unknown constant A . To determine the $N+1$ unknowns, we divide the dipole antenna into N segments. We choose segments of equal lengths $\Delta z = l/N$, equal to amount of expansion functions, N functions, and select $N+1$ matching points, equal to unknown variables, such as $z = -l/2, -l/2 + \Delta z, \dots, l/2 - \Delta z, l/2$.

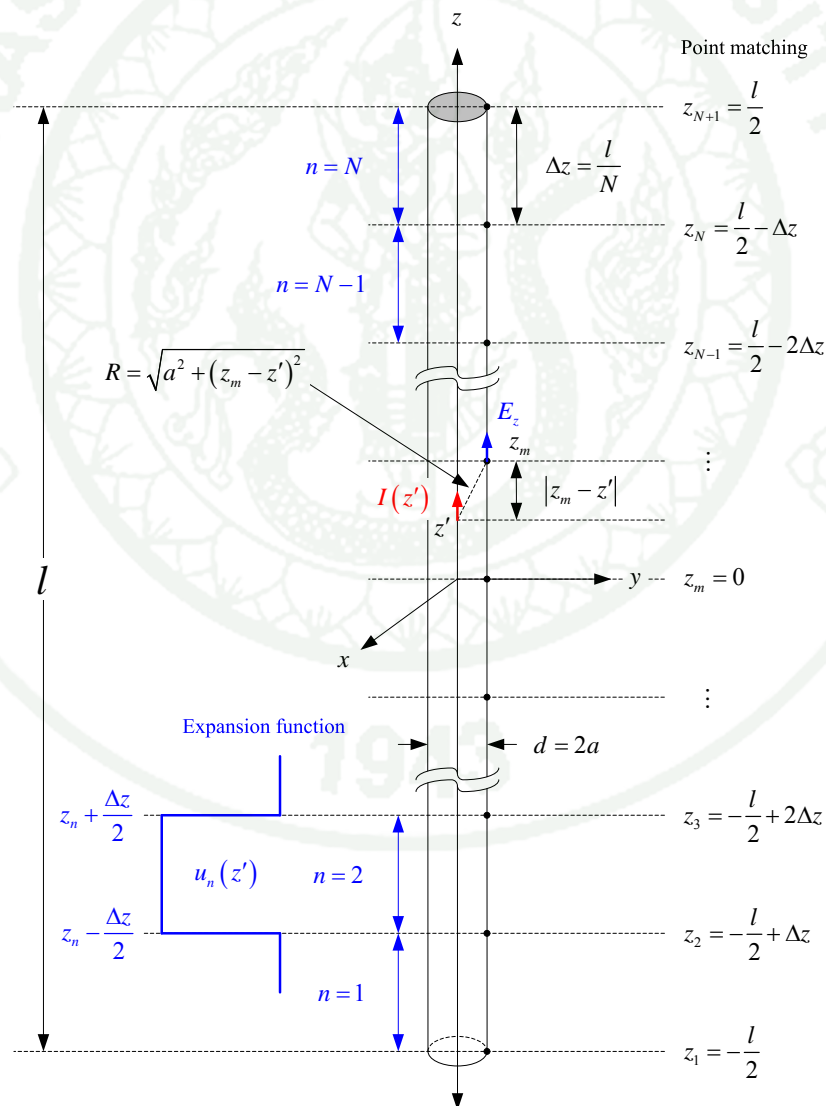


Figure 18 The segmentation of dipole antenna.

where $n=1, 2, \dots, N$, $m=1, 2, \dots, N+1$, $k = \frac{2\pi}{\lambda}$, $\eta = \eta_0 = 377 \Omega$ and

$R_m = \sqrt{a^2 + (z_m - z')^2}$. Equation (78) can be rewritten as

$$\sum_{n=1}^N I_n \int_{z_n - \frac{\Delta z}{2}}^{z_n + \frac{\Delta z}{2}} \frac{e^{-jkR_m}}{4\pi R_m} dz' + \frac{j}{\eta_0} (A \cos kz_m) = -\frac{jV_s}{2\eta_0} \sin k|z_m| \quad (79)$$

It is apparent that Equation (79) has a set of $N+1$ simultaneous equations, which can be cast in matrix form as

$$\begin{bmatrix} G_{1,1} & G_{1,2} & \cdots & G_{1,N} & \frac{j}{\eta_0} \cos(kz_1) \\ G_{2,1} & G_{2,2} & \cdots & G_{2,N} & \frac{j}{\eta_0} \cos(kz_2) \\ \vdots & \vdots & \vdots & \vdots & \vdots \\ G_{N+1,1} & G_{N+1,2} & \cdots & G_{N+1,N} & \frac{j}{\eta_0} \cos(kz_{N+1}) \end{bmatrix} \begin{bmatrix} I_1 \\ \vdots \\ I_N \\ A \end{bmatrix} = \begin{bmatrix} -\frac{jV_s}{2\eta_0} \sin k|z_1| \\ -\frac{jV_s}{2\eta_0} \sin k|z_2| \\ \vdots \\ -\frac{jV_s}{2\eta_0} \sin k|z_{N+1}| \end{bmatrix} \quad (80)$$

Also, it can be rewritten in compact form as

$$[G][I] = [V] \quad (81)$$

$[G]_{N+1 \times N} = [G]_{m \times n}$. All the elements in this matrix are defined as

$$G_{m,n} = \int_{z_n - \frac{\Delta z}{2}}^{z_n + \frac{\Delta z}{2}} \frac{e^{-jkR_m}}{4\pi R_m} dz' \quad (82)$$

In order to approximate Equation (82), the $G_{m,n}$ is evaluated analytically rather than numerically. We separate Green's function to real and imaginary parts (Sadiku, 2001).

$$G_{m,n} = \int_{z_n - \frac{\Delta z}{2}}^{z_n + \frac{\Delta z}{2}} \frac{e^{-jkR_m}}{4\pi R_m} dz' = \int_{z_n - \frac{\Delta z}{2}}^{z_n + \frac{\Delta z}{2}} \frac{\cos kR_m - j \sin kR_m}{4\pi R_m} dz' \quad (83)$$

The real part is implemented as $\text{Re}(G_{m,n})$, and its value changes rapidly as

$z_m \rightarrow z'$ due to $R_m = \sqrt{a^2 + (z_m - z')^2}$. Therefore

$$\begin{aligned} \text{Re}(G_{m,n}) &= \frac{1}{4\pi} \int_{z_n - \frac{\Delta z}{2}}^{z_n + \frac{\Delta z}{2}} \frac{\cos kR_m}{R_m} dz' \approx \frac{\cos k\sqrt{a^2 + (z_m - z_n)^2}}{4\pi} \int_{z_n - \frac{\Delta z}{2}}^{z_n + \frac{\Delta z}{2}} \frac{1}{R_m} dz' \\ &= \frac{\cos k\sqrt{a^2 + (z_m - z_n)^2}}{4\pi} \int_{z_n - \frac{\Delta z}{2}}^{z_n + \frac{\Delta z}{2}} \frac{1}{\sqrt{a^2 + (z_m - z')^2}} d(z_m - z') \\ &\quad \left(\because \int \frac{du}{\sqrt{u^2 + a^2}} = \ln(u + \sqrt{u^2 + a^2}) + C \right) \\ &= \frac{\cos k\sqrt{a^2 + (z_m - z_n)^2}}{4\pi} \\ &\quad \times \ln \left((z_m - z') + \sqrt{(z_m - z')^2 + a^2} \right) \Big|_{z_n - \frac{\Delta z}{2}}^{z_n + \frac{\Delta z}{2}} \\ &= \frac{\cos k\sqrt{a^2 + (z_m - z_n)^2}}{4\pi} \\ &\quad \times \ln \left(\frac{\left(z_m - z_n - \frac{\Delta z}{2} \right) + \sqrt{\left(z_m - z_n - \frac{\Delta z}{2} \right)^2 + a^2}}{\left(z_m - z_n + \frac{\Delta z}{2} \right) + \sqrt{\left(z_m - z_n + \frac{\Delta z}{2} \right)^2 + a^2}} \right) \\ \text{Re}(G_{m,n}) &= \frac{\cos k\sqrt{a^2 + (z_m - z_n)^2}}{4\pi} \\ &\quad \times \ln \left(\frac{\left(z_m - z_n + \frac{\Delta z}{2} \right) + \sqrt{\left(z_m - z_n + \frac{\Delta z}{2} \right)^2 + a^2}}{\left(z_m - z_n - \frac{\Delta z}{2} \right) + \sqrt{\left(z_m - z_n - \frac{\Delta z}{2} \right)^2 + a^2}} \right) \end{aligned} \quad (84)$$

On the other hand, the imaginary part is implemented as $\text{Im}(G_{m,n})$, and it as a function of z' is a smooth curve so that

$$\begin{aligned} \text{Im}(G_{m,n}) &= -\frac{1}{4\pi} \int_{z_n - \frac{\Delta z}{2}}^{z_n + \frac{\Delta z}{2}} \frac{\sin kR_m}{R_m} dz' \\ &\approx -\frac{\Delta z \sin k \sqrt{a^2 + (z_m - z_n)^2}}{4\pi \sqrt{a^2 + (z_m - z_n)^2}} \end{aligned} \quad (85)$$

The approximation is accurate as long as $\Delta z < 0.05\lambda$. From Equation (84) and Equation (85), the $G_{m,n}$ is represented as

$$\begin{aligned} G_{m,n} &= \frac{\cos k \sqrt{a^2 + (z_m - z_n)^2}}{4\pi} \\ &\times \ln \left(\frac{\left(z_m - z_n + \frac{\Delta z}{2} \right) + \sqrt{\left(z_m - z_n + \frac{\Delta z}{2} \right)^2 + a^2}}{\left(z_m - z_n - \frac{\Delta z}{2} \right) + \sqrt{\left(z_m - z_n - \frac{\Delta z}{2} \right)^2 + a^2}} \right) \\ &- j \frac{\Delta z \sin k \sqrt{a^2 + (z_m - z_n)^2}}{4\pi \sqrt{a^2 + (z_m - z_n)^2}} \end{aligned} \quad (86)$$

For instance, the dipole antenna was divided into 512 segments for $a = l/1024$ so that we can find its relative current distribution ($|I|$) and its phase ($\angle I$) as a function of the ratio of dipole's length per wavelength (l/λ), using Gauss eliminate. Also, we can find the input impedance by assume $V_s = 1$. Thus

$$Z_i = \frac{V_s}{\left(\frac{I_N + I_{N+1}}{2} \right)} = \frac{2}{I_{\frac{N}{2}} + I_{\frac{N}{2}+1}} \quad (87)$$

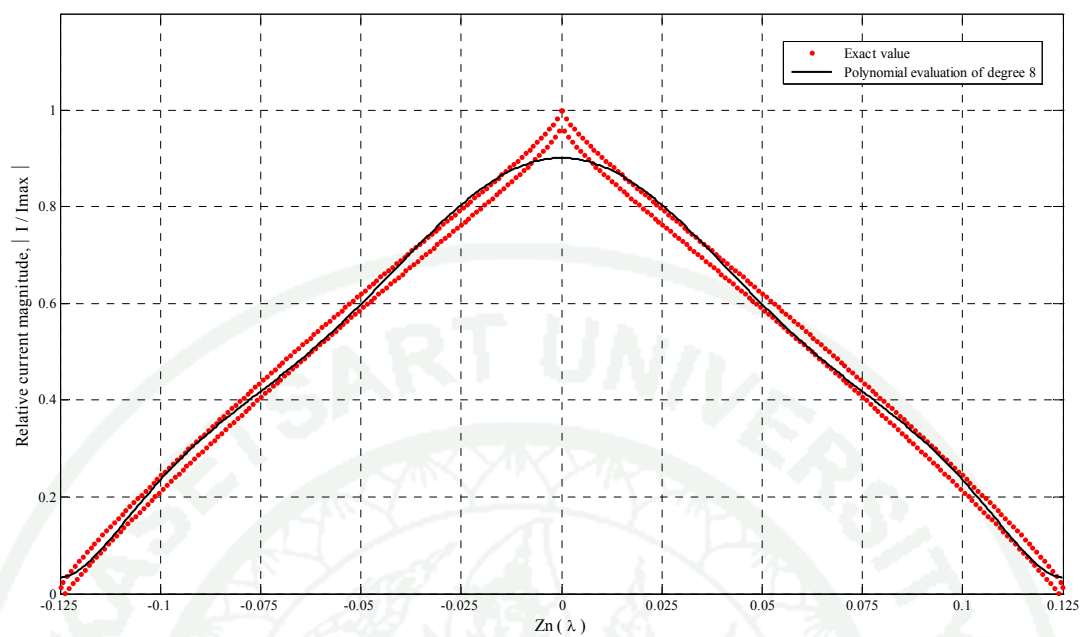


Figure 19 Relative current magnitude of a dipole antenna,

$$l = \frac{\lambda}{4}, N = 512 \text{ and } a = l/1024.$$

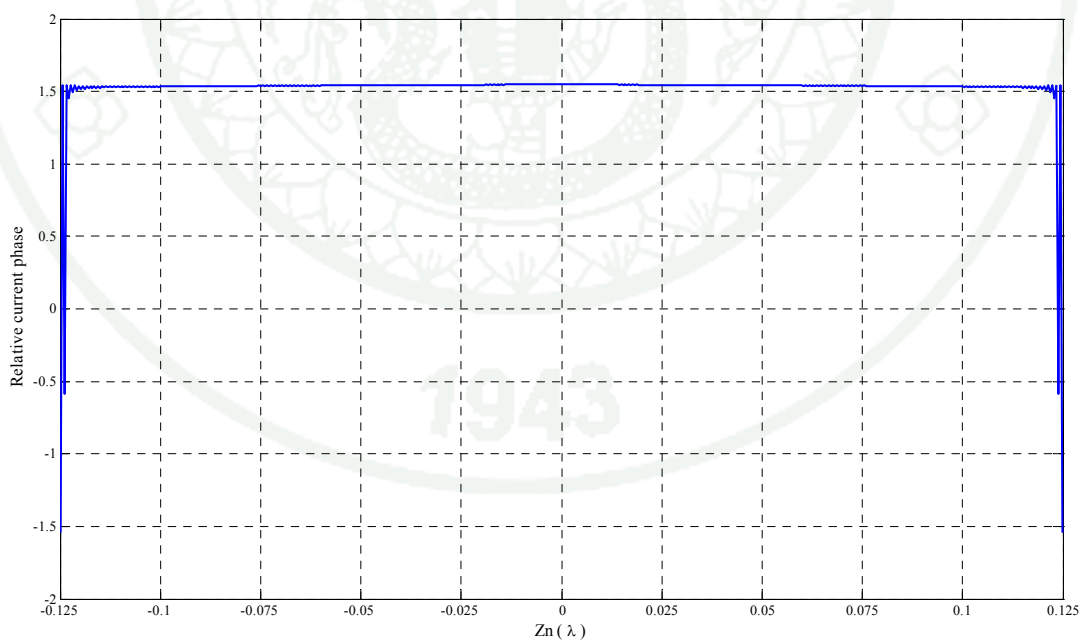


Figure 20 Relative current phase of a dipole antenna,

$$l = \frac{\lambda}{4}, N = 512 \text{ and } a = l/1024.$$

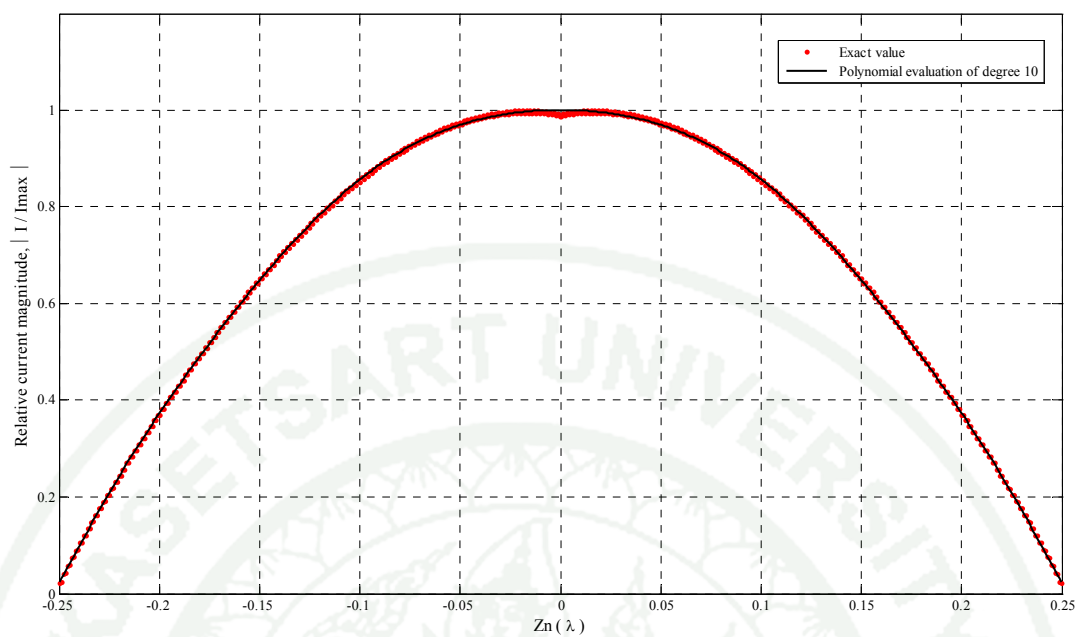


Figure 21 Relative current magnitude of a dipole antenna,

$$l = \frac{\lambda}{2}, N = 512 \text{ and } a = l/1024.$$

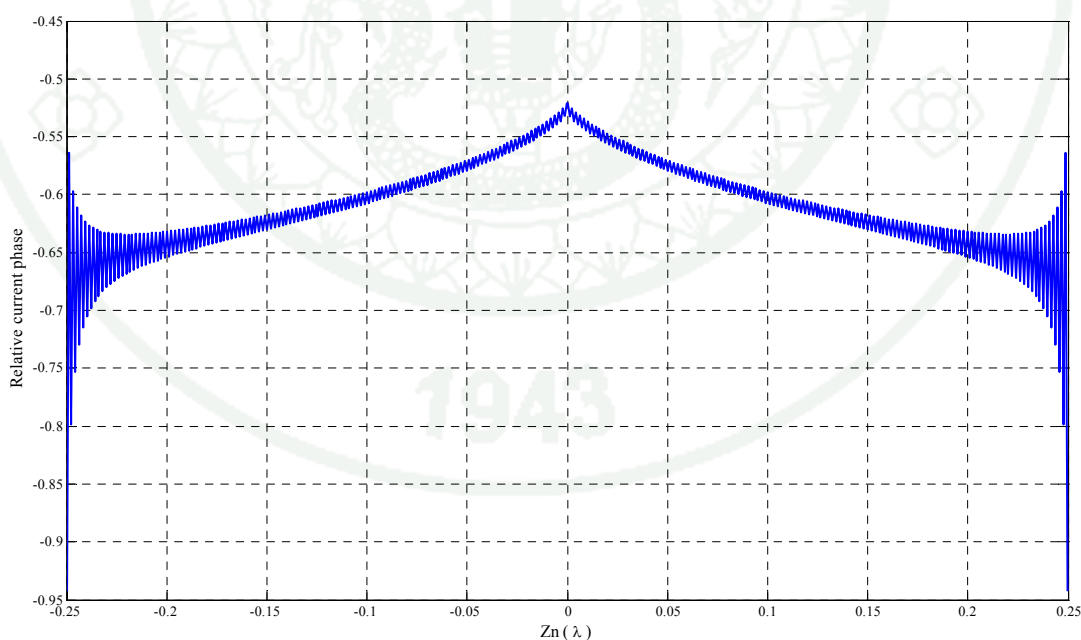


Figure 22 Relative current phase of a dipole antenna,

$$l = \frac{\lambda}{2}, N = 512 \text{ and } a = l/1024.$$

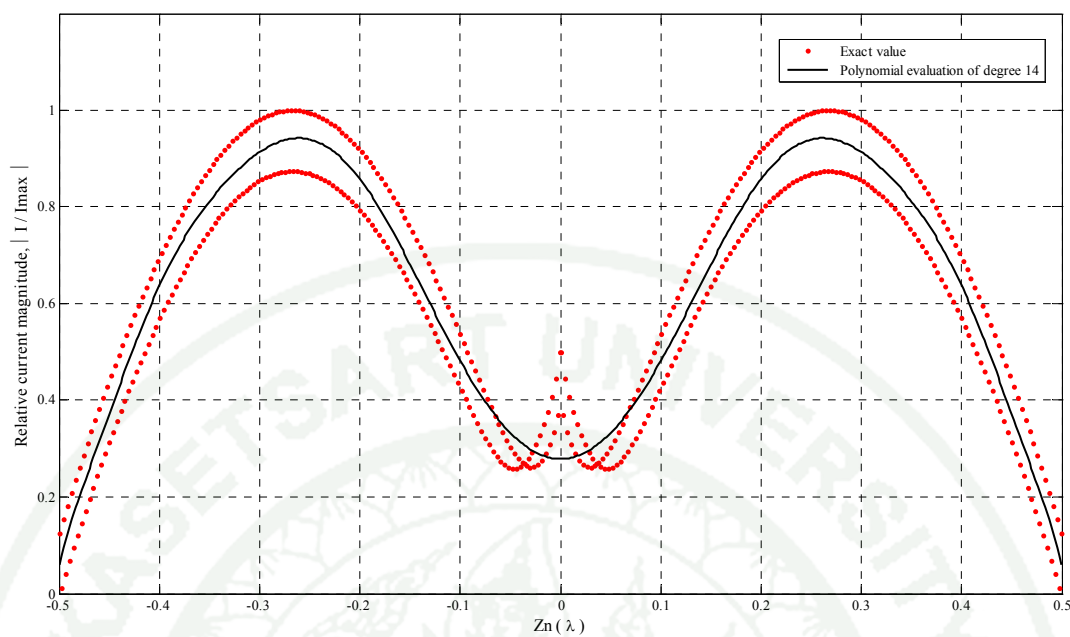


Figure 23 Relative current magnitude of a dipole antenna,
 $l = \lambda$, $N = 512$ and $a = l/1024$.

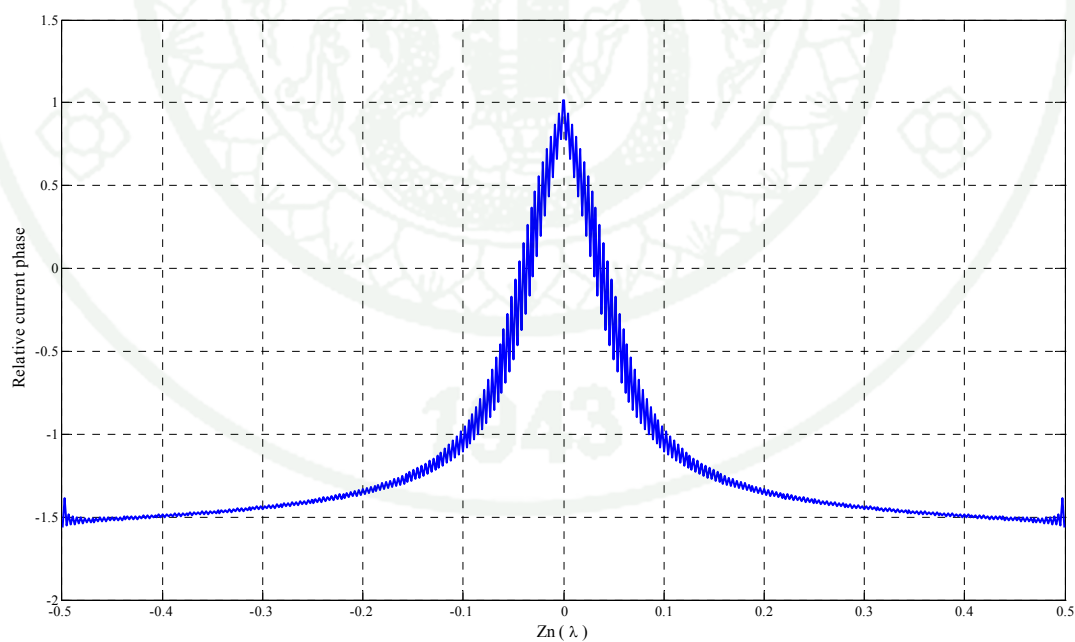


Figure 24 Relative current phase of a dipole antenna,
 $l = \lambda$, $N = 512$ and $a = l/1024$.

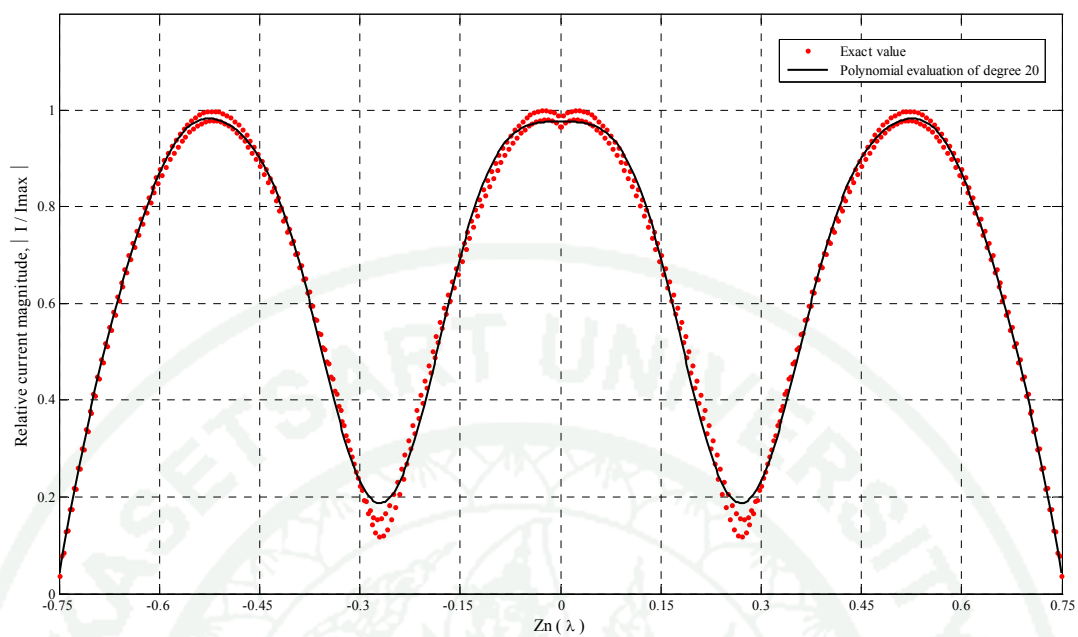


Figure 25 Relative current magnitude of a dipole antenna,

$$l = \frac{3}{2}\lambda, N = 512 \text{ and } a = l/1024.$$

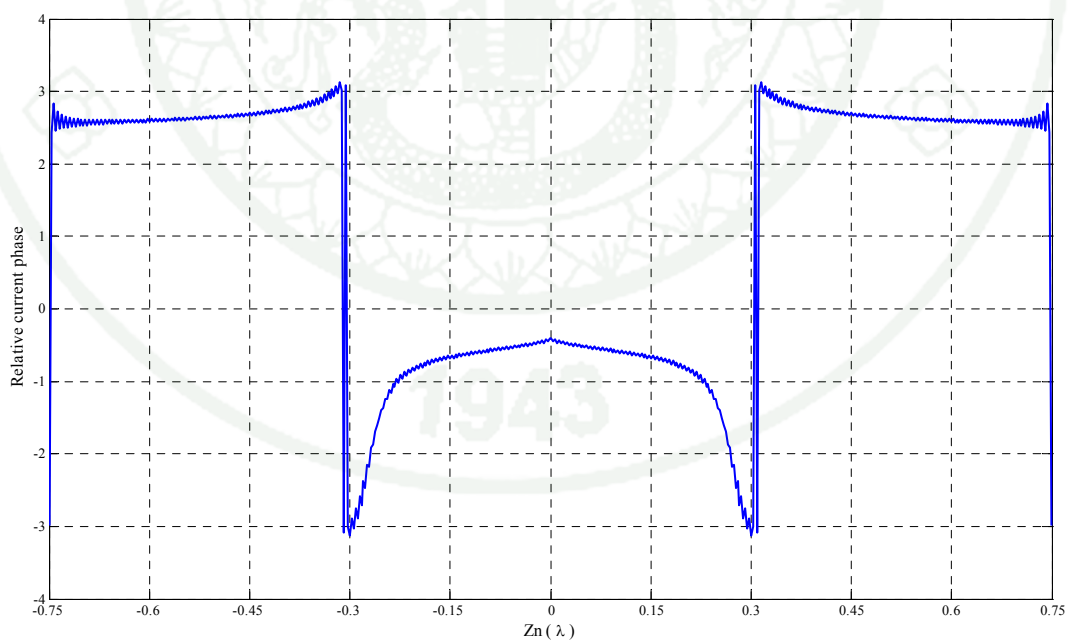


Figure 26 Relative current phase of a dipole antenna,

$$l = \frac{3}{2}\lambda, N = 512 \text{ and } a = l/1024.$$

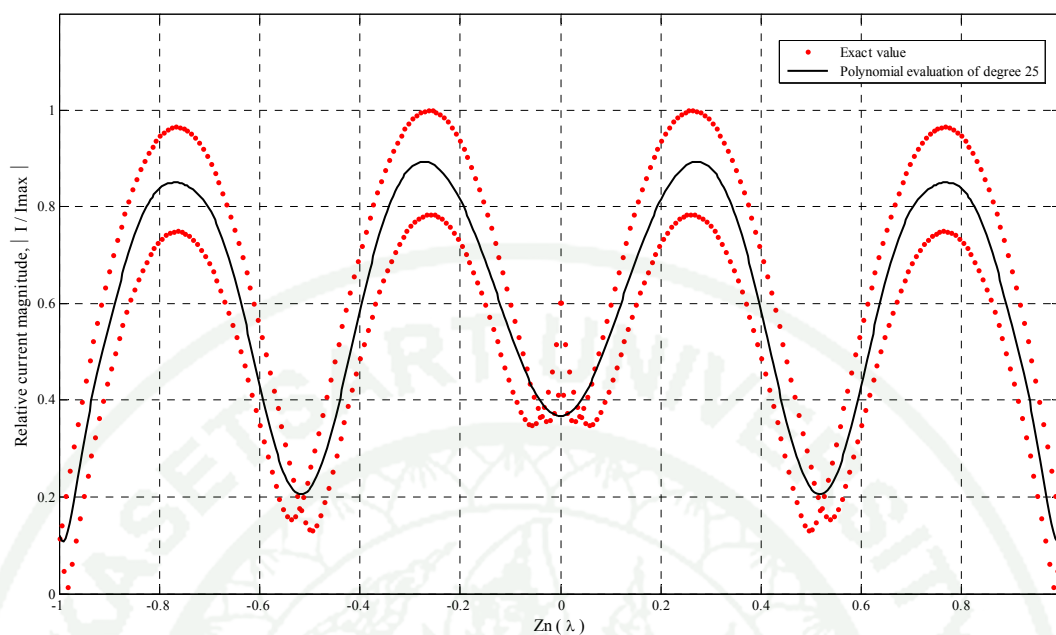


Figure 27 Relative current magnitude of a dipole antenna,
 $l = 2\lambda$, $N = 512$ and $a = l/1024$.

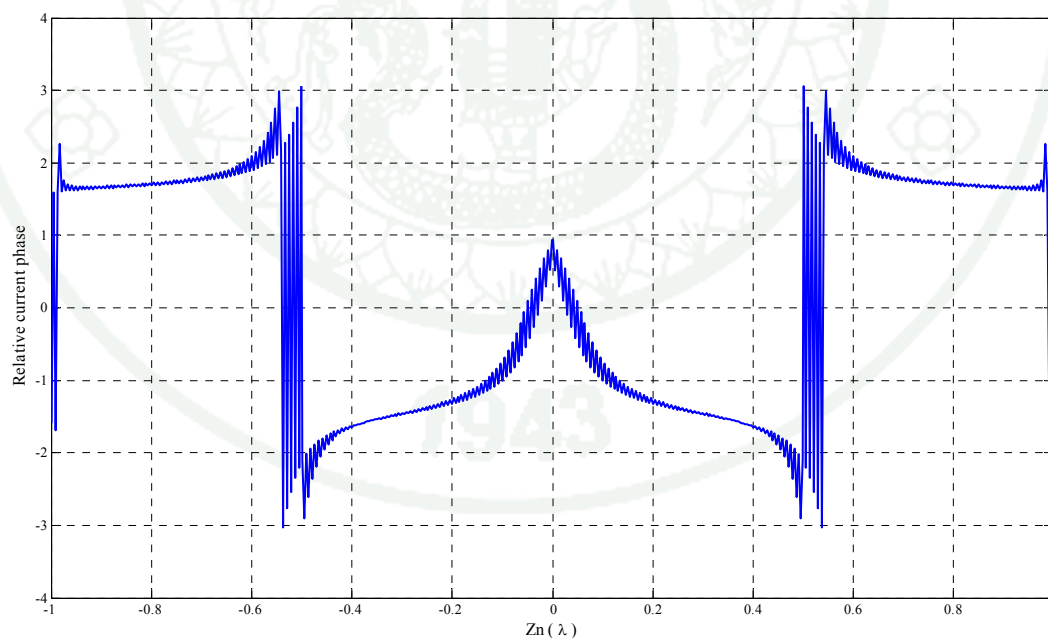


Figure 28 Relative current phase of a dipole antenna,
 $l = 2\lambda$, $N = 512$ and $a = l/1024$.

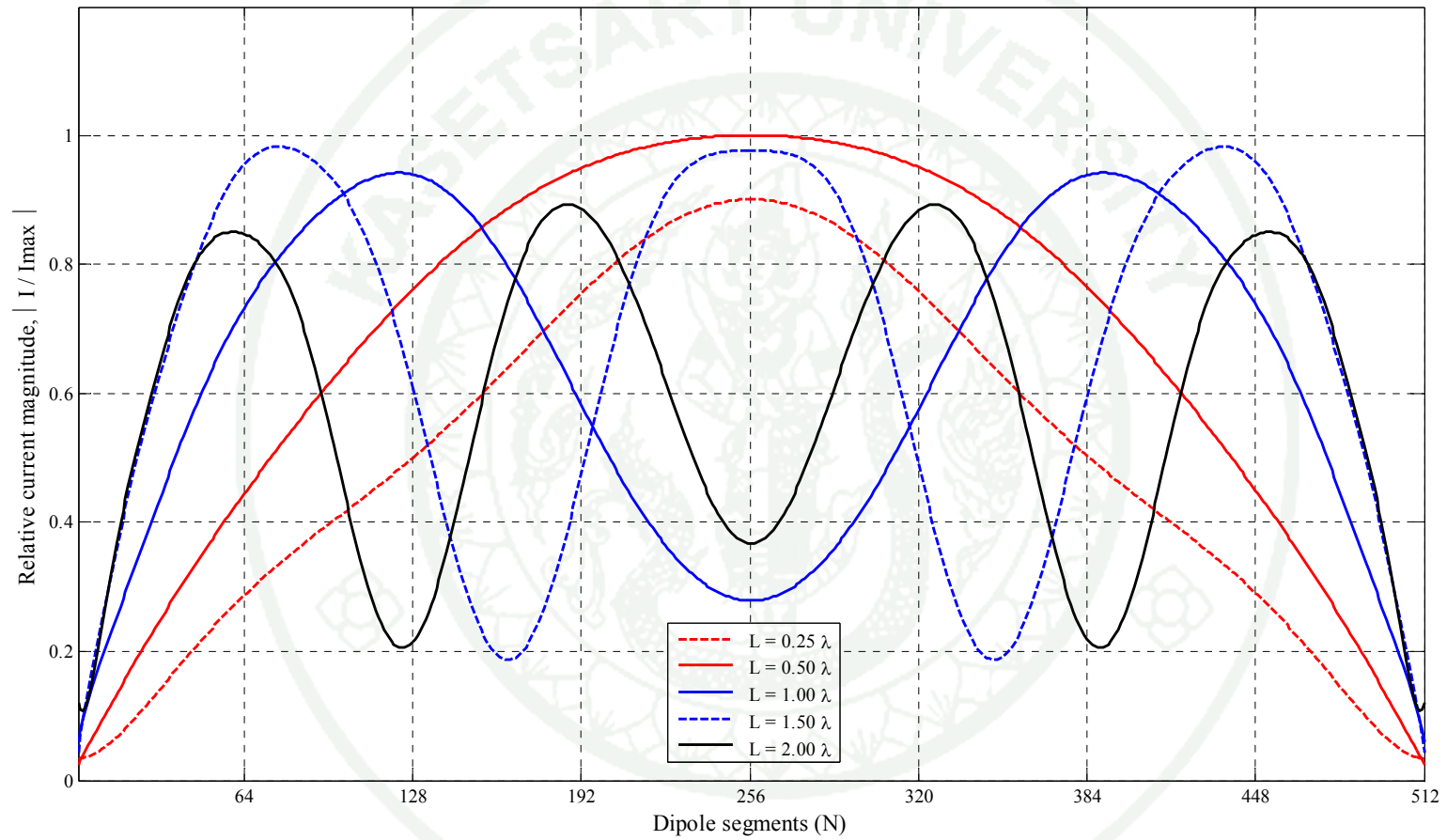


Figure 29 The comparison graph of relative current distribution on a dipole antenna, $l = 0.25, 0.50, 1.00, 1.50$ and 2.00λ , $N = 512$ and $a = l / 1024$.

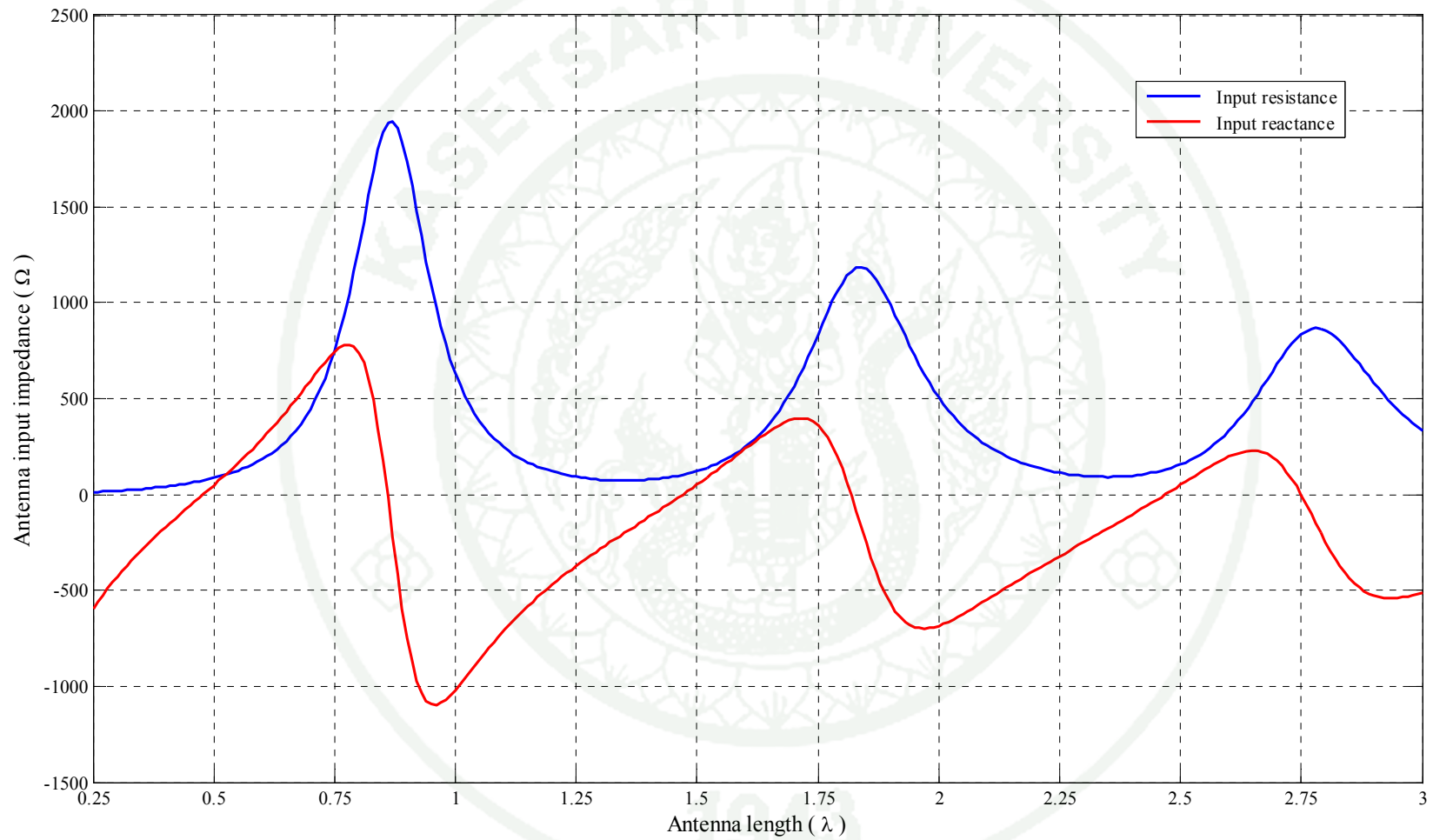


Figure 30 The input impedance of a dipole antenna, $N = 512$ and $a = l / 1024$.

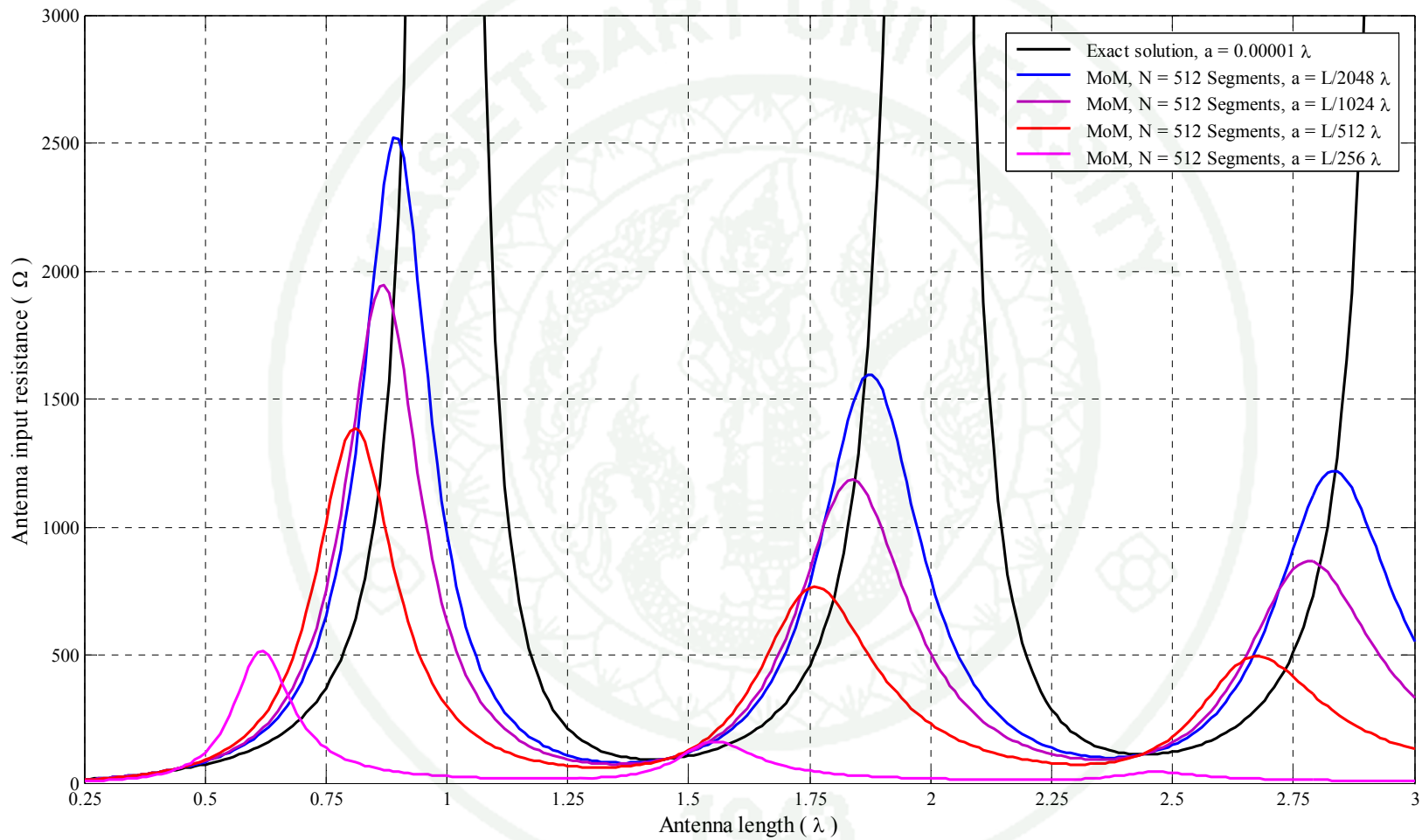


Figure 31 The comparison graph of the antenna input resistance between the Exact Solution ($a = 0.00001 \lambda$) and MoM ($N = 512$).

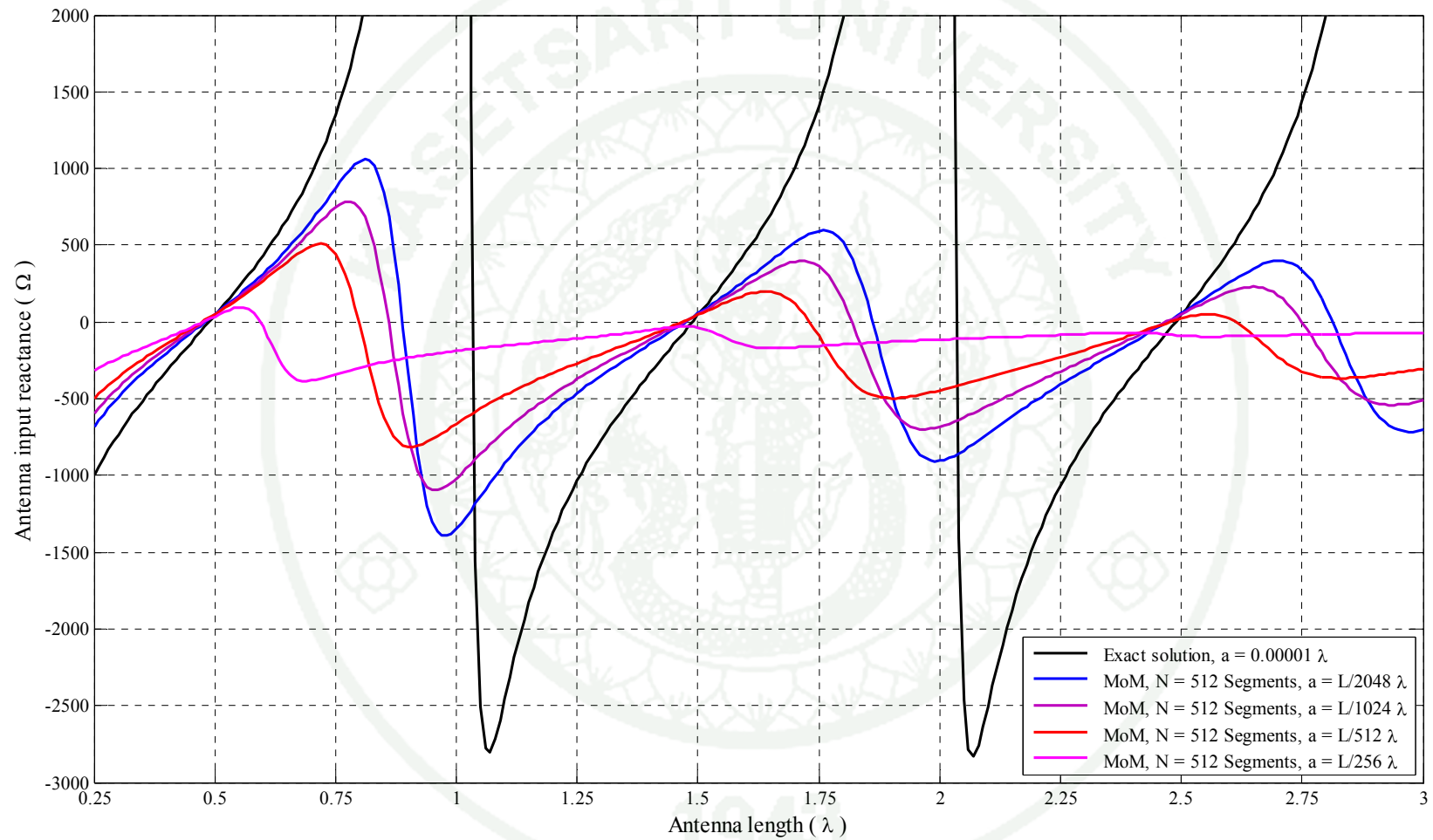


Figure 32 The comparison graph of the antenna input reactance between the Exact Solution ($a = 0.00001 \lambda$) and MoM ($N = 512$).

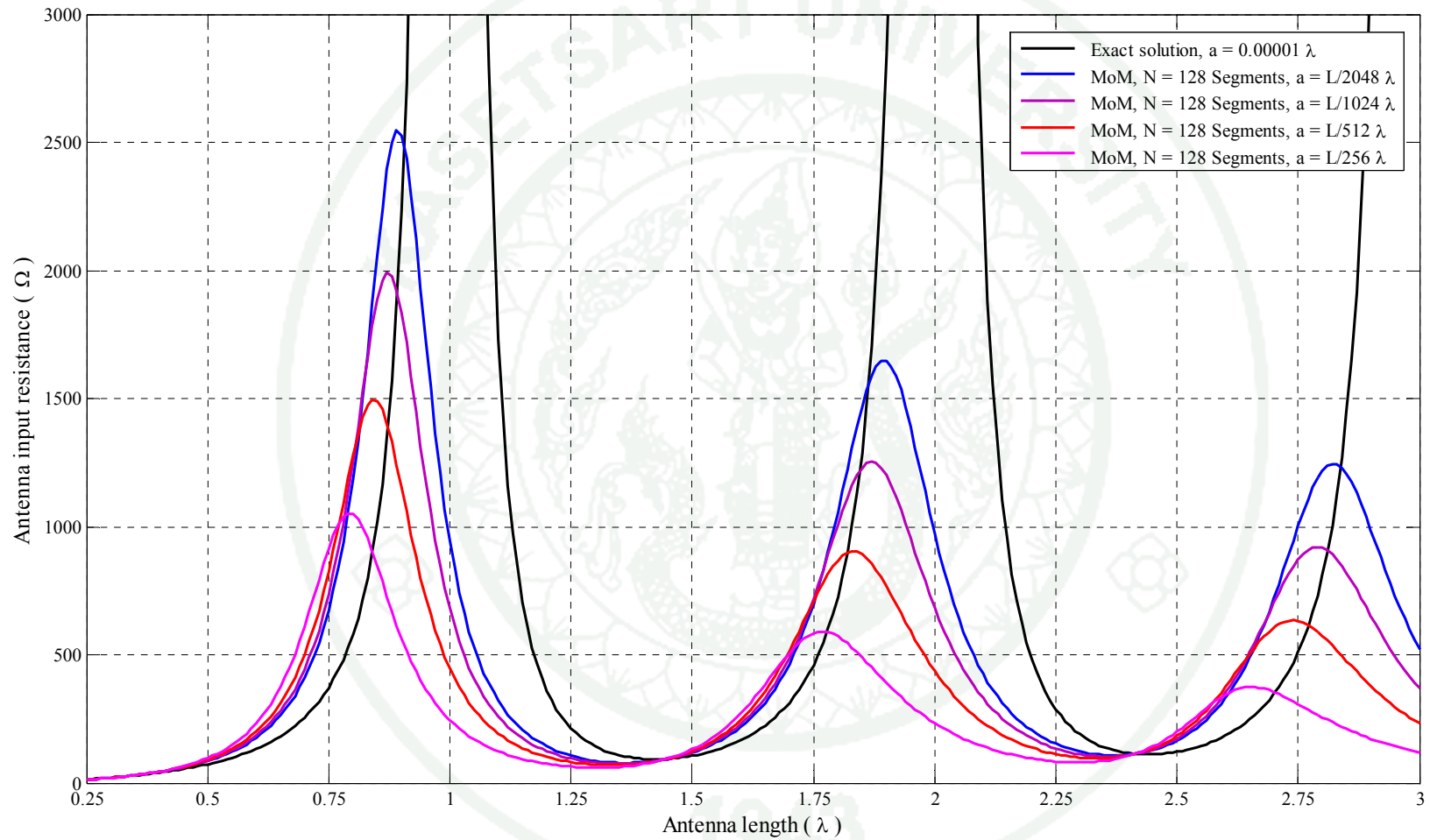


Figure 33 The comparison graph of the antenna input resistance between the Exact Solution ($a = 0.00001 \lambda$) and MoM ($N = 128$).

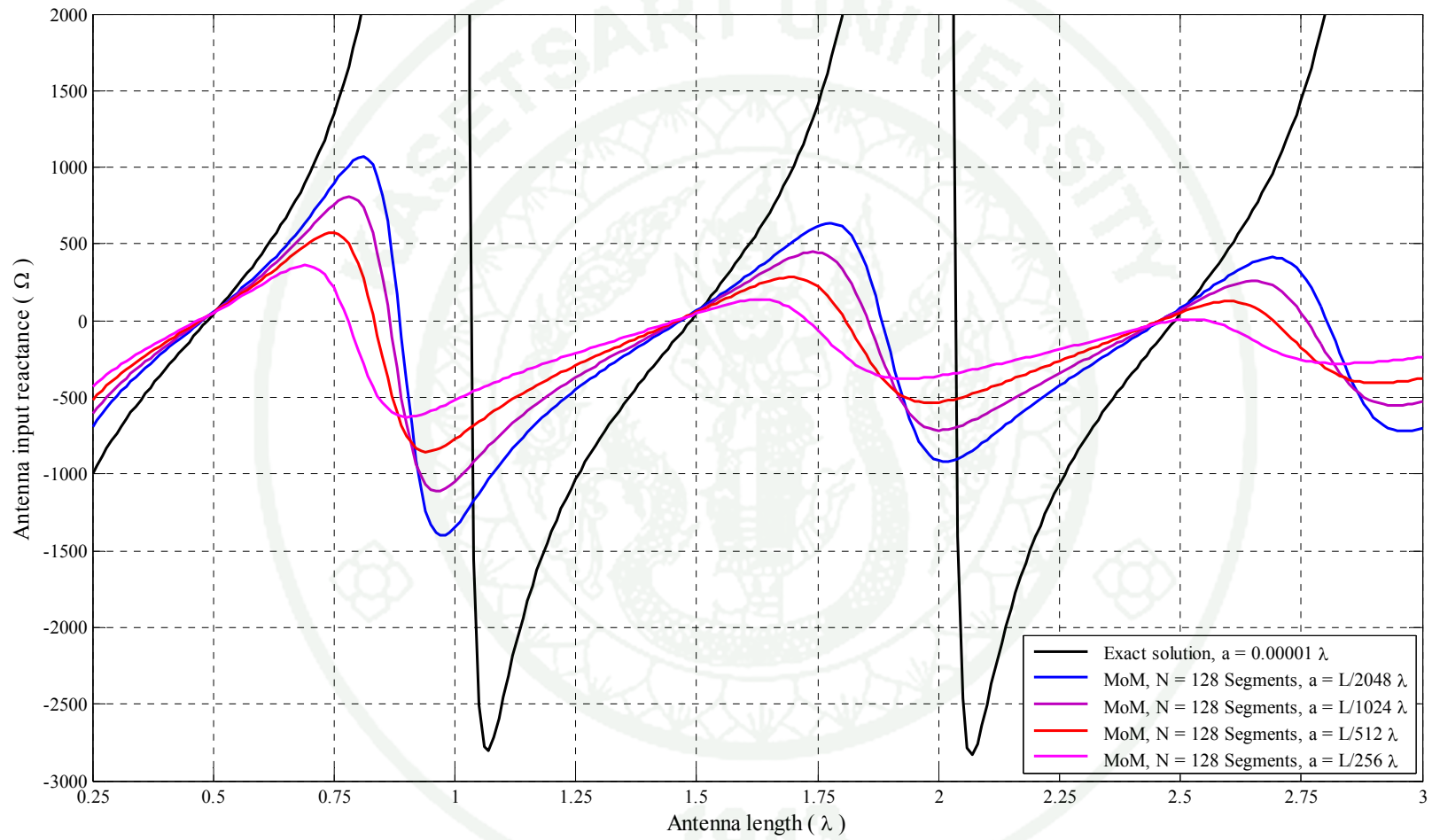


Figure 34 The comparison graph of the antenna input reactance between the Exact Solution ($a = 0.00001 \lambda$) and MoM ($N = 128$).

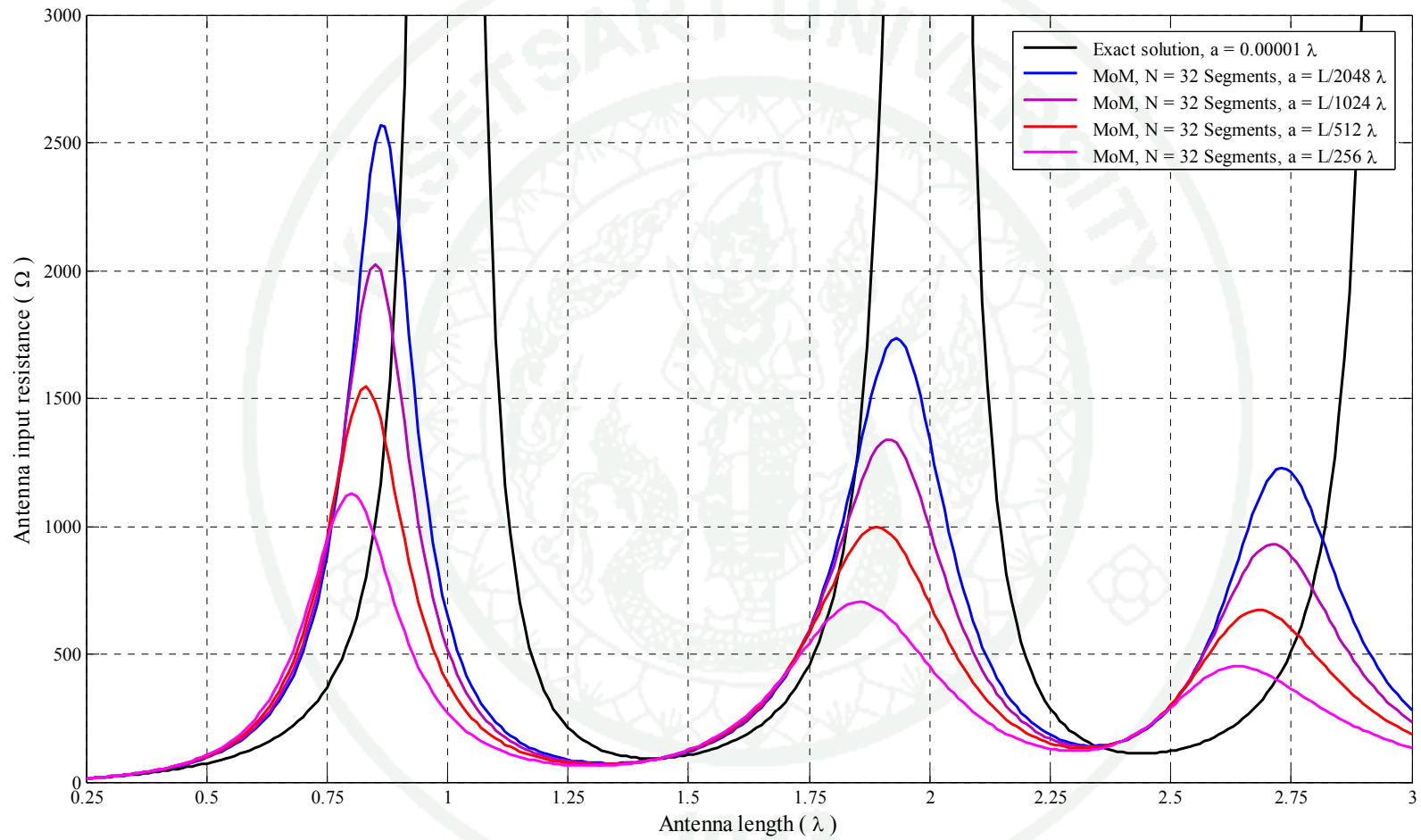


Figure 35 The comparison graph of the antenna input resistance between the Exact Solution ($a = 0.00001 \lambda$) and MoM ($N = 32$).

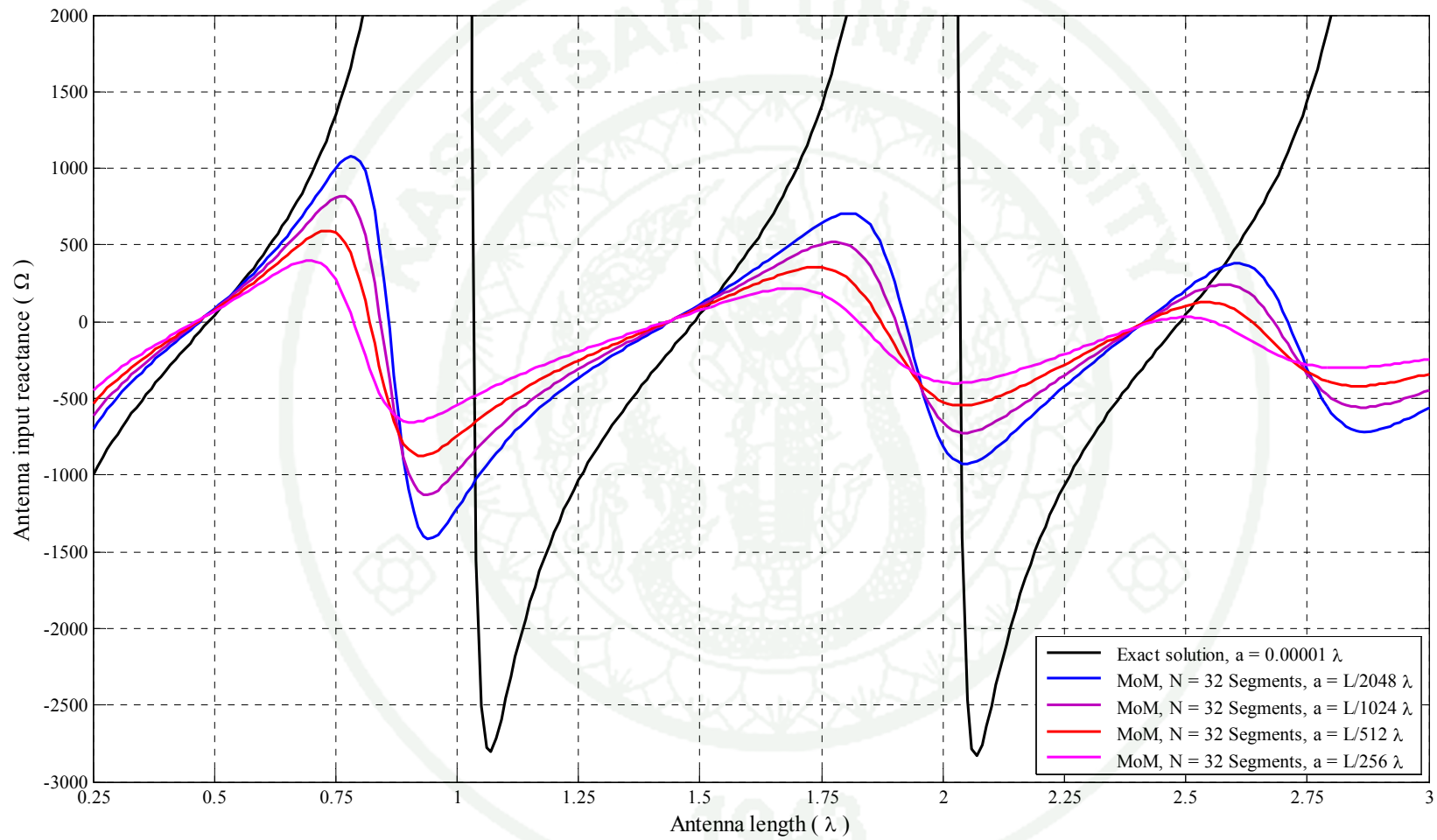


Figure 36 The comparison graph of the antenna input reactance between the Exact Solution ($a = 0.00001 \lambda$) and MoM ($N = 32$).

In this research, we use the Exact Solution of the input impedance of the half wavelength dipole antenna as a reference, radius of the dipole (a) = 0.00001 λ and $R_{i, \text{Exact}}(0.5\lambda) + jX_{i, \text{Exact}}(0.5\lambda) \approx 73.129131844670740 + j42.544547283978790 \Omega$. Also, the illustration of the absolute error between the Exact Solution and MoM is defined as the following picture

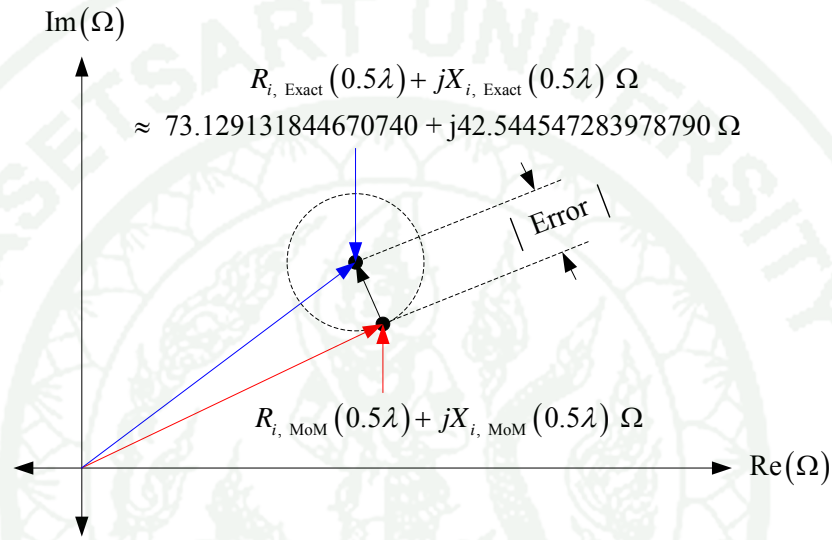


Figure 37 The illustration of the absolute error between the Exact Solution and MoM.

The equation of the absolute error and the % of the absolute error are defined as the following equations, respectively,

$$| \text{Error} | = \left| \left(R_{i, \text{Exact}}(0.5\lambda) + jX_{i, \text{Exact}}(0.5\lambda) \right) - \left(R_{i, \text{MoM}}(0.5\lambda) + jX_{i, \text{MoM}}(0.5\lambda) \right) \right| \quad (88)$$

$$\% \text{ Error} = 100 \times \frac{| \text{Error} |}{\left| R_{i, \text{Exact}}(0.5\lambda) + jX_{i, \text{Exact}}(0.5\lambda) \right|} \quad (89)$$

For example, the input impedance, which is computed by MoM $\left(l = \frac{\lambda}{2}, N = 512 \text{ and } a = l / 2048 \right)$, is $83.208982076653610 + j48.501934770617560$.

Then, the % of the absolute error is about 13.839356971163323 %.

Table 1 The % of the absolute error between the Exact Solution and MoM (N = 512).

Antenna Length = 0.5λ		
MoM	Input Impedance (Ohms)	Error (%)
N = 512, a = $l / 2048$	83.209 + j48.502	13.839
N = 512, a = $l / 1024$	85.573 + j49.124	16.638
N = 512, a = $l / 512$	90.623 + j49.919	22.44
N = 512, a = $l / 256$	120.16 + j36.478	56.044

Table 2 The % of the absolute error between the Exact Solution and MoM (N = 128).

Antenna Length = 0.5λ		
MoM	Input Impedance (Ohms)	Error (%)
N = 128, a = $l / 2048$	85.419 + j54.388	20.173
N = 128, a = $l / 1024$	87.421 + j53.823	21.519
N = 128, a = $l / 512$	90.608 + j53.416	24.33
N = 128, a = $l / 256$	96.672 + j52.973	30.435

Table 3 The % of the absolute error between the Exact Solution and MoM (N = 32).

Antenna Length = 0.5λ		
MoM	Input Impedance (Ohms)	Error (%)
N = 32, a = $l / 2048$	95.661 + j82.044	53.749
N = 32, a = $l / 1024$	97.681 + j77.708	50.691
N = 32, a = $l / 512$	100.61 + j73.268	48.722
N = 32, a = $l / 256$	105.25 + j68.504	48.812

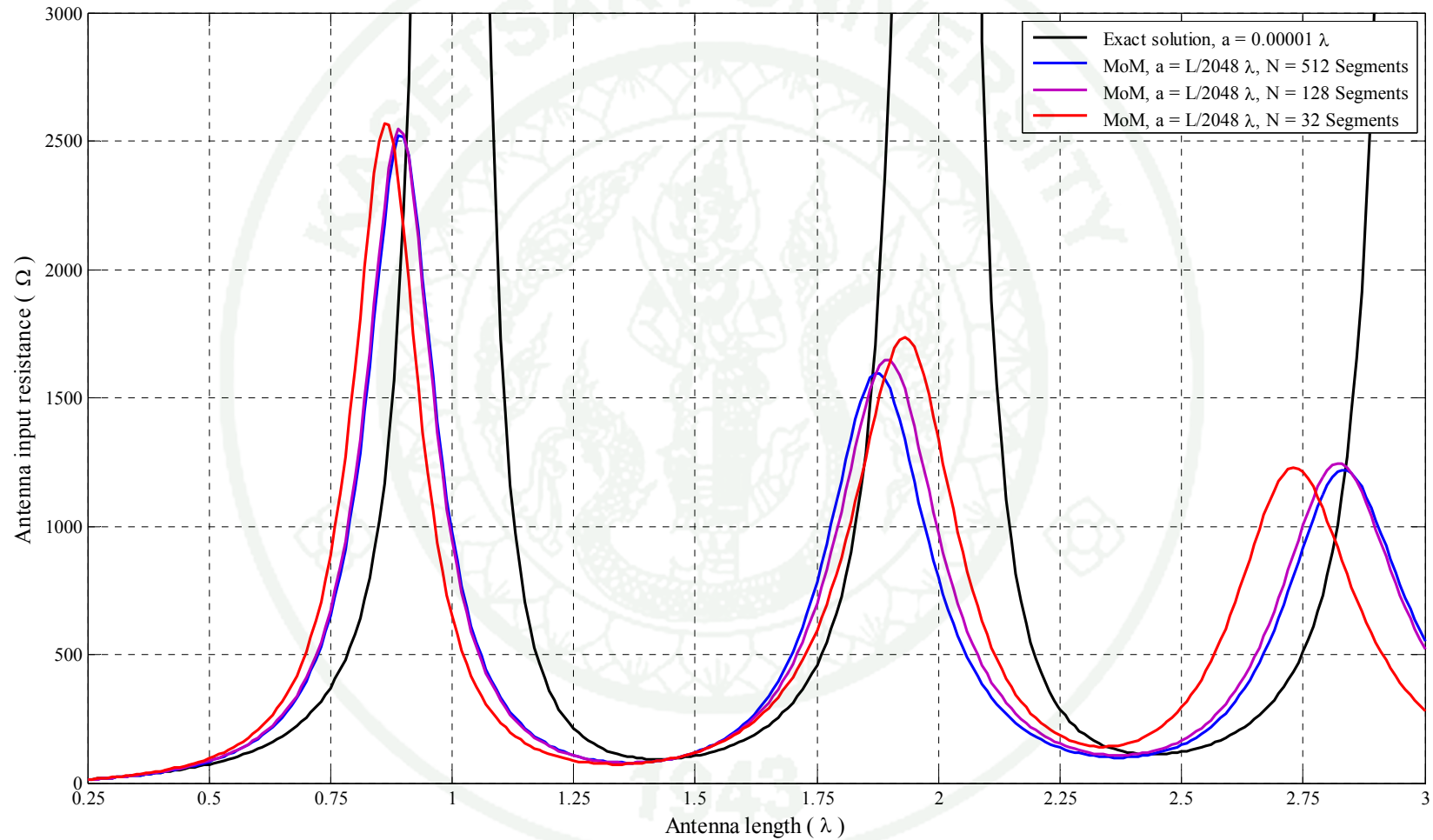


Figure 38 The comparison graph of the antenna input resistance between the Exact Solution ($a = 0.00001 \lambda$) and MoM ($a = l / 2048 \lambda$).

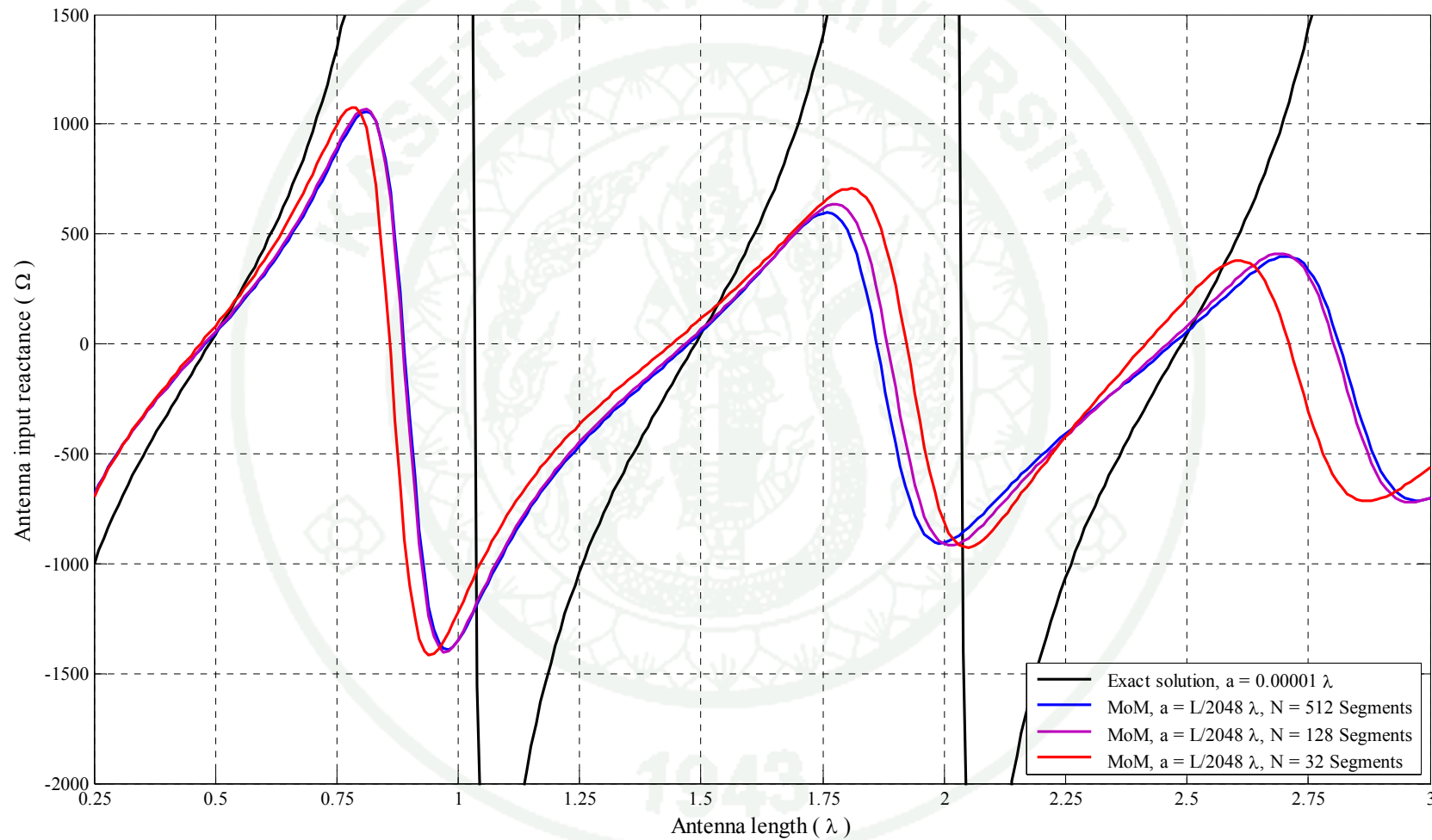


Figure 39 The comparison graph of the antenna input reactance between the Exact Solution ($a = 0.00001 \lambda$) and MoM ($a = l / 2048 \lambda$).

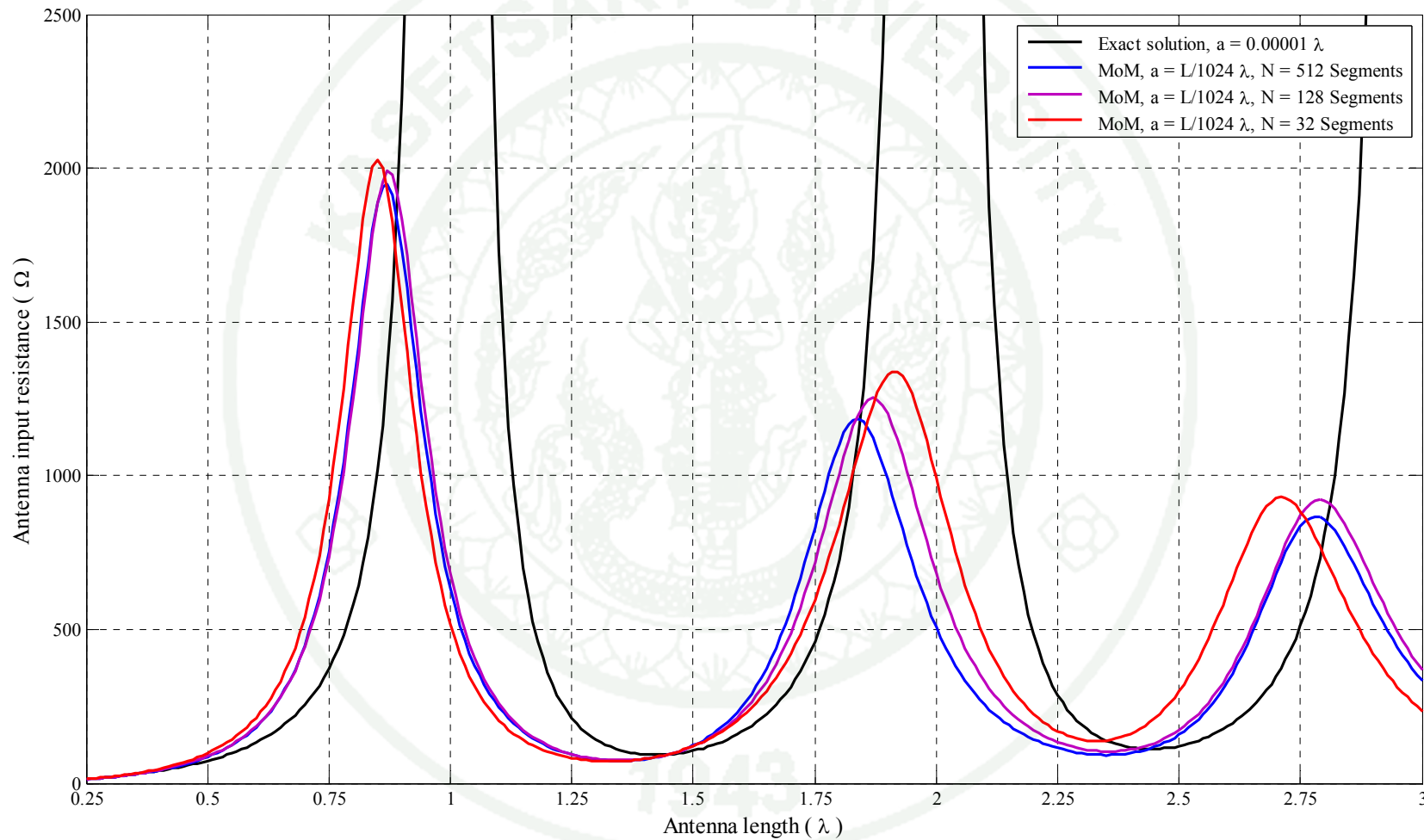


Figure 40 The comparison graph of the antenna input resistance between the Exact Solution ($a = 0.00001 \lambda$) and MoM ($a = l / 1024 \lambda$).

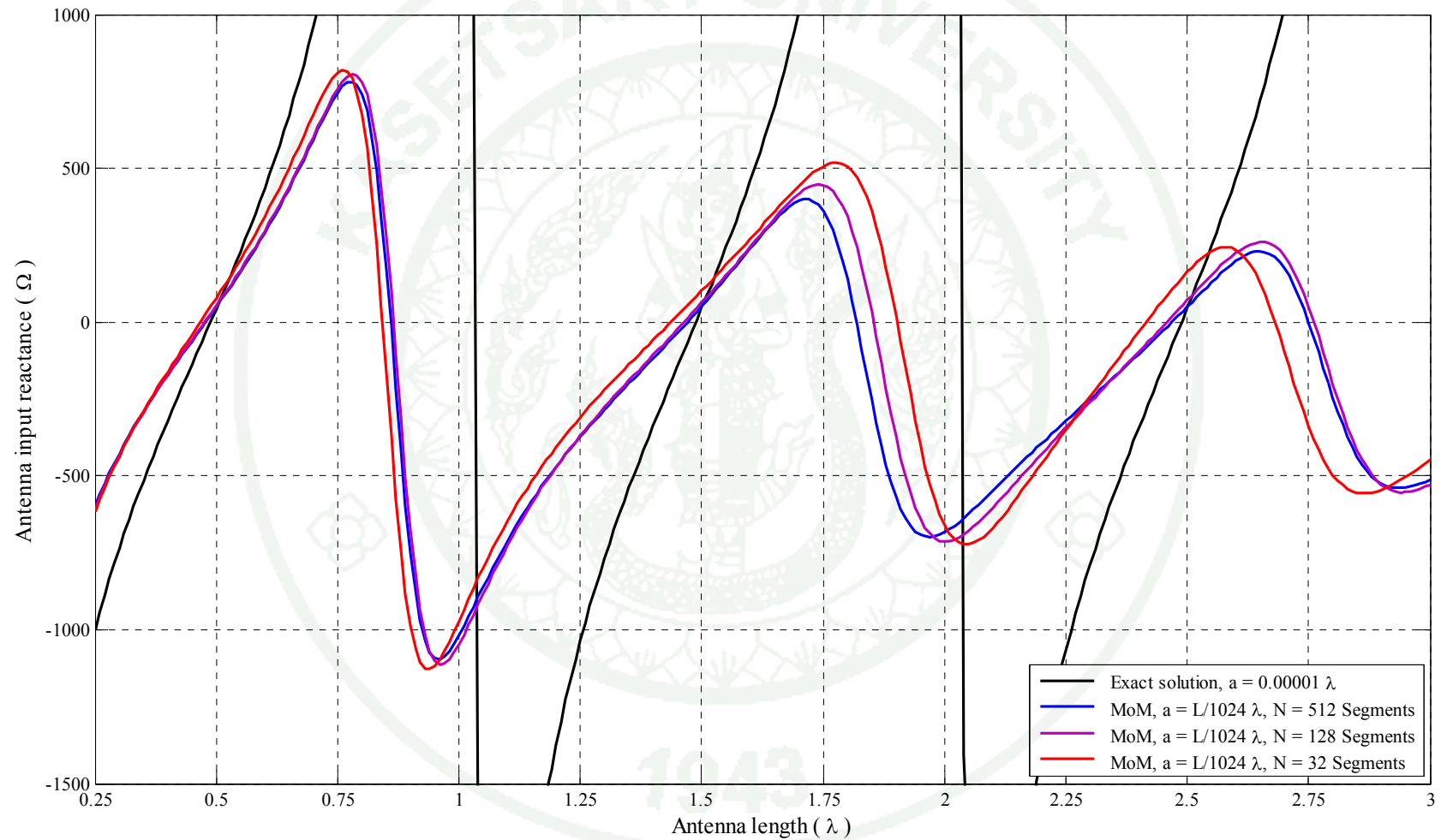


Figure 41 The comparison graph of the antenna input reactance between the Exact Solution ($a = 0.00001 \lambda$) and MoM ($a = l / 1024 \lambda$).

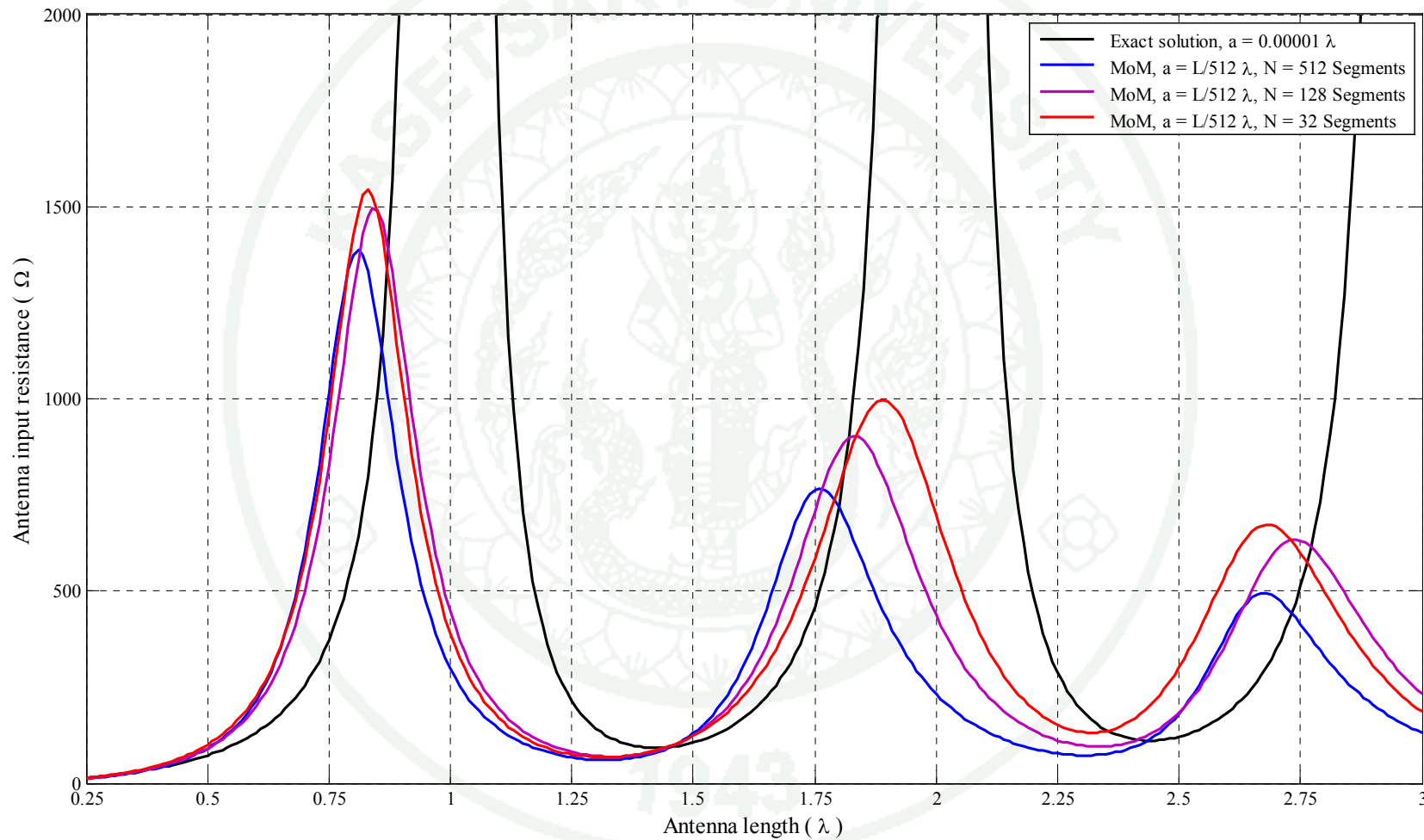


Figure 42 The comparison graph of the antenna input resistance between the Exact Solution ($a = 0.00001 \lambda$) and MoM ($a = l / 512 \lambda$).

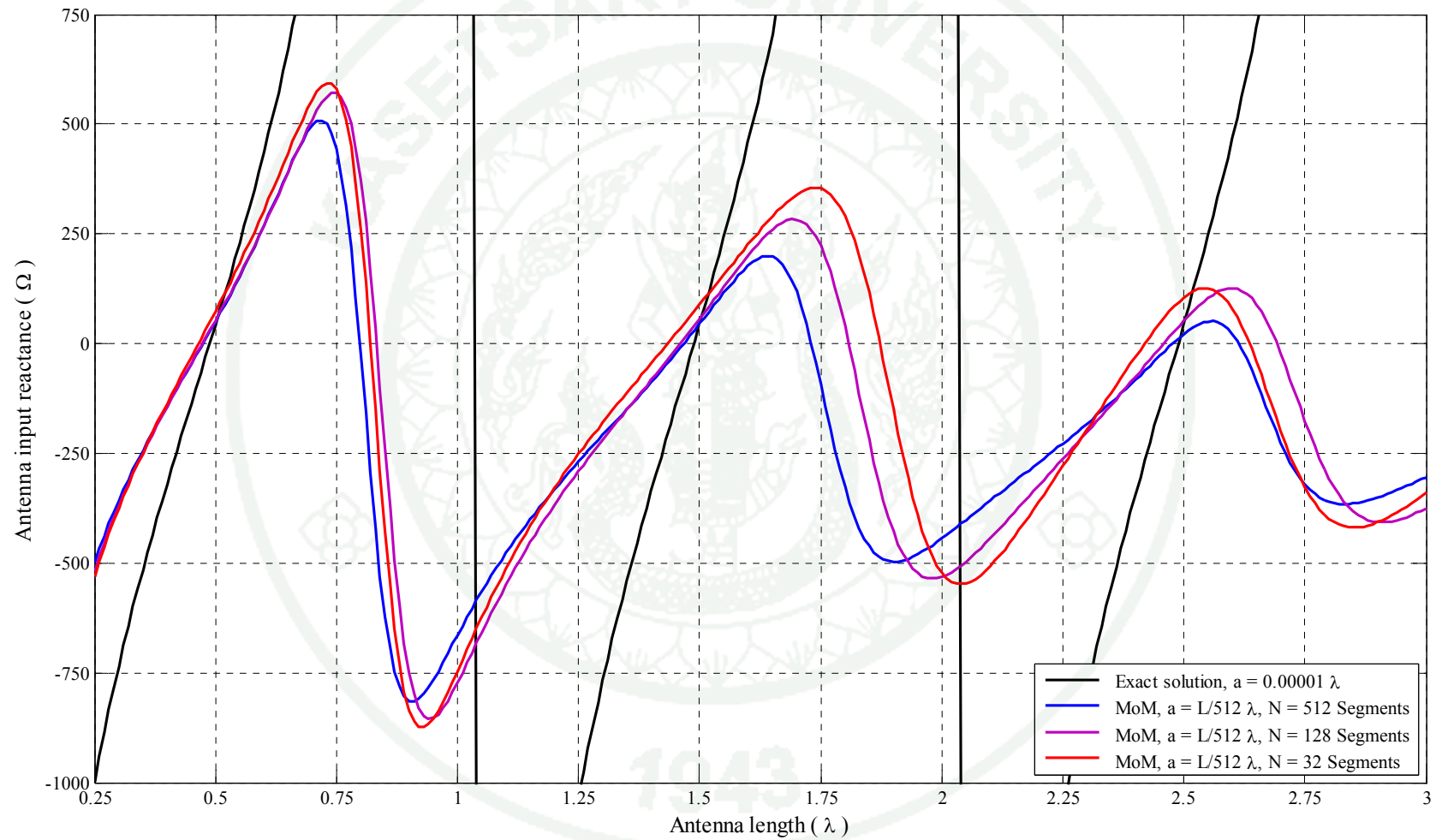


Figure 43 The comparison graph of the antenna input reactance between the Exact Solution ($a = 0.00001 \lambda$) and MoM ($a = l / 512 \lambda$).

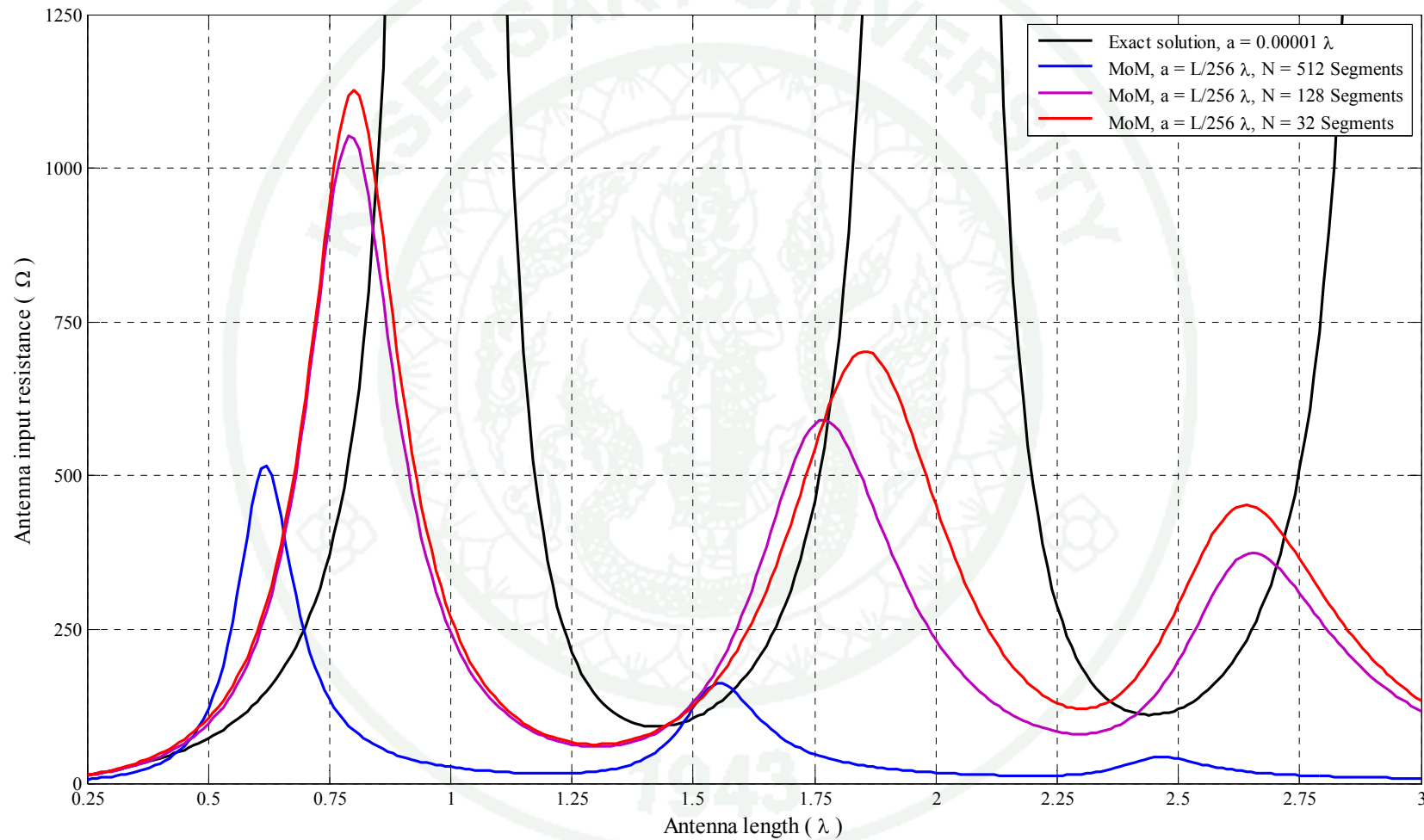


Figure 44 The comparison graph of the antenna input resistance between the Exact Solution ($a = 0.00001 \lambda$) and MoM ($a = l / 256 \lambda$).

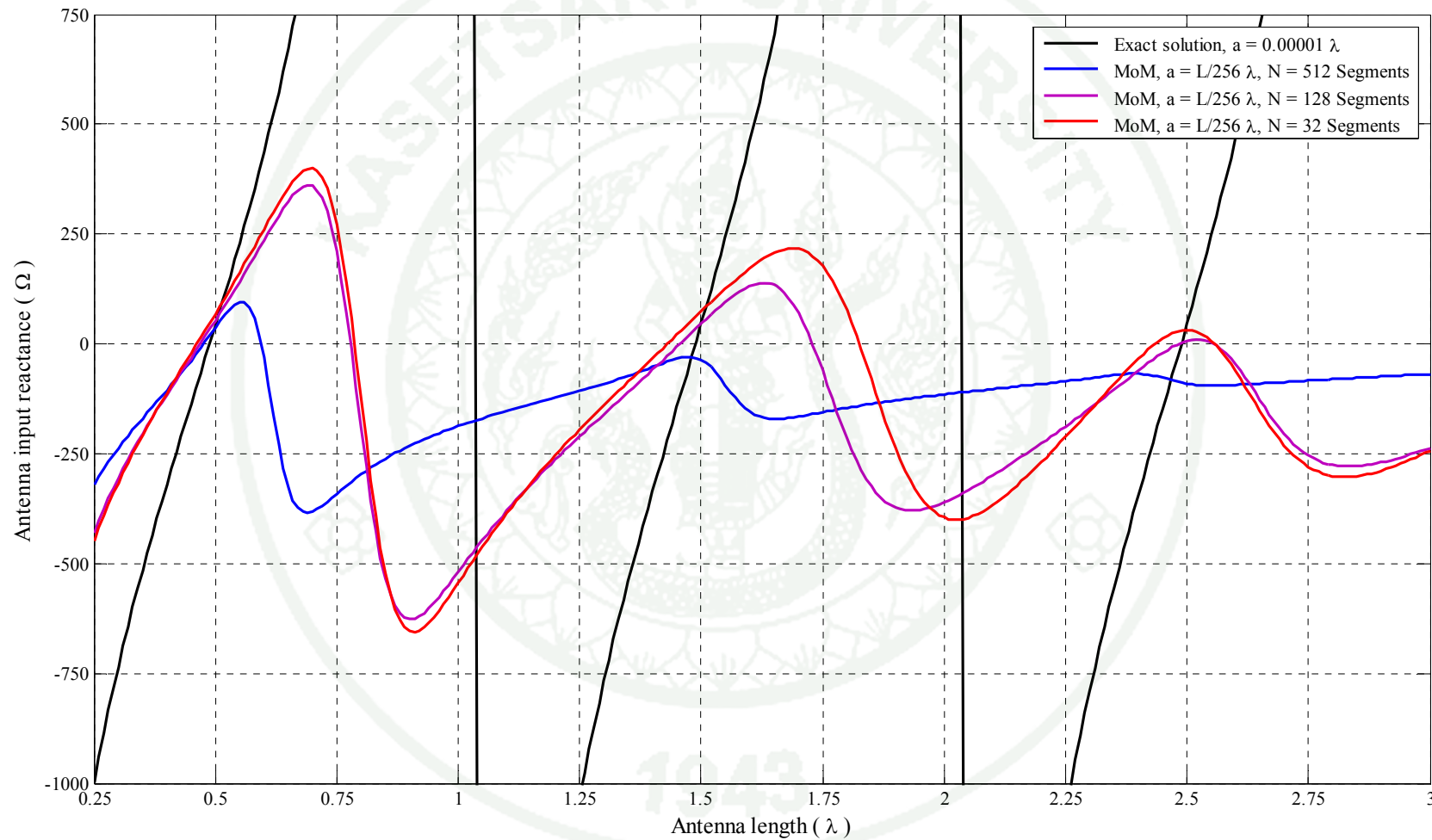


Figure 45 The comparison graph of the antenna input reactance between the Exact Solution ($a = 0.00001 \lambda$) and MoM ($a = l / 256 \lambda$).

Table 4 The % of the absolute error between the Exact Solution and MoM
($a = l / 2048$).

Antenna Length = 0.5λ		
MoM	Input Impedance (Ohms)	Error (%)
$a = l / 2048, N = 512$	$83.209 + j48.502$	13.839
$a = l / 2048, N = 128$	$85.419 + j54.388$	20.173
$a = l / 2048, N = 32$	$95.661 + j82.044$	53.749

Table 5 The % of the absolute error between the Exact Solution and MoM
($a = l / 1024$).

Antenna Length = 0.5λ		
MoM	Input Impedance (Ohms)	Error (%)
$a = l / 1024, N = 512$	$85.573 + j49.124$	16.638
$a = l / 1024, N = 128$	$87.421 + j53.823$	21.519
$a = l / 1024, N = 32$	$97.681 + j77.708$	50.691

Table 6 The % of the absolute error between the Exact Solution and MoM
($a = l / 512$).

Antenna Length = 0.5λ		
MoM	Input Impedance (Ohms)	Error (%)
$a = l / 512, N = 512$	$90.623 + j49.919$	22.44
$a = l / 512, N = 128$	$90.608 + j53.416$	24.33
$a = l / 512, N = 32$	$100.61 + j73.268$	48.722

Table 7 The % of the absolute error between the Exact Solution and MoM
($a = l / 256$).

Antenna Length = 0.5λ		
MoM	Input Impedance (Ohms)	Error (%)
$a = l / 256, N = 512$	$120.16 + j36.478$	56.044
$a = l / 256, N = 128$	$96.672 + j52.973$	30.435
$a = l / 256, N = 32$	$105.25 + j68.504$	48.812

In conclusion, almost the entire % of the absolute errors varies depending on the radius of dipole antenna. In addition, Table 1 to Table 2, the small radius gives the small error. However, as shown in Table 3, the big radius gives the small error.

On the other hand, Table 4 to Table 6, all of the % of the absolute errors varies inversely with the dipole segmentation. The more segments give the small error. However, Table 7, the low segments gives the small error.

2.7 Multigrid methods

In this section, the essential principle of Multigrid methods for numerical computation will be implemented in order to solve for the current distribution on a dipole antenna. The advantage of this methodology is to accelerate the rate of convergence of a basic iterative method by global correction from time to time, accomplished by solving a coarse problem. The main idea is similar to interpolation between coarser and finer grids. Moreover, it has the advantage over other methods that it often scales linearly with the number of discrete nodes used. The example application for Multigrid is in the numerical solution of the current distribution (Kuhiran *et al.*, 2004). The introductions to the basic principles of Multigrid methods are given by Brandt and Wesseling (Wesseling, 1992). More advanced expositions are given by Zhu (Zhu, 2006).

By using Multigrid methods, we don't want to solve Equation (81) directly so that Equation (81), as well as Equation (15), must be rewritten as the following aspects

$$[G]_{\text{Fine grid}} [I]_{\text{Fine grid}} = [V]_{\text{Fine grid}} \quad (90)$$

$$\begin{aligned} & \left[\langle W_m, G_{m,n}(u_n) \rangle \right]_{m \times n} \left[\langle W_m, I_m \rangle \right]_{m \times 1} = \left[\langle W_m, V_m \rangle \right]_{m \times 1} \\ [G]_{\text{Fine grid}} &= \begin{bmatrix} \langle W_1, G_{1,1}(u_1) \rangle & \langle W_1, G_{1,2}(u_2) \rangle & \cdots & \langle W_1, G_{1,N+1}(u_{N+1}) \rangle \\ \langle W_2, G_{2,1}(u_1) \rangle & \langle W_2, G_{2,2}(u_2) \rangle & \cdots & \langle W_2, G_{2,N+1}(u_{N+1}) \rangle \\ \vdots & \vdots & \ddots & \vdots \\ \langle W_{N+1}, G_{N+1,1}(u_1) \rangle & \langle W_{N+1}, G_{N+1,2}(u_2) \rangle & \cdots & \langle W_{N+1}, G_{N+1,N+1}(u_{N+1}) \rangle \end{bmatrix} \\ [I]_{\text{Fine grid}} &= \begin{bmatrix} \langle W_1, I_1 \rangle \\ \langle W_2, I_2 \rangle \\ \vdots \\ \langle W_{N+1}, I_{N+1} \rangle \end{bmatrix} \\ [V]_{\text{Fine grid}} &= \begin{bmatrix} \langle W_1, V_1 \rangle \\ \langle W_2, V_2 \rangle \\ \vdots \\ \langle W_{N+1}, V_{N+1} \rangle \end{bmatrix} \end{aligned}$$

If we define the relation of basis function between coarse grid, W'_i, u'_j , and fine grid, W_i, u_j , as

$$W'_i = \frac{W_i + W_{i+1}}{\sqrt{2}} \quad (91)$$

$$u'_j = \frac{u_j + u_{j+1}}{\sqrt{2}} \quad (92)$$

We suggest a recursive scheme in which successively coarser grids are used, where the descent to coarser levels continues until the convergence rate of relaxation is acceptable. Then Equation (90) is represented in coarse grid as

$$[G]_{\text{Coarse grid}} [I]_{\text{Coarse grid}} = [V]_{\text{Coarse grid}} \quad (93)$$

$$\begin{aligned} & \left[\langle W'_{i'}, G'_{i',j'}(u'_{j'}) \rangle \right]_{i' \times j'} \left[\langle W'_{i'}, I'_{i'} \rangle \right]_{i' \times 1} = \left[\langle W'_{i'}, V'_{i'} \rangle \right]_{i' \times 1} \\ \langle W'_{i'}, G'_{i',j'}(u'_{j'}) \rangle &= \left\langle \frac{W_i + W_{i+1}}{\sqrt{2}}, G'_{i',j'}(u'_{j'}) \right\rangle \\ &= \frac{1}{\sqrt{2}} \left(\langle W_i, G'_{i',j'}(u'_{j'}) \rangle + \langle W_{i+1}, G'_{i',j'}(u'_{j'}) \rangle \right) \\ &= \frac{1}{\sqrt{2}} \left(\left\langle W_i, G_{i,j} \left(\frac{u_j + u_{j+1}}{\sqrt{2}} \right) \right\rangle + \left\langle W_{i+1}, G_{i+1,j} \left(\frac{u_j + u_{j+1}}{\sqrt{2}} \right) \right\rangle \right) \\ &= \frac{1}{2} \left(\langle W_i, G_{i,j}(u_j) \rangle + \langle W_i, G_{i,j+1}(u_{j+1}) \rangle + \right. \\ & \quad \left. \langle W_{i+1}, G_{i+1,j}(u_j) \rangle + \langle W_{i+1}, G_{i+1,j+1}(u_{j+1}) \rangle \right) \\ \langle W'_{i'}, I'_{i'} \rangle &= \left\langle \frac{W_i + W_{i+1}}{\sqrt{2}}, I_i \right\rangle \\ &= \frac{1}{\sqrt{2}} \left(\langle W_i, I_i \rangle + \langle W_{i+1}, I_{i+1} \rangle \right) \\ \langle W'_{i'}, V'_{i'} \rangle &= \left\langle \frac{W_i + W_{i+1}}{\sqrt{2}}, V_i \right\rangle \\ &= \frac{1}{\sqrt{2}} \left(\langle W_i, V_i \rangle + \langle W_{i+1}, V_{i+1} \rangle \right) \end{aligned}$$

The iteration of Equation (90) is started in the coarse grid, Equation (93), using zero as initial guess. The computation uses Gauss-Seidel method. The Gauss-Seidel method is a variation of Gauss elimination. The major difference is that when an unknown is eliminated in the Gauss-Seidel method, it is eliminated from all other

equations rather than just the subsequent ones. In matrix $[G]$, all rows are normalized by dividing them by their pivot elements and the elements above the major diagonal are eliminated (made zero) as well as the elements below the major diagonal. This matrix is transformed to diagonal matrix. In addition, the elimination step results in an identity matrix rather than a triangular matrix. Consequently, it is not necessary to employ back substitution to obtain the solution (Chapra and Canale, 2002). Suppose the Equation (93) has a unique solution and that the percent of the absolute of a Round Error (RE) is defined by

$$|RE_i| = \left| \frac{\tilde{I}_{i,t} - \tilde{I}_{i,t-1}}{\tilde{I}_{i,t}} \right| \times 100 \quad (94)$$

$|RE_i|$ = The absolute of a Round Error (RE) of element i , %.

t = Iterations round.

This error is also a vector and its magnitude may be measured by any of the standard vector norms. The most commonly used norms for this purpose are the maximum (or infinity) norm and the Euclidean or 2-norm, defined, respectively, by (Briggs *et al.*, 2000)

$$\|RE\|_{\infty} = \max_{1 \leq i \leq P} |RE_i| \quad \text{and} \quad \|RE\|_2 = \left(\sum_{i=1}^P RE_i^2 \right)^{\frac{1}{2}} \quad (95)$$

This research uses maximum norm of this error. Unfortunately, this error is just as inaccessible as the exact solution itself. The Gauss-Seidel method is repeated itself until this error is acceptable. Similarly, the accuracy of this approximate method is also measured by a Relative Error (RLE) (Hoffman, 2001). The percent of the absolute of a Relative Error is defined as

$$|RLE_i| = \left| \frac{\tilde{I}_{i,t} - \tilde{I}_{i,\text{Exact}}}{\tilde{I}_{i,\text{Exact}}} \right| \times 100 \quad (96)$$

$|RLE_i|$ = The absolute of a Relative Error (RLE) of element i , %.

t = Iterations rounds.

Correspondingly, this research uses Equation (95), maximum norm of the error, in order to finish the Gauss-Seidel method.

$$\|RLE\|_{\infty} = \max_{1 \leq i \leq P} |RLE_i| \quad (97)$$

Hence, Multigrid methods are a simple way to approximate the best approximation in the subspace. In addition, the approximated best approximation can serve as an initial guess if we choose an appropriate subspace—the exact solution of Equation (90) almost belongs to the subspace.

In this case, we use the Gauss-Seidel method as a reference. The dipole has N segments (100, 512 and 1,024 segments), $a = 0.00001 \lambda$ and $l = 1 \lambda$. A WHILE LOOP is used when a set of errors, $|RE_i|$, has to be executed as long as a condition is true, $\|RE\|_{\infty} > 0.5\%$. The flowchart is as the following figure

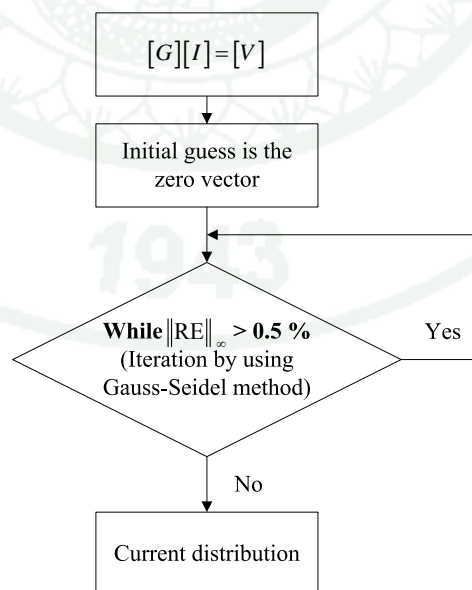
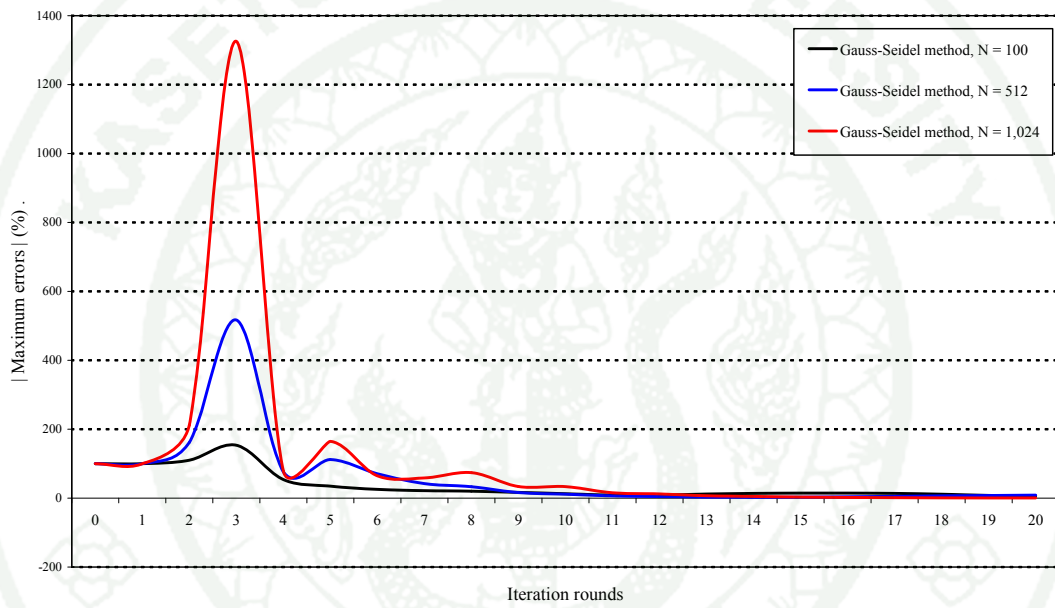


Figure 46 The flow chart of Gauss-Seidel method using $\|RE\|_{\infty}$.

Table 8 The iteration rounds in the Gauss-Seidel method depending on $\|\text{RE}\|_{\infty}$.

Algorithm	Dipole segments		
	N = 100	N = 512	N = 1,024
	Iteration rounds	Iteration rounds	Iteration rounds
	While $\ \text{RE}\ _{\infty} > 0.5\%$	While $\ \text{RE}\ _{\infty} > 0.5\%$	While $\ \text{RE}\ _{\infty} > 0.5\%$
Gauss-Seidel method	73	1,039	20

**Figure 47** $\|\text{RE}\|_{\infty}$ computed by the Gauss-Seidel method.

First, if we applied index of Equation (93), $i' = i$ and $j' = j$, then

$$\begin{aligned} \langle W'_i, G'_{i,j}(u'_j) \rangle &= \frac{1}{2} \left(\langle W_i, G_{i,j}(u_j) \rangle + \langle W_i, G_{i,j+1}(u_{j+1}) \rangle + \right. \\ &\quad \left. \langle W_{i+1}, G_{i+1,j}(u_j) \rangle + \langle W_{i+1}, G_{i+1,j+1}(u_{j+1}) \rangle \right) \\ \langle W'_1, G'_{1,1}(u'_1) \rangle &= \frac{1}{2} \left(\langle W_1, G_{1,1}(u_1) \rangle + \langle W_1, G_{1,2}(u_2) \rangle + \langle W_2, G_{2,1}(u_1) \rangle + \langle W_2, G_{2,2}(u_2) \rangle \right) \\ \langle W'_2, G'_{2,1}(u'_1) \rangle &= \frac{1}{2} \left(\langle W_2, G_{2,1}(u_1) \rangle + \langle W_2, G_{2,2}(u_2) \rangle + \langle W_3, G_{3,1}(u_1) \rangle + \langle W_3, G_{3,2}(u_2) \rangle \right) \\ &\vdots \end{aligned}$$

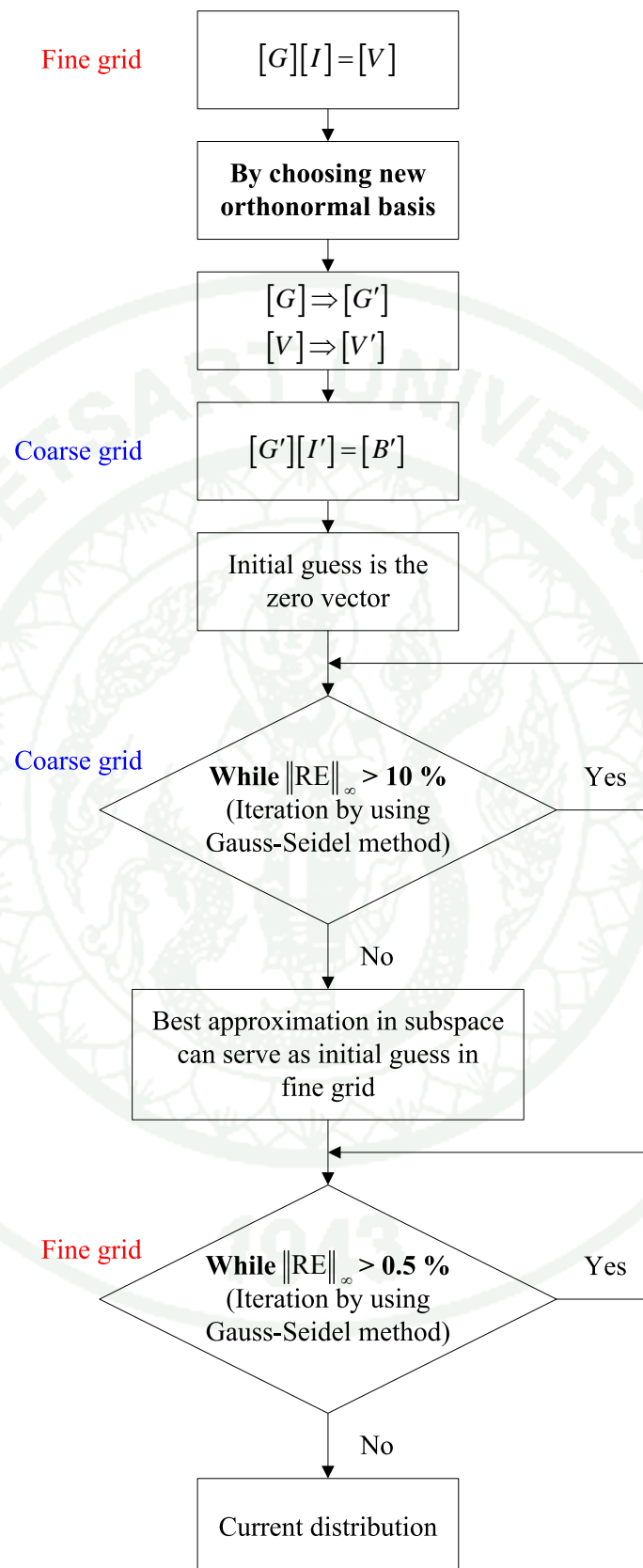


Figure 48 The flowchart of Multigrid method using $\|RE\|_{\infty}$.

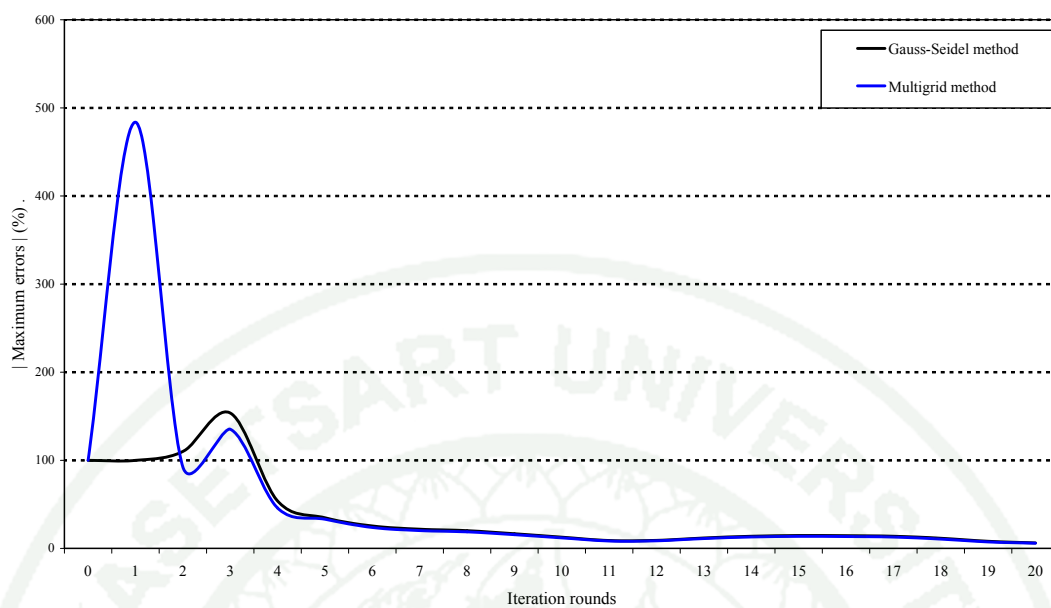


Figure 50 $\|RE\|_{\infty}$ computed by the Multigrid method, $N = 100$.

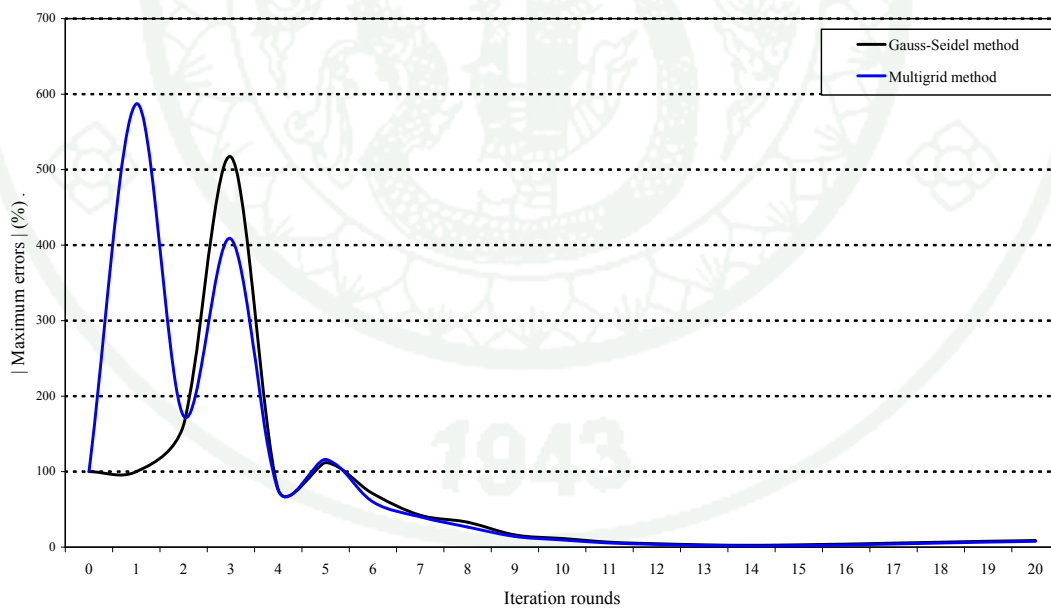


Figure 51 $\|RE\|_{\infty}$ computed by the Multigrid method, $N = 512$.

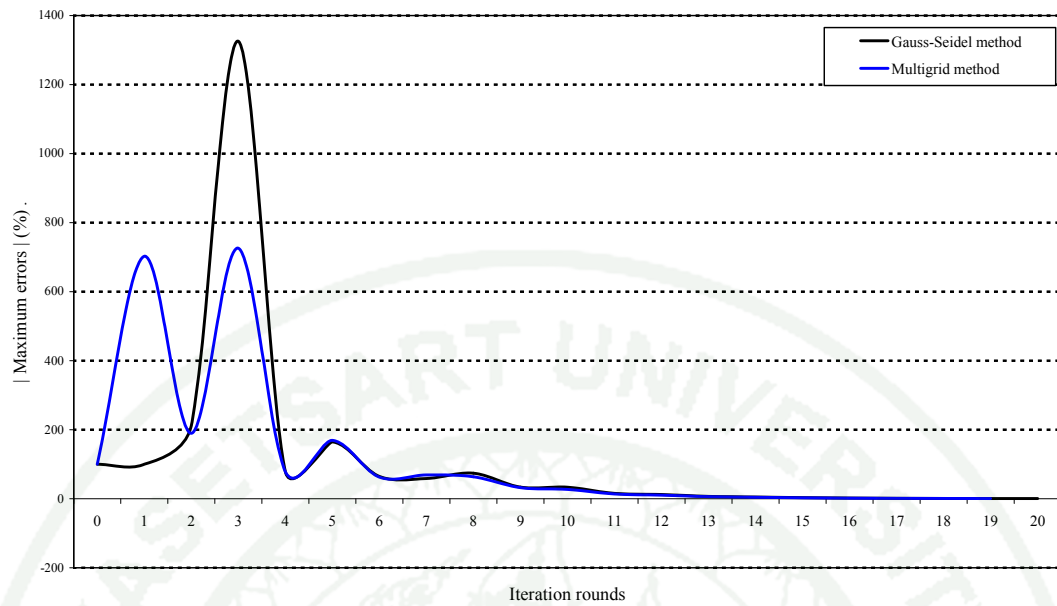


Figure 52 $\|RE\|_{\infty}$ computed by the Multigrid method, $N = 1,024$.

It should be noted that the transformation of the best approximation in subspace to fine grid must be obeyed this rule, the reversion of Equation (93),

$$\text{for } i = 1 \text{ to } \frac{N}{2} : \langle W_{2i-1}, I_{2i-1} \rangle = \langle W_{2i}, I_{2i} \rangle = \frac{\langle W'_i, I'_i \rangle}{\sqrt{2}} \text{ and } \langle W_{N+1}, I_{N+1} \rangle = 0$$

Second, we will modify index of Equation (93), $i+1=2i'$ and $j+1=2j'$, so that this index can be represented almost all the elements in matrix $[G]$ and $[V]$.

For example

$$\begin{aligned} \langle W'_{i'}, G'_{i',j'}(u'_{j'}) \rangle &= \frac{1}{2} \left(\langle W_{2i'-1}, G_{2i'-1,2j'-1}(u_{2j'-1}) \rangle + \langle W_{2i'-1}, G_{2i'-1,2j'}(u_{2j'}) \rangle + \right. \\ &\quad \left. \langle W_{2i'}, G_{2i',2j'-1}(u_{2j'-1}) \rangle + \langle W_{2i'}, G_{2i',2j'}(u_{2j'}) \rangle \right) \\ \langle W'_1, G'_{1,1}(u'_1) \rangle &= \frac{1}{2} \left(\langle W_1, G_{1,1}(u_1) \rangle + \langle W_1, G_{1,2}(u_2) \rangle + \langle W_2, G_{2,1}(u_1) \rangle + \langle W_2, G_{2,2}(u_2) \rangle \right) \\ \langle W'_2, G'_{2,1}(u'_1) \rangle &= \frac{1}{2} \left(\langle W_3, G_{3,1}(u_1) \rangle + \langle W_3, G_{3,2}(u_2) \rangle + \langle W_4, G_{4,1}(u_1) \rangle + \langle W_4, G_{4,2}(u_2) \rangle \right) \\ &\vdots \end{aligned}$$

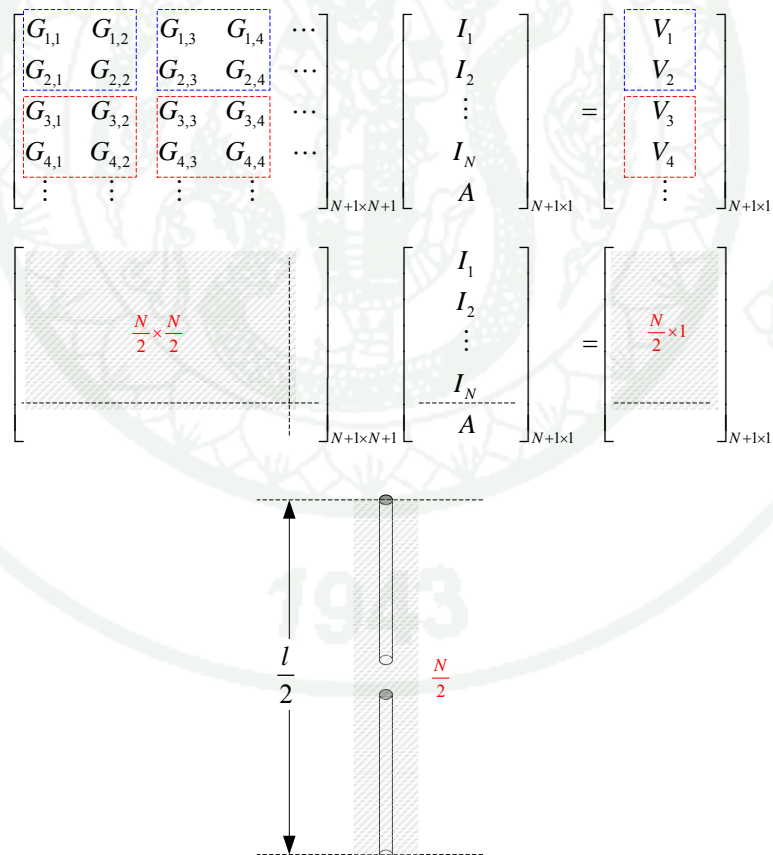


Figure 53 The cover area of using basis in the Multigrid method with an expandable basis.

Table 10 The comparison of iteration rounds between the Gauss-Seidel method and the Multigrid method with an expandable basis depending on $\|RE\|_{\infty}$.

Algorithm	Dipole segments					
	N = 100		N = 512		N = 1,024	
	Iteration rounds		Iteration rounds		Iteration rounds	
	Coarse grid	Fine grid	Coarse grid	Fine grid	Coarse grid	Fine grid
	While	While	While	While	While	While
	$\ RE\ _{\infty}$					
	> 10 %	> 0.5 %	> 10 %	> 0.5 %	> 10 %	> 0.5 %
1. Gauss-Seidel method	-	73	-	1,039	-	20
2. Multigrid method	7	69	15	942	29	19
3. Multigrid method with an expandable basis	4	72	5	1,038	6	78

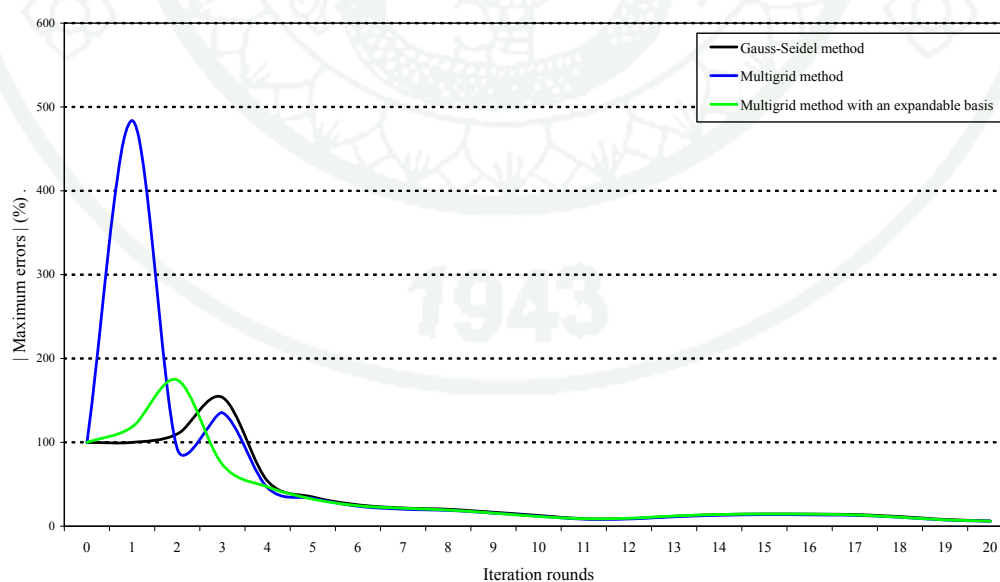


Figure 54 $\|RE\|_{\infty}$ computed by the Multigrid method with an expandable basis, N = 100.

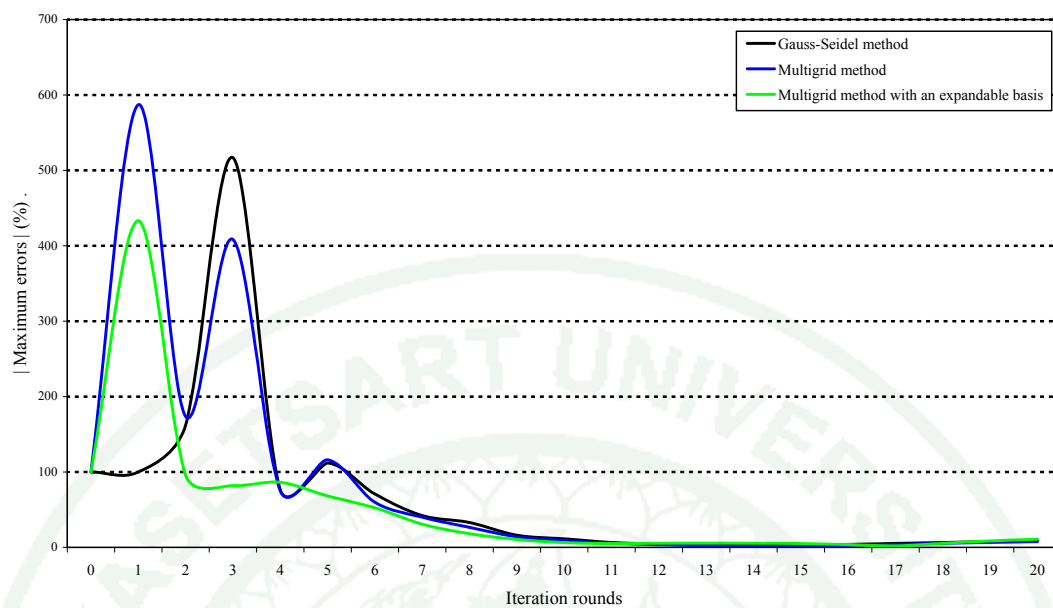


Figure 55 $\|RE\|_{\infty}$ computed by the Multigrid method with an expandable basis,
 $N = 512$.

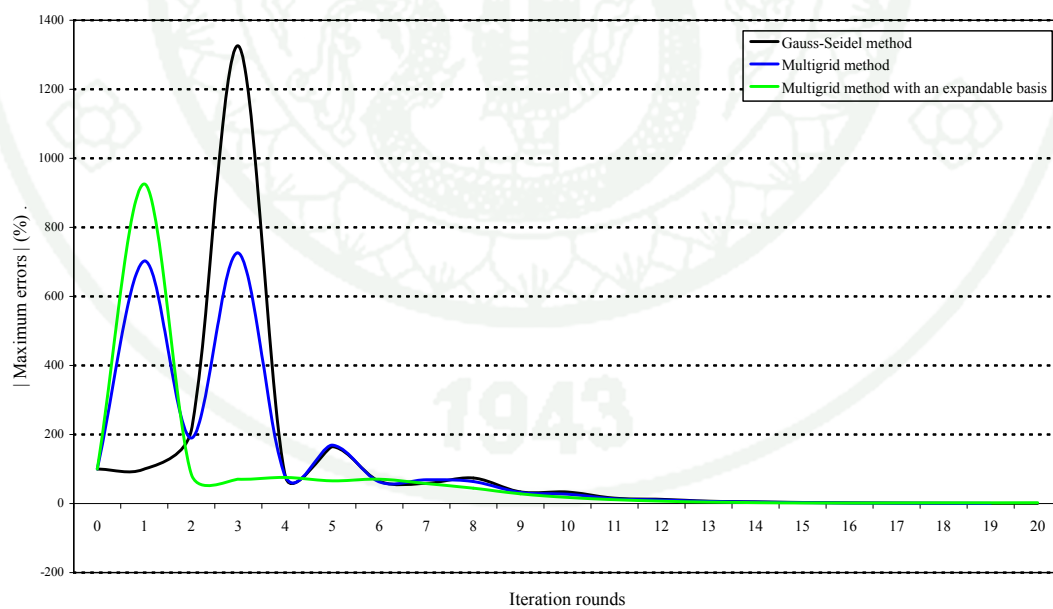


Figure 56 $\|RE\|_{\infty}$ computed by the Multigrid method with an expandable basis,
 $N = 1,024$.

It is apparent that the transformation of the best approximation in subspace to fine grid must be obeyed this rule, the reversion of Equation (93),

$$\text{for } i=1 \text{ to } \frac{N}{2}: \langle W_{2i-1}, I_{2i-1} \rangle = \langle W_{2i}, I_{2i} \rangle = \frac{\langle W'_i, I'_i \rangle}{\sqrt{2}} \text{ and } \langle W_{N+1}, I_{N+1} \rangle = 0$$

Finally, we observed that Equation (93) couldn't totally represent the matrix $[G]$. Then we expand the size of matrix $[G]_{N+1 \times N+1}$ to $[G]_{N+2 \times N+2}$ in order that the basis of Equation (93) can represent the unknown A in Equation (80). The simple algorithm is as the following example

$$\text{for } i=1 \text{ to } N+1: [G(i, N+2)] = [G(i, N+1)]$$

$$\text{for } j=1 \text{ to } N+2: [G(N+2, j)] = [G(N+1, j)]$$

$$[V(N+2, 1)] = [V(N+1, 1)]$$

As a result, matrix $[G]_{N+2 \times N+2}$ becomes $[G']_{\frac{N}{2}+1 \times \frac{N}{2}+1}$. Corresponding, matrix $[V]_{N+2 \times 1}$ becomes $[V']_{\frac{N}{2}+1 \times 1}$. We still use index of Equation (93), $i+1=2i'$ and $j+1=2j'$. In particular, the transformation of the best approximation in subspace to fine grid must be obeyed this rule, the reversion of Equation (93),

$$\text{for } i=1 \text{ to } \frac{N}{2}: \langle W_{2i-1}, I_{2i-1} \rangle = \langle W_{2i}, I_{2i} \rangle = \frac{\langle W'_i, I'_i \rangle}{\sqrt{2}}$$

$$\text{for } i = \frac{N}{2} + 1: \langle W_{2i-1}, I_{2i-1} \rangle = \sqrt{2} \langle W'_i, I'_i \rangle$$

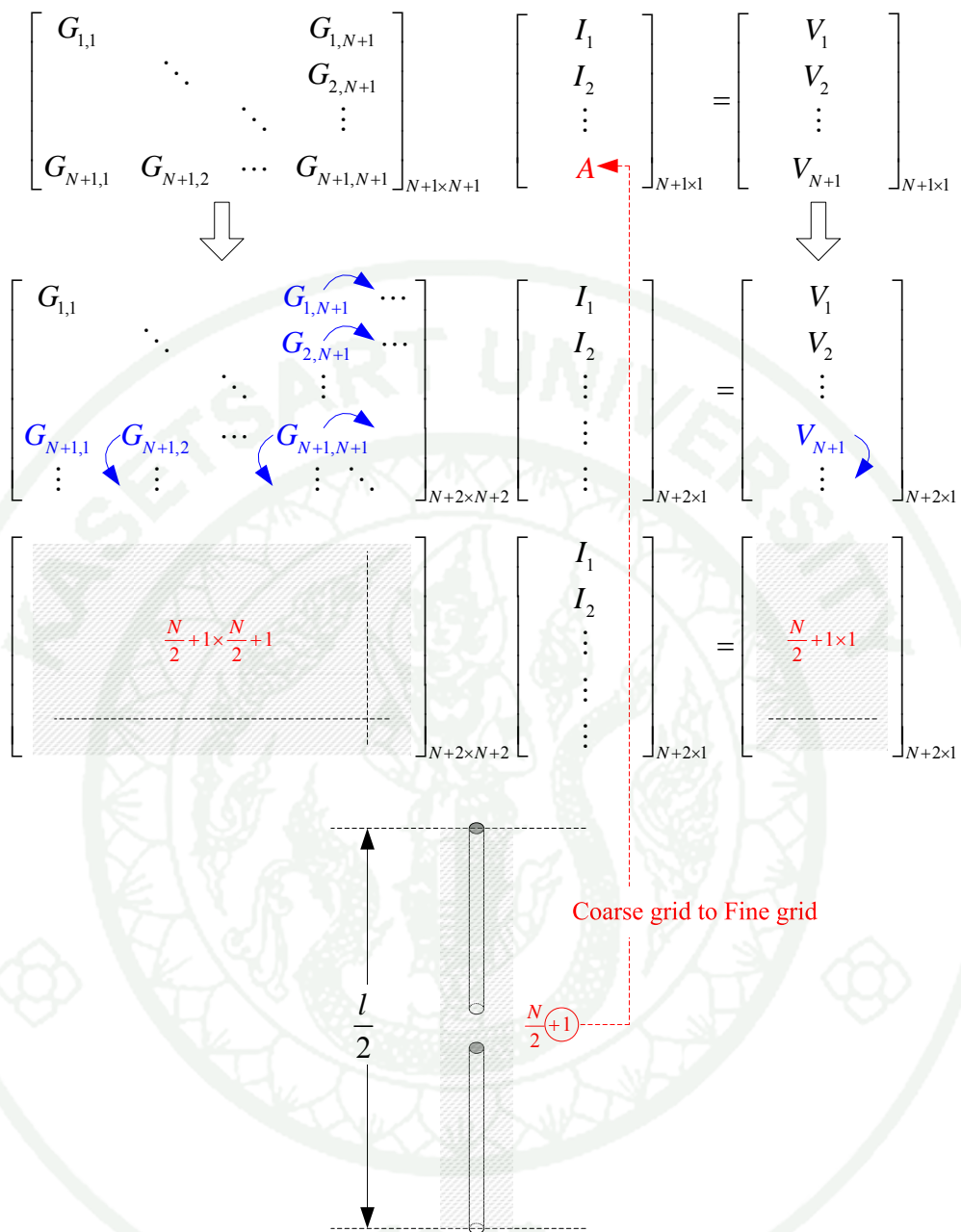


Figure 57 The cover area of using basis in Multigrid method with a compensatory basis.

Table 11 The comparison of iteration rounds between the Gauss-Seidel method and the Multigrid method with a compensatory basis depending on $\|RE\|_{\infty}$.

Algorithm	Dipole segments					
	N = 100		N = 512		N = 1,024	
	Iteration rounds		Iteration rounds		Iteration rounds	
	Coarse grid	Fine grid	Coarse grid	Fine grid	Coarse grid	Fine grid
	While $\ RE\ _{\infty} > 10\%$	While $\ RE\ _{\infty} > 0.5\%$	While $\ RE\ _{\infty} > 10\%$	While $\ RE\ _{\infty} > 0.5\%$	While $\ RE\ _{\infty} > 10\%$	While $\ RE\ _{\infty} > 0.5\%$
1. Gauss-Seidel method	-	73	-	1,039	-	20
2. Multigrid method	7	69	15	942	29	19
3. Multigrid method with an expandable basis	4	72	5	1,038	6	78
4. Multigrid method with a compensatory basis	5	56	8	59	10	79

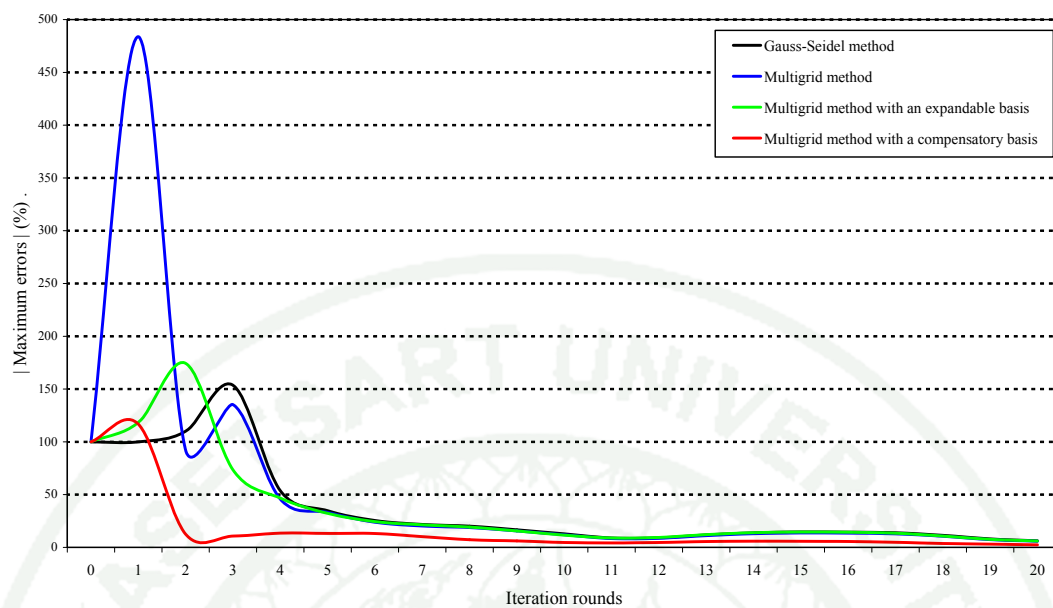


Figure 58 $\|RE\|_{\infty}$ computed by the Multigrid method with a compensatory basis,
 $N = 100$.

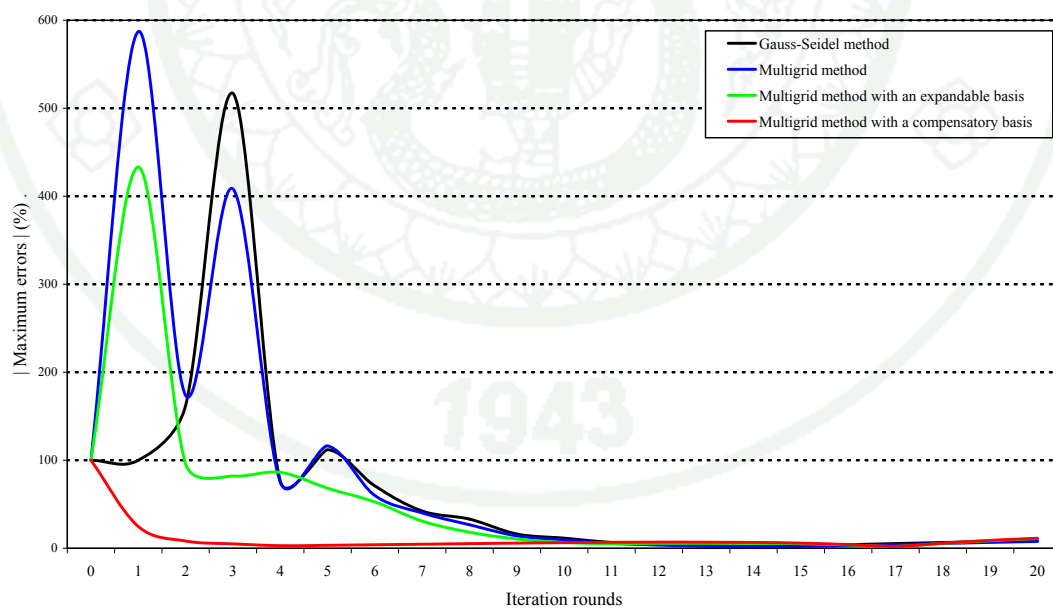


Figure 59 $\|RE\|_{\infty}$ computed by the Multigrid method with a compensatory basis,
 $N = 512$.

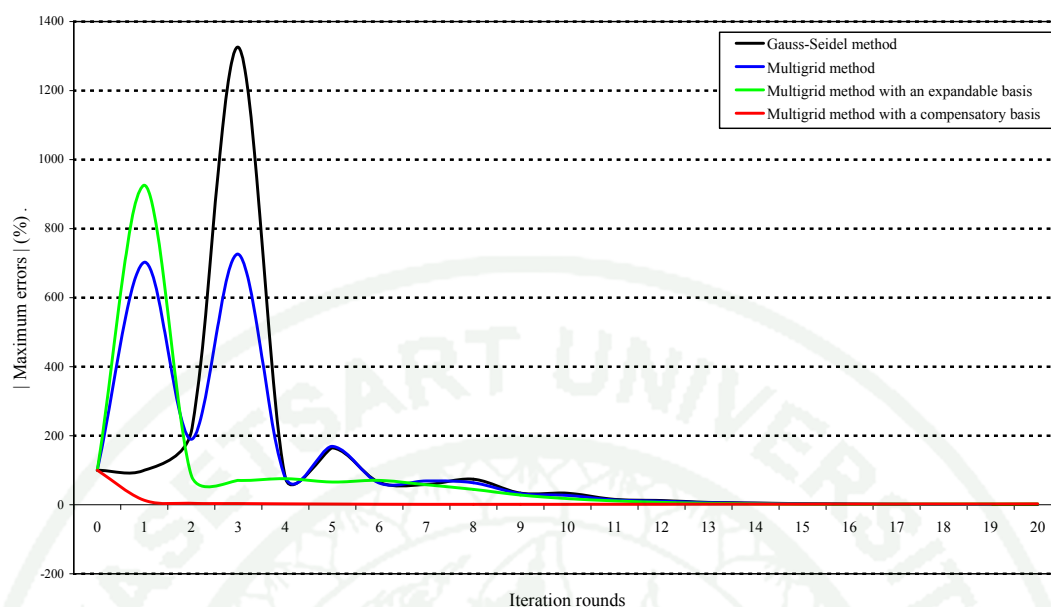


Figure 60 $\|RE\|_{\infty}$ computed by the Multigrid method with a compensatory basis, $N = 1,024$.

The definition of $\|RLE\|_{\infty}$ is slightly different from $\|RE\|_{\infty}$. Clearly, $|RLE|$ is computed by the exact solution resulted from Gauss Eliminate, standard algorithm in MATLAB iteration methods. A reference model is set as well as Figure 46, replacing $\|RE\|_{\infty}$ with $\|RLE\|_{\infty}$. The results are as follow

Table 12 The iteration rounds in the Gauss-Seidel method depending on $\|RLE\|_{\infty}$.

Algorithm	Dipole segments		
	N = 100	N = 512	N = 1,024
	Iteration rounds	Iteration rounds	Iteration rounds
	While $\ RLE\ _{\infty} > 0.5\%$	While $\ RLE\ _{\infty} > 0.5\%$	While $\ RLE\ _{\infty} > 0.5\%$
Gauss-Seidel method	92	2,877	15,915

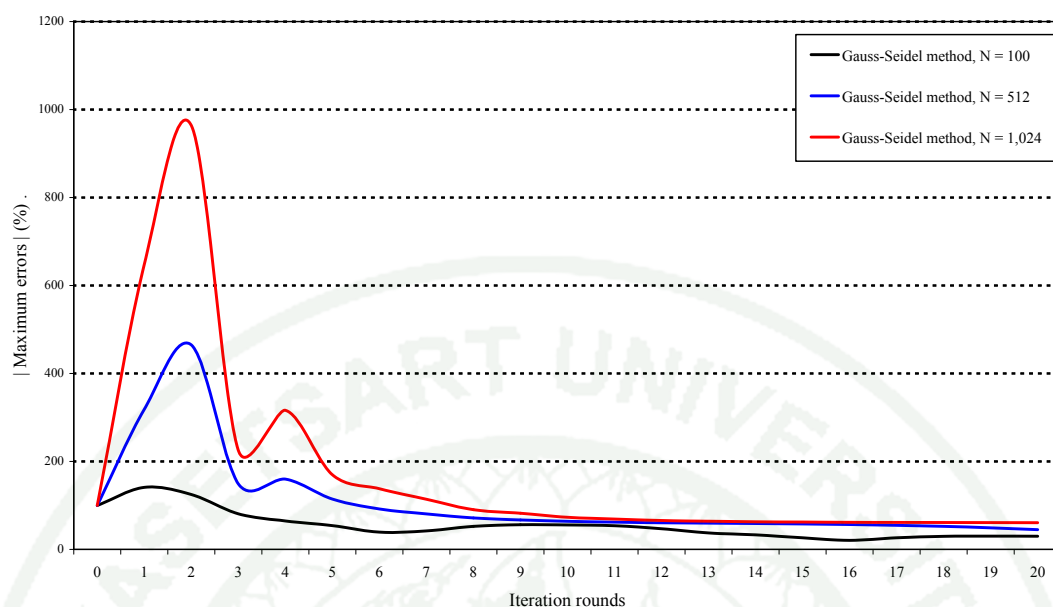


Figure 61 $\|RLE\|_{\infty}$ computed by the Gauss-Seidel method.

In the simulation, it is important to be aware that computed solutions are not exact mathematical solutions. By Figure 61, observe that as N is greater than 100 the $\|RLE\|_{\infty}$ gives higher value and more fluctuation. The rate of convergence of the numerical solution can be diminished in both Multigrid method and the modified Multigrid methods. Understanding this result can often guide a programmer in the proper implementation and development of electromagnetic numerical algorithms. The Multigrid methods computed by the constrain of $\|RLE\|_{\infty}$ has its algorithm as the following flowchart

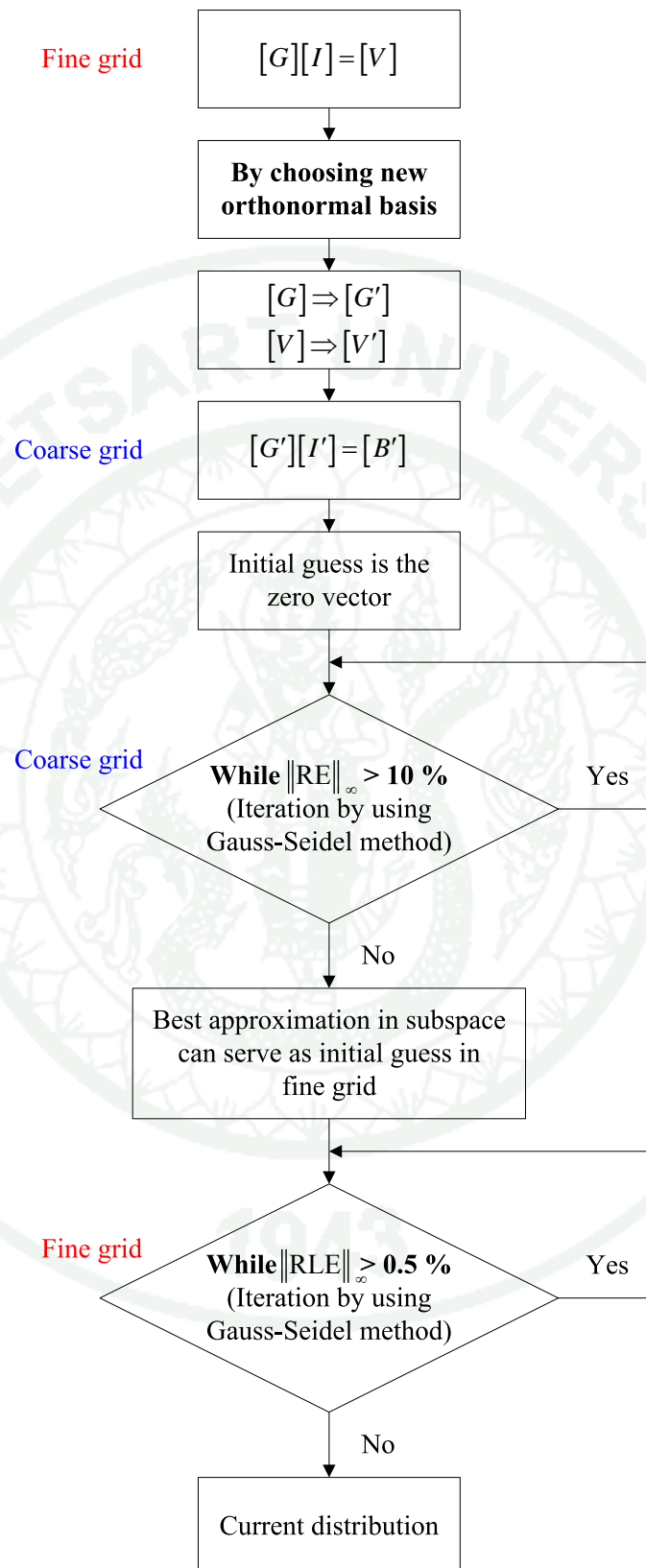


Figure 62 The flowchart of Multigrid method using $\|RLE\|_{\infty}$.

Table 13 The comparison of iteration rounds between the Gauss-Seidel method and the Multigrid methods depending on $\|RLE\|_{\infty}$.

Algorithm	Dipole segments					
	N = 100		N = 512		N = 1,024	
	Iteration rounds		Iteration rounds		Iteration rounds	
	Coarse grid	Fine grid	Coarse grid	Fine grid	Coarse grid	Fine grid
	While	While	While	While	While	While
$\ RE\ _{\infty}$	$\ RLE\ _{\infty}$	$\ RE\ _{\infty}$	$\ RLE\ _{\infty}$	$\ RE\ _{\infty}$	$\ RLE\ _{\infty}$	
> 10 %	> 0.5 %	> 10 %	> 0.5 %	> 10 %	> 0.5 %	
1. Gauss-Seidel method	-	92	-	2,877	-	15,915
2. Multigrid method	7	91	15	2,819	29	15,615
3. Multigrid method with an expandable basis	4	91	5	2,856	6	15,793
4. Multigrid method with a compensatory basis	5	73	8	2,548	10	14,419

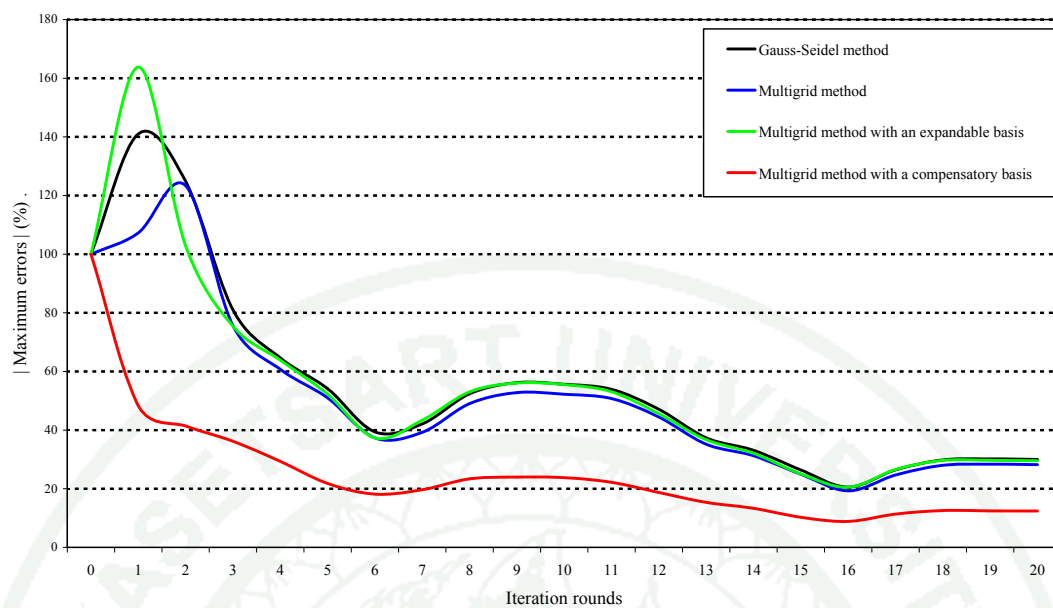


Figure 63 $\|RLE\|_{\infty}$ computed by the Gauss-Seidel method and the Multigrid methods, $N = 100$.

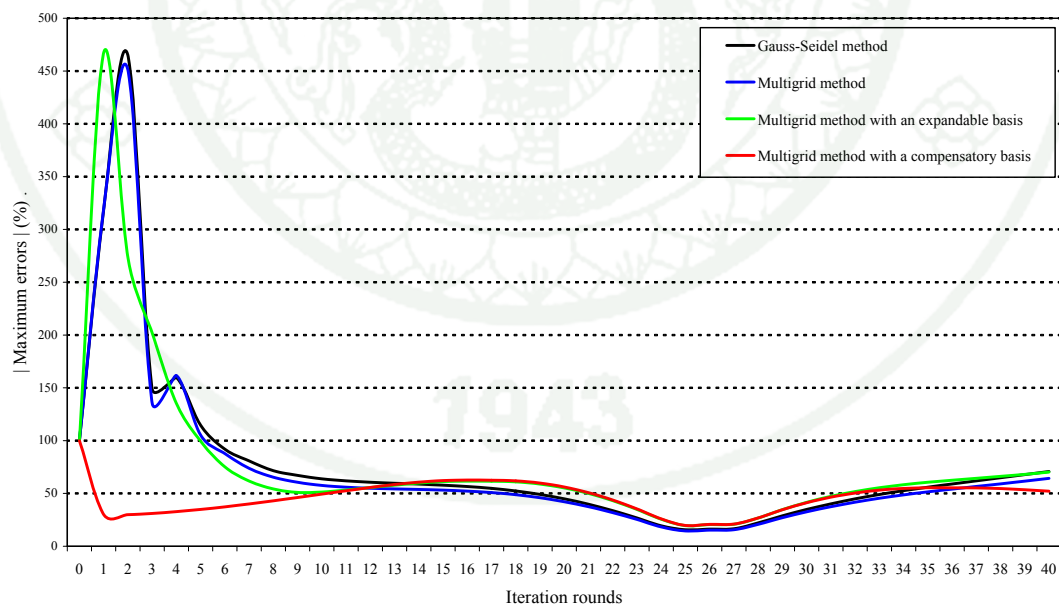


Figure 64 $\|RLE\|_{\infty}$ computed by the Gauss-Seidel method and the Multigrid methods, $N = 512$.

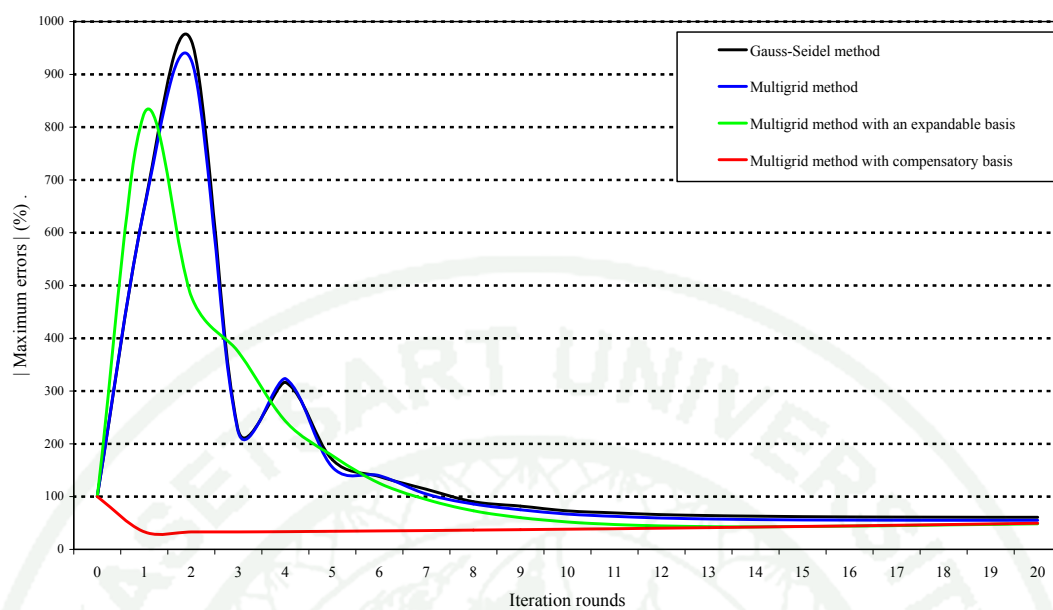


Figure 65 $\|RLE\|_{\infty}$ computed by the Gauss-Seidel method and the Multigrid methods, $N = 1,024$.

In this simulation, the author uses the V-Shape algorithm of the Multigrid methods. In brief, the V-Shape algorithm can illustrate as the following figure

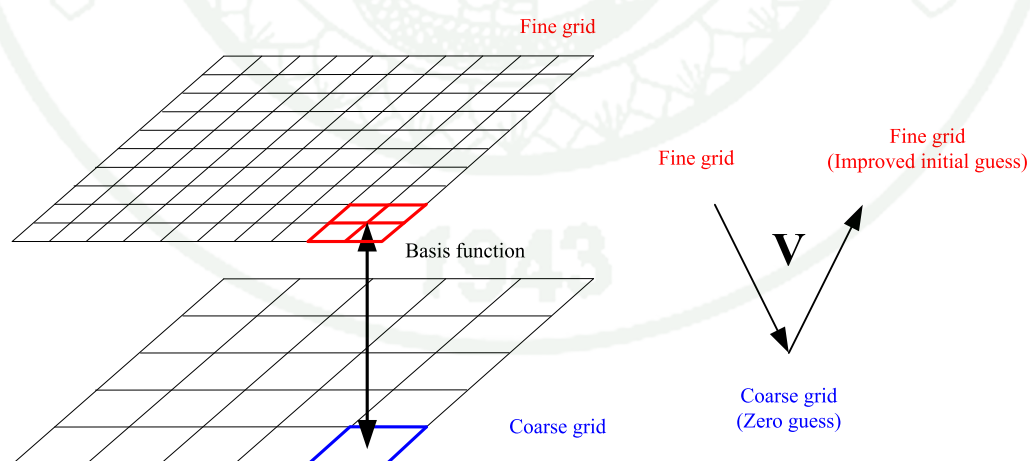


Figure 66 The V-Shape algorithm of the Multigrid methods.

3. The Finite Difference Time Domain (FDTD)

3.1 Introduction to the Finite Difference Time Domain (FDTD)

Especially in today's world, the Finite Difference Time Domain (FDTD), which was introduced by K.S. Yee in 1966 (Yee, 1966), is a powerful solution tool for solving the Maxwell's equations. FDTD is becoming more and more widely used and thousands of paper are published each year in this scheme. Generally, it is a time domain method so that its solution can cover a wide frequency range with a single simulation run. In addition, it well suited to analyzing transient response which is hard to deal with by frequency domain methods, MoM. For example, MoM is inadequate for both pulsed excitations and various transient phenomena. These problems require data to be computed over a range of frequencies and all of the required frequency range can be generated from time domain method via Fourier transformation (Stutzman and Thiele, 1998). Furthermore, FDTD is capable of computing electromagnetic problems with complex geometric structures which are difficult to analyze by MoM.

The FDTD algorithm is involves direct discretizations of the time dependent Maxwell's equations by writing the spatial and time derivatives in a central finite difference form. It requires the electric and magnetic fields to be updated at staggered half-time steps from one another in space, leap-frogging algorithm. The update procedure is explicit; the update values of electromagnetic field components depend only on these values at previous time and half-time steps. In conclusion, the FDTD algorithm gives a complete full-wave electromagnetic solution simply in a single simulation run.

3.2 The generalized time domain Maxwell's equations

James Clark Maxwell (1831-1879), who was a British physicist, collected all of the electromagnetic laws and rules from Faraday's law, Michael Faraday (1791-1867), and Ampere's law, Andre Marie Ampere (1775-1836), together with his

famous Maxwell's displacement current rule (Pojar, 1998) to create a group of Maxwell's equations. The Maxwell's equations in differential form were expressed in Equation (26) to Equation (29). Now, these equations are substituted with four medium-dependent equations $\bar{D} = \varepsilon_0 \varepsilon_r \bar{E}$, $\bar{B} = \mu_0 \mu_r \bar{H}$, $\bar{J}_e = \sigma \bar{E}$ and $\bar{J}_m = 0$. The results are as the following two equations

$$\nabla \times \bar{E} = -\mu_0 \mu_r \frac{\partial \bar{H}}{\partial t} \quad (98)$$

$$\nabla \times \bar{H} = \varepsilon_0 \varepsilon_r \frac{\partial \bar{E}}{\partial t} + \sigma \bar{E} \quad (99)$$

In the Cartesian coordinate

$$\nabla \times \bar{A} = \begin{vmatrix} \hat{a}_x & \hat{a}_y & \hat{a}_z \\ \frac{\partial}{\partial x} & \frac{\partial}{\partial y} & \frac{\partial}{\partial z} \\ A_x & A_y & A_z \end{vmatrix}$$

$$\nabla \times \bar{A} = \left(\frac{\partial A_z}{\partial y} - \frac{\partial A_y}{\partial z} \right) \hat{a}_x + \left(\frac{\partial A_x}{\partial z} - \frac{\partial A_z}{\partial x} \right) \hat{a}_y + \left(\frac{\partial A_y}{\partial x} - \frac{\partial A_x}{\partial y} \right) \hat{a}_z \quad (100)$$

Then Equation (98) and Equation (99) can be rewritten in matrix form as

$$\begin{bmatrix} \frac{\partial E_z}{\partial y} - \frac{\partial E_y}{\partial z} \\ \frac{\partial E_x}{\partial z} - \frac{\partial E_z}{\partial x} \\ \frac{\partial E_y}{\partial x} - \frac{\partial E_x}{\partial y} \end{bmatrix} = -\mu_0 \begin{bmatrix} \mu_{xx} & 0 & 0 \\ 0 & \mu_{yy} & 0 \\ 0 & 0 & \mu_{zz} \end{bmatrix} \cdot \begin{bmatrix} \frac{\partial H_x}{\partial t} \\ \frac{\partial H_y}{\partial t} \\ \frac{\partial H_z}{\partial t} \end{bmatrix} \quad (101)$$

$$\begin{bmatrix} \frac{\partial H_z}{\partial y} - \frac{\partial H_y}{\partial z} \\ \frac{\partial H_x}{\partial z} - \frac{\partial H_z}{\partial x} \\ \frac{\partial H_y}{\partial x} - \frac{\partial H_x}{\partial y} \end{bmatrix} = \varepsilon_0 \begin{bmatrix} \varepsilon_{xx} & 0 & 0 \\ 0 & \varepsilon_{yy} & 0 \\ 0 & 0 & \varepsilon_{zz} \end{bmatrix} \cdot \begin{bmatrix} \frac{\partial E_x}{\partial t} \\ \frac{\partial E_y}{\partial t} \\ \frac{\partial E_z}{\partial t} \end{bmatrix} + \begin{bmatrix} \sigma_{exx} & 0 & 0 \\ 0 & \sigma_{eyy} & 0 \\ 0 & 0 & \sigma_{ezz} \end{bmatrix} \cdot \begin{bmatrix} E_x \\ E_y \\ E_z \end{bmatrix} \quad (102)$$

$$\mu_0 = 4\pi \times 10^{-7} \text{ H / m}, \quad \varepsilon_0 = 8.845 \times 10^{-12} \text{ F / m}$$

From Equation (101) and (102), we applied the central difference scheme to Maxwell's equations in differential form. For simplicity, consider a function $f(x)$ as shown in the following figure

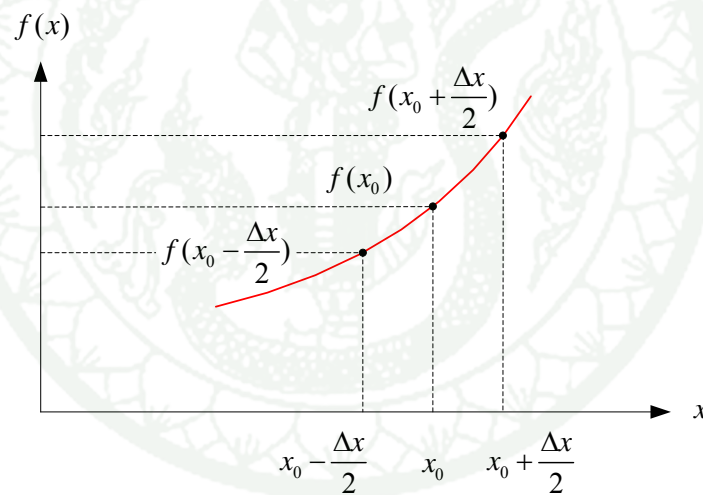


Figure 67 The central difference scheme.

There are three types of finite difference approximations which can be used to estimate the derivative of $f(x_0)$: the forward finite difference, the backward finite difference and the central finite difference. Since the central difference yields a more accurate approximation, it is considered in this research. By the extension of Taylor series

$$f(x_{i+1}) = f(x_i) + f'(x_i)h + \frac{f''(x_i)}{2!}h^2 + \frac{f'''(x_i)}{3!}h^3 + \dots + \frac{f^n(x_i)}{n!}h^n + R_n \quad (103)$$

By expanding both $f\left(x_0 + \frac{\Delta x}{2}\right)$ and $f\left(x_0 - \frac{\Delta x}{2}\right)$ into a Taylor series

$$f\left(x_0 + \frac{\Delta x}{2}\right) = f(x_0) + f'(x_0)\left(\frac{\Delta x}{2}\right) + \frac{f''(x_0)}{2!}\left(\frac{\Delta x}{2}\right)^2 + \frac{f'''(x_0)}{3!}\left(\frac{\Delta x}{2}\right)^3 + \dots \quad (104)$$

$$f\left(x_0 - \frac{\Delta x}{2}\right) = f(x_0) - f'(x_0)\left(\frac{\Delta x}{2}\right) + \frac{f''(x_0)}{2!}\left(\frac{\Delta x}{2}\right)^2 - \frac{f'''(x_0)}{3!}\left(\frac{\Delta x}{2}\right)^3 + \dots \quad (105)$$

Subtracting Equation (104) by Equation (105) and neglecting all higher order terms over $(\Delta x)^3$ the expression becomes

$$f\left(x_0 + \frac{\Delta x}{2}\right) - f\left(x_0 - \frac{\Delta x}{2}\right) \cong f'(x_0)\Delta x$$

As a result, the central difference in distance and the central difference in time are shown as the following two equations, respectively

$$f'(x_0) = \frac{f\left(x_0 + \frac{\Delta x}{2}\right) - f\left(x_0 - \frac{\Delta x}{2}\right)}{\Delta x} \quad (106)$$

$$f'(x_0) = \frac{f^{n+1}(x_0) - f^n(x_0)}{\Delta t} \quad (107)$$

3.2.1. Yee's cell model

The Yee's cell model has been used in this research so as to be the smallest unit (Yee, 1966). It is apparent that the symmetrical of this structure is corresponding to the FDTD scheme.

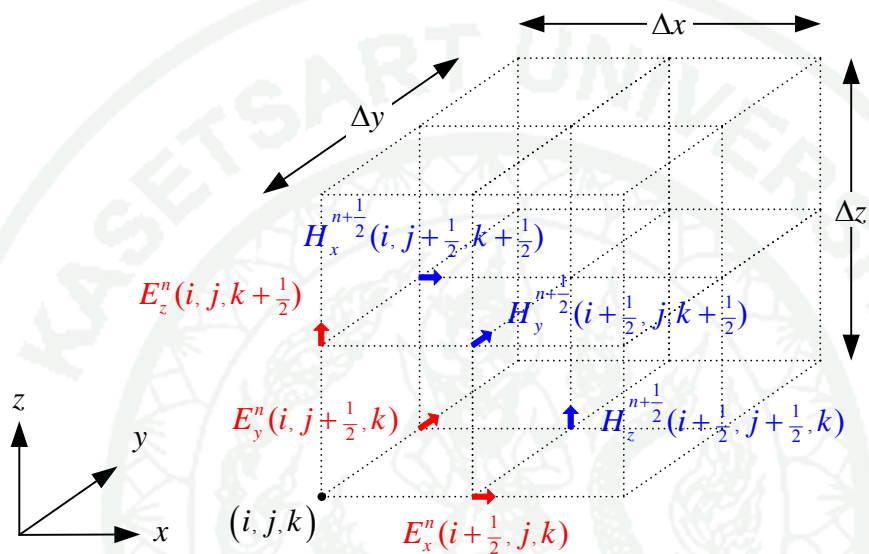


Figure 68 The Yee's cell model.

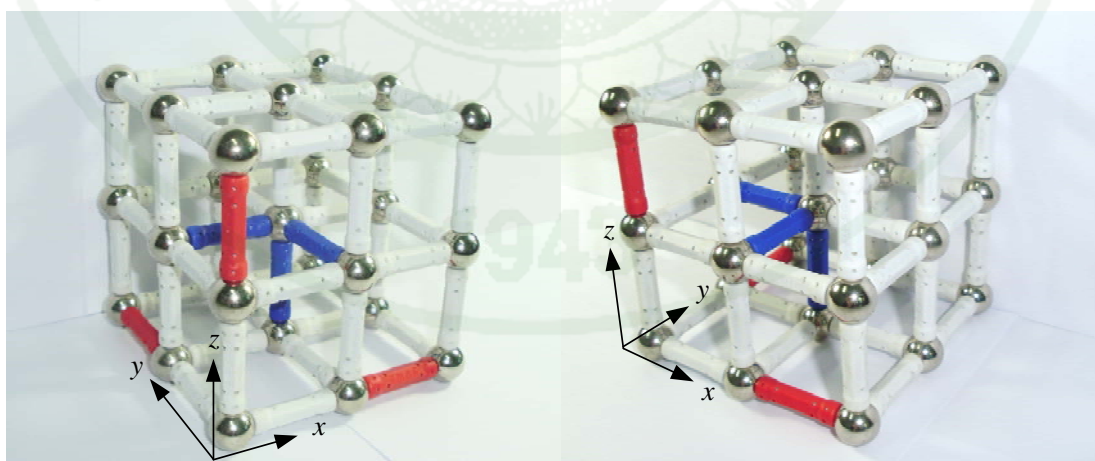


Figure 69 The physical Yee's cell model.

It should be noted that all of the electric field components lie tangentially on the lattice edges of Yee's cell model and are located half cell apart from the reference point (i, j, k) . On the other hand, all of the magnetic field components lie normally on the surfaces of Yee's cell model and are located half cell apart from the electric fields defined in the cell

Because the algorithm for solve all of the six scalar equations in both Equation (101) and Equation (102) is exactly the same, herein simply one component from electric and magnetic fields is about to be derived. We choose Equation (102) only in z-axis, then

$$\frac{\partial H_y}{\partial x} - \frac{\partial H_x}{\partial y} = \varepsilon_0 \varepsilon_{zz} \frac{\partial E_z}{\partial t} + \sigma_{zz} E_z \quad (108)$$

By referring the Yee's cell model, we substitute both Equation (106) and Equation (107) into Equation (108), then

$$\begin{aligned} & \frac{H_y^{n+\frac{1}{2}}(i+\frac{1}{2}, j, k+\frac{1}{2}) - H_y^{n+\frac{1}{2}}(i-\frac{1}{2}, j, k+\frac{1}{2})}{\Delta x} - \frac{H_x^{n+\frac{1}{2}}(i, j+\frac{1}{2}, k+\frac{1}{2}) - H_x^{n+\frac{1}{2}}(i, j-\frac{1}{2}, k+\frac{1}{2})}{\Delta y} \\ & = \varepsilon_0 \varepsilon_{zz} \frac{E_z^{n+1}(i, j, k+\frac{1}{2}) - E_z^n(i, j, k+\frac{1}{2})}{\Delta t} + \sigma_{zz}(i, j, k+\frac{1}{2}) E_z^{n+\frac{1}{2}}(i, j, k+\frac{1}{2}) \end{aligned} \quad (109)$$

According to the pattern of discretization system, the value of $E_z^{n+\frac{1}{2}}(i, j, k+\frac{1}{2})$ is approximated by an average of $E_z^{n+1}(i, j, k+\frac{1}{2})$ and $E_z^n(i, j, k+\frac{1}{2})$.

$$E_z^{n+\frac{1}{2}}(i, j, k+\frac{1}{2}) = \frac{E_z^{n+1}(i, j, k+\frac{1}{2}) + E_z^n(i, j, k+\frac{1}{2})}{2}$$

When back substituting to Equation (109) gives.

$$\begin{aligned}
& \frac{H_y^{n+\frac{1}{2}}(i+\frac{1}{2}, j, k+\frac{1}{2}) - H_y^{n+\frac{1}{2}}(i-\frac{1}{2}, j, k+\frac{1}{2})}{\Delta x} - \frac{H_x^{n+\frac{1}{2}}(i, j+\frac{1}{2}, k+\frac{1}{2}) - H_x^{n+\frac{1}{2}}(i, j-\frac{1}{2}, k+\frac{1}{2})}{\Delta y} \\
& = \varepsilon_0 \varepsilon_{zz} \frac{E_z^{n+1}(i, j, k+\frac{1}{2}) - E_z^n(i, j, k+\frac{1}{2})}{\Delta t} + \sigma_{zz}(i, j, k+\frac{1}{2}) \frac{E_z^{n+1}(i, j, k+\frac{1}{2}) + E_z^n(i, j, k+\frac{1}{2})}{2}
\end{aligned}$$

Finally, we have one of the six equations of the Maxwell's equations in time domain.

$$\begin{aligned}
E_z^{n+1}(i, j, k+\frac{1}{2}) &= \frac{1 - \Delta t \sigma_{zz}(i, j, k+\frac{1}{2}) / [2\varepsilon_0 \varepsilon_{zz}(i, j, k+\frac{1}{2})]}{1 + \Delta t \sigma_{zz}(i, j, k+\frac{1}{2}) / [2\varepsilon_0 \varepsilon_{zz}(i, j, k+\frac{1}{2})]} E_z^n(i, j, k+\frac{1}{2}) \\
&+ \frac{\Delta t / [\varepsilon_0 \varepsilon_{zz}(i, j, k+\frac{1}{2})]}{1 + \Delta t \sigma_{zz}(i, j, k+\frac{1}{2}) / [2\varepsilon_0 \varepsilon_{zz}(i, j, k+\frac{1}{2})]} \left\{ \frac{H_y^{n+\frac{1}{2}}(i+\frac{1}{2}, j, k+\frac{1}{2})}{\Delta x} \right. \\
&\left. - \frac{H_y^{n+\frac{1}{2}}(i-\frac{1}{2}, j, k+\frac{1}{2})}{\Delta x} - \frac{H_x^{n+\frac{1}{2}}(i, j+\frac{1}{2}, k+\frac{1}{2}) - H_x^{n+\frac{1}{2}}(i, j-\frac{1}{2}, k+\frac{1}{2})}{\Delta y} \right\} \quad (110)
\end{aligned}$$

This equation spells that $E_z^{n+1}(i, j, k+\frac{1}{2})$ can be calculated with values of E and H at previous instants of time at adjacent spatial positions as located by Yee' cell model. Apparently, we need the basis for a method that can move a field behavior forward in space and time through the use of difference equations as updated equations

By analogy, the other equations can be solved based on Yee's cell model. Therefore, the six Maxwell's equations in time domain are presented as.

$$H_x^{n+\frac{1}{2}}(i, j+\frac{1}{2}, k+\frac{1}{2}) = H_x^{n-\frac{1}{2}}(i, j+\frac{1}{2}, k+\frac{1}{2}) + \frac{\Delta t}{\mu_0 \mu_{xx}(i, j+\frac{1}{2}, k+\frac{1}{2})} \left\{ \frac{E_y^n(i, j+\frac{1}{2}, k+1) - E_y^n(i, j+\frac{1}{2}, k)}{\Delta z} - \frac{E_z^n(i, j+1, k+\frac{1}{2}) - E_z^n(i, j, k+\frac{1}{2})}{\Delta y} \right\} \quad (111)$$

$$H_y^{n+\frac{1}{2}}(i+\frac{1}{2}, j, k+\frac{1}{2}) = H_y^{n-\frac{1}{2}}(i+\frac{1}{2}, j, k+\frac{1}{2}) + \frac{\Delta t}{\mu_0 \mu_{yy}(i+\frac{1}{2}, j, k+\frac{1}{2})} \left\{ \frac{E_z^n(i+1, j, k+\frac{1}{2}) - E_z^n(i, j, k+\frac{1}{2})}{\Delta x} - \frac{E_x^n(i+\frac{1}{2}, j, k+1) - E_x^n(i+\frac{1}{2}, j, k)}{\Delta z} \right\} \quad (112)$$

$$H_z^{n+\frac{1}{2}}(i+\frac{1}{2}, j+\frac{1}{2}, k) = H_z^{n-\frac{1}{2}}(i+\frac{1}{2}, j+\frac{1}{2}, k) + \frac{\Delta t}{\mu_0 \mu_{zz}(i+\frac{1}{2}, j+\frac{1}{2}, k)} \left\{ \frac{E_x^n(i+\frac{1}{2}, j+1, k) - E_x^n(i+\frac{1}{2}, j, k)}{\Delta y} - \frac{E_y^n(i+1, j+\frac{1}{2}, k) - E_y^n(i, j+\frac{1}{2}, k)}{\Delta x} \right\} \quad (113)$$

$$E_x^{n+1}(i+\frac{1}{2}, j, k) = \frac{1 - \Delta t \sigma_{xx}(i+\frac{1}{2}, j, k) / [2\varepsilon_0 \varepsilon_{xx}(i+\frac{1}{2}, j, k)]}{1 + \Delta t \sigma_{xx}(i+\frac{1}{2}, j, k) / [2\varepsilon_0 \varepsilon_{xx}(i+\frac{1}{2}, j, k)]} E_x^n(i+\frac{1}{2}, j, k) + \frac{\Delta t / [\varepsilon_0 \varepsilon_{xx}(i+\frac{1}{2}, j, k)]}{1 + \Delta t \sigma_{xx}(i+\frac{1}{2}, j, k) / [2\varepsilon_0 \varepsilon_{xx}(i+\frac{1}{2}, j, k)]} \left\{ \frac{H_z^{n+\frac{1}{2}}(i+\frac{1}{2}, j+\frac{1}{2}, k)}{\Delta y} - \frac{H_z^{n+\frac{1}{2}}(i+\frac{1}{2}, j-\frac{1}{2}, k)}{\Delta y} - \frac{H_y^{n+\frac{1}{2}}(i+\frac{1}{2}, j, k+\frac{1}{2}) - H_y^{n+\frac{1}{2}}(i+\frac{1}{2}, j, k-\frac{1}{2})}{\Delta z} \right\} \quad (114)$$

$$\begin{aligned}
E_y^{n+1}(i, j + \frac{1}{2}, k) &= \frac{1 - \Delta t \sigma_{yy}(i, j + \frac{1}{2}, k) / [2\varepsilon_0 \varepsilon_{yy}(i, j + \frac{1}{2}, k)]}{1 + \Delta t \sigma_{yy}(i, j + \frac{1}{2}, k) / [2\varepsilon_0 \varepsilon_{yy}(i, j + \frac{1}{2}, k)]} E_y^n(i, j + \frac{1}{2}, k) \\
&+ \frac{\Delta t / [\varepsilon_0 \varepsilon_{yy}(i, j + \frac{1}{2}, k)]}{1 + \Delta t \sigma_{yy}(i, j + \frac{1}{2}, k) / [2\varepsilon_0 \varepsilon_{yy}(i, j + \frac{1}{2}, k)]} \left\{ \frac{H_x^{n+\frac{1}{2}}(i, j + \frac{1}{2}, k + \frac{1}{2})}{\Delta z} \right. \\
&\left. - \frac{H_x^{n+\frac{1}{2}}(i, j + \frac{1}{2}, k - \frac{1}{2})}{\Delta z} - \frac{H_z^{n+\frac{1}{2}}(i + \frac{1}{2}, j + \frac{1}{2}, k) - H_z^{n+\frac{1}{2}}(i - \frac{1}{2}, j + \frac{1}{2}, k)}{\Delta x} \right\} \quad (115)
\end{aligned}$$

$$\begin{aligned}
E_z^{n+1}(i, j, k + \frac{1}{2}) &= \frac{1 - \Delta t \sigma_{zz}(i, j, k + \frac{1}{2}) / [2\varepsilon_0 \varepsilon_{zz}(i, j, k + \frac{1}{2})]}{1 + \Delta t \sigma_{zz}(i, j, k + \frac{1}{2}) / [2\varepsilon_0 \varepsilon_{zz}(i, j, k + \frac{1}{2})]} E_z^n(i, j, k + \frac{1}{2}) \\
&+ \frac{\Delta t / [\varepsilon_0 \varepsilon_{zz}(i, j, k + \frac{1}{2})]}{1 + \Delta t \sigma_{zz}(i, j, k + \frac{1}{2}) / [2\varepsilon_0 \varepsilon_{zz}(i, j, k + \frac{1}{2})]} \left\{ \frac{H_y^{n+\frac{1}{2}}(i + \frac{1}{2}, j, k + \frac{1}{2})}{\Delta x} \right. \\
&\left. - \frac{H_y^{n+\frac{1}{2}}(i - \frac{1}{2}, j, k + \frac{1}{2})}{\Delta x} - \frac{H_x^{n+\frac{1}{2}}(i, j + \frac{1}{2}, k + \frac{1}{2}) - H_x^{n+\frac{1}{2}}(i, j - \frac{1}{2}, k + \frac{1}{2})}{\Delta y} \right\} \quad (116)
\end{aligned}$$

It is very critical to appropriate select the spatial grids Δx , Δy and Δz and the time step Δt so as to control the accuracy and the stability of the computations. Also, it was called Courant-Friedrichs-Lewy Stability Criterion

$$\Delta x_{\max}, \Delta y_{\max} \text{ and } \Delta z_{\max} \leq \frac{\lambda_{\min}}{15} \text{ or } \frac{\lambda_{\min}}{20}, \lambda_{\min} = \frac{c}{f_{\max} \sqrt{\mu_r, \max \varepsilon_r, \max}} \quad (117)$$

$$\Delta t \leq \frac{1}{c \sqrt{\frac{1}{\Delta x^2} + \frac{1}{\Delta y^2} + \frac{1}{\Delta z^2}}}, \quad c = \frac{1}{\sqrt{\mu \varepsilon}} \quad (118)$$

3.2.2. Perfectly Matched Layer (PML)

Whenever we solve the Maxwell's equations numerically by a volume discretization, the interested domain must be truncated in some way without introducing significant artifacts into itself. If we set the incorrect boundary layer, for example, the electromagnetic field outside the computational domain all equal to zero, then the electromagnetic wave will be reflected back to the system. The results were as the following figure (Jariyanorawiss, 2004; Jariyanorawiss and Homsup, 2005a)

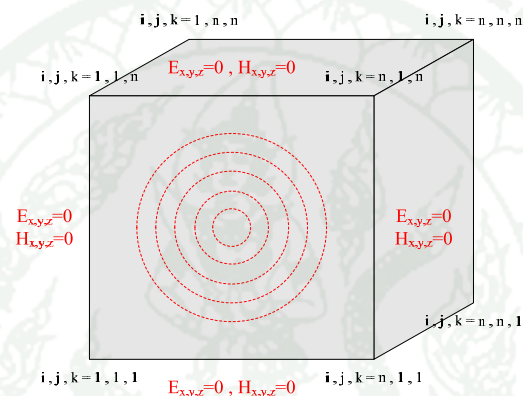


Figure 70 The model of the incorrect boundary layer.

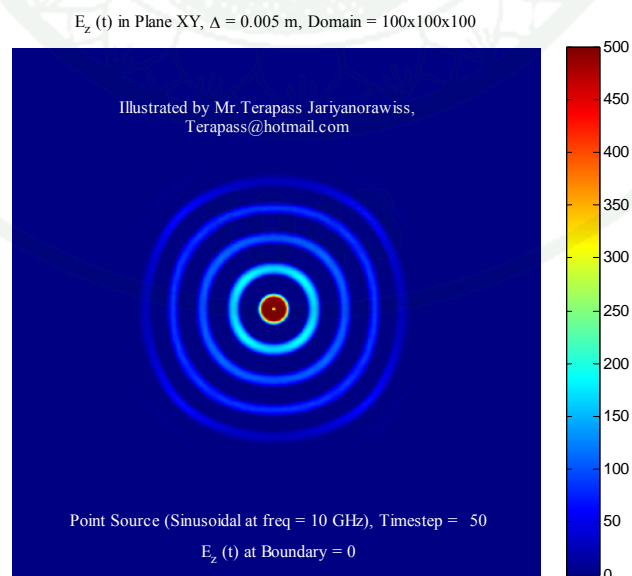


Figure 71 Cross-section of the applied incorrect boundary layer (Timestep = 50).

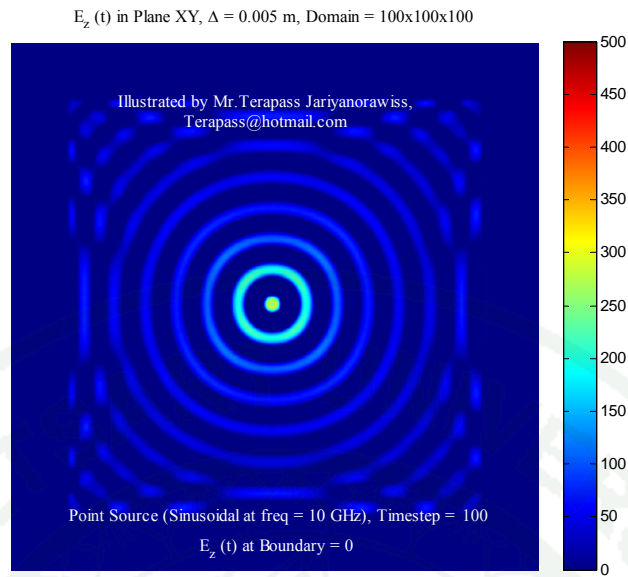


Figure 72 Cross-section of the applied incorrect boundary layer (Timestep = 100).

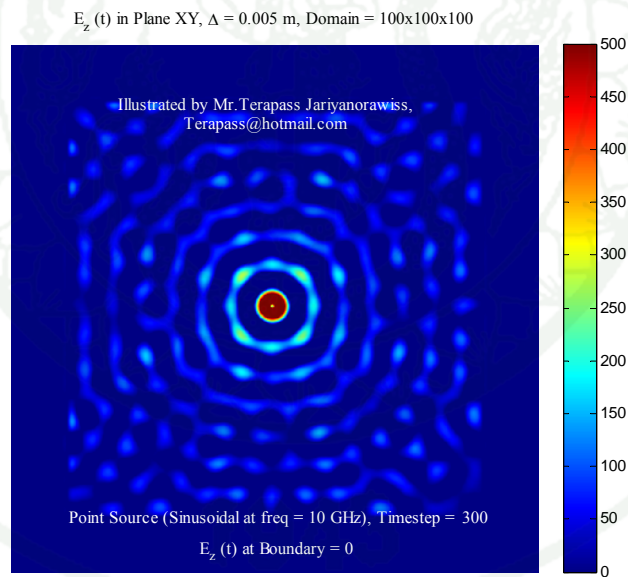


Figure 73 Cross-section of the applied incorrect boundary layer (Timestep = 300).

As a result, the simulated electromagnetic fields were reflected to the computational domain and made the system chaotically. On the other hand, Taflove tried to truncate computational domain on a discrete grid by boundary conditions, a rule to set the value at the edge of the grid (Taflove, 1995). It turns out

that, a boundary condition is possible to do perfectly in only one dimension. In 1994, however, Berenger proposed the advanced idea by changing the question (Berenger, 1994). He found an absorbing boundary layer instead of finding an absorbing boundary condition. Then, he introduced the highly effective, Perfectly Matched Layer (PML) for two-dimensional FDTD grids, which was extended to three dimensions by Katz (Katz *et al.*, 1994). In addition, this technique is based on the use of a specified layer designed to absorb the electromagnetic waves without reflection from the vacuum-layer interfaces. In 1996, once again, the theory of the PML was generalized to three dimensions by Berenger (Berenger, 1996). As can be expected, in the PML medium, each component of the electromagnetic fields was split into two parts. In Cartesian coordinate, the six components yield 12 subcomponents presented as E_{xy} , E_{xz} , E_{yz} , E_{yx} , E_{zx} , E_{zy} , H_{xy} , H_{xz} , H_{yz} , H_{yx} , H_{zx} and H_{zy} . In conclusion, the Maxwell's equations were represented as the following 12 equations

$$\varepsilon \frac{\partial E_{xy}}{\partial t} + \sigma_y E_{xy} = \frac{\partial (H_{zx} + H_{zy})}{\partial y} \quad (119)$$

$$\varepsilon \frac{\partial E_{xz}}{\partial t} + \sigma_z E_{xz} = -\frac{\partial (H_{yz} + H_{yx})}{\partial z} \quad (120)$$

$$\varepsilon \frac{\partial E_{yz}}{\partial t} + \sigma_z E_{yz} = \frac{\partial (H_{xy} + H_{xz})}{\partial z} \quad (121)$$

$$\varepsilon \frac{\partial E_{yx}}{\partial t} + \sigma_x E_{yx} = -\frac{\partial (H_{zx} + H_{zy})}{\partial x} \quad (122)$$

$$\varepsilon \frac{\partial E_{zx}}{\partial t} + \sigma_x E_{zx} = \frac{\partial (H_{yz} + H_{yx})}{\partial x} \quad (123)$$

$$\varepsilon \frac{\partial E_{zy}}{\partial t} + \sigma_y E_{zy} = -\frac{\partial (H_{xy} + H_{xz})}{\partial y} \quad (124)$$

$$\mu \frac{\partial H_{xy}}{\partial t} + \sigma_y^* H_{xy} = -\frac{\partial (E_{zx} + E_{zy})}{\partial y} \quad (125)$$

$$\mu \frac{\partial H_{xz}}{\partial t} + \sigma_z^* H_{xz} = \frac{\partial (E_{yz} + E_{yx})}{\partial z} \quad (126)$$

$$\mu \frac{\partial H_{yz}}{\partial t} + \sigma_z^* H_{yz} = -\frac{\partial (E_{xy} + E_{xz})}{\partial z} \quad (127)$$

$$\mu \frac{\partial H_{yx}}{\partial t} + \sigma_x^* H_{yx} = \frac{\partial (E_{zx} + E_{zy})}{\partial x} \quad (128)$$

$$\mu \frac{\partial H_{zx}}{\partial t} + \sigma_x^* H_{zx} = -\frac{\partial (E_{yz} + E_{yx})}{\partial x} \quad (129)$$

$$\mu \frac{\partial H_{zy}}{\partial t} + \sigma_y^* H_{zy} = \frac{\partial (E_{xy} + E_{xz})}{\partial y} \quad (130)$$

Recently, it has been two contemporary PML: the stretching coordinate PML and the lossy uniaxial medium. First, the stretching coordinate PML is based on complex coordinates stretching (Chew *et al.*, 1994)

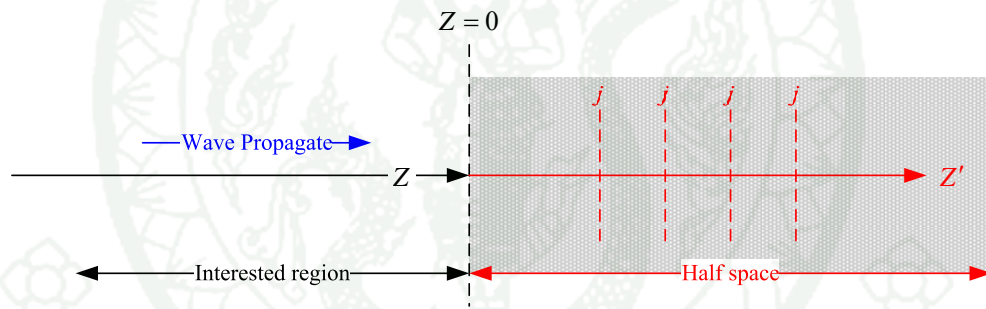


Figure 74 Illustration of complex coordinates stretching.

In this case, we have some region of interest near the origin $z = 0$ and we need to truncate half-space, which is lying outside interested region, in such a way so as to absorb radiating electromagnetic waves (Johnson, 2010). Then, we define the complex coordinate stretching as $z' = z + jf(z)$; the first component is the real coordinate normal to the layer surface and the other is a tuned lossy uniaxial. We now have $\partial z = \left(1 - j \frac{\partial f(z)}{\partial z'}\right) \partial z'$. If we try to terminate the electromagnetic wave in z-axis

($\sigma_x, \sigma_y = 0$) then it is appropriate to give the value of $\frac{\partial f(z)}{\partial z'} = \frac{\sigma_z}{2\pi f \varepsilon}$, in sense for absorbing all frequencies. As a result, $\partial z = \left(1 + \frac{\sigma_z}{j\omega\varepsilon}\right) \partial z'$ or $\frac{\partial}{\partial z} = \frac{1}{\left(1 + \frac{\sigma_z}{j\omega\varepsilon}\right)} \frac{\partial}{\partial z'}$.

Second, the anisotropic PML is based on complex material. Such a medium was originally suggested by Sacks *et al.* (Sacks *et al.*, 1995). It is a layer of diagonally anisotropic material tensor to absorb outgoing waves from the interested domain. An anisotropic material is a material in which the electric polarization vector is not in the same direction as the electric field. The value of ε , μ and σ are depend on the field direction. In addition, the isotropic material is a material whose properties are not dependent on the direction along which they are measured. Isotropic material is uniformity in all directions.

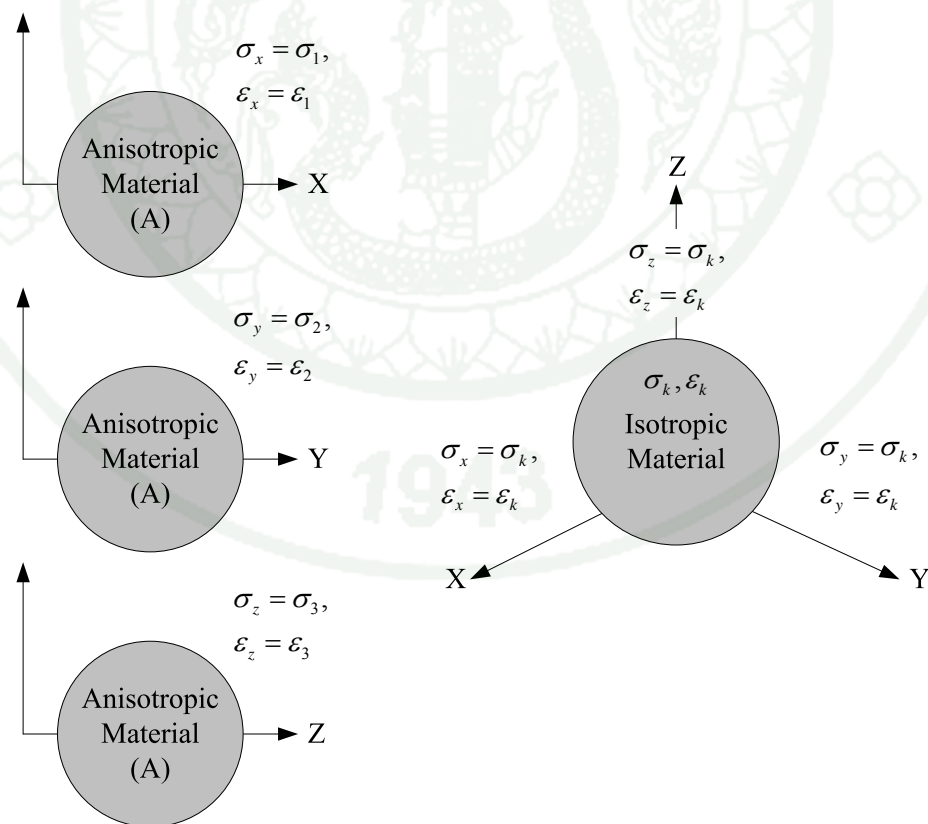


Figure 75 Illustration of anisotropic material and isotropic material.

It is apparent that the material properties must be chosen such that the interface between the absorbing material and Free-Space is reflection less for all frequencies, polarizations, and angles of incidence. To put it more simply, Gedney proposed the relative permittivity and permeability tensors for the case of an electromagnetic waves incident on a single boundary layer z-axis, as the following equation (Gedney, 1996a)

$$\underline{\underline{\epsilon}}_z = \underline{\underline{\mu}}_z = \begin{bmatrix} 1 + \frac{\sigma_z}{j\omega\epsilon_0} & 0 & 0 \\ 0 & 1 + \frac{\sigma_z}{j\omega\epsilon_0} & 0 \\ 0 & 0 & \frac{1}{1 + \frac{\sigma_z}{j\omega\epsilon_0}} \end{bmatrix} \quad (131)$$

In brief, the stretching coordinate PML can be made equivalent to anisotropic medium by Zhao and Candgellaris (Zhao and Candgellaris, 1996a).

The generalized PML formulation was proposed by Gedney (Gedney, 1996a)—Berenger's equations using the modified Ampere-Maxwell's law can be expressed in the frequency, then Equation (119) to Equation (124) become

$$j\omega\epsilon_0\epsilon_r \left(1 + \frac{\sigma_y}{j\omega\epsilon_0\epsilon_r} \right) E_{xy} = \frac{\partial (H_{zx} + H_{zy})}{\partial y} \quad (132)$$

$$j\omega\epsilon_0\epsilon_r \left(1 + \frac{\sigma_z}{j\omega\epsilon_0\epsilon_r} \right) E_{xz} = -\frac{\partial (H_{yz} + H_{yx})}{\partial z} \quad (133)$$

$$j\omega\epsilon_0\epsilon_r \left(1 + \frac{\sigma_z}{j\omega\epsilon_0\epsilon_r} \right) E_{yz} = \frac{\partial (H_{xy} + H_{xz})}{\partial z} \quad (134)$$

$$j\omega\epsilon_0\epsilon_r \left(1 + \frac{\sigma_x}{j\omega\epsilon_0\epsilon_r} \right) E_{yx} = -\frac{\partial (H_{zx} + H_{zy})}{\partial x} \quad (135)$$

$$j\omega\varepsilon_0\varepsilon_r\left(1+\frac{\sigma_x}{j\omega\varepsilon_0\varepsilon_r}\right)E_{zx}=\frac{\partial(H_{yz}+H_{yx})}{\partial x} \quad (136)$$

$$j\omega\varepsilon_0\varepsilon_r\left(1+\frac{\sigma_y}{j\omega\varepsilon_0\varepsilon_r}\right)E_{zy}=-\frac{\partial(H_{xy}+H_{xz})}{\partial y} \quad (137)$$

Gedney assumed that the interface between the PML medium and the isotropic space is a constant z -plane. Subsequently, let $\sigma_x = \sigma_y = 0$, $\varepsilon_r = 1$ and using the relationship $E_x = E_{xy} + E_{xz}$, $E_y = E_{yx} + E_{yz}$ and $E_z = E_{zx} + E_{zy}$, then

$$j\omega\varepsilon_0\varepsilon_r E_x = \frac{\partial H_z}{\partial y} - \frac{\frac{\partial H_y}{\partial z}}{\left(1+\frac{\sigma_z}{j\omega\varepsilon_0}\right)} = \frac{\partial H_z}{\partial y} - \frac{1}{\left(1+\frac{\sigma_z}{j\omega\varepsilon_0}\right)} \cdot \frac{\partial H_y}{\partial z} \quad (138)$$

$$j\omega\varepsilon_0\varepsilon_r E_y = \frac{\frac{\partial H_x}{\partial z}}{\left(1+\frac{\sigma_z}{j\omega\varepsilon_0}\right)} - \frac{\partial H_z}{\partial x} = \frac{1}{\left(1+\frac{\sigma_z}{j\omega\varepsilon_0}\right)} \cdot \frac{\partial H_x}{\partial z} - \frac{\partial H_z}{\partial x} \quad (139)$$

$$j\omega\varepsilon_0\varepsilon_r E_z = \frac{\partial H_y}{\partial x} - \frac{\partial H_x}{\partial y} \quad (140)$$

By this algorithm, it is similarly for the magnetic field intensities leads to (Gedney, 1996a)

$$-j\omega\mu_0\mu_r H_x = \frac{\partial E_z}{\partial y} - \frac{\frac{\partial E_y}{\partial z}}{\left(1+\frac{\sigma_z}{j\omega\varepsilon_0}\right)} = \frac{\partial E_z}{\partial y} - \frac{1}{\left(1+\frac{\sigma_z}{j\omega\varepsilon_0}\right)} \cdot \frac{\partial E_y}{\partial z} \quad (141)$$

$$-j\omega\mu_0\mu_r H_y = \frac{\frac{\partial E_x}{\partial z}}{\left(1+\frac{\sigma_z}{j\omega\varepsilon_0}\right)} - \frac{\partial E_z}{\partial x} = \frac{1}{\left(1+\frac{\sigma_z}{j\omega\varepsilon_0}\right)} \cdot \frac{\partial E_x}{\partial z} - \frac{\partial E_z}{\partial x} \quad (142)$$

$$-j\omega\mu_0\mu_r H_z = \frac{\partial E_y}{\partial x} - \frac{\partial E_x}{\partial y} \quad (143)$$

Using Rappaport's mapping (Rappaport, 1995), the real coordinate z-axis is mapped into the complex coordinate stretching with complex spatial variable

$$z = z' \left(1 + \frac{\sigma_z}{j\omega\epsilon_0} \right), \quad \frac{\partial}{\partial z} = \frac{1}{\left(1 + \frac{\sigma_z}{j\omega\epsilon_0} \right)} \frac{\partial}{\partial z'} \quad (144)$$

Equation (144) implies that there is a scaling of the normal electric and magnetic fields intensities where (Gedney, 1996a)

$$E_z = \frac{E'_z}{\left(1 + \frac{\sigma_z}{j\omega\epsilon_0} \right)} \quad \text{and} \quad H_z = \frac{H'_z}{\left(1 + \frac{\sigma_z}{j\omega\epsilon_0} \right)} \quad (145)$$

By applied the scaling of the normal electric and magnetic field intensities, Equation (138) to Equation (143) become (Gedney, 1996a)

$$j\omega\epsilon_0\epsilon_r \left(1 + \frac{\sigma_z}{j\omega\epsilon_0} \right) E_x = \frac{\partial H'_z}{\partial y} - \frac{\partial H'_y}{\partial z'} \quad (146)$$

$$j\omega\epsilon_0\epsilon_r \left(1 + \frac{\sigma_z}{j\omega\epsilon_0} \right) E_y = \frac{\partial H'_x}{\partial z'} - \frac{\partial H'_z}{\partial x} \quad (147)$$

$$j\omega\epsilon_0\epsilon_r \left(\frac{1}{1 + \frac{\sigma_z}{j\omega\epsilon_0}} \right) E'_z = \frac{\partial H'_y}{\partial x} - \frac{\partial H'_x}{\partial y} \quad (148)$$

$$-j\omega\mu_0\mu_r \left(1 + \frac{\sigma_z}{j\omega\epsilon_0} \right) H_x = \frac{\partial E'_z}{\partial y} - \frac{\partial E'_y}{\partial z'} \quad (149)$$

$$-j\omega\mu_0\mu_r \left(1 + \frac{\sigma_z}{j\omega\epsilon_0} \right) H_y = \frac{\partial E'_x}{\partial z'} - \frac{\partial E'_z}{\partial x} \quad (150)$$

$$-j\omega\mu_0\mu_r \left(\frac{1}{1 + \frac{\sigma_z}{j\omega\epsilon_0}} \right) H'_z = \frac{\partial E'_y}{\partial x} - \frac{\partial E'_x}{\partial y} \quad (151)$$

Alternatively, if assume that σ_x, σ_y and σ_z is valued in complex coordinates stretching, then Equation (138) become $j\omega\varepsilon_0\varepsilon_r E_x = \frac{\partial H_z}{\partial y} - \frac{\partial H_y}{\partial z}$. By using Equation (144) and Equation (145) then (constant z-plane)

$$j\omega\varepsilon_0\varepsilon_r E_x = \frac{1}{\left(1 + \frac{\sigma_z}{j\omega\varepsilon_0}\right)} \frac{\partial H'_z}{\partial y} - \frac{1}{\left(1 + \frac{\sigma_z}{j\omega\varepsilon_0}\right)} \frac{\partial H_y}{\partial z'}$$

$$j\omega\varepsilon_0\varepsilon_r \left(1 + \frac{\sigma_z}{j\omega\varepsilon_0}\right) E_x = \frac{\partial H'_z}{\partial y} - \frac{\partial H_y}{\partial z'}$$

Equation (139) to Equation (143) can be derived in this manner. In conclusion, the compact form of these equations is as the following equation

$$\begin{bmatrix} \frac{\partial H'_z}{\partial y} - \frac{\partial H_y}{\partial z'} \\ \frac{\partial H_x}{\partial z'} - \frac{\partial H'_z}{\partial x} \\ \frac{\partial H_y}{\partial x} - \frac{\partial H_x}{\partial y} \end{bmatrix} = j\omega\varepsilon_0\varepsilon_r \begin{bmatrix} 1 + \frac{\sigma_z}{j\omega\varepsilon_0} & 0 & 0 \\ 0 & 1 + \frac{\sigma_z}{j\omega\varepsilon_0} & 0 \\ 0 & 0 & \frac{1}{1 + \frac{\sigma_z}{j\omega\varepsilon_0}} \end{bmatrix} \begin{bmatrix} E_x \\ E_y \\ E'_z \end{bmatrix} \quad (152)$$

Equation (152) is similar to the Ampere-Maxwell's law represented in the uniaxial medium, which was described in Equation (131).

$$\begin{bmatrix} \frac{\partial H_z}{\partial y} - \frac{\partial H_y}{\partial z} \\ \frac{\partial H_x}{\partial z} - \frac{\partial H_z}{\partial x} \\ \frac{\partial H_y}{\partial x} - \frac{\partial H_x}{\partial y} \end{bmatrix} = j\omega\varepsilon_0\varepsilon_r \begin{bmatrix} 1 + \frac{\sigma_z}{j\omega\varepsilon_0} & 0 & 0 \\ 0 & 1 + \frac{\sigma_z}{j\omega\varepsilon_0} & 0 \\ 0 & 0 & \frac{1}{1 + \frac{\sigma_z}{j\omega\varepsilon_0}} \end{bmatrix} \begin{bmatrix} E_x \\ E_y \\ E_z \end{bmatrix} \quad (153)$$

Gedney stated that a mathematical relationship between the two methods is not obvious (Gedney, 1996a). However, this research has verifying the mathematical relationship between two methods.

It is apparent that Berenger's formulation can be derived from two contemporary PMLs via a mapping and scaling of the normal field intensities. The advantage of this formulation over Berenger's PML method are this formulation is based on Maxwell's equations, rather than a modified set of equations. In brief, the implementation to FDTD method is more numerically efficient and it can be extended to non orthogonal an unstructured grid technique (Gedney, 1996a).

Gedney also proposed the PML formulation in the corner regions where there is more than one boundary layer. Alternatively, Zhao and Candgellaris (Zhao and Candgellaris, 1996b) presented their PML very attractively in view of its systematic of the Generalized Theory of Perfectly Matched Layer (GT-PMLs). However, GT-PMLs required three different types of PML related to the faces, edges and corners of the PML region. Therefore, this research uses the New Generalized Perfectly Matched Layer (NGPML), which was proposed by Ling *et al.* (Ling *et al.*, 2002). They had generalized Gedney's formulation in three dimensional axes. Especially, only one type of simple formulation is needed to resolve the above three types of PMLs (GT-PMLs). Also, NGPML is presented for general lossy and dispersive medium. In addition, dispersive medium is presented as the value of ε , μ and σ are depend on frequency. In conclusion, the computational domain is divided to two sub-domains, the simulated physical domain and the simulated artificial absorbing layer, however, Maxwell's curl equations can be written in one formulation by the following (Ling *et al.*, 2002)

$$\nabla \times \bar{H} = j\omega\varepsilon_0\hat{\varepsilon}_r(\omega)\bar{E} \quad (154)$$

$$\nabla \times \bar{E} = -j\omega\mu_0\hat{\mu}_r(\omega)\bar{H} \quad (155)$$

where $\varepsilon_r(\omega)$ and $\mu_r(\omega)$ are relative permittivity and relative permeability in the whole computational domain (isotropic medium), respectively, and

$$\hat{\varepsilon}_r(\omega) = \varepsilon_r(\omega) + \frac{\sigma_r(\omega)}{j\omega\varepsilon_0}, \quad \hat{\mu}_r(\omega) = 1 \quad (156)$$

For a lossy uniaxial medium, the relative permittivity and permeability tensors are

$$\bar{\varepsilon} = \bar{\mu} = \begin{bmatrix} \frac{a_y a_z}{a_x} & 0 & 0 \\ 0 & \frac{a_x a_z}{a_y} & 0 \\ 0 & 0 & \frac{a_x a_y}{a_z} \end{bmatrix}, \quad a_i = k + \frac{\sigma_i}{j\omega\varepsilon_0}, \quad i = x, y, z - \text{axis} \quad (157)$$

Berenger found that if σ_i , $i = x, y, z$ -axis, is constant via PML region, significant reflections are encountered at the interface of the PML (Berenger, 1994). It is due to the discrete approximation of the fields and the material parameters between two mediums: space and lossy anisotropic medium. To reduce the effect of surface condition changing rapidly in PML region, this research using a spatially varying conductivity of PML in three axes as

$$\sigma_i = \sigma_{\max} \left(\frac{|\Delta d|}{d} \right)^m, \quad i = x, y, z - \text{axis} \quad (158)$$

For applied PML to any computer programming, we had set spatial conductivity to i -axis ($i = x, y, z$), side by side. For example, if electromagnetic wave travels in PML along the x -axis, then σ_y and σ_z are equal to zero, however, only σ_x is effected in Equation (158). Currently, we are showing how to set the spatial conductivity of PML in x, y, z -axis, respectively (Jariyanorawiss, 2004)

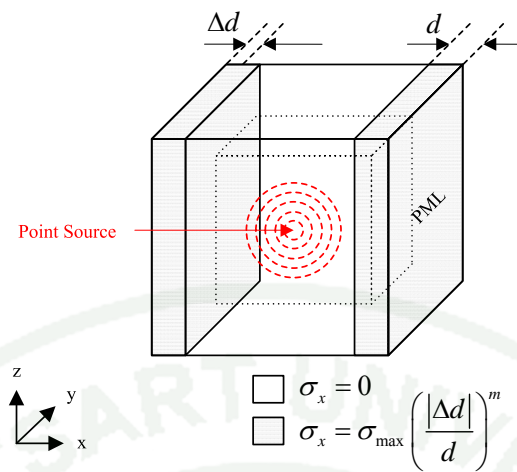


Figure 76 The spatial conductivity of PML in x-axis.

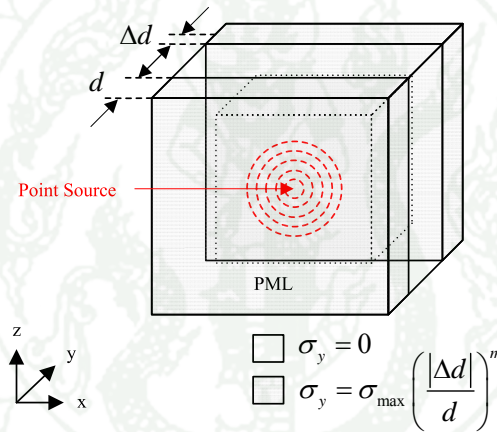


Figure 77 The spatial conductivity of PML in y-axis.

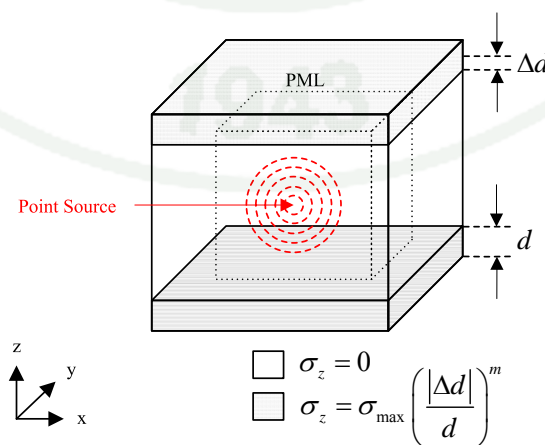


Figure 78 The spatial conductivity of PML in z-axis.

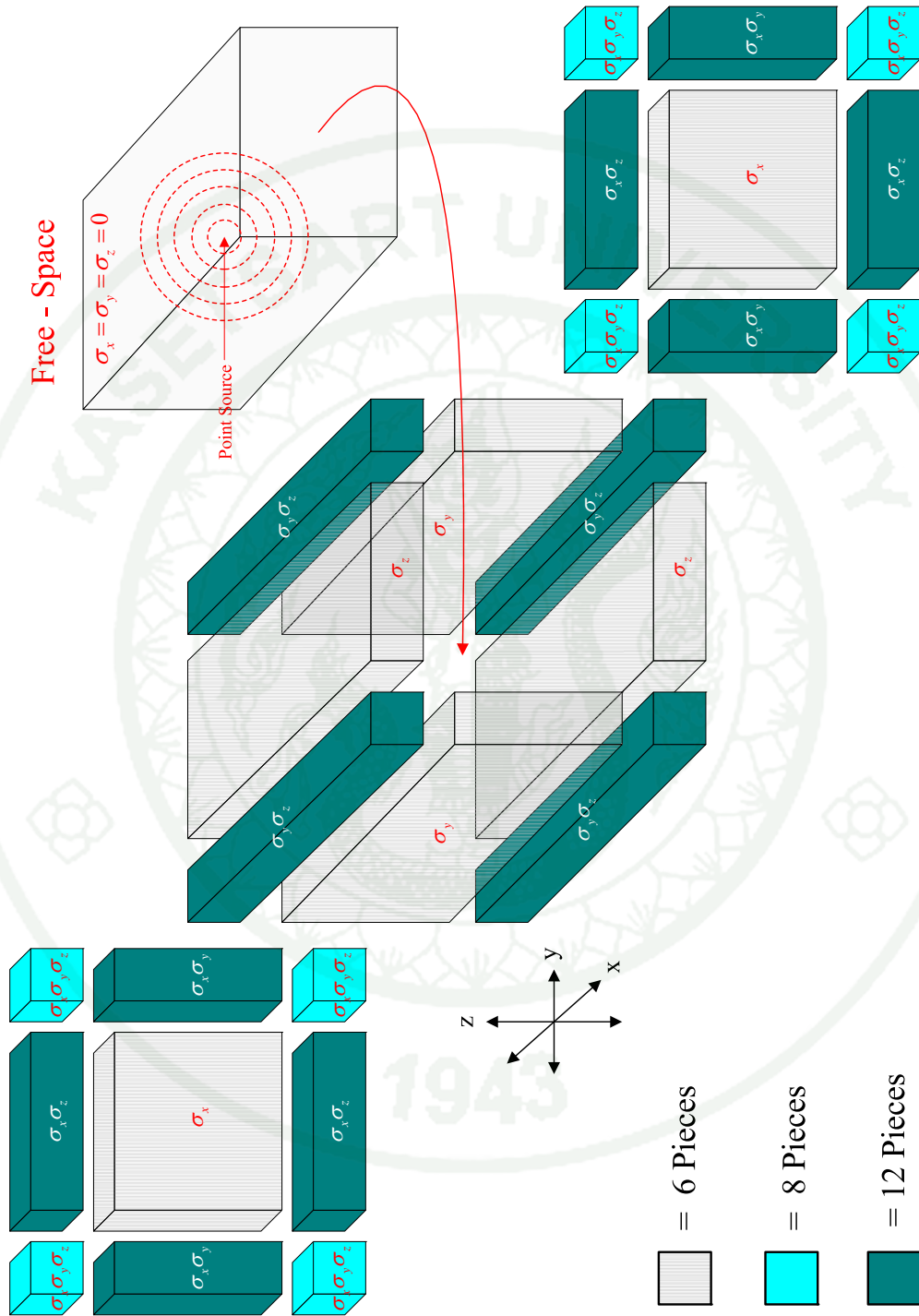


Figure 79 The intersection of spatial conductivity in x, y, z-axis.

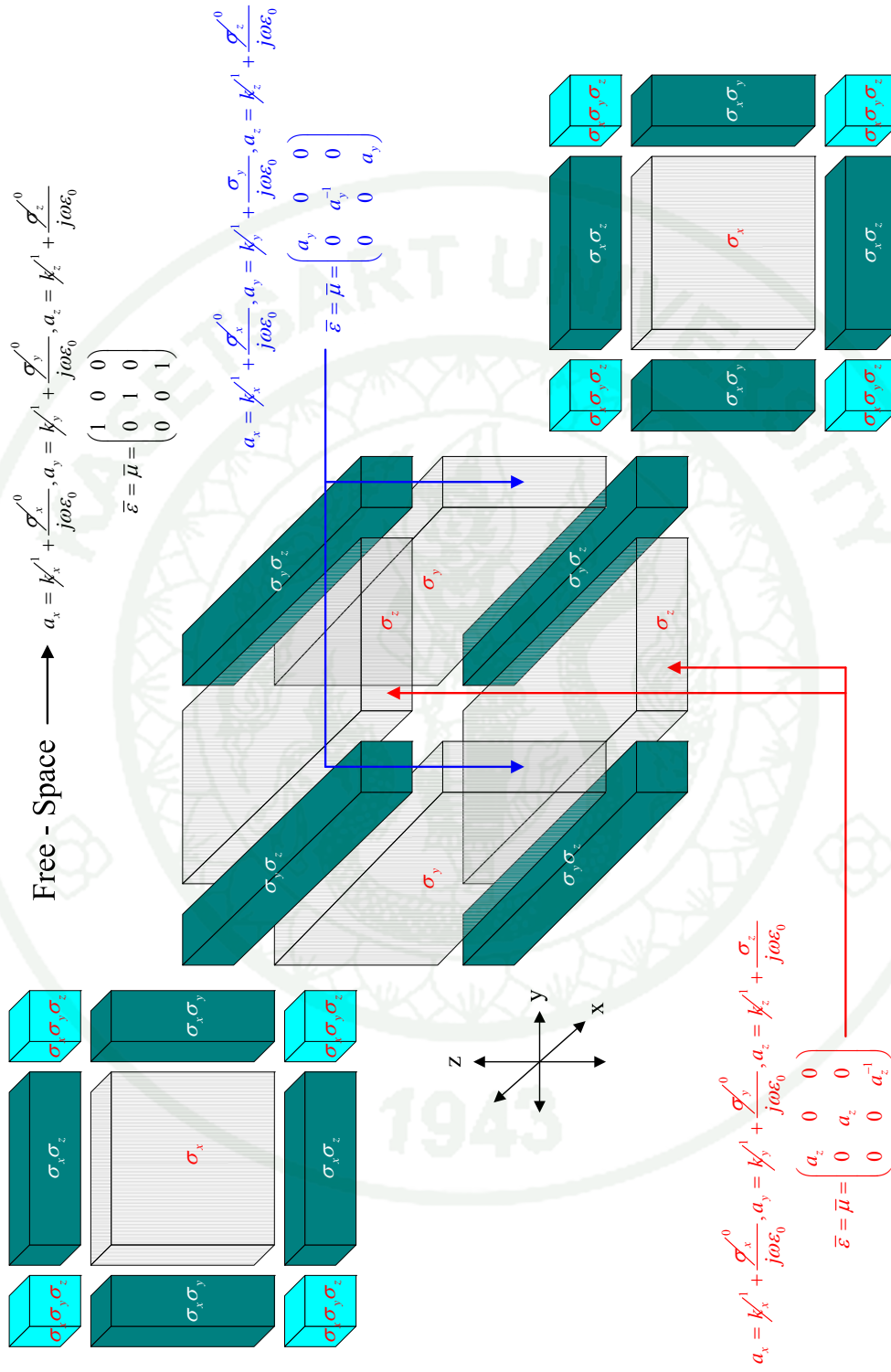


Figure 80 The relationship of spatial conductivity with Maxwell's equations in both Equation (154) and Equation (155).

From Figure 80 shown that the spatial conductivity in Free-Space domains, values of σ_x, σ_y and σ_z all equal to zero will effect both Equation (154) and Equation (155) changed to Maxwell's equations in Free-Space automatically, from Equation (111) to Equation (116). For example,

$$\nabla \times \bar{H} = j\omega\epsilon_0\hat{\epsilon}_r(\omega) \begin{bmatrix} 1 & 0 & 0 \\ 0 & 1 & 0 \\ 0 & 0 & 1 \end{bmatrix} \bar{E}$$

$$\nabla \times \bar{E} = -j\omega\mu_0\hat{\mu}_r(\omega) \begin{bmatrix} 1 & 0 & 0 \\ 0 & 1 & 0 \\ 0 & 0 & 1 \end{bmatrix} \bar{H}$$

These results associated with generalized Maxwell's equations. In other words, the Maxwell's equations in Free-Space domain can be derived from Equation (154) and Equation (155) as

$$\nabla \times \bar{H} = j\omega\epsilon_0\hat{\epsilon}_r(\omega)\bar{E} \quad (159)$$

$$\nabla \times \bar{E} = -j\omega\mu_0\hat{\mu}_r(\omega)\bar{H} \quad (160)$$

Consequently, Gedney suggested that by properly choosing the constitutive parameters of the uniaxial media both propagating and evanescent waves can be highly attenuated within anisotropic medium. Also, it resolves the concern that the original Berenger's formulation for a PML medium does not attenuate evanescent waves. In brief, the real term k in $a_i = k + \frac{\sigma_i}{j\omega\epsilon_0}$, $i = x, y, z$ -axis amplifies the attenuation of highly attenuative modes and σ attenuates the propagating modes (Gedney, 1996b).

Corresponding to Figure 71, the simulation was computed once again by applied absorbing boundary layer with NGPML. The results are as follow (Jariyanorawiss, 2004)

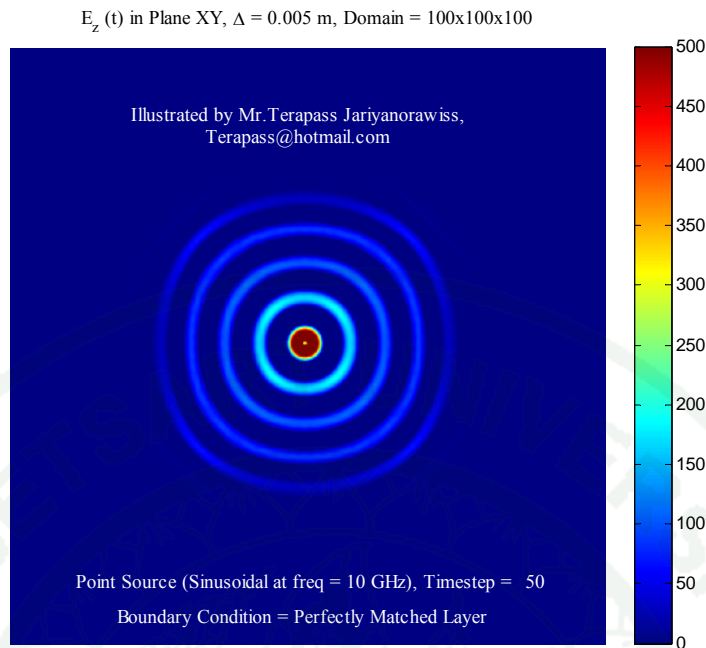


Figure 81 Cross-section of the applied absorbing boundary layer (PML) to the computational domain (Timestep = 50).

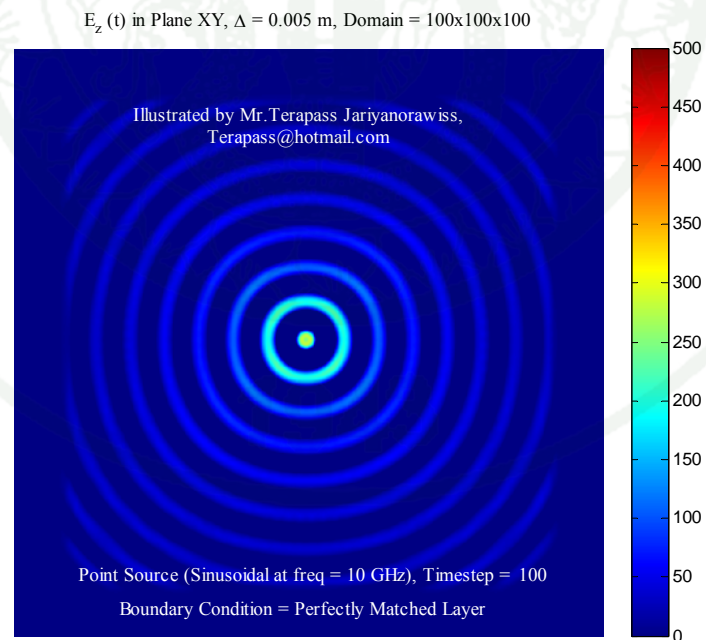


Figure 82 Cross-section of the applied absorbing boundary layer (PML) to the computational domain (Timestep = 100).

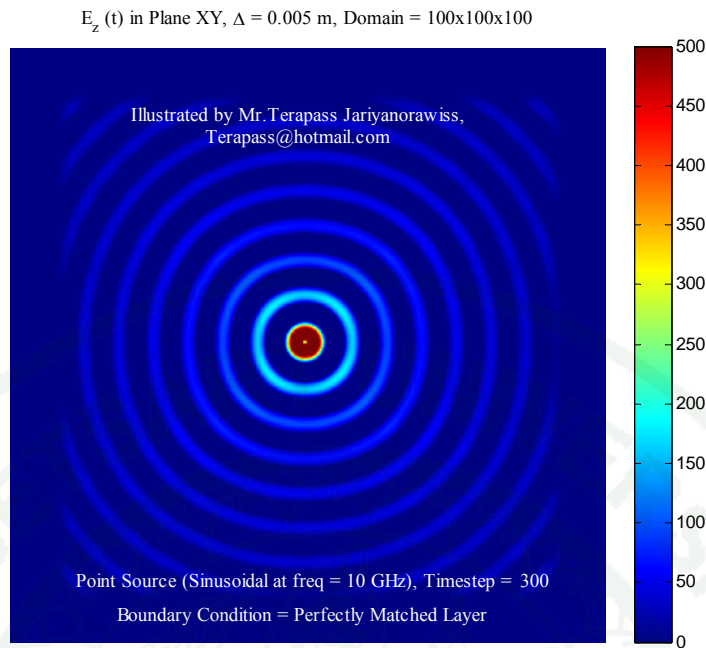


Figure 83 Cross-section of the applied absorbing boundary layer (PML) to the computational domain (Timestep = 300).

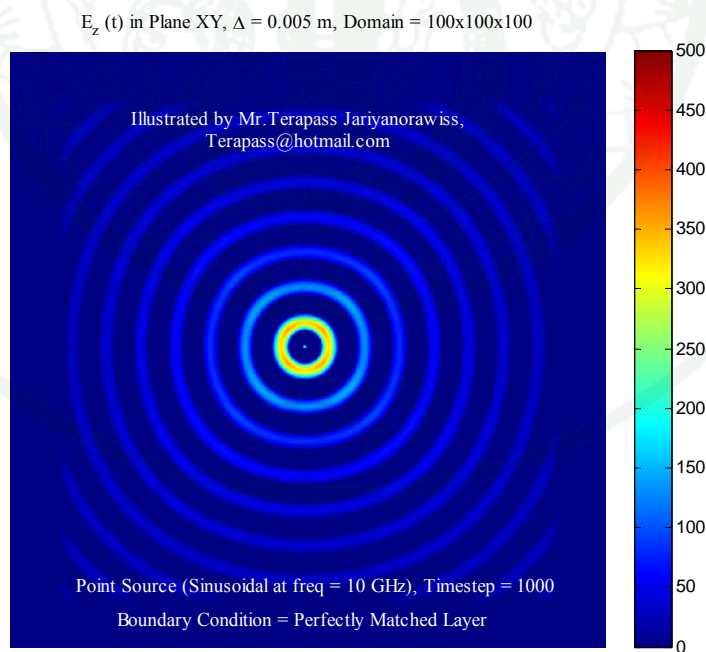


Figure 84 Cross-section of the applied absorbing boundary layer (PML) to the computational domain (Timestep = 1000).

The result shows that none of the electromagnetic wave was reflected back to the system, even how long the time spent on the simulation. It is the same principle of secret intelligence air-plane, Stealth Aircraft. Especially, this explains why Stealth Aircraft is totally invisible from radar.

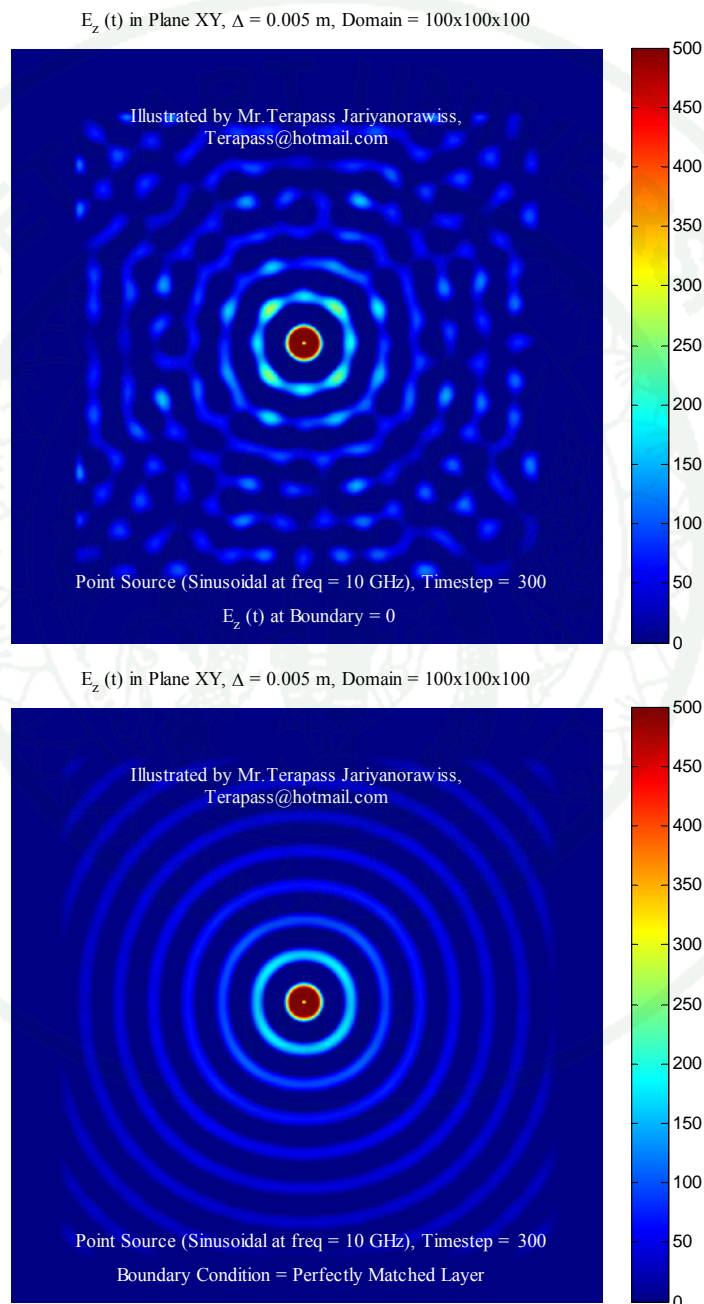


Figure 85 Comparison cross-section of the applied incorrect boundary layer and the applied absorbing boundary layer (PML) at timestep = 300.

3.2.3. The analysis of generalized Maxwell's equations

In 2003, Professor Dr. Wiroj Homsup and Associated Professor Dr. Nuttaka Homsup introduced the author the smart algorithm to generalize Maxwell's equations. The author has been applied this smart algorithm to analyze all the electromagnetic simulation problems. Consider the following equations

$$\nabla \times \bar{H} = j\omega \varepsilon_0 \hat{\varepsilon}_r(\omega) \bar{E} \quad (161)$$

$$\nabla \times \bar{E} = -j\omega \mu_0 \hat{\mu}_r(\omega) \bar{H} \quad (162)$$

First, we set the matrix \bar{D} as

$$\bar{D} = \varepsilon_0 \hat{\varepsilon}_r(\omega) \bar{E} \quad (163)$$

$$\hat{\varepsilon}_r(\omega) = \varepsilon_r(\omega) + \frac{\sigma_r(\omega)}{j\omega \varepsilon_0}, \quad \hat{\mu}_r(\omega) = 1$$

Also, we set both matrix \bar{R} and \bar{G} as

$$\bar{R} = \begin{bmatrix} \frac{a_y}{a_x} & 0 & 0 \\ 0 & \frac{a_z}{a_y} & 0 \\ 0 & 0 & \frac{a_x}{a_z} \end{bmatrix} \bar{H} \quad (164)$$

$$\bar{G} = \begin{bmatrix} \frac{a_y}{a_x} & 0 & 0 \\ 0 & \frac{a_z}{a_y} & 0 \\ 0 & 0 & \frac{a_x}{a_z} \end{bmatrix} \bar{D} \quad (165)$$

Then, the $\bar{R}^{n+\frac{1}{2}}$ can be computed from

$$\nabla \times \bar{E} = -j\omega\mu_0 \begin{bmatrix} a_z & 0 & 0 \\ 0 & a_x & 0 \\ 0 & 0 & a_y \end{bmatrix} \bar{R} \quad (166)$$

and the $\bar{H}^{n+\frac{1}{2}}$ is computed from Equation (164). Then, the $\bar{G}^{n+\frac{1}{2}}$ is computed from

$$\nabla \times \bar{H} = j\omega \begin{bmatrix} a_z & 0 & 0 \\ 0 & a_x & 0 \\ 0 & 0 & a_y \end{bmatrix} \bar{G} \quad (167)$$

and the $\bar{D}^{n+\frac{1}{2}}$ is computed from (165). Finally, $\bar{E}^{n+\frac{1}{2}}$ is computed from (163). This smart algorithm repeats itself until the end of simulation time.

3.2.4. Global error

In order to evaluate the performance of absorbing boundary layer, it is appropriate to compute from E_z which is travelling in a computational grid. In general, there are two types of a computational grids, an infinite grid (Ω_{inf}) and a finite grid (Ω_{PML}). A point source is generating E_z in both Ω_{inf} and Ω_{PML} as the same time. It is apparent that Ω_{inf} has an infinite length $i, j, k \rightarrow \infty$ and a computation should be done by a time limit. However, on the contrary, Ω_{PML} has a finite length but the computational time is unlimited. Finally, it should be globally measured as the sum of the squares of the error at each grid point in the domain covered by size of $\Omega_{\text{inf}} \cap \text{PML}$ (Ling *et al.*, 2002; Homsup *et al.*, 2004; Jariyanorawiss, 2004).

$$(\text{Global error})_{t=n\Delta t} = \sum_i \sum_j \sum_k \left(E_z^{\Omega_{\text{inf}} \cap \text{PML}}(i, j, k) - E_z^{\Omega_{\text{PML}}}(i, j, k) \right)^2 \quad (168)$$

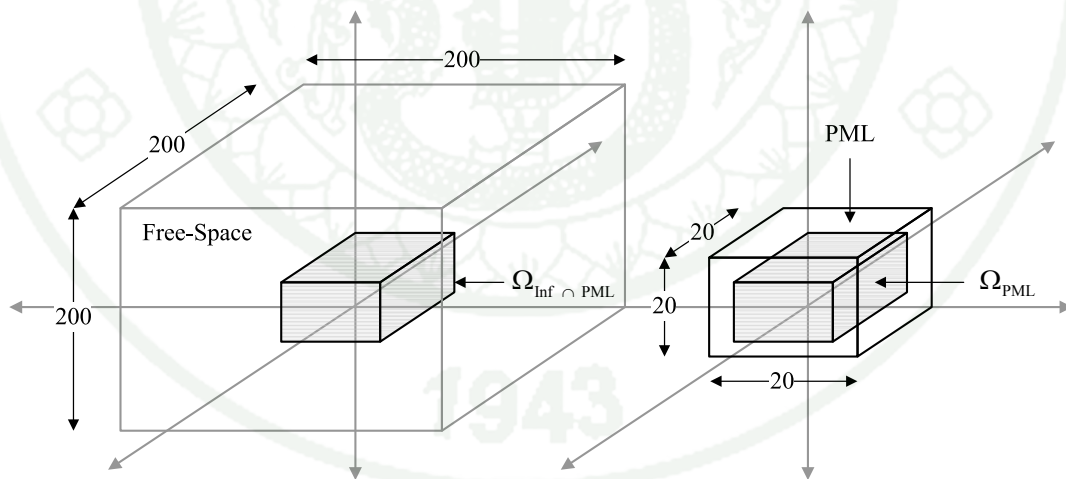


Figure 86 Global error illustration.

Source: Jariyanorawiss (2004)

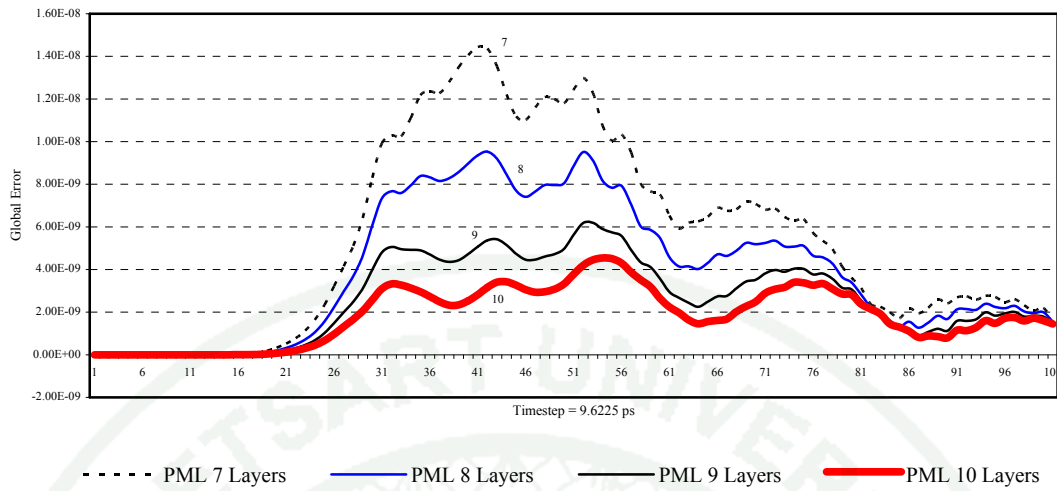


Figure 87 Comparison between Global error and PML layers.

Source: Jariyanorawiss (2004)

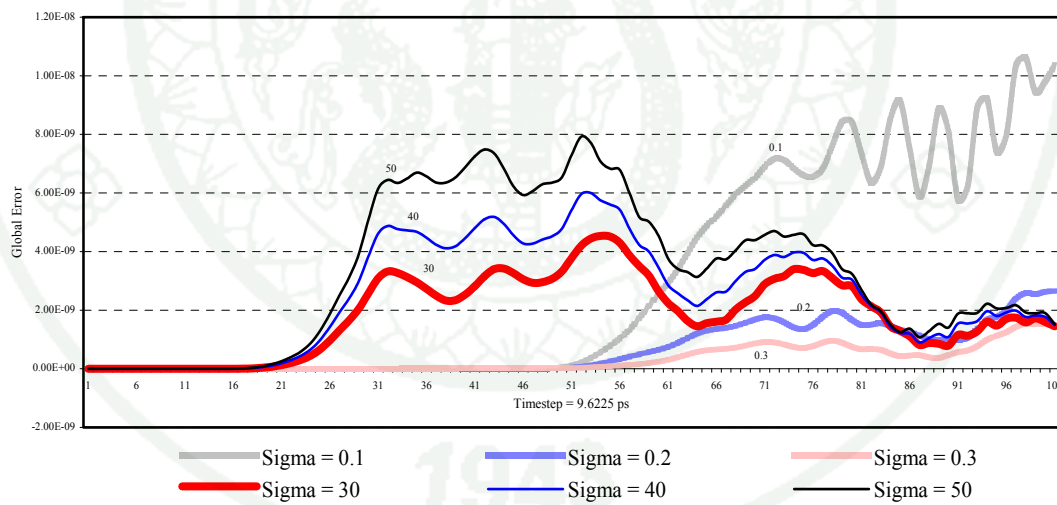


Figure 88 Comparison between Global error and maximum conductivity.

Source: Jariyanorawiss (2004)

3.3 The verification of the FDTD programming

There are three methods to verify the FDTD programming with PML. First, it is usually done by visualization as well as the Figure 85. This method is very simple and easy to implement with any computer programming. Second, Global error is an explicit solution, which is numerical solution. However, these two verifications were derived from one equation, a generalized Maxwell's equations, but it was presented in a difference grid. Third, the FDTD simulation of a dipole, both the input impedance and the return loss at the center-fed are the results to compare with the reference method, MoM. Additionally, MoM usually simulates the dipole antenna by either Hallen's Equation or Pocklington's Equation. Apparently, this verification method is the comparison between time domain and frequency domain. In conclusion, these three methods can use to verify the FDTD programming.

3.3.1. An improved FDTD model for the feeding gap of a Thin-Wire antenna

In general, a radiating efficiency of antennas is usually expressed in terms of radiation impedance. The radiation impedance, which is determined by the geometry of the antennas, is obtained from the radiation reaction of conduction electrons in the dipole. In theory, the radiation impedance or the input impedance is referred to either the ratio of the voltage to current at a pair of terminals or the ratio of the appropriate components of the electric fields to magnetic fields at a point. The input impedance consists of two components, the real and the imaginary. It should be note that the input impedance is more practical than the radiation resistance. In conclusion the input impedance was derived by both an explicit solution (The Exact Solution) and the implicit solution (MoM and FDTD).

Watanabe and Taki (Watanabe and Taki, 1998) showed that the one-cell gap model for a thin-wire antenna can cause error in calculated antenna input impedance and this error is strongly dependent on the FDTD cell grid. The dipole was assumed to a slender dipole. In time domain simulation, they use FDTD. Also, they

used 2nd approximations of Mur's absorbing boundary condition and applied subcell method (Kunz and Luebbers, 1993) to model a compensated one-cell gap dipole. In frequency domain simulation, they use MoM calculation by applied the Galerkin's method with piecewise sinusoidal functions (Stutzman and Thiele, 1998).

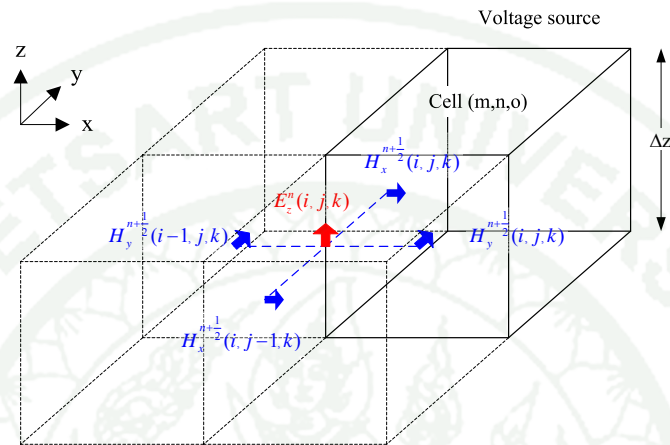


Figure 89 The quaternary H - field around the narrow feeding gap.

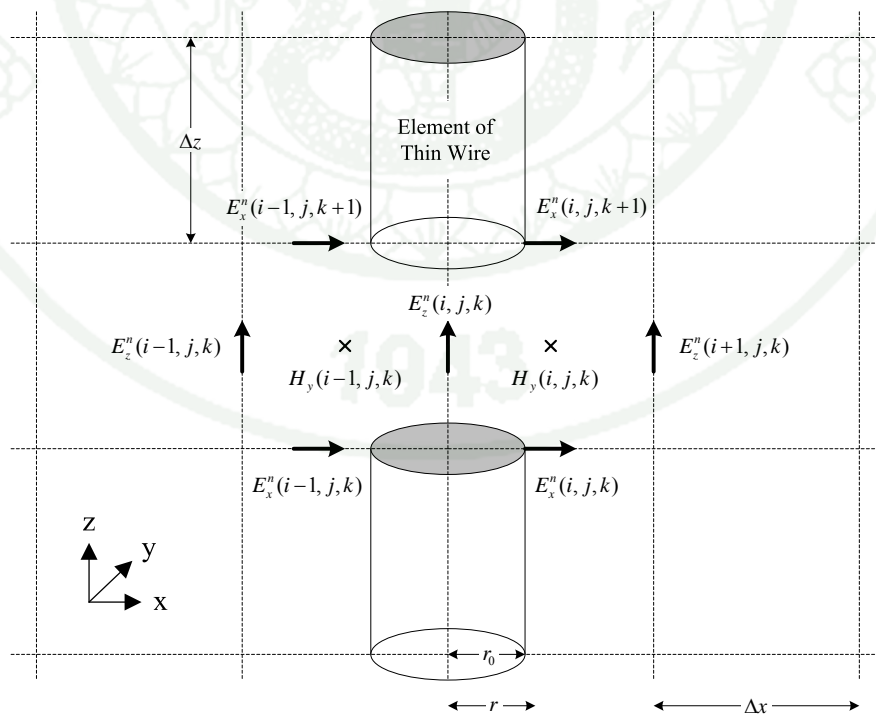


Figure 90 The one-cell gap model of a thin-wire dipole antenna.

By the conventional FDTD formula, for example, the H-fields (y-axis) around the one-cell gap model are given by

$$H_y^{n+\frac{1}{2}}(i, j, k) = H_y^{n-\frac{1}{2}}(i, j, k) - \left(\frac{\Delta t}{\mu} \right) \left(\left(\frac{E_x^n(i, j, k+1) - E_x^n(i, j, k)}{\Delta z} \right) - \left(\frac{E_z^n(i+1, j, k) - E_z^n(i, j, k)}{\Delta x} \right) \right) \quad (169)$$

Also, the $H_y^{n+\frac{1}{2}}(i-1, j, k)$, $H_x^{n+\frac{1}{2}}(i, j, k)$ and $H_x^{n+\frac{1}{2}}(i, j-1, k)$ components must be computed using the conventional FDTD formula. The feeding source is given by the E-field in the air gap corresponding to one-space interval of Yee's lattice as the following equation

$$E_z^n(i, j, k) = -\frac{V_s(t)}{\Delta z} = -\frac{V_{\max} e^{-\frac{(t-t_0)^2}{2\sigma^2}}}{\Delta z} = -\frac{V_{\max} e^{-\frac{(t-t_0)^2}{2\sigma^2}}}{\text{Grid Size}} \quad (170)$$

Additionally, the input impedance was computed by the FDTD simulation using the current (I_s) surrounding the one-cell gap. By applying Ampere's law plus Maxwell's displacement current on the narrow gap (Kouveliotis *et al.*, 2002)

$$I_s = \oint \vec{H} \cdot d\vec{l} \quad (171)$$

The discretization of Equation (171) depends on FDTD scheme. If $\Delta = \Delta x = \Delta y = \Delta z$, then the result is as the following equation

$$I_s(t) = \Delta \cdot \left(H_x^{n+\frac{1}{2}}(i, j-1, k) - H_x^{n+\frac{1}{2}}(i, j, k) + H_y^{n+\frac{1}{2}}(i, j, k) - H_y^{n+\frac{1}{2}}(i-1, j, k) \right) \quad (172)$$

H_x , H_y are components of the magnetic field in the x, y-axis, respectively. i , j and k represent the indexes for each spatial segment corresponding

to the x, y and z direction respectively. Also, n stands for the time-step index. It should be noted that Equation (172) derives, considering a z -directed infinitesimal dipole and a Yee's cell is sizeable (Δ) equal in the three directions. When result of distribution of the voltage and current on the dipole's narrow gap are obtained by FDTD simulation, then the input impedance can easily be computed. The simple method is done by calculating the values of voltage $V_s(f)$ and current $I_s(f)$ in the frequency domain using Discrete Fourier Transform (DFT) (Haykin, 2001).

$$Z_{in}(f) = \frac{V_s(f)}{I_s(f)} \quad (173)$$

$$\Gamma = \frac{Z_{Load} - Z_{Source}}{Z_{Load} + Z_{Source}} \quad (174)$$

The antenna input impedance of a thin-wire dipole antenna in Free-Space calculated using the one-cell gap model were compared with MoM (Stutzman and Thiele, 1998), which assumes an infinitesimal gap. As a simulation result, error of calculation of input impedance can be happened if the size of Yee's cell is different (Watanabe and Taki, 1998).

By subcell method (Kunz and Luebbers, 1993), the computational cost of the FDTD technique scales directly with the number of cells. Reducing the cell size throughout the FDTD computational space is one method for dealing with this situation, but it is computationally expensive and this method may not even be programmed if the computer resources are inadequate. Applied subcell method to the conventional FDTD formula, the H-fields (y -axis) around the one-cell gap become

$$H_y^{n+\frac{1}{2}}(i, j, k) = H_y^{n-\frac{1}{2}}(i, j, k) - \left(\frac{\Delta t}{\mu} \right) \left[\left(\frac{E_x^n(i, j, k+1) - E_x^n(i, j, k)}{\Delta z} \right) - \left(\frac{2}{\ln\left(\frac{\Delta x}{r_0}\right)} \right) \left(\frac{E_z^n(i+1, j, k) - \left(\frac{-V_s(t)}{\Delta z}\right)}{\Delta x} \right) \right] \quad (175)$$

The other three components, the $H_y^{n+\frac{1}{2}}(i-1, j, k)$, $H_x^{n+\frac{1}{2}}(i, j, k)$ and $H_x^{n+\frac{1}{2}}(i, j-1, k)$ can be computed in the same manner. Finally, Watanabe and Taki (Watanabe and Taki, 1998) showed that the improved feeding gap model for a narrow gap made the FDTD calculation agree well with MoM calculation assuming an infinitesimal gap. Especially, they were barely affected by the cell size.

In brief, the comparison between the FDTD and the MoM presented by input impedance can be verified the FDTD programming.

To summaries, there are three computer programming for simulate dipole: the Exact Solution, MoM and FDTD. The most interesting computer programming is the FDTD because the FDTD gives a complete full-wave electromagnetic solution simply in a single simulation run and also the FDTD is capable of computing electromagnetic problems with complex geometric structures which are difficult to analyze by MoM.

The Reference Model

The FDTD computer programming has been widely using during the past two decades. There is Open-source, Freeware and commercial software. The Open-source is JFDTD, WOLFSIM, Meep, (Geo-) Radar FDTD, bigboy, toyFDTD, FDTD codes in C++, FDTD code in Fortran 90 and FDTD code in C for 2D EM Wave simulation. The Freeware but closed source is GprMax. The commercial software is exist more than twenty names, for instance, CST Microwave Studio and XFDTD. All of them are electromagnetic simulation software.

It is application of FDTD, including antenna design, microwave circuits, radar tracing, wireless simulation, Electromagnetic Compatibility (EMC), Electromagnetic Interference (EMI), photonics and Bio/EM effects. This research is compatible with all application as describe above but the interaction between a mobile phone and the human head is the main proposed on this paper. The simulated model is shown in the following figure

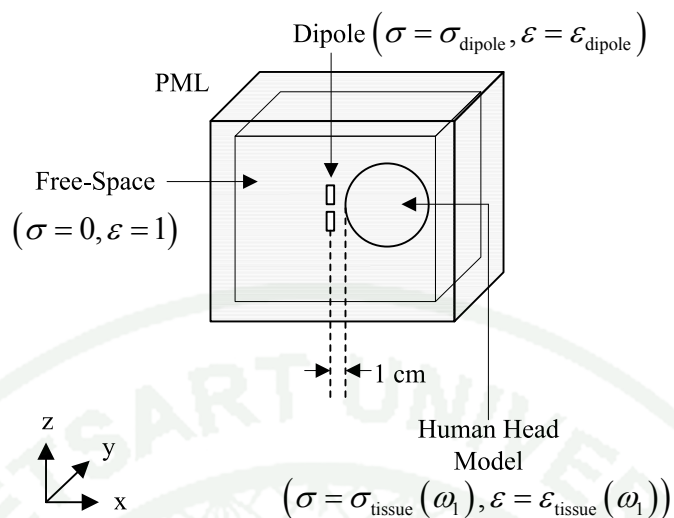


Figure 91 Geometry for the reference model.

The reference model is consisted of two domains: the physical domain and the absorbing boundary layer, (Appendix Figure A2). The simulated physical domain contains a dipole antenna and a human head model. σ_{metal} and $\sigma_{\text{tissue}}(\omega_1)$ are the conductivity of dipole antenna and human head model, respectively. Also, ϵ_{metal} and $\epsilon_{\text{tissue}}(\omega_1)$ are the permittivity of dipole antenna and a human head model, respectively. Additionally, the ω is presented as the dispersive medium, which is the value of ϵ , μ and σ are depend on frequency. The infinitesimal dipole represents a mobile phone and an antenna is operated at 900 MHz and 1.8 GHz. It is located at the 1 cm from a human head model. In this case, the PML acts as an electromagnetics fields absorbing boundary layer and is backed by a perfect electric conductor.

Sir Peter Mansfield is a British physicist who was awarded the 2003 Nobel Prize in Physiology or Medicine for his discoveries concerning Magnetic Resonance Imaging (MRI). The Nobel Prize was shared with Paul Lauterbur who also contributed to the development of MRI. By using electromagnetic machine, the scanning technique can detect the medical diagnosis in human body like Pancreas and Bile Duct. Now, almost all the scanning methods have been replaced by MRI. It is very useful for medical diagnosis, especially unusual function of human brain and Spinal Cord, for

example. The principle of MRI scanner can offer more accurate of liquid solution classification. In addition, it can offer 1 % in different.

In brief, the principle method of MRI is when protons constituting in human head associate with in the magnetic field, it can absorb and generate electromagnetic wave. Amount of generating energy will be varied depend on amount of proton in each cell. However, the signal intensity generated depends on the cell properties. This research will be shown by the figure of MRI to create the human head model. By using a Gray scale method, we can classify the different cells as the following picture

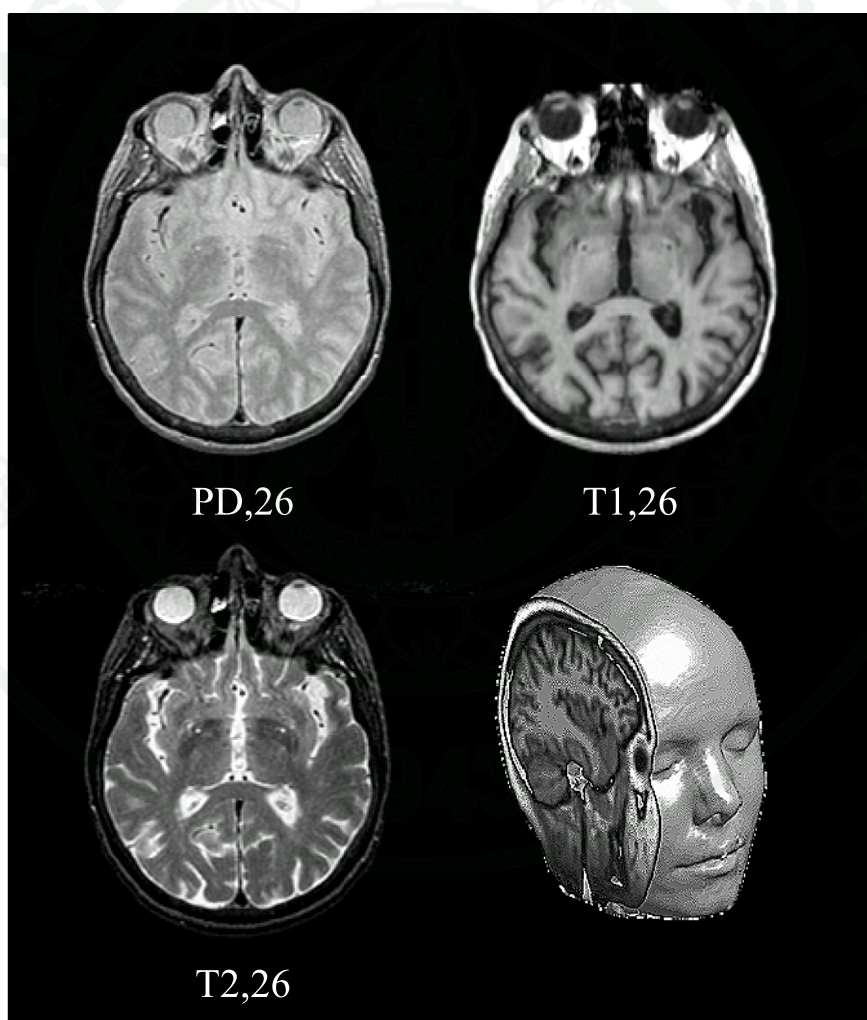


Figure 92 MRI Images of PD, T1 and T2 at layer 26th.

Source: Keith and Becker (2010)



Figure 93 MRI machine.

There are three types of MRI images: PD, T1 and T2. First, PD images represent for Skull, Muscle and Skin. Second, T1 images represent for Brain and Fat. Third, T2 images represent for Blood and Eye. This research uses Gray scale from 0-255 in order to extract each type of cells from PD, T1 and T2 images—PD = Skull, Muscle and Skin, T1 = Brain and Fat, T2 = Blood and Eye, (Yahya, 2010).

Table 14 The relation between Gray scale and types of cell in human head.

Material	Gray Level
Air	0 - 59
Skin	60 - 89
Bone	90 - 109
Muscle	110 - 129
Fat	130 - 159
Brain	160 - 199
Eye	200 - 219
Blood	220 - 255

Source: Yahya (2010)

This research uses total amount of MRI 159 images from 3 sets of PD, T1 and T2 for 53 images each to model the human head with 53 layers in different. For example in layer 30th, these can find out the cells of Skull, Muscle and Skin in figure PD images, in the same layer, it can find out the cells of Brain and Fat from T1 images, and the cells of Blood and Eye from T2 images. After all the cells are located, these specified positions can be created a layer 30th of a model. The sum of 53 layers will produce the complete model as a human head. If the cell's dimension is given for 0.005 cm, then the size of human head will be 21x22x26.5 cm³ in approximate.



Figure 94 Artificial human head cross-section at layer 26th created by computer.

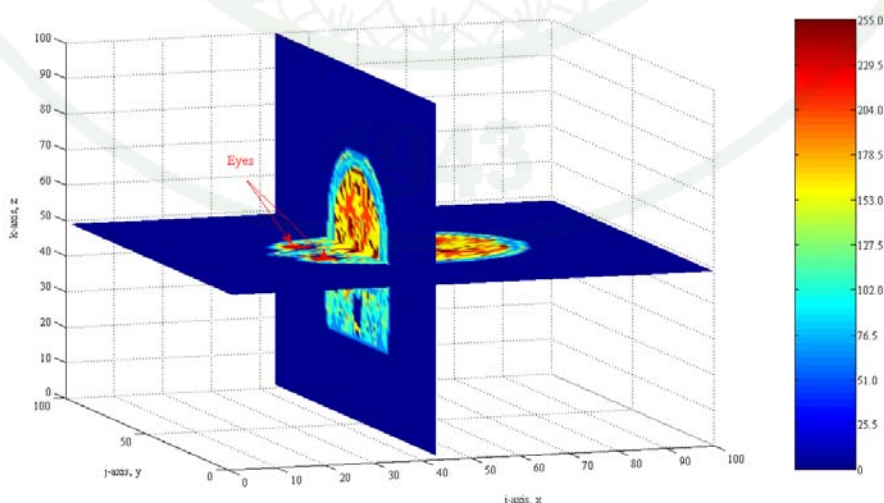


Figure 95 Artificial human head side view created by computer.

Value of electromagnetic parameter in human head will vary with the operating center frequency. Equation (170), the Gaussian's signal in time domain must have the large width so that it can generate the narrow bandwidth around the center frequency (f_c). Consequently, this will lead to the acceptable constant values of relative permittivity (ϵ_r) and conductivity of each tissue in human head (σ_{tissue}). These can be applied to the generalized Maxwell's equations. Also, the simulation time for this computational model should be greater enough in order to reach the steady state.

Table 15 Electromagnetic parameter values in human head for 900 MHz (f_c).

Material	ϵ_r	ρ (kg / m^3)	σ (S/m)
Air	1	1	0
Skin	35	1100	0.60
Bone	8	1850	0.11
Muscle	58	1040	1.21
Fat	9.99	920	0.17
Brain	49	1030	1.10
Eye	73	1010	1.97
Blood	64	1060	1.24

Source: Gandhi (1996)

The following formula for find mass of each cell used in the simulation

$$m = \rho V, V = \Delta x \times \Delta y \times \Delta z \text{ m}^3 \quad (176)$$

Table 16 Electromagnetic parameter values in human head for 1.8 GHz (f_c).

Material	ϵ_r	ρ (kg/m^3)	σ (S/m)
Air	1	1	0
Skin	35	1100	0.60
Bone	8	1850	0.11
Muscle	58	1040	1.21
Fat	9.99	920	0.17
Brain	49	1030	1.10
Eye	73	1010	1.97
Blood	64	1060	1.24

Source: Gandhi (1996)

Previously, it is assumed that the medium within primary grid is homogeneous. However, we shall now consider the inhomogeneous medium case. Boundary condition for the concatenate cell of dielectric is necessary for the continuity of the tangential \bar{E} and \bar{H} fields in the direction of dielectric surface (dielectric-dielectric interface). This research assumes the model is non-magnetic $\mu(x, y, z) = \mu_0$ since the element of electromagnetic field is always in the horizontal direction. In addition, the primary edge passing through the centroid of the face is tangential to the interface of a boundary layer shared by the four dielectric materials: $(\sigma_{\text{tissue},1}(\omega), \epsilon_{\text{tissue},1}(\omega))$, $(\sigma_{\text{tissue},2}(\omega), \epsilon_{\text{tissue},2}(\omega))$, $(\sigma_{\text{tissue},3}(\omega), \epsilon_{\text{tissue},3}(\omega))$ and $(\sigma_{\text{tissue},4}(\omega), \epsilon_{\text{tissue},4}(\omega))$. The generalized Maxwell's equations should be slightly updated. For example, E_x is surrounded by four adjacent cells with different permittivity and conductivity. The face is defined as the surface S bound by the contour C .

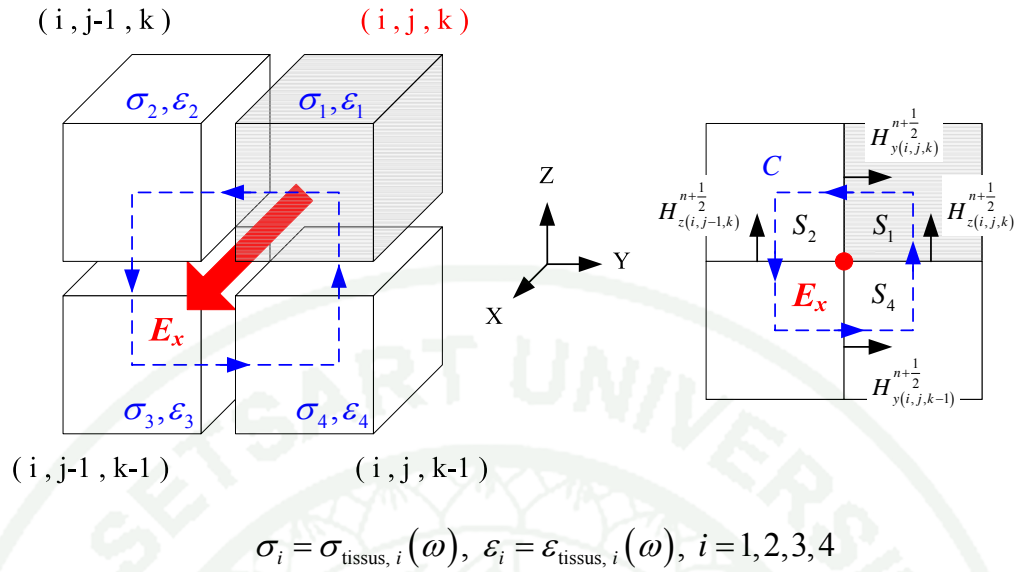


Figure 96 Cell surface with inhomogeneous medium.

Ampere's law must be valid over this surface. However, as stated, the conductivity and permittivity of the face are ambiguous as referenced to the electric field passing through its centroid. Subsequently, this surface is decomposed into four distinct surfaces. Therefore, Ampere's law plus Maxwell's displacement current is expressed as (Taflove, 1995; Lee, 2003)

$$\sum_{i=1}^4 \left(\oint_C \bar{H} \cdot d\bar{l} \right) = \sum_{i=1}^4 \left(\frac{\partial}{\partial t} \iint_{S_i} \epsilon_i \bar{E} \cdot d\bar{s} + \iint_{S_i} \sigma_i \bar{E} \cdot d\bar{s} \right) \quad (177)$$

$$\begin{aligned} \oint_C \bar{H} \cdot d\bar{l} &= \oint_{S_1} \bar{H} \cdot d\bar{l} + \oint_{S_2} \bar{H} \cdot d\bar{l} + \oint_{S_3} \bar{H} \cdot d\bar{l} + \oint_{S_4} \bar{H} \cdot d\bar{l} \\ &= \iint_{S_1} \left(\epsilon_1 \frac{\partial \bar{E}}{\partial t} + \sigma_1 \bar{E} \right) \cdot d\bar{s} + \iint_{S_2} \left(\epsilon_2 \frac{\partial \bar{E}}{\partial t} + \sigma_2 \bar{E} \right) \cdot d\bar{s} \\ &\quad + \iint_{S_3} \left(\epsilon_3 \frac{\partial \bar{E}}{\partial t} + \sigma_3 \bar{E} \right) \cdot d\bar{s} + \iint_{S_4} \left(\epsilon_4 \frac{\partial \bar{E}}{\partial t} + \sigma_4 \bar{E} \right) \cdot d\bar{s} \end{aligned}$$

Using central difference algorithm as well as Equation (106) and Equation (107), this equation can be approximated as

$$\begin{aligned}
& - \left(H_{y(i,j,k)}^{n+\frac{1}{2}} - H_{y(i,j,k-1)}^{n+\frac{1}{2}} \right) \Delta y + \left(H_{z(i,j,k)}^{n+\frac{1}{2}} - H_{z(i,j-1,k)}^{n+\frac{1}{2}} \right) \Delta z = \\
& \left(\sigma_1 \frac{E_{x(i,j,k)}^{n+1} + E_{x(i,j,k)}^n}{2} + \varepsilon_1 \frac{E_{x(i,j,k)}^{n+1} - E_{x(i,j,k)}^n}{\Delta t} \right) \frac{\Delta y \Delta z}{4} \\
& + \left(\sigma_2 \frac{E_{x(i,j,k)}^{n+1} + E_{x(i,j,k)}^n}{2} + \varepsilon_2 \frac{E_{x(i,j,k)}^{n+1} - E_{x(i,j,k)}^n}{\Delta t} \right) \frac{\Delta y \Delta z}{4} \\
& + \left(\sigma_3 \frac{E_{x(i,j,k)}^{n+1} + E_{x(i,j,k)}^n}{2} + \varepsilon_3 \frac{E_{x(i,j,k)}^{n+1} - E_{x(i,j,k)}^n}{\Delta t} \right) \frac{\Delta y \Delta z}{4} \\
& + \left(\sigma_4 \frac{E_{x(i,j,k)}^{n+1} + E_{x(i,j,k)}^n}{2} + \varepsilon_4 \frac{E_{x(i,j,k)}^{n+1} - E_{x(i,j,k)}^n}{\Delta t} \right) \frac{\Delta y \Delta z}{4}
\end{aligned}$$

When rearranging the terms, the generalized Maxwell's equations for E_x is

$$E_{x(i,j,k)}^{n+1} = \left(\frac{1 - \frac{\sigma' \Delta t}{2\varepsilon'}}{1 + \frac{\sigma' \Delta t}{2\varepsilon'}} \right) E_{x(i,j,k)}^n + \frac{\Delta t}{1 + \frac{\sigma' \Delta t}{2\varepsilon'}} \left(\frac{H_{z(i,j,k)}^{n+\frac{1}{2}} - H_{z(i,j-1,k)}^{n+\frac{1}{2}}}{\Delta y} - \frac{H_{y(i,j,k)}^{n+\frac{1}{2}} - H_{y(i,j,k-1)}^{n+\frac{1}{2}}}{\Delta z} \right) \quad (178)$$

$$\varepsilon' = \frac{\varepsilon_1 + \varepsilon_2 + \varepsilon_3 + \varepsilon_4}{4}, \quad \sigma' = \frac{\sigma_1 + \sigma_2 + \sigma_3 + \sigma_4}{4} \quad (179)$$

By taking the permittivity and the conductivity as the average of four adjacent cubes surrounding the E field component, it automatically guarantees the continuity of the tangential E_x field component. Similarly, this procedure is applied to E_y and E_z .

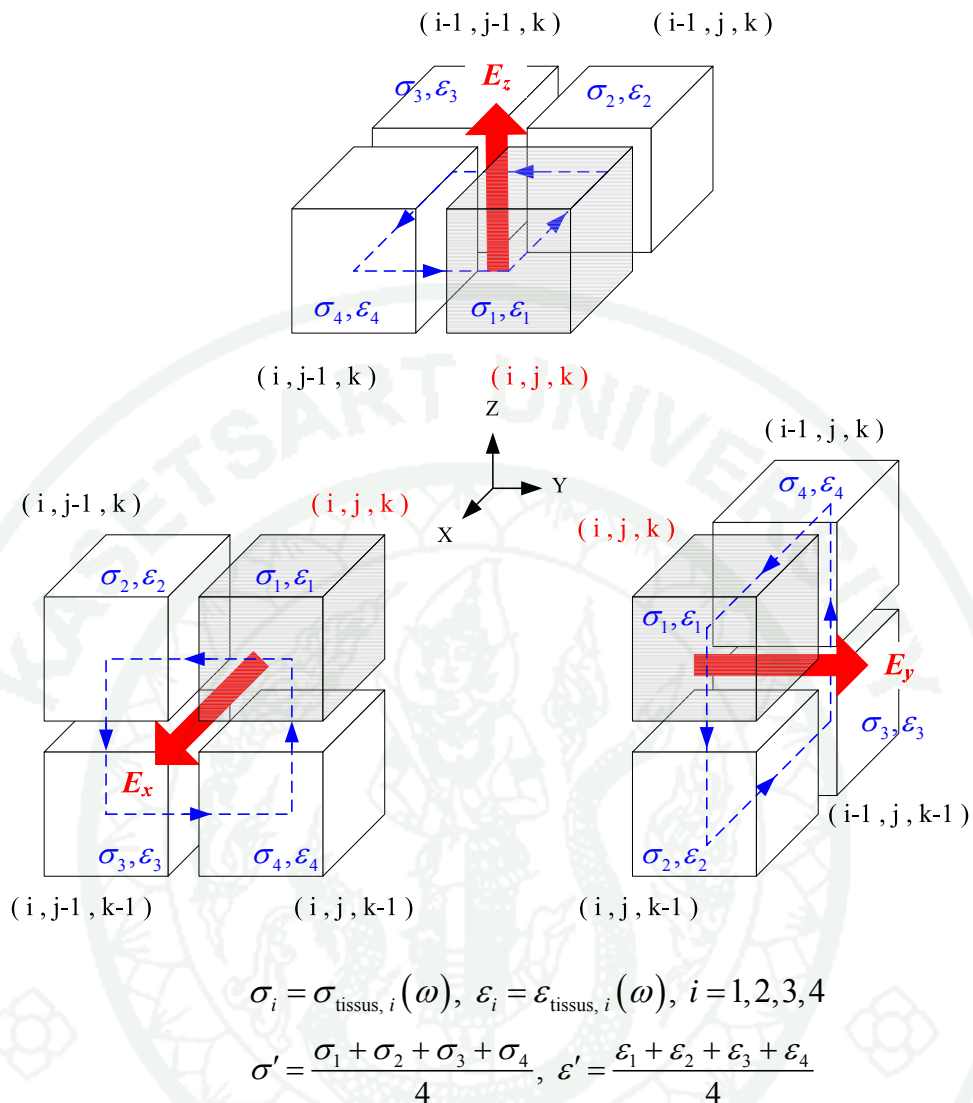


Figure 97 E_x, E_y and E_z field components.

Engineering research on the subject of wireless phones and radio frequency (RF) energy has been conducted worldwide for many years. The Federal Communications Commission (FCC) established RF exposure safety guidelines for wireless phones (Federal Communications Commission [FCC], 1998). Before a wireless phone model is available for sale to the public, it must be tested by the manufacturer and certified by the FCC that it does not exceed limits established by the FCC. One of these limits is expressed as a Specific Absorption Rate (SAR). In 1996, the FCC adopted updated guidelines for evaluating human exposure to radio frequency fields from fixed transmitting antennas such as those used for a mobile phone. Also,

the new guidelines for a mobile phone are identical to those recommended by the National Council on Radiation Protection and Measurements (NCRP). Furthermore, these guidelines are also similar to the 1992 guidelines recommended by the American National Standards Institute/Institute of Electrical and Electronics Engineers (ANSI/IEEE). In general, IEEE standard required that the SAR 1-g of handheld wireless phones not exceed 1.6 watts/kg, averaged over 1-g mass of tissues (The Institute of Electrical and Electronics Engineers [IEEE], 2003). Although the SAR 1-g is determined at the highest power level, the actual SAR 1-g value while operating depends on factors such as the proximity of the antenna to the human head while in use.

IEEE (IEEE, 2002) provides the definition of SAR as the time derivative (rate) of the incremental energy (dW) absorbed by (dissipated in) an incremental mass (dm) contained in a volume element (dV) of a given density ($d\rho$).

$$\text{SAR} = \frac{d}{dt} \left(\frac{dW}{dm} \right) = \frac{d}{dt} \left(\frac{dW}{\rho dV} \right) \quad (180)$$

SAR is expressed in units of watts per kilogram (W/kg). Also, SAR can be related to the electric field at a point by

$$\text{SAR}(t) = \sigma \frac{|E|^2}{\rho} \quad (181)$$

σ = Conductivity of the tissue (S/m).

ρ = Mass density of the tissue (kg/m^3).

E = Root Mean Square (RMS) electric field strength (V/m).

Also, IEEE (IEEE, 2002) provides the definition of the spatial-average SAR as the maximum local SAR averaged over a specified volume or mass, e.g., any 1-g or 10-g mass of tissue in the shape of a cube. SAR_{avg} or SAR is expressed in units of watts per kilogram (W/kg)

Value of SAR 1-g can be obtained from Equation (181), averaged over the period ($T = t_2 - t_1$), with condition that concatenate cells must be 1 g in cumulative weight and value should be obtained from several cells. This research proposed the method to compute 1 g mass of tissues by the following figure

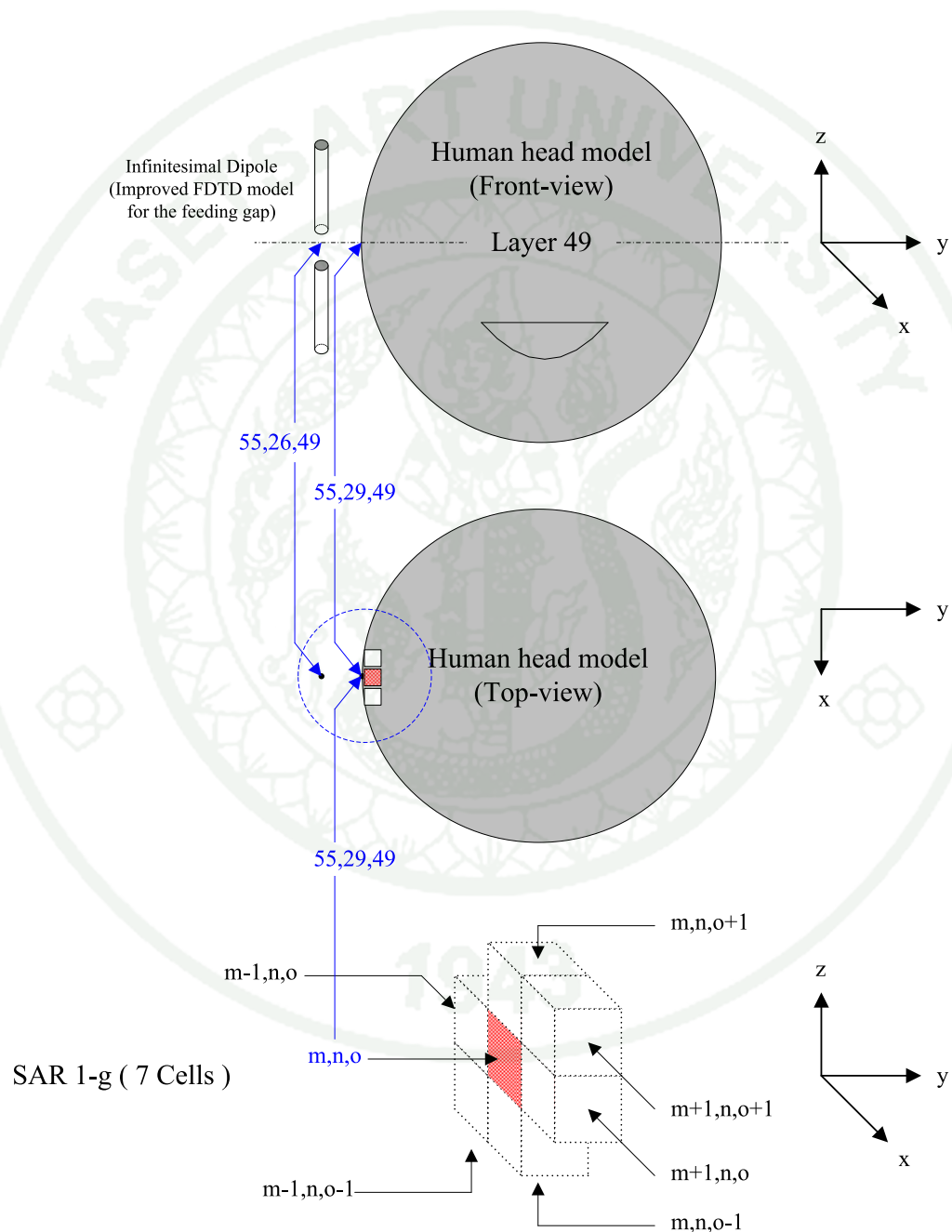


Figure 98 Sample figure of the spatial-average SAR 1-g, located at the position closed to dipole feeding gap.

Also, value of SAR 10-g can be obtained from Equation (181), averaged over the period ($T = t_2 - t_1$), with condition that concatenate cells must be 10 g in cumulative weight and value should be obtained from several cells. This research proposed the method to compute 10 g mass of tissues by the following figure

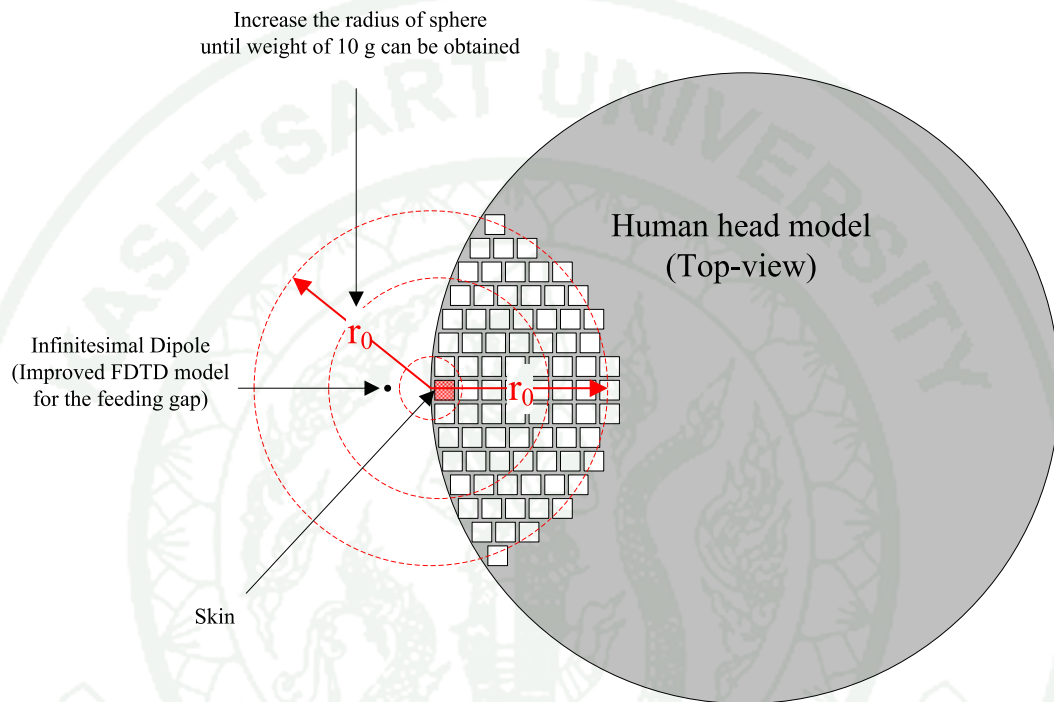


Figure 99 Sample figure of the spatial-average SAR 10-g, located at the position closed to dipole feeding gap.

This research compared the total energy absorbed by human head between using a mobile phone operated at 900 MHz and 1.8 GHz. Additionally, total energy absorbed into the model of human head is expressed in units of watts (W). It can be calculated from the following equation

$$P(t) = \int_V \sigma |E|^2 dV \quad (182)$$

σ = Conductivity of the tissue (S/m).

E = Root Mean Square (RMS) of electric field strength (V/m).

The average power absorbed by any material (P_{avg}) can be expressed as

$$P_{\text{avg}} = \frac{1}{T} \left(\int_{t_1}^{t_2} P(t) dt \right), T = t_2 - t_1 \quad (183)$$

Subsequently, the next SAR: $\text{SAR}_{\text{Cell-1}}$ 1-g, $\text{SAR}_{\text{Cell-2}}$ 1-g and so on, were calculated as well as the SAR 1-g in Equation (181), however, only the specific positions in human head is changed from one side to the other side: (m,n,o) , $(m,n+1,o)$, $(m,n+2,o)$, ..., (m,j,o) .

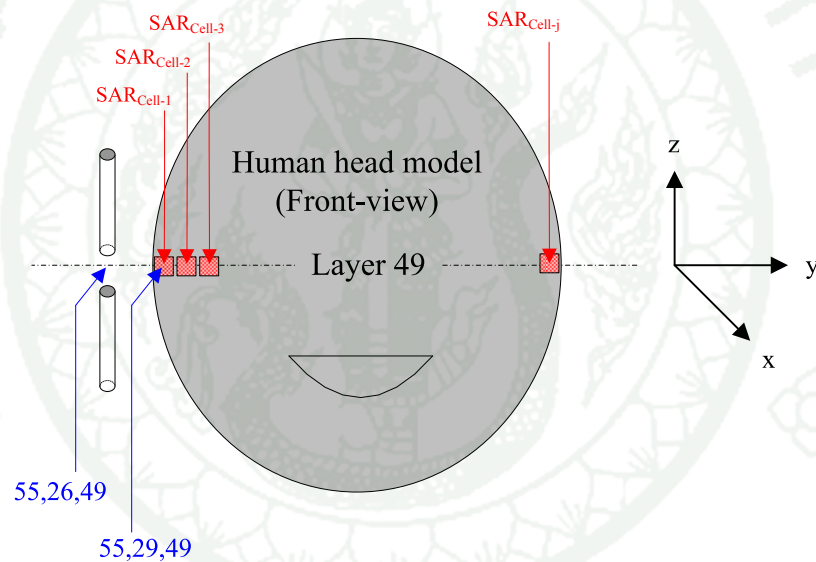


Figure 100 Sample figure of the spatial-average $\text{SAR}_{\text{Cell-1}}$ 1-g, $\text{SAR}_{\text{Cell-2}}$ 1-g, and so on located by the incremental n.

By the reference model, this research had simulated the SAR_{Cell-1} 1-g to SAR_{Cell-j} 1-g between a mobile phone operated at 900 MHz and 1.8 GHz. It was computed from a position deepened in human head from the surface, a skin. Additionally, the dipole is fixed at 1 cm from the human surface. The results were normalized by SAR_{Cell-1} 1-g at center frequency.

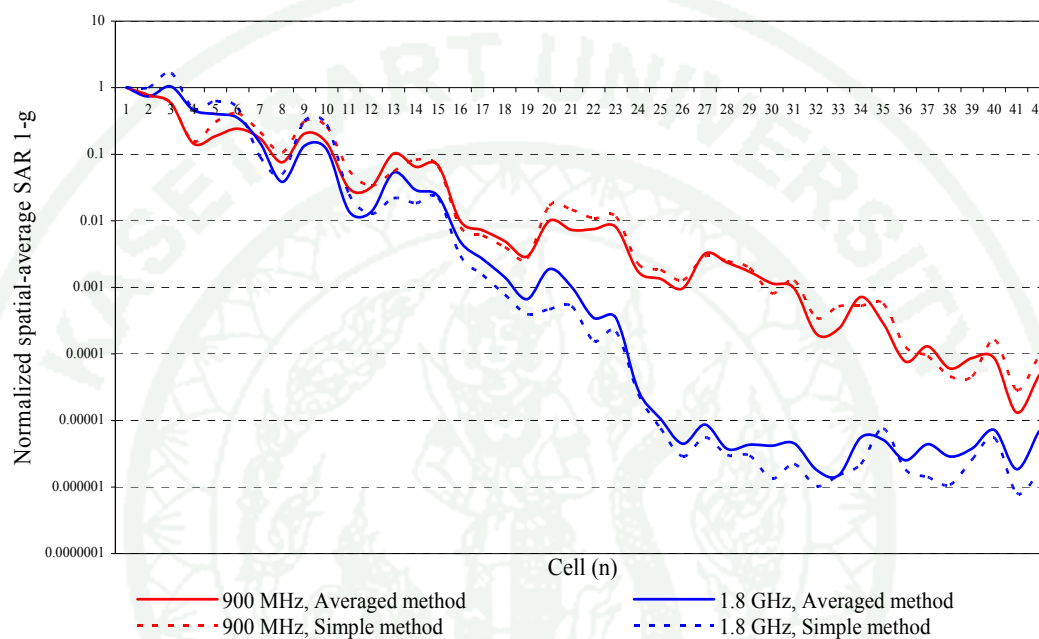


Figure 101 The comparison graph of the normalized spatial-average $SAR_{Cell\ n}$ 1-g at various distances in a human head between the method of using averaged dielectric constant in a human head and the simple method.

Source: Jariyanorawiss (2004); Jariyanorawiss and Homsup (2005a)

From Figure 101, the result of experiment shows that the normalized spatial-average $SAR_{Cell\ n}$ 1-g with the method of using averaged dielectric constant in a human head give the value lower than the simple method for $n = 1$ to 12 at both frequencies (Jariyanorawiss, 2004).

Table 17 The comparison table of the spatial-average SAR_{Cell-1} 1-g, SAR_{Cell-2} 1-g and SAR_{Cell-3} 1-g in the reference model.

Cell (n)	The spatial-average SAR 1-g (W/kg)	
	900 MHz	1.8 GHz
1	1.44307	1.28455
2	1.12532	0.92336
3	0.84079	1.15199

Source: Jariyanorawiss (2004)

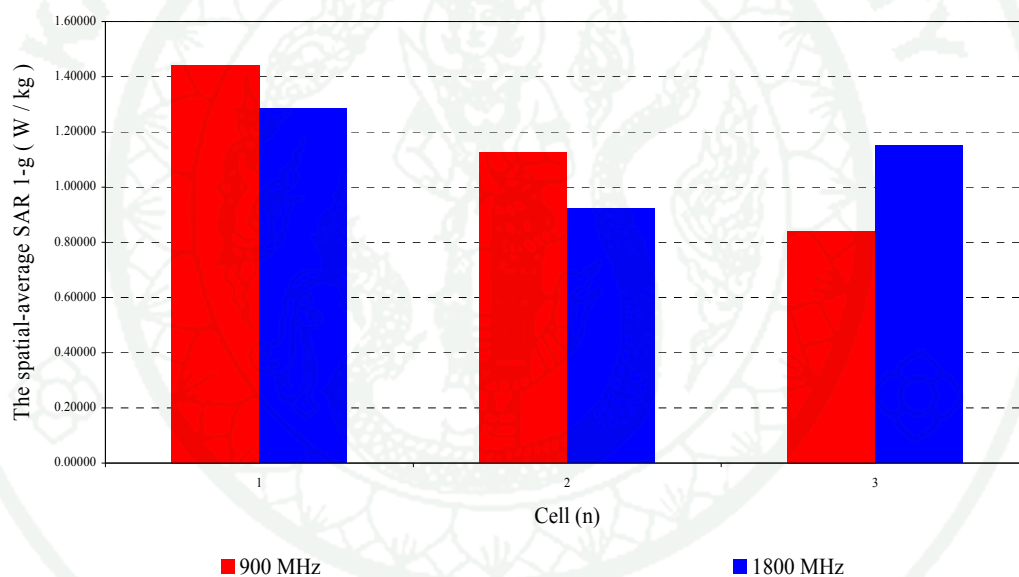


Figure 102 The comparison bar of the spatial-average SAR_{Cell-1} 1-g, SAR_{Cell-2} 1-g and SAR_{Cell-3} 1-g in the reference model.

Source: Jariyanorawiss (2004)

Table 18 The comparison table of the spatial-average SAR_{Cell-1} 1-g, SAR_{Cell-1} 10-g, and the average power absorbed by a human head in the reference model.

Frequency	The spatial-average SAR 1-g in cell 1 (W/kg)	The spatial-average SAR 10-g in cell 1 (W/kg)	The average power absorbed by a human head (Watts)
900 MHz	1.44307	1.30634	0.21486
1.8 GHz	1.28455	1.17044	0.11773

Source: Jariyanorawiss (2004)

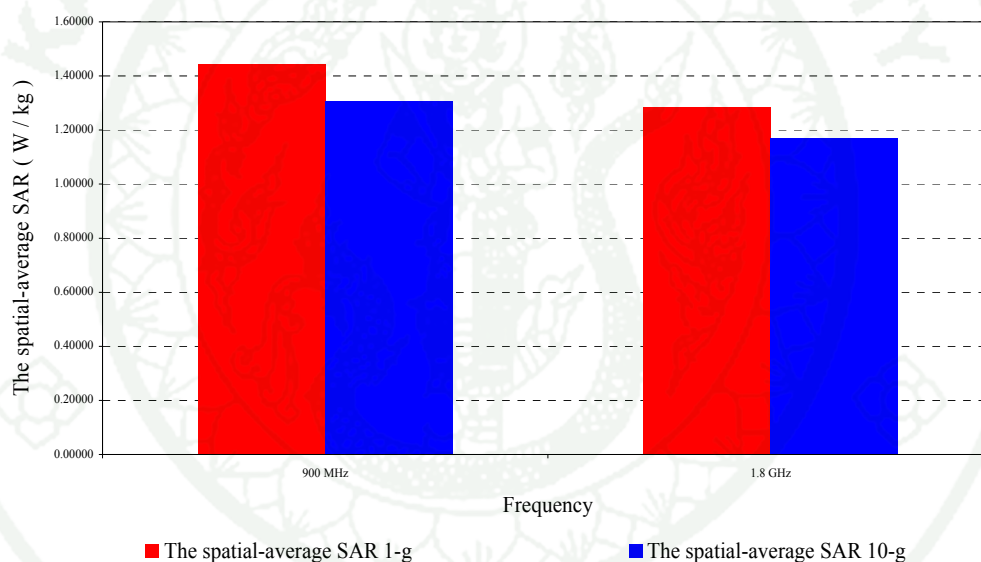


Figure 103 The comparison bar of the spatial-average SAR_{Cell-1} 1-g and SAR_{Cell-1} 10-g between 900 MHz and 1.8 GHz in the reference model.

From Table 18, the simulation result shows that the mobile phone operated at 900 MHz give the three values: SAR 1-g, SAR 10-g and P_{avg} , higher than the mobile phone operated at 1.8 GHz. However, SAR 1-g is lower than the standard from IEEE (IEEE, 2003): 1.6 W/kg, at both frequencies. In addition, SAR 1-g calculated from weight of 1 g and SAR 10-g calculated from weight of 10.088 g (Jariyanorawiss, 2004).

Table 19 The comparison table of the average power absorbed by any material in a human head between 900 MHz and 1.8 GHz in the reference model.

Material	The average power absorbed by any material in a human head (Watts)	
	900 MHz	1.8 GHz
Skin	0.10554	0.05307
Bone	0.01128	0.00638
Muscle	0.03020	0.02013
Fat	0.02236	0.01317
Eyes	0.0000375	0.0000059
Brain	0.02541	0.01252
Blood	0.02189	0.01267
Total	0.21486	0.11773

Source: Jariyanorawiss (2004)

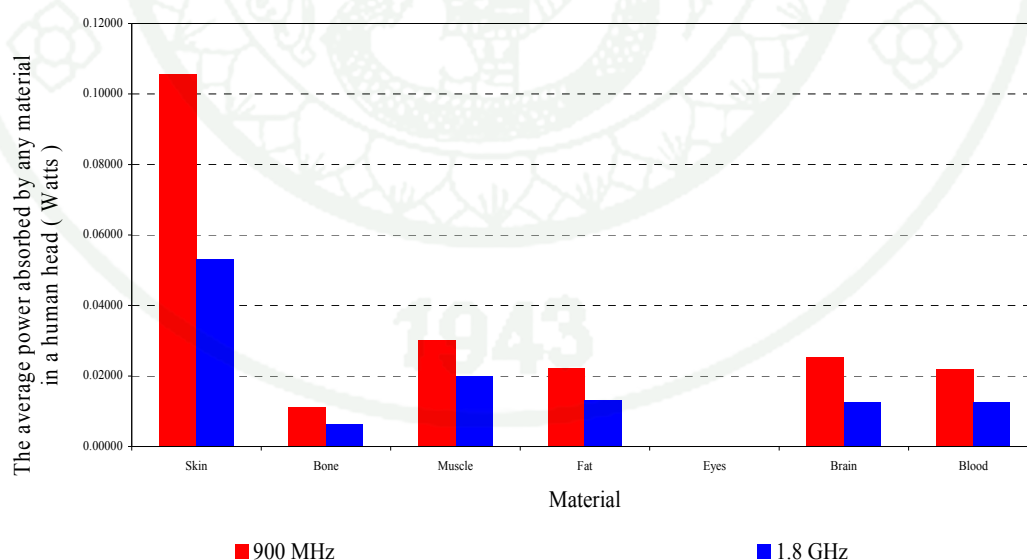


Figure 104 The comparison bar of the average power absorbed by any material in a human head between 900 MHz and 1.8 GHz in the reference model.

From Table 19, the simulation results show that the mobile phone operated at 900 MHz (0.6 W) gives the averaged power absorbed by seven materials in a human head: Skin, Bone, Muscle, Fat, Eyes, Brain and Blood, higher than the mobile phone operated at 1.8 GHz (0.6 W). It should be interesting noted that the skin is the best absorber. It can absorb 106 mW and 53 mW for operating frequency 900 MHz and 1.8 GHz, respectively. Apparently, the human brain can absorb power about 10 % at two frequencies, $f_{900 \text{ MHz}} = \frac{0.025}{0.215} \times 100\%$ and $f_{1.8 \text{ GHz}} = \frac{0.013}{0.118} \times 100\%$. In conclusion, the total average power absorbed by a human head is about 215 mW (900 MHz) and 118 mW (1.8 GHz) (Jariyanorawiss, 2004).

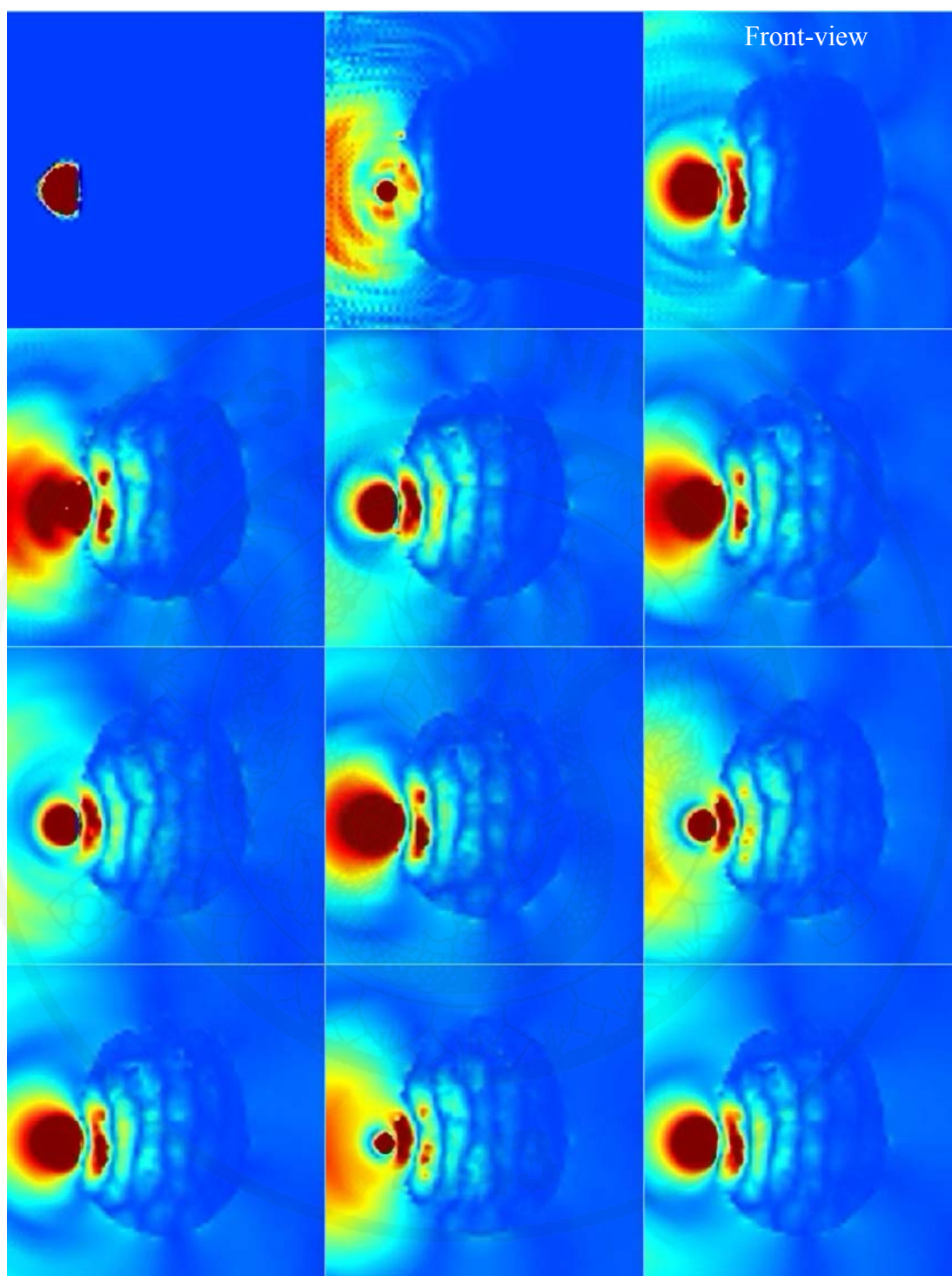


Figure 105 The simulation of a mobile phone located at 1 cm from a human head and a mobile phone operated at 900 MHz (the reference model). The simulation start from 0 and end with $1000\Delta t$.

Source: Jariyanorawiss (2004)

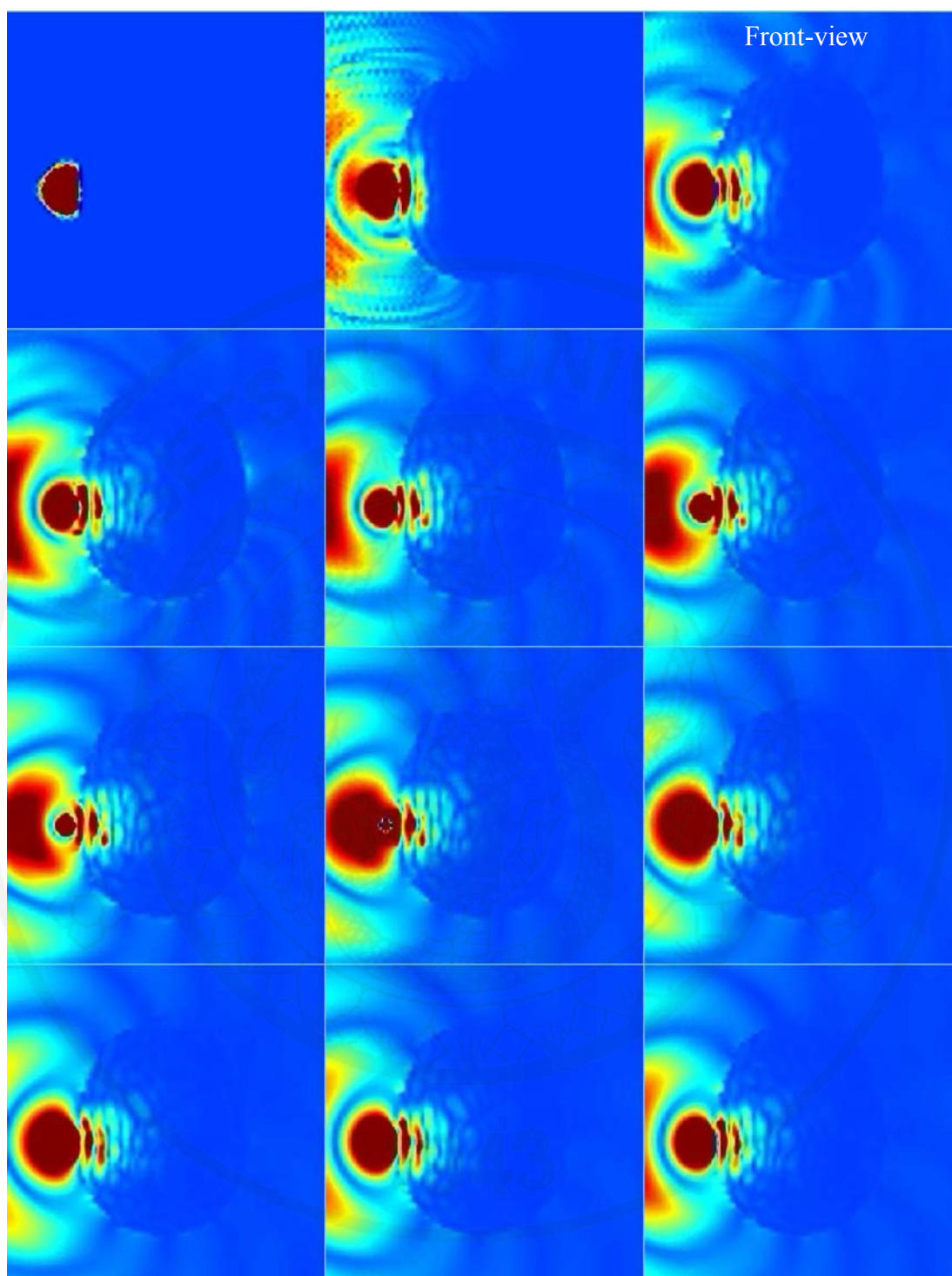


Figure 106 The simulation of a mobile phone located at 1 cm from a human head and a mobile phone operated at 1.8 GHz (the reference model). The simulation start from 0 and end with $1000\Delta t$.

Source: Jariyanorawiss (2004)

Both Figure 105 and Figure 106 show (E_{Total}), total electric field intensity, plot for a mobile phone located at 1 cm from a human head and a mobile phone operated at 900 MHz and 1.8 GHz, respectively. In general, the total electric field intensity (E_{Total}) can be computed from the following equation (Homsup *et al.*, 2009a)

$$E_t(t) = \sqrt{E_x^2(i, j, k, t) + E_y^2(i, j, k, t) + E_z^2(i, j, k, t)} \quad (184)$$

$E_t(t) = E_{\text{Total}}$, The instantaneous electromagnetic field intensity (V / m).

In addition, the update method of the dipole feeding gap using in this research is the hard source assigning a desired time function to specific electric of magnetic field components in the FDTD grid. On the other hand, the soft source allows a new value of the electric field at the source location to equal the update value plus the value of an impressed electric field described by the time function (Stutzman and Thiele, 1998).

MATERIALS AND METHODS

Materials

1. Personal computer with an operating system.
2. Computer programming, for example, MATLAB, Scilab, C, C++ or Java.

Methods

1. How to Verify the Electromagnetic Simulation Software in Time Domain

This research proposes the new methodology for applied subcell method to the generalized Maxwell's equations in the feeding gap models of a dipole antenna (Appendix Figure A3). Also, its results can verify the FDTD programming.

1.1 The one-cell gap model

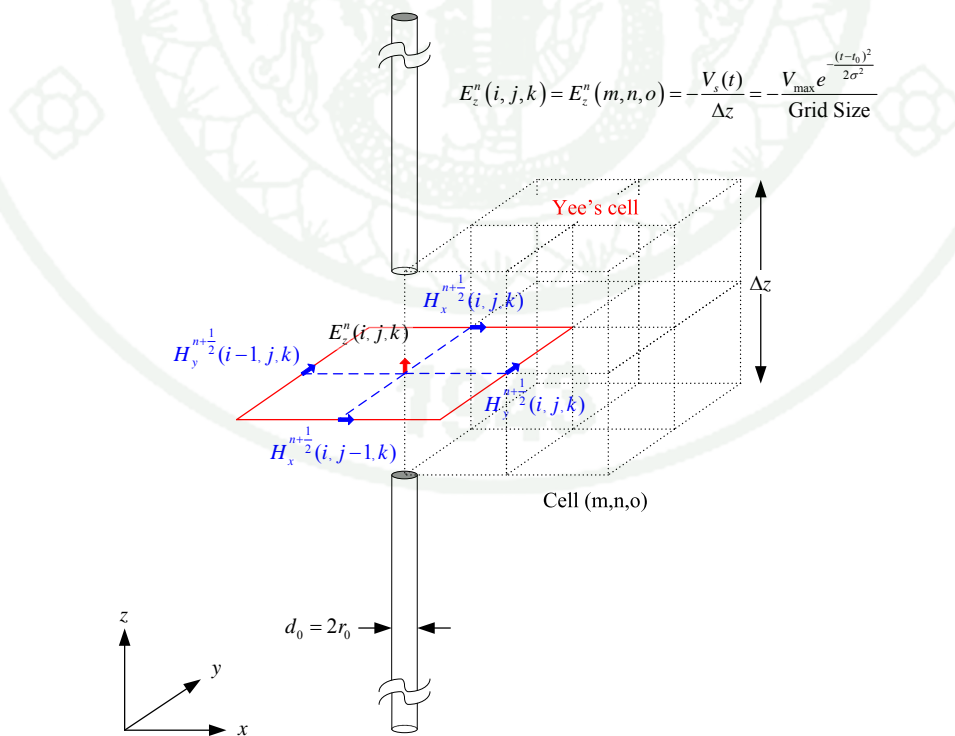


Figure 107 The quaternary H - field around the one-cell gap model.

The one-cell gap model

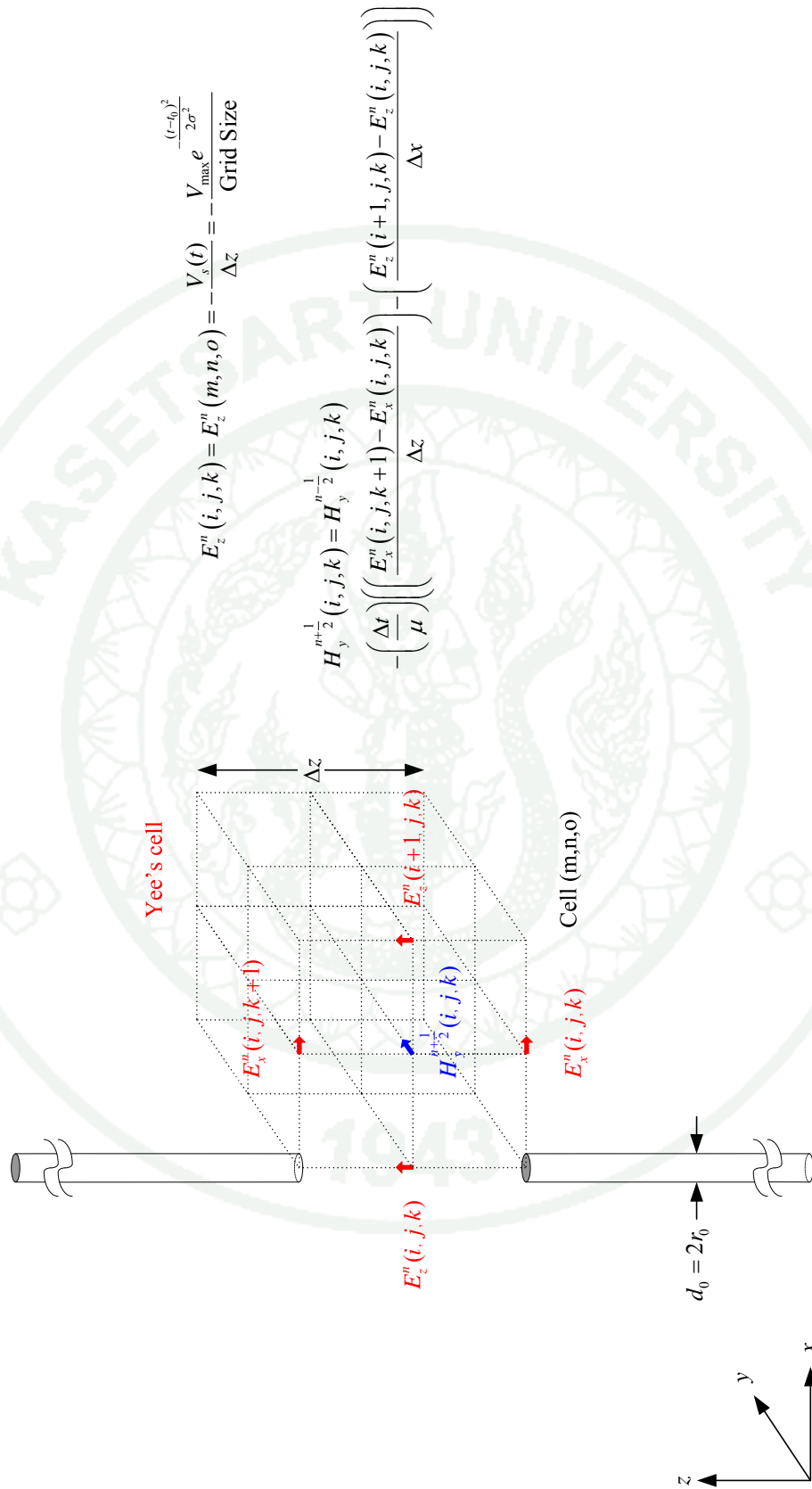


Figure 108 Guideline for the formulation of the one-cell gap model.

1.2 The electromagnetic field along z-axis

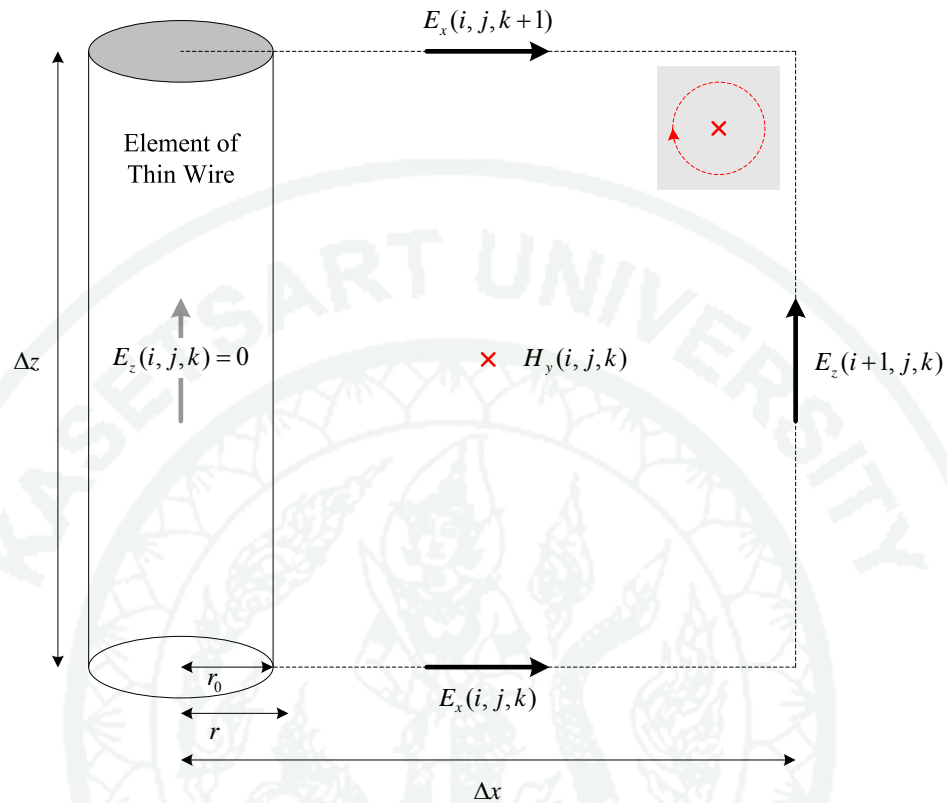


Figure 109 Field locations and geometry for thin wire.

Source: Kunz and Luebbers (1993)

$$H_y(r, j, k) \approx H_y(i, j, k) \left(\frac{\Delta x}{2} \right) \left(\frac{1}{r} \right), \quad E_x(r, j, k) \approx E_x(i, j, k) \left(\frac{\Delta x}{2} \right) \left(\frac{1}{r} \right)$$

Apply the Faraday's law of magnetic induction $\oint_c \bar{E} \cdot d\bar{l} = -\mu \frac{\partial}{\partial t} \iint_s \bar{H} \cdot d\bar{S}$

$$-\mu \frac{\partial}{\partial t} \int_{r_0}^{\Delta x} H_y(r, j, k) dr \Delta z = 0 - E_z^n(i+1, j, k) \Delta z$$

$$+ \int_{r_0}^{\Delta x} E_x^n(r, j, k+1) dr - \int_{r_0}^{\Delta x} E_x^n(r, j, k) dr$$

$$\begin{aligned}
& -\mu\Delta z \frac{\partial}{\partial t} \int_{r_0}^{\Delta x} H_y(i, j, k) \left(\frac{\Delta x}{2}\right) \left(\frac{1}{r}\right) dr = -\Delta z E_z^n(i+1, j, k) \\
& \quad + \left(\int_{r_0}^{\Delta x} E_x^n(i, j, k+1) \left(\frac{\Delta x}{2}\right) \left(\frac{1}{r}\right) dr - \int_{r_0}^{\Delta x} E_x^n(i, j, k) \left(\frac{\Delta x}{2}\right) \left(\frac{1}{r}\right) dr \right) \\
& -\mu\Delta z \left(\frac{\Delta x}{2} \ln r \Big|_{r_0}^{\Delta x}\right) \frac{\partial}{\partial t} H_y(i, j, k) = -\Delta z E_z^n(i+1, j, k) \\
& \quad + \left(E_x^n(i, j, k+1) \left(\frac{\Delta x}{2} \ln r \Big|_{r_0}^{\Delta x}\right) - E_x^n(i, j, k) \left(\frac{\Delta x}{2} \ln r \Big|_{r_0}^{\Delta x}\right) \right) \\
& \frac{\partial}{\partial t} H_y(i, j, k) = \frac{1}{\mu \left(\frac{\Delta x}{2} \ln r \Big|_{r_0}^{\Delta x}\right)} E_z^n(i+1, j, k) \\
& \quad - \frac{1}{\mu\Delta z} (E_x^n(i, j, k+1) - E_x^n(i, j, k)) \\
& \frac{H_y^{n+\frac{1}{2}}(i, j, k) - H_y^{n-\frac{1}{2}}(i, j, k)}{\Delta t} = \left(\frac{1}{\mu}\right) \left(\frac{2}{\ln\left(\frac{\Delta x}{r_0}\right)}\right) \left(\frac{E_z^n(i+1, j, k)}{\Delta x}\right) \\
& \quad - \left(\frac{1}{\mu}\right) \left(\frac{E_x^n(i, j, k+1) - E_x^n(i, j, k)}{\Delta z}\right) \\
& \frac{H_y^{n+\frac{1}{2}}(i, j, k) - H_y^{n-\frac{1}{2}}(i, j, k)}{\Delta t} = \\
& \quad - \left(\frac{1}{\mu}\right) \left(\frac{E_x^n(i, j, k+1) - E_x^n(i, j, k)}{\Delta z}\right) - \left(\frac{2}{\ln\left(\frac{\Delta x}{r_0}\right)}\right) \left(\frac{E_z^n(i+1, j, k)}{\Delta x}\right) \\
& H_y^{n+\frac{1}{2}}(i, j, k) = H_y^{n-\frac{1}{2}}(i, j, k) \\
& \quad - \left(\frac{\Delta t}{\mu}\right) \left(\frac{E_x^n(i, j, k+1) - E_x^n(i, j, k)}{\Delta z}\right) - \left(\frac{2}{\ln\left(\frac{\Delta x}{r_0}\right)}\right) \left(\frac{E_z^n(i+1, j, k)}{\Delta x}\right) \quad (185)
\end{aligned}$$

1.3 The improved one-cell gap model

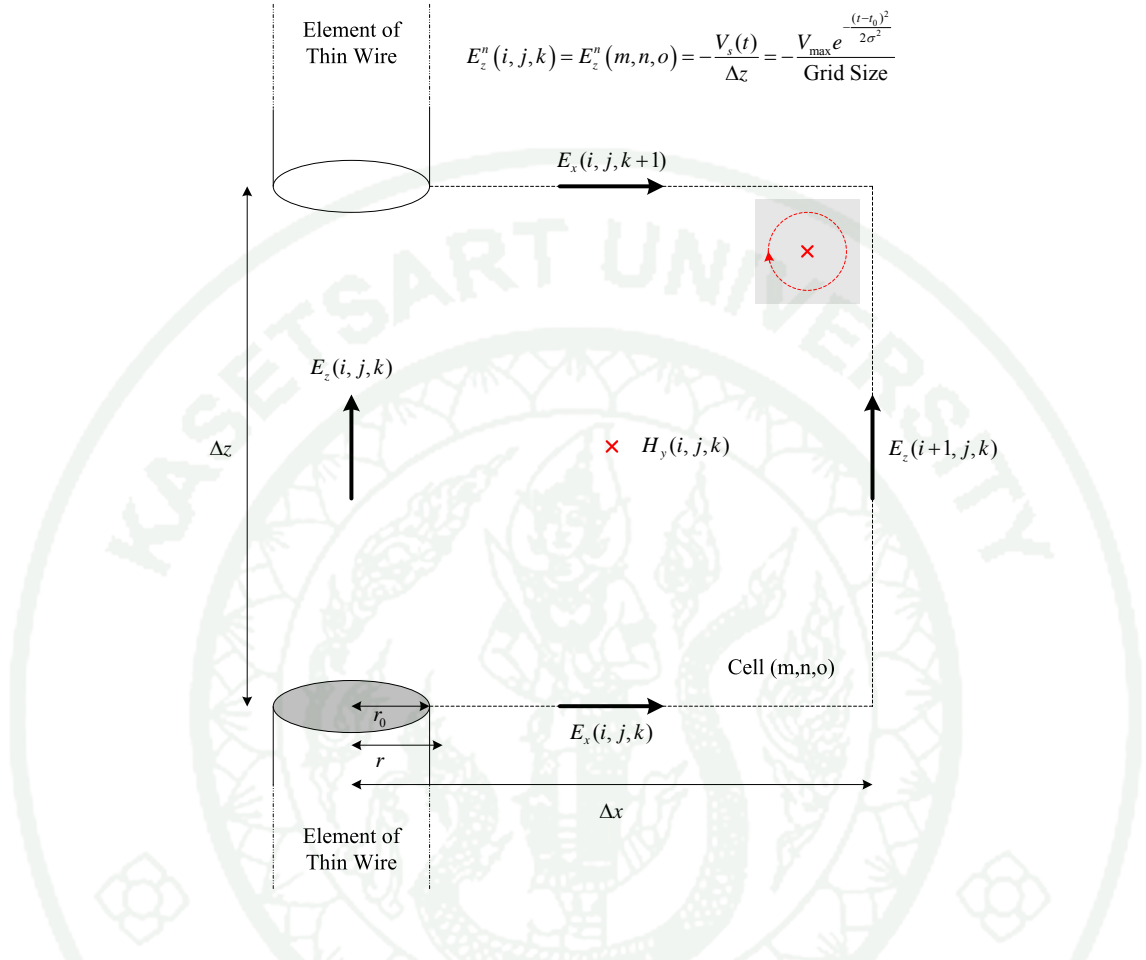


Figure 110 Field locations of the improved one-cell gap model.

$$H_y(r, j, k) \approx H_y(i, j, k) \left(\frac{\Delta x}{2} \right) \left(\frac{1}{r} \right), \quad E_x(r, j, k) \approx E_x(i, j, k) \left(\frac{\Delta x}{2} \right) \left(\frac{1}{r} \right)$$

Apply the Faraday's law of magnetic induction $\oint_C \vec{E} \cdot d\vec{l} = -\mu \frac{\partial}{\partial t} \iint_S \vec{H} \cdot d\vec{S}$

$$\begin{aligned}
 -\mu \frac{\partial}{\partial t} \int_{r_0}^{\Delta x} H_y(r, j, k) dr \Delta z &= E_z^n(i, j, k) \Delta z - E_z^n(i+1, j, k) \Delta z \\
 &+ \int_{r_0}^{\Delta x} E_x^n(r, j, k+1) dr - \int_{r_0}^{\Delta x} E_x^n(r, j, k) dr
 \end{aligned}$$

$$\begin{aligned}
-\mu\Delta z \frac{\partial}{\partial t} \int_{r_0}^{\Delta x} H_y(i, j, k) \left(\frac{\Delta x}{2} \right) \left(\frac{1}{r} \right) dr &= -\Delta z (E_z^n(i+1, j, k) - E_z^n(i, j, k)) \\
&+ \left(\int_{r_0}^{\Delta x} E_x^n(i, j, k+1) \left(\frac{\Delta x}{2} \right) \left(\frac{1}{r} \right) dr - \int_{r_0}^{\Delta x} E_x^n(i, j, k) \left(\frac{\Delta x}{2} \right) \left(\frac{1}{r} \right) dr \right)
\end{aligned}$$

$$\begin{aligned}
-\mu\Delta z \left(\frac{\Delta x}{2} \ln r \Big|_{r_0}^{\Delta x} \right) \frac{\partial}{\partial t} H_y(i, j, k) &= -\Delta z (E_z^n(i+1, j, k) - E_z^n(i, j, k)) \\
&+ \left(E_x^n(i, j, k+1) \left(\frac{\Delta x}{2} \ln r \Big|_{r_0}^{\Delta x} \right) - E_x^n(i, j, k) \left(\frac{\Delta x}{2} \ln r \Big|_{r_0}^{\Delta x} \right) \right)
\end{aligned}$$

$$\begin{aligned}
\frac{\partial}{\partial t} H_y(i, j, k) &= \frac{1}{\mu \left(\frac{\Delta x}{2} \ln r \Big|_{r_0}^{\Delta x} \right)} (E_z^n(i+1, j, k) - E_z^n(i, j, k)) \\
&- \frac{1}{\mu\Delta z} (E_x^n(i, j, k+1) - E_x^n(i, j, k))
\end{aligned}$$

$$\begin{aligned}
\frac{H_y^{n+\frac{1}{2}}(i, j, k) - H_y^{n-\frac{1}{2}}(i, j, k)}{\Delta t} &= \left(\frac{1}{\mu} \right) \left(\frac{2}{\ln \left(\frac{\Delta x}{r_0} \right)} \right) \left(\frac{E_z^n(i+1, j, k) - E_z^n(i, j, k)}{\Delta x} \right) \\
&- \left(\frac{1}{\mu} \right) \left(\frac{E_x^n(i, j, k+1) - E_x^n(i, j, k)}{\Delta z} \right)
\end{aligned}$$

$$\begin{aligned}
\frac{H_y^{n+\frac{1}{2}}(i, j, k) - H_y^{n-\frac{1}{2}}(i, j, k)}{\Delta t} &= \\
&- \left(\frac{1}{\mu} \right) \left(\frac{E_x^n(i, j, k+1) - E_x^n(i, j, k)}{\Delta z} \right) - \left(\frac{2}{\ln \left(\frac{\Delta x}{r_0} \right)} \right) \left(\frac{E_z^n(i+1, j, k) - E_z^n(i, j, k)}{\Delta x} \right)
\end{aligned}$$

$$H_y^{n+\frac{1}{2}}(i, j, k) = H_y^{n-\frac{1}{2}}(i, j, k) - \left(\frac{\Delta t}{\mu} \right) \left(\frac{E_x^n(i, j, k+1) - E_x^n(i, j, k)}{\Delta z} \right) - \left(\frac{2}{\ln\left(\frac{\Delta x}{r_0}\right)} \right) \left(\frac{E_z^n(i+1, j, k) - \left(\frac{-V_s(t)}{\Delta z}\right)}{\Delta x} \right)$$

This equation is similar to Equation (175). The other three components, the $H_y^{n+\frac{1}{2}}(i-1, j, k)$, $H_x^{n+\frac{1}{2}}(i, j, k)$ and $H_x^{n+\frac{1}{2}}(i, j-1, k)$ must be computed using the appropriate variation. In this case, the other elements of a thin wire dipole are located along the z-axis so that we must set all of E_z (dipole) are equal to zero as well as Equation (185). In other words, if we assume the gap of dipole is infinitesimal gap then we must assume $E_z(i, j, k) = -V_s(t)\delta(z)$ (Watanabe and Taki, 1998).

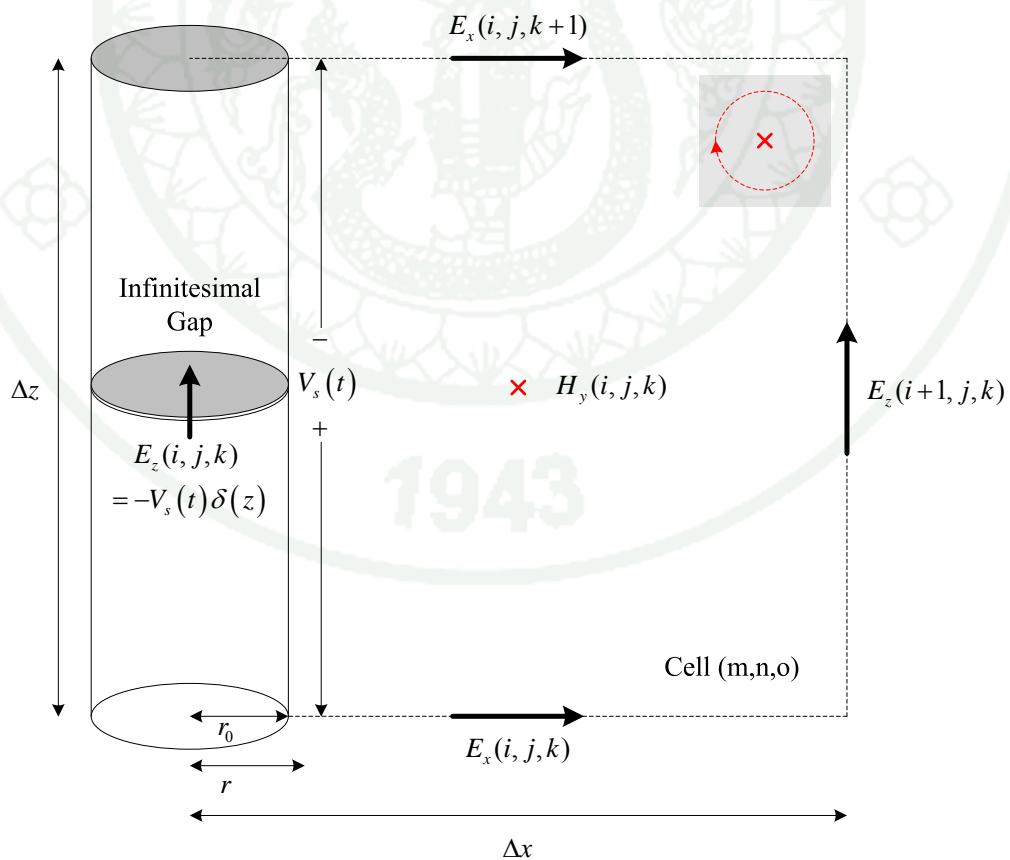


Figure 111 Field locations of the infinitesimal gap model.

$$H_y(r, j, k) \approx H_y(i, j, k) \left(\frac{\Delta x}{2} \right) \left(\frac{1}{r} \right), \quad E_x(r, j, k) \approx E_x(i, j, k) \left(\frac{\Delta x}{2} \right) \left(\frac{1}{r} \right)$$

Apply the Faraday's law of magnetic induction $\oint_c \vec{E} \cdot d\vec{l} = -\mu \frac{\partial}{\partial t} \iint_s \vec{H} \cdot d\vec{S}$

$$\begin{aligned} -\mu \frac{\partial}{\partial t} \int_{r_0}^{\Delta x} H_y(r, j, k) dr \Delta z &= -V_s(t) \delta(z) - E_z^n(i+1, j, k) \Delta z \\ &\quad + \int_{r_0}^{\Delta x} E_x^n(r, j, k+1) dr - \int_{r_0}^{\Delta x} E_x^n(r, j, k) dr \\ -\mu \Delta z \frac{\partial}{\partial t} \int_{r_0}^{\Delta x} H_y(i, j, k) \left(\frac{\Delta x}{2} \right) \left(\frac{1}{r} \right) dr &= -\Delta z \left(E_z^n(i+1, j, k) - \left(\frac{-V_s(t)}{\Delta z} \right) \right) \\ &\quad + \left(\int_{r_0}^{\Delta x} E_x^n(i, j, k+1) \left(\frac{\Delta x}{2} \right) \left(\frac{1}{r} \right) dr - \int_{r_0}^{\Delta x} E_x^n(i, j, k) \left(\frac{\Delta x}{2} \right) \left(\frac{1}{r} \right) dr \right) \\ -\mu \Delta z \left(\frac{\Delta x}{2} \ln r \Big|_{r_0}^{\Delta x} \right) \frac{\partial}{\partial t} H_y(i, j, k) &= -\Delta z \left(E_z^n(i+1, j, k) - \left(\frac{-V_s(t)}{\Delta z} \right) \right) \\ &\quad + \left(E_x^n(i, j, k+1) \left(\frac{\Delta x}{2} \ln r \Big|_{r_0}^{\Delta x} \right) - E_x^n(i, j, k) \left(\frac{\Delta x}{2} \ln r \Big|_{r_0}^{\Delta x} \right) \right) \\ \frac{\partial}{\partial t} H_y(i, j, k) &= \frac{1}{\mu \left(\frac{\Delta x}{2} \ln r \Big|_{r_0}^{\Delta x} \right)} \left(E_z^n(i+1, j, k) - \left(\frac{-V_s(t)}{\Delta z} \right) \right) \\ &\quad - \frac{1}{\mu \Delta z} (E_x^n(i, j, k+1) - E_x^n(i, j, k)) \end{aligned}$$

$$\begin{aligned} \frac{H_y^{n+\frac{1}{2}}(i, j, k) - H_y^{n-\frac{1}{2}}(i, j, k)}{\Delta t} &= \left(\frac{1}{\mu} \right) \left(\frac{2}{\ln \left(\frac{\Delta x}{r_0} \right)} \right) \left(\frac{E_z^n(i+1, j, k) - \left(\frac{-V_s(t)}{\Delta z} \right)}{\Delta x} \right) \\ &\quad - \left(\frac{1}{\mu} \right) \left(\frac{E_x^n(i, j, k+1) - E_x^n(i, j, k)}{\Delta z} \right) \end{aligned}$$

$$\frac{H_y^{n+\frac{1}{2}}(i, j, k) - H_y^{n-\frac{1}{2}}(i, j, k)}{\Delta t} = -\left(\frac{1}{\mu}\right) \left(\frac{E_x^n(i, j, k+1) - E_x^n(i, j, k)}{\Delta z} \right) - \left(\frac{2}{\ln\left(\frac{\Delta x}{r_0}\right)} \right) \left(\frac{E_z^n(i+1, j, k) - \left(\frac{-V_s(t)}{\Delta z}\right)}{\Delta x} \right)$$

$$H_y^{n+\frac{1}{2}}(i, j, k) = H_y^{n-\frac{1}{2}}(i, j, k) - \left(\frac{\Delta t}{\mu}\right) \left(\frac{E_x^n(i, j, k+1) - E_x^n(i, j, k)}{\Delta z} \right) - \left(\frac{2}{\ln\left(\frac{\Delta x}{r_0}\right)} \right) \left(\frac{E_z^n(i+1, j, k) - \left(\frac{-V_s(t)}{\Delta z}\right)}{\Delta x} \right)$$

It is apparent that this equation is similar to the equation of improved one-cell gap and Equation (175). The illustration is as follow

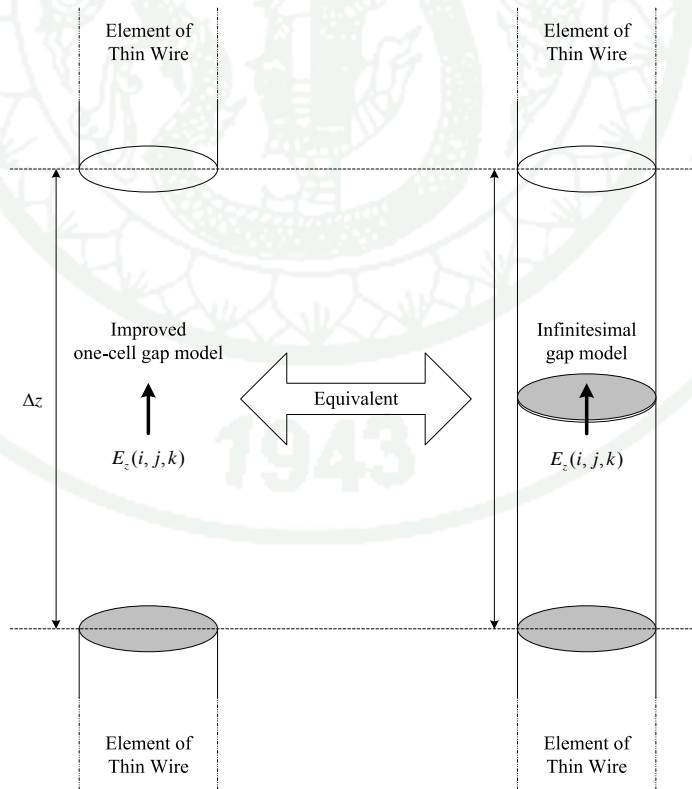


Figure 112 The improved one-cell gap model is the infinitesimal gap model.

The improved one-cell gap model or the infinitesimal gap model

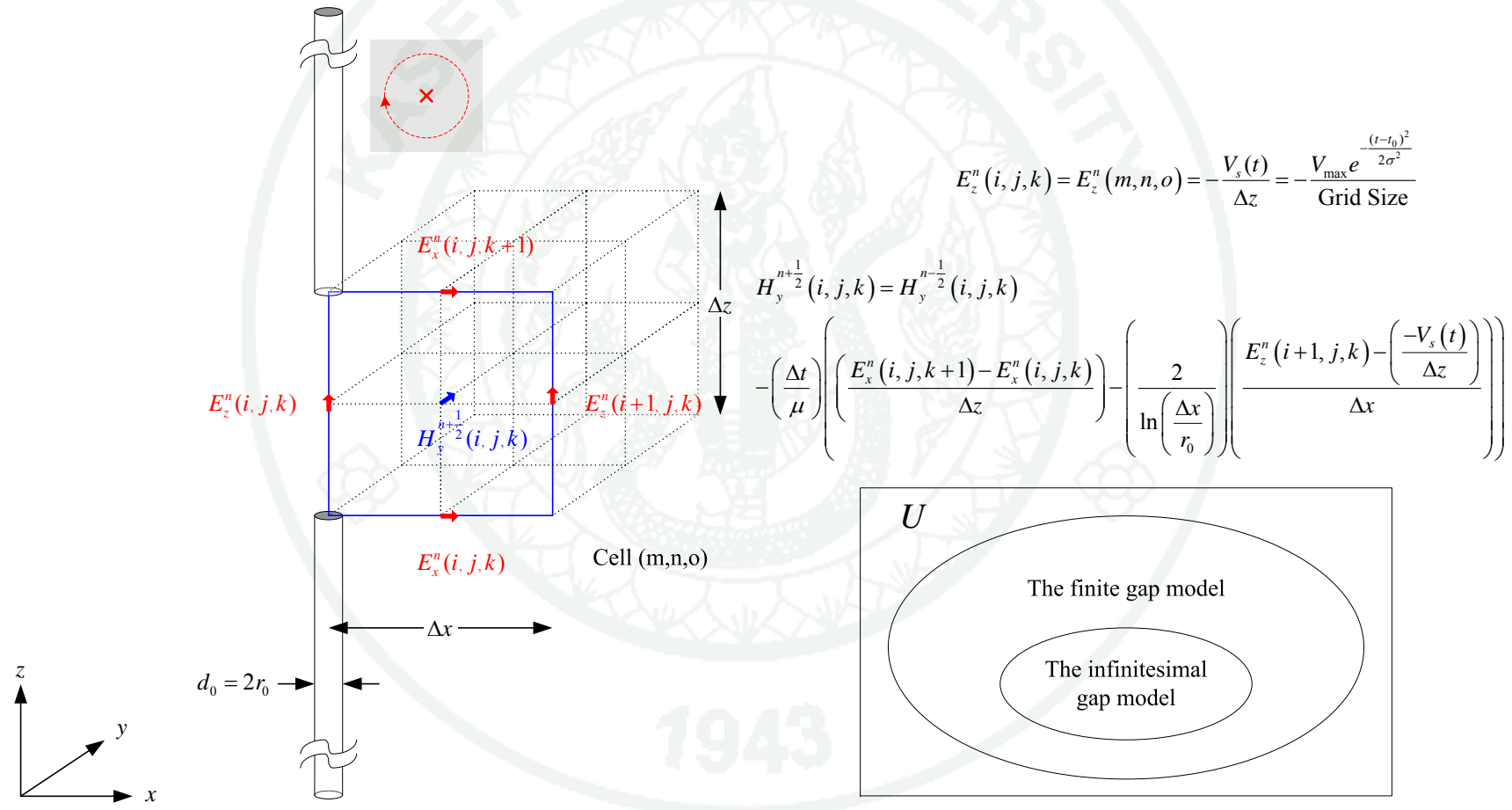


Figure 113 The summary of the improved one-cell gap model or the infinitesimal gap model.

1.4 The finite gap model

In this section, the author proposes the new idea to generalize the finite gap model formulas. By nature of FDTD and the function of for-loop, all updating equation must be centered at the cell (i, j, k) . When the timestep is increasing, the center cell is moving to the concatenate cell, for example, the cell $(i+1, j, k)$. Additionally, in the next timestep, that concatenate cell will become the center cell (i, j, k) , automatically. As a result, the author derives the four equations corresponding to the center cell (i, j, k) so that these can make a general form (Homsup *et al.*, 2010).

The author assumes the center cell (i, j, k) locating at cell $(m-1, n, o)$ while the finite feeding gap is positioned at cell (m, n, o) . It should be noted that the H -field component no.1, $H_y^{n+\frac{1}{2}}(i, j, k)$, is located at the left-side of the finite feeding gap, Figure 114, and its direction is lied along y-axis.

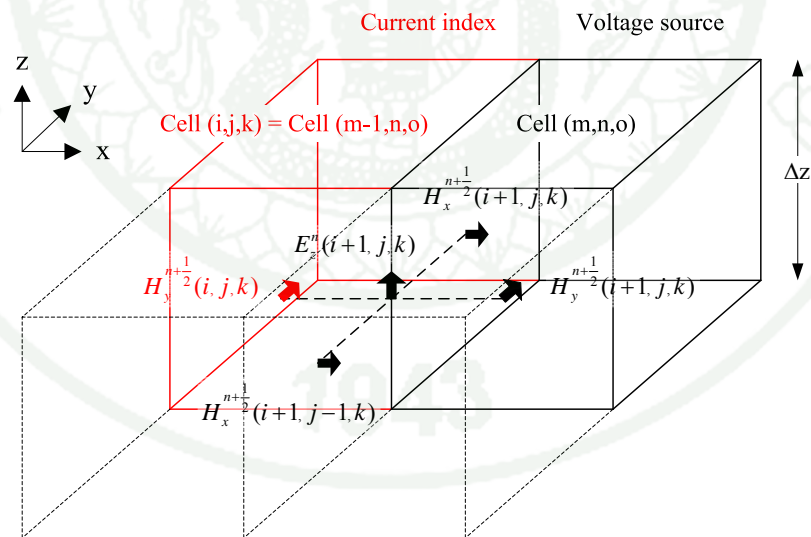


Figure 114 The H -field component no.1.

With the above assumption, the author defines $E_z(m, n, o) = -\frac{V_s(t)}{\Delta z}$ as the exciting field and the author approximates the spatial field as the following figure

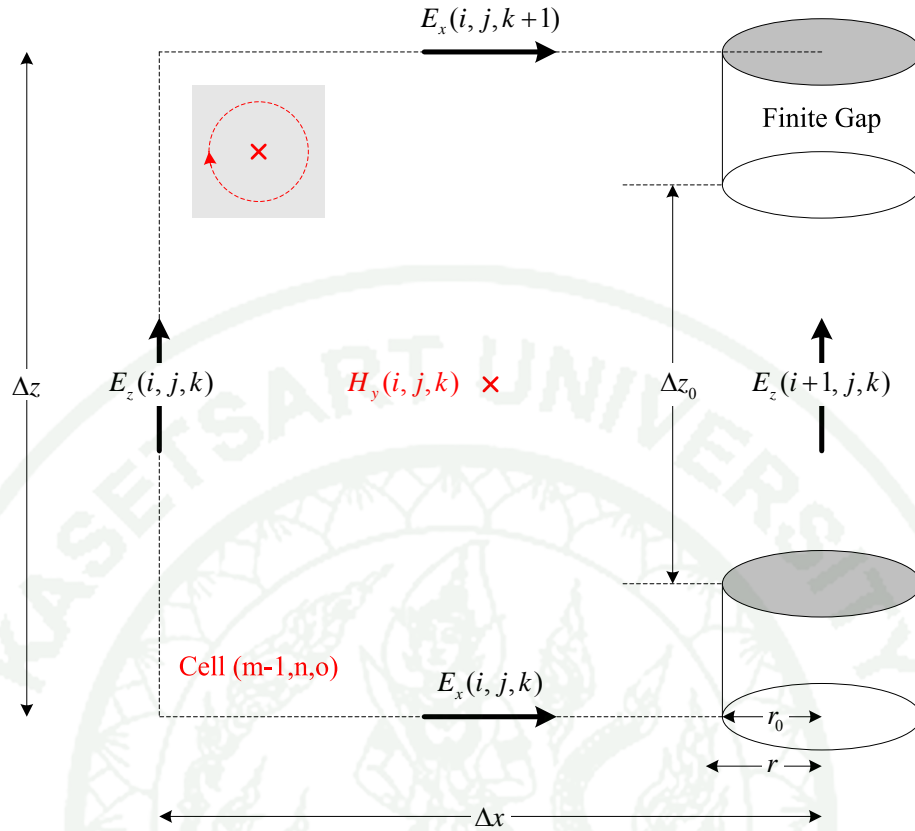


Figure 115 Spatial field locations for H - field component no.1.

$$H_y(r, j, k) \approx H_y(i, j, k) \left(\frac{\Delta x}{2} \right) \left(\frac{1}{r} \right), \quad E_x(r, j, k) \approx E_x(i, j, k) \left(\frac{\Delta x}{2} \right) \left(\frac{1}{r} \right)$$

Apply Faraday's law of magnetic induction $\oint_C \bar{E} \cdot d\bar{l} = -\mu \frac{\partial}{\partial t} \iint_S \bar{H} \cdot d\bar{S}$

$$-\mu \frac{\partial}{\partial t} \int_{r_0}^{\Delta x} H_y(r, j, k) dr \Delta z = E_z^n(i, j, k) \Delta z - E_z^n(i+1, j, k) \Delta z_0$$

$$+ \int_{r_0}^{\Delta x} E_x^n(r, j, k+1) dr - \int_{r_0}^{\Delta x} E_x^n(r, j, k) dr$$

$$-\mu \Delta z \frac{\partial}{\partial t} \int_{r_0}^{\Delta x} H_y(i, j, k) \left(\frac{\Delta x}{2} \right) \left(\frac{1}{r} \right) dr = -\Delta z \left(\left(\frac{\Delta z_0}{\Delta z} \right) E_z^n(i+1, j, k) - E_z^n(i, j, k) \right)$$

$$+ \left(\int_{r_0}^{\Delta x} E_x^n(i, j, k+1) \left(\frac{\Delta x}{2} \right) \left(\frac{1}{r} \right) dr - \int_{r_0}^{\Delta x} E_x^n(i, j, k) \left(\frac{\Delta x}{2} \right) \left(\frac{1}{r} \right) dr \right)$$

$$-\mu\Delta z \left(\frac{\Delta x}{2} \ln r \Big|_{r_0}^{\Delta x} \right) \frac{\partial}{\partial t} H_y(i, j, k) = -\Delta z \left(\left(\frac{\Delta z_0}{\Delta z} \right) E_z^n(i+1, j, k) - E_z^n(i, j, k) \right) \\ + \left(E_x^n(i, j, k+1) \left(\frac{\Delta x}{2} \ln r \Big|_{r_0}^{\Delta x} \right) - E_x^n(i, j, k) \left(\frac{\Delta x}{2} \ln r \Big|_{r_0}^{\Delta x} \right) \right)$$

$$\frac{\partial}{\partial t} H_y(i, j, k) = \frac{1}{\mu \left(\frac{\Delta x}{2} \ln r \Big|_{r_0}^{\Delta x} \right)} \left(\left(\frac{\Delta z_0}{\Delta z} \right) E_z^n(i+1, j, k) - E_z^n(i, j, k) \right) \\ - \frac{1}{\mu\Delta z} \left(E_x^n(i, j, k+1) - E_x^n(i, j, k) \right)$$

$$\frac{H_y^{n+\frac{1}{2}}(i, j, k) - H_y^{n-\frac{1}{2}}(i, j, k)}{\Delta t} = \left(\frac{1}{\mu} \right) \left(\frac{2}{\ln \left(\frac{\Delta x}{r_0} \right)} \right) \left(\frac{\left(\frac{\Delta z_0}{\Delta z} \right) E_z^n(i+1, j, k) - E_z^n(i, j, k)}{\Delta x} \right) \\ - \left(\frac{1}{\mu} \right) \left(\frac{E_x^n(i, j, k+1) - E_x^n(i, j, k)}{\Delta z} \right)$$

$$\frac{H_y^{n+\frac{1}{2}}(i, j, k) - H_y^{n-\frac{1}{2}}(i, j, k)}{\Delta t} = - \left(\frac{1}{\mu} \right) \left(\frac{E_x^n(i, j, k+1) - E_x^n(i, j, k)}{\Delta z} \right) \\ + \left(\frac{1}{\mu} \right) \left(\frac{2}{\ln \left(\frac{\Delta x}{r_0} \right)} \right) \left(\frac{\left(\frac{\Delta z_0}{\Delta z} \right) E_z^n(i+1, j, k) - E_z^n(i, j, k)}{\Delta x} \right)$$

$$H_y^{n+\frac{1}{2}}(i, j, k) = H_y^{n-\frac{1}{2}}(i, j, k)$$

$$- \left(\frac{\Delta t}{\mu} \right) \left(\frac{E_x^n(i, j, k+1) - E_x^n(i, j, k)}{\Delta z} \right) - \left(\frac{2}{\ln \left(\frac{\Delta x}{r_0} \right)} \right) \left(\frac{\left(\frac{\Delta z_0}{\Delta z} \right) E_z^n(i+1, j, k) - E_z^n(i, j, k)}{\Delta x} \right)$$

(186)

The finite gap model no.1

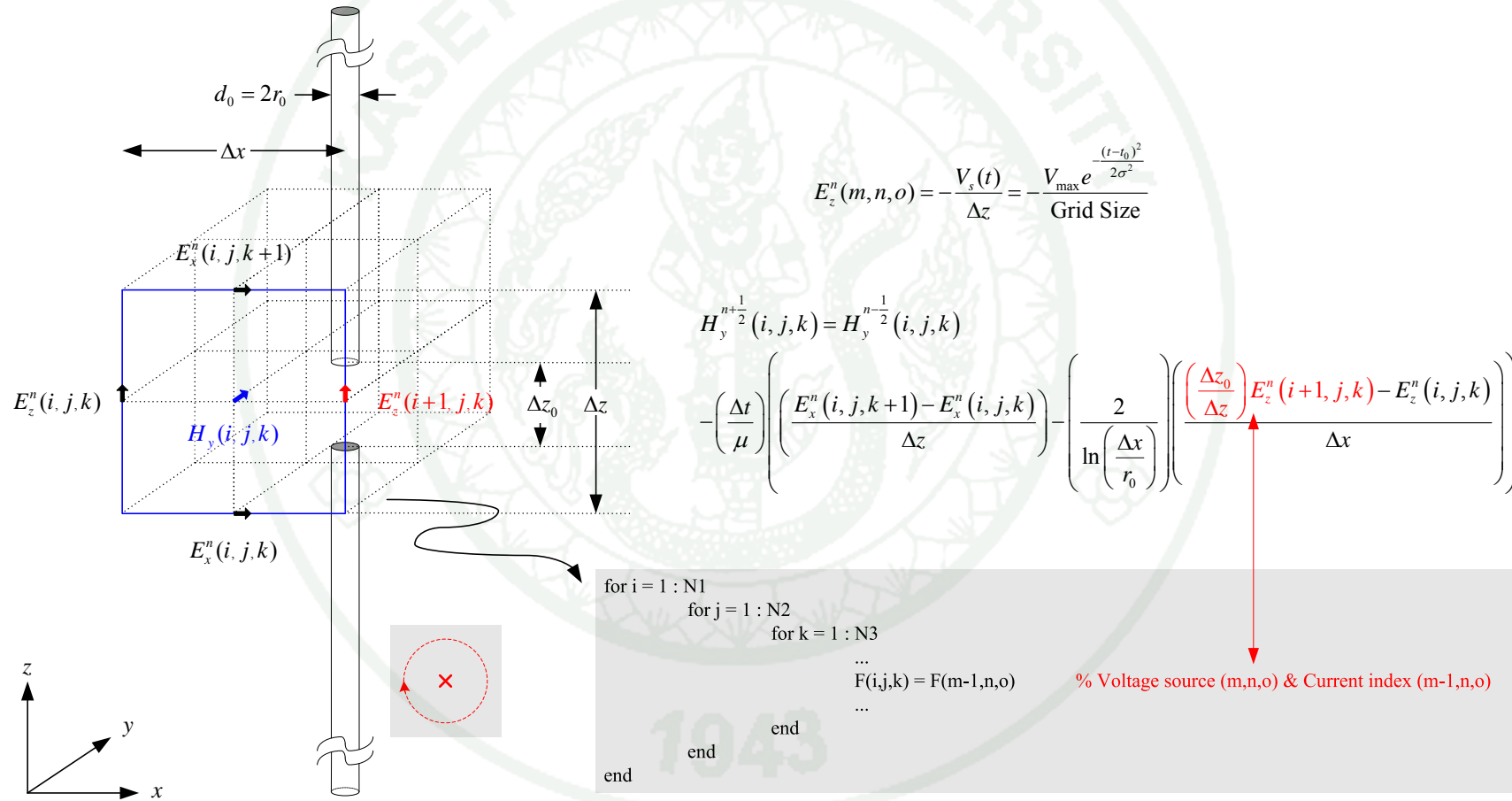


Figure 116 The summary of the finite gap model no.1.

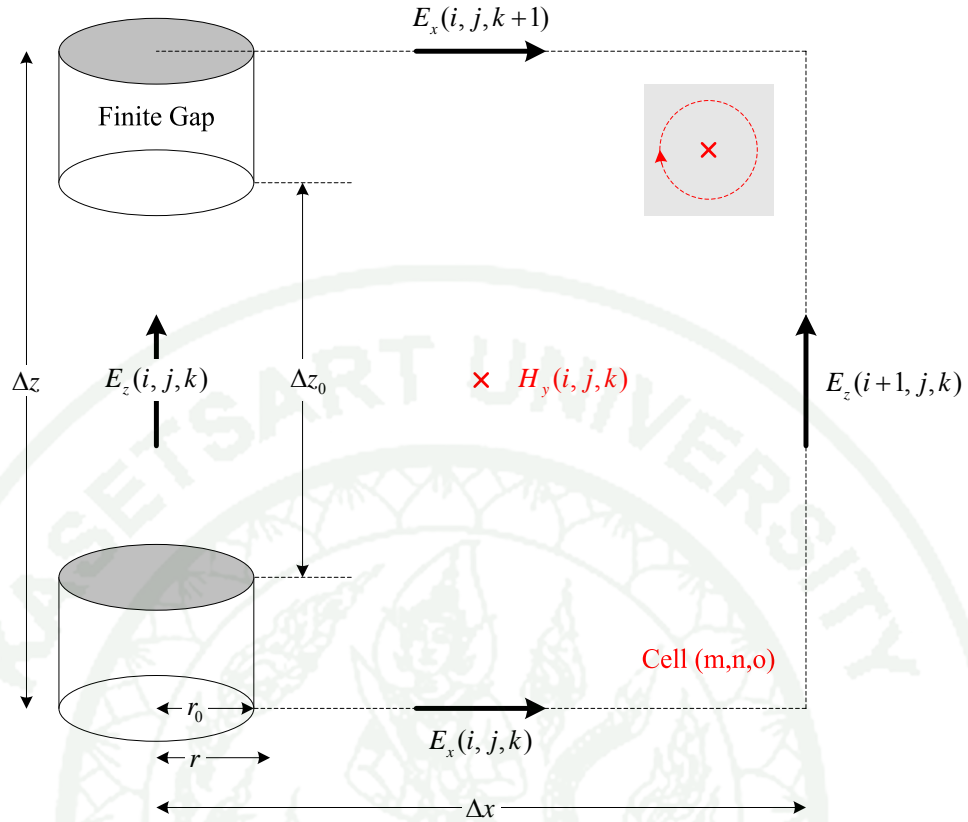


Figure 117 Spatial field locations for H - field component no.2.

$$H_y(r, j, k) \approx H_y(i, j, k) \left(\frac{\Delta x}{2} \right) \left(\frac{1}{r} \right), \quad E_x(r, j, k) \approx E_x(i, j, k) \left(\frac{\Delta x}{2} \right) \left(\frac{1}{r} \right)$$

Apply Faraday's law of magnetic induction $\oint_C \bar{E} \cdot d\bar{l} = -\mu \frac{\partial}{\partial t} \iint_S \bar{H} \cdot d\bar{S}$

$$-\mu \frac{\partial}{\partial t} \int_{r_0}^{\Delta x} H_y(r, j, k) dr \Delta z = E_z^n(i, j, k) \Delta z_0 - E_z^n(i+1, j, k) \Delta z$$

$$+ \int_{r_0}^{\Delta x} E_x^n(r, j, k+1) dr - \int_{r_0}^{\Delta x} E_x^n(r, j, k) dr$$

$$-\mu \Delta z \frac{\partial}{\partial t} \int_{r_0}^{\Delta x} H_y(i, j, k) \left(\frac{\Delta x}{2} \right) \left(\frac{1}{r} \right) dr = -\Delta z \left(E_z^n(i+1, j, k) - \left(\frac{\Delta z_0}{\Delta z} \right) E_z^n(i, j, k) \right) \\ + \left(\int_{r_0}^{\Delta x} E_x^n(i, j, k+1) \left(\frac{\Delta x}{2} \right) \left(\frac{1}{r} \right) dr - \int_{r_0}^{\Delta x} E_x^n(i, j, k) \left(\frac{\Delta x}{2} \right) \left(\frac{1}{r} \right) dr \right)$$

$$-\mu\Delta z\left(\frac{\Delta x}{2}\ln r\Big|_{r_0}^{\Delta x}\right)\frac{\partial}{\partial t}H_y(i,j,k)=-\Delta z\left(E_z^n(i+1,j,k)-\left(\frac{\Delta z_0}{\Delta z}\right)E_z^n(i,j,k)\right) \\ +\left(E_x^n(i,j,k+1)\left(\frac{\Delta x}{2}\ln r\Big|_{r_0}^{\Delta x}\right)-E_x^n(i,j,k)\left(\frac{\Delta x}{2}\ln r\Big|_{r_0}^{\Delta x}\right)\right)$$

$$\frac{\partial}{\partial t}H_y(i,j,k)=\frac{1}{\mu\left(\frac{\Delta x}{2}\ln r\Big|_{r_0}^{\Delta x}\right)}\left(E_z^n(i+1,j,k)-\left(\frac{\Delta z_0}{\Delta z}\right)E_z^n(i,j,k)\right) \\ -\frac{1}{\mu\Delta z}\left(E_x^n(i,j,k+1)-E_x^n(i,j,k)\right)$$

$$\frac{H_y^{n+\frac{1}{2}}(i,j,k)-H_y^{n-\frac{1}{2}}(i,j,k)}{\Delta t}=\left(\frac{1}{\mu}\right)\left(\frac{2}{\ln\left(\frac{\Delta x}{r_0}\right)}\right)\left(\frac{E_z^n(i+1,j,k)-\left(\frac{\Delta z_0}{\Delta z}\right)E_z^n(i,j,k)}{\Delta x}\right) \\ -\left(\frac{1}{\mu}\right)\left(\frac{E_x^n(i,j,k+1)-E_x^n(i,j,k)}{\Delta z}\right)$$

$$\frac{H_y^{n+\frac{1}{2}}(i,j,k)-H_y^{n-\frac{1}{2}}(i,j,k)}{\Delta t}=-\left(\frac{1}{\mu}\right)\left(\frac{E_x^n(i,j,k+1)-E_x^n(i,j,k)}{\Delta z}\right) \\ +\left(\frac{1}{\mu}\right)\left(\frac{2}{\ln\left(\frac{\Delta x}{r_0}\right)}\right)\left(\frac{E_z^n(i+1,j,k)-\left(\frac{\Delta z_0}{\Delta z}\right)E_z^n(i,j,k)}{\Delta x}\right)$$

$$H_y^{n+\frac{1}{2}}(i,j,k)=H_y^{n-\frac{1}{2}}(i,j,k)$$

$$-\left(\frac{\Delta t}{\mu}\right)\left(\frac{E_x^n(i,j,k+1)-E_x^n(i,j,k)}{\Delta z}\right)-\left(\frac{2}{\ln\left(\frac{\Delta x}{r_0}\right)}\right)\left(\frac{E_z^n(i+1,j,k)-\left(\frac{\Delta z_0}{\Delta z}\right)E_z^n(i,j,k)}{\Delta x}\right)$$

(187)

The finite gap model no.2

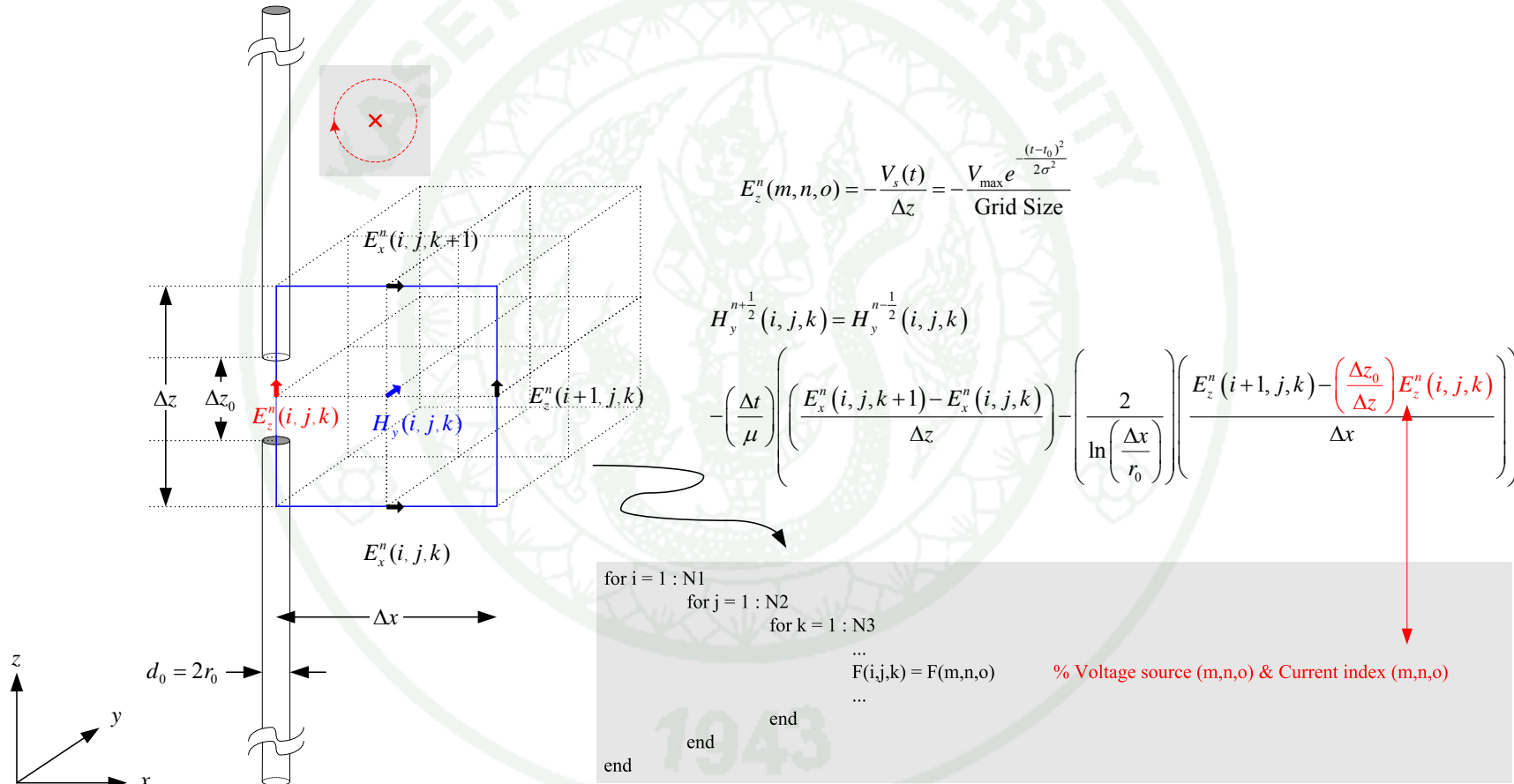


Figure 118 The summary of the finite gap model no.2.

$$-\mu\Delta z\left(\frac{\Delta y}{2}\ln r\Big|_{r_0}^{\Delta y}\right)\frac{\partial}{\partial t}H_x(i,j,k)=\Delta z\left(\left(\frac{\Delta z_0}{\Delta z}\right)E_z^n(i,j+1,k)-E_z^n(i,j,k)\right) \\ -\left(E_y^n(i,j,k+1)\left(\frac{\Delta y}{2}\ln r\Big|_{r_0}^{\Delta y}\right)-E_y^n(i,j,k)\left(\frac{\Delta y}{2}\ln r\Big|_{r_0}^{\Delta y}\right)\right)$$

$$\frac{\partial}{\partial t}H_x(i,j,k)=-\frac{1}{\mu\left(\frac{\Delta y}{2}\ln r\Big|_{r_0}^{\Delta y}\right)}\left(\left(\frac{\Delta z_0}{\Delta z}\right)E_z^n(i,j+1,k)-E_z^n(i,j,k)\right) \\ +\frac{1}{\mu\Delta z}\left(E_y^n(i,j,k+1)-E_y^n(i,j,k)\right)$$

$$\frac{H_x^{n+\frac{1}{2}}(i,j,k)-H_x^{n-\frac{1}{2}}(i,j,k)}{\Delta t}=-\left(\frac{1}{\mu}\right)\left(\frac{2}{\ln\left(\frac{\Delta y}{r_0}\right)}\right)\left(\frac{\left(\frac{\Delta z_0}{\Delta z}\right)E_z^n(i,j+1,k)-E_z^n(i,j,k)}{\Delta y}\right) \\ +\left(\frac{1}{\mu}\right)\left(\frac{E_y^n(i,j,k+1)-E_y^n(i,j,k)}{\Delta z}\right)$$

$$H_x^{n+\frac{1}{2}}(i,j,k)=H_x^{n-\frac{1}{2}}(i,j,k)$$

$$-\left(\frac{\Delta t}{\mu}\right)\left(\left(\frac{2}{\ln\left(\frac{\Delta y}{r_0}\right)}\right)\left(\frac{\left(\frac{\Delta z_0}{\Delta z}\right)E_z^n(i,j+1,k)-E_z^n(i,j,k)}{\Delta y}\right)-\left(\frac{E_y^n(i,j,k+1)-E_y^n(i,j,k)}{\Delta z}\right)\right)$$

(188)

The finite gap model no.3

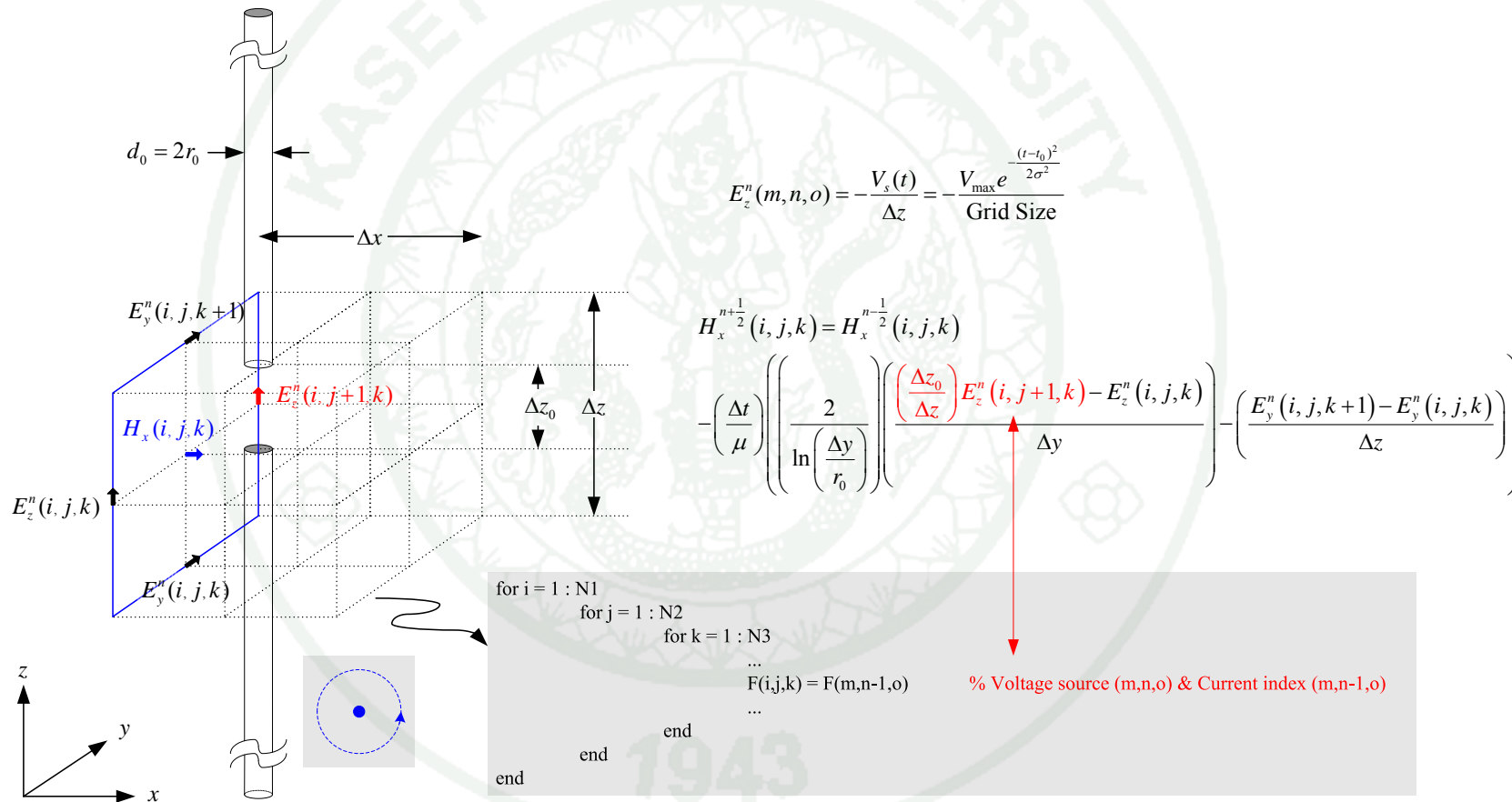


Figure 120 The summary of the finite gap model no.3.

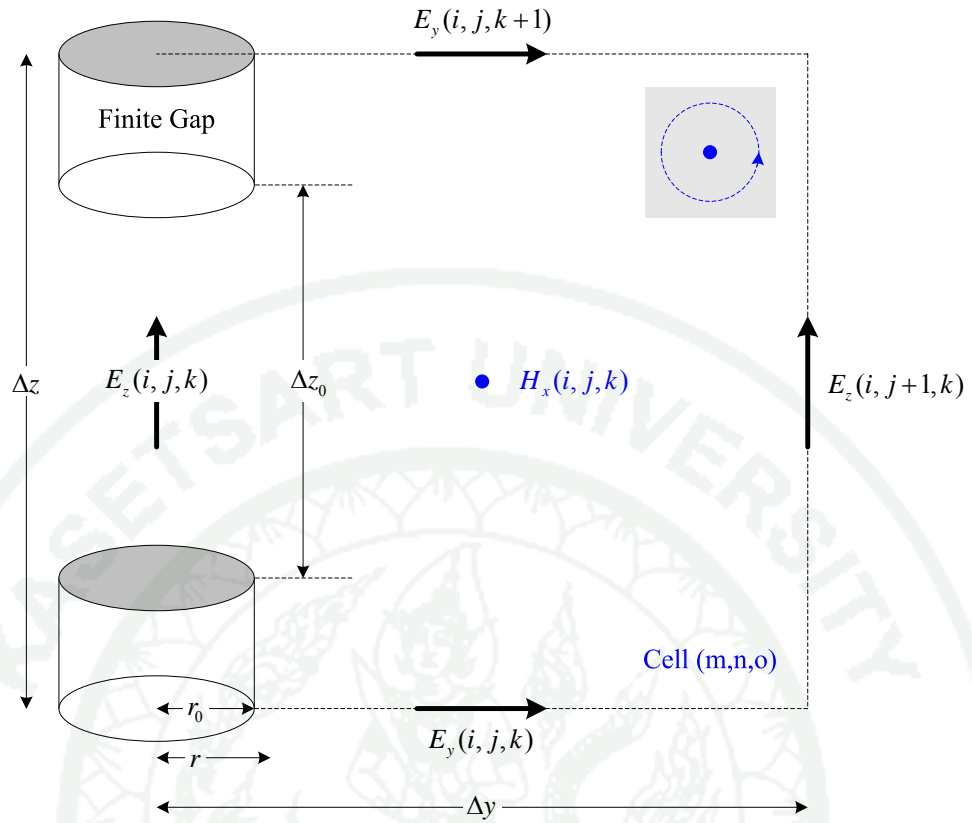


Figure 121 Spatial field locations for H - field component no.4.

$$H_x(r, j, k) \approx H_x(i, j, k) \left(\frac{\Delta y}{2} \right) \left(\frac{1}{r} \right), \quad E_y(r, j, k) \approx E_y(i, j, k) \left(\frac{\Delta y}{2} \right) \left(\frac{1}{r} \right)$$

$$\text{Apply Faraday's law of magnetic induction } \oint_C \bar{E} \cdot d\bar{l} = -\mu \frac{\partial}{\partial t} \iint_S \bar{H} \cdot d\bar{S}$$

$$-\mu \frac{\partial}{\partial t} \int_{r_0}^{\Delta y} H_x(r, j, k) dr \Delta z = -E_z^n(i, j, k) \Delta z_0 + E_z^n(i, j+1, k) \Delta z$$

$$- \int_{r_0}^{\Delta y} E_y^n(r, j, k+1) dr + \int_{r_0}^{\Delta y} E_y^n(r, j, k) dr$$

$$-\mu \Delta z \frac{\partial}{\partial t} \int_{r_0}^{\Delta y} H_x(i, j, k) \left(\frac{\Delta y}{2} \right) \left(\frac{1}{r} \right) dr = \Delta z \left(E_z^n(i, j+1, k) - \left(\frac{\Delta z_0}{\Delta z} \right) E_z^n(i, j, k) \right)$$

$$- \left(\int_{r_0}^{\Delta y} E_y^n(i, j, k+1) \left(\frac{\Delta y}{2} \right) \left(\frac{1}{r} \right) dr - \int_{r_0}^{\Delta y} E_y^n(i, j, k) \left(\frac{\Delta y}{2} \right) \left(\frac{1}{r} \right) dr \right)$$

$$-\mu\Delta z\left(\frac{\Delta y}{2}\ln r\Big|_{r_0}^{\Delta y}\right)\frac{\partial}{\partial t}H_x(i,j,k)=\Delta z\left(E_z^n(i,j+1,k)-\left(\frac{\Delta z_0}{\Delta z}\right)E_z^n(i,j,k)\right) \\ -\left(E_y^n(i,j,k+1)\left(\frac{\Delta y}{2}\ln r\Big|_{r_0}^{\Delta y}\right)-E_y^n(i,j,k)\left(\frac{\Delta y}{2}\ln r\Big|_{r_0}^{\Delta y}\right)\right)$$

$$\frac{\partial}{\partial t}H_x(i,j,k)=-\frac{1}{\mu\left(\frac{\Delta y}{2}\ln r\Big|_{r_0}^{\Delta y}\right)}\left(E_z^n(i,j+1,k)-\left(\frac{\Delta z_0}{\Delta z}\right)E_z^n(i,j,k)\right) \\ +\frac{1}{\mu\Delta z}\left(E_y^n(i,j,k+1)-E_y^n(i,j,k)\right)$$

$$\frac{H_x^{n+\frac{1}{2}}(i,j,k)-H_x^{n-\frac{1}{2}}(i,j,k)}{\Delta t}=-\left(\frac{1}{\mu}\right)\left(\frac{2}{\ln\left(\frac{\Delta y}{r_0}\right)}\right)\left(\frac{E_z^n(i,j+1,k)-\left(\frac{\Delta z_0}{\Delta z}\right)E_z^n(i,j,k)}{\Delta y}\right) \\ +\left(\frac{1}{\mu}\right)\left(\frac{E_y^n(i,j,k+1)-E_y^n(i,j,k)}{\Delta z}\right)$$

$$H_x^{n+\frac{1}{2}}(i,j,k)=H_x^{n-\frac{1}{2}}(i,j,k)$$

$$-\left(\frac{\Delta t}{\mu}\right)\left(\left(\frac{2}{\ln\left(\frac{\Delta y}{r_0}\right)}\right)\left(\frac{E_z^n(i,j+1,k)-\left(\frac{\Delta z_0}{\Delta z}\right)E_z^n(i,j,k)}{\Delta y}\right)-\left(\frac{E_y^n(i,j,k+1)-E_y^n(i,j,k)}{\Delta z}\right)\right)$$

(189)

The finite gap model no.4

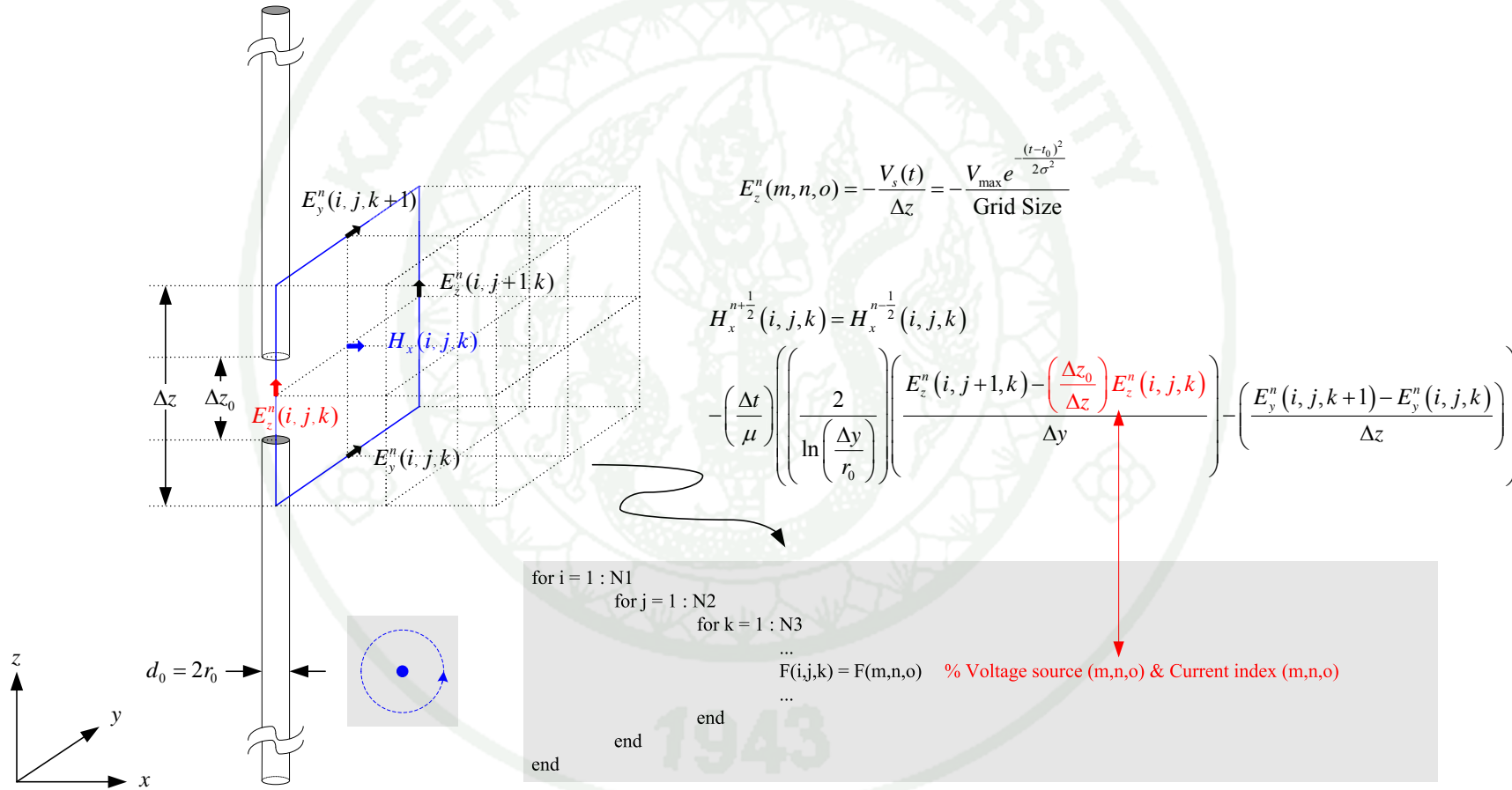


Figure 122 The summary of the finite gap model no.4.

Typically, the simplest situation is a voltage source. In this case

$$E_z^n(m, n, o) = -\frac{V_s(t)}{\Delta z} = -\frac{V_{\max} e^{-\frac{(t-t_0)^2}{2\sigma^2}}}{\Delta z} = -\frac{V_{\max} e^{-\frac{(t-t_0)^2}{2\sigma^2}}}{\text{Grid Size}}$$

As describe above, from Equation (186) to Equation (189), these can be rewritten into two general forms, which suitable for programming, like the following equations

$$H_y^{n+\frac{1}{2}}(i, j, k) = H_y^{n-\frac{1}{2}}(i, j, k) - \left(\frac{\Delta t}{\mu}\right) \left(\dots \right. \\ \left. \left(\frac{E_x^n(i, j, k+1) - E_x^n(i, j, k)}{\Delta z} \right) \right. \\ \left. - \left(\frac{2}{\ln\left(\frac{\Delta x}{r_0}\right)} \right) \left(\frac{GF(i+1, j, k) \cdot E_z^n(i+1, j, k) - GF(i, j, k) \cdot E_z^n(i, j, k)}{\Delta x} \right) \right) \quad (190)$$

$$H_x^{n+\frac{1}{2}}(i, j, k) = H_x^{n-\frac{1}{2}}(i, j, k) - \left(\frac{\Delta t}{\mu}\right) \left(\dots \right. \\ \left. \left(\frac{2}{\ln\left(\frac{\Delta y}{r_0}\right)} \right) \left(\frac{GF(i, j+1, k) \cdot E_z^n(i, j+1, k) - GF(i, j, k) \cdot E_z^n(i, j, k)}{\Delta y} \right) \right. \\ \left. - \left(\frac{E_y^n(i, j, k+1) - E_y^n(i, j, k)}{\Delta z} \right) \right) \quad (191)$$

From Equation (190) to Equation (191), the author assigns value for $GF(i, j, k)$ in the computer programming as the following (Homsup *et al.*, 2010)

$$GF(i, j, k) \begin{cases} = \frac{\Delta z_0}{\Delta z} \in (0, 1] \leftrightarrow (i = m, j = n, k = o) \\ = 1 \leftrightarrow \text{Otherwise} \end{cases} \quad (192)$$

If $\frac{\Delta z_0}{\Delta z} = 1$ then these two equations present the infinitesimal gap model.

If $\widehat{GF}_x(i, j, k) = 2 / \left(\ln \left(\frac{\Delta x}{r_0} \right) \right)$ and $\widehat{GF}_y(i, j, k) = 2 / \left(\ln \left(\frac{\Delta y}{r_0} \right) \right)$ then

$$H_y^{n+\frac{1}{2}}(i, j, k) = H_y^{n-\frac{1}{2}}(i, j, k) - \left(\frac{\Delta t}{\mu} \right) \left(\dots \right. \\ \left. \left(\frac{E_x^n(i, j, k+1) - E_x^n(i, j, k)}{\Delta z} \right) \right. \\ \left. - \left(\frac{GF(i+1, j, k) \cdot \widehat{GF}_x(i+1, j, k) \cdot E_z^n(i+1, j, k) - GF(i, j, k) \cdot \widehat{GF}_x(i, j, k) \cdot E_z^n(i, j, k)}{\Delta x} \right) \right) \quad (193)$$

$$H_x^{n+\frac{1}{2}}(i, j, k) = H_x^{n-\frac{1}{2}}(i, j, k) - \left(\frac{\Delta t}{\mu} \right) \left(\dots \right. \\ \left. \left(\frac{GF(i, j+1, k) \cdot \widehat{GF}_y(i, j+1, k) \cdot E_z^n(i, j+1, k) - GF(i, j, k) \cdot \widehat{GF}_y(i, j, k) \cdot E_z^n(i, j, k)}{\Delta y} \right) \right. \\ \left. - \left(\frac{E_y^n(i, j, k+1) - E_y^n(i, j, k)}{\Delta z} \right) \right) \quad (194)$$

It is apparent that if Equation (193) and Equation (194) are located in Free-Space then these equations are similar to Equation (112) and Equation (111), respectively. The author assigns E_z - field along the dipole equal to zero, except the feeding gap as the following figure

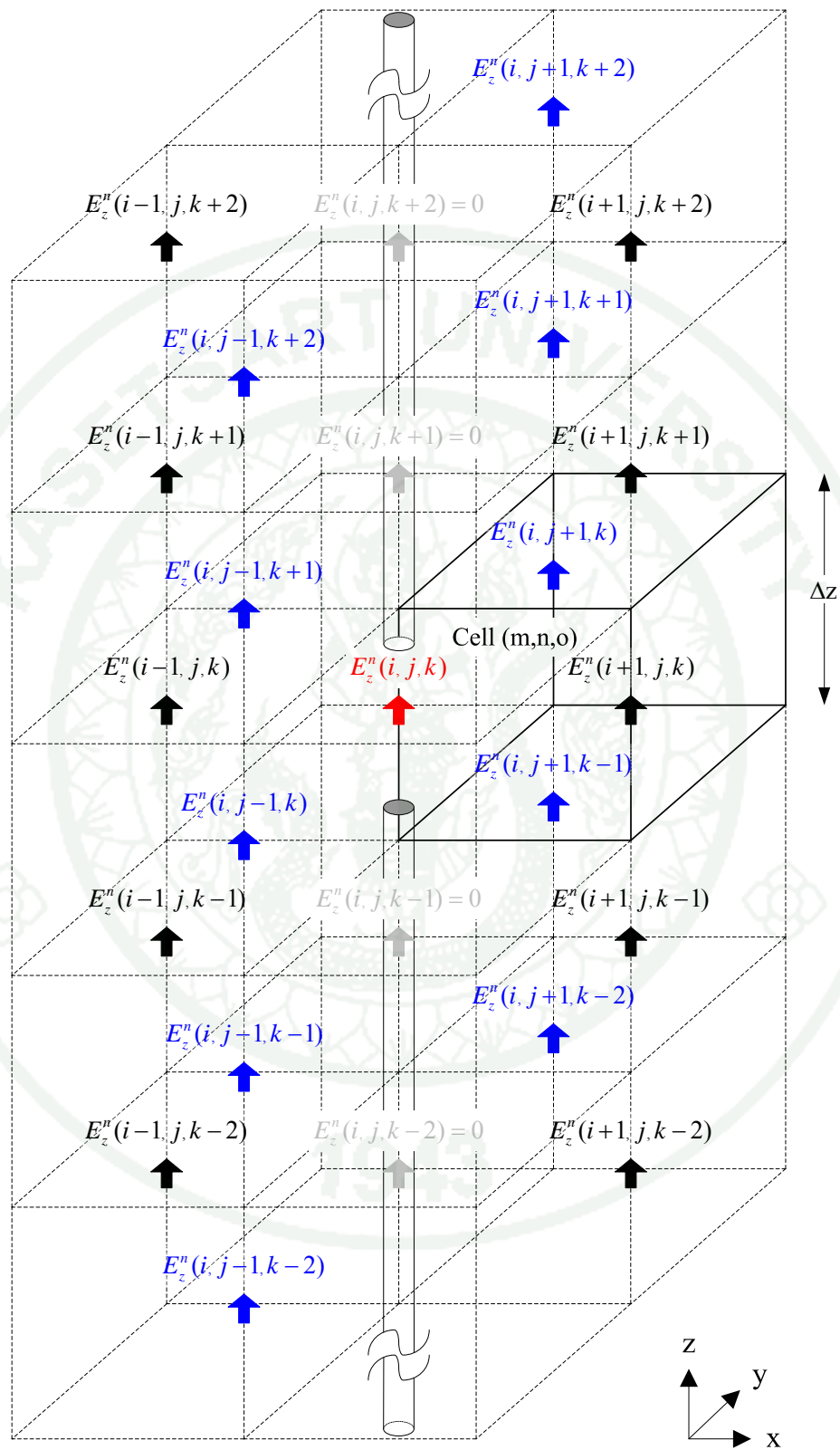


Figure 123 Spatial E_z - field locations surround the dipole.

From Equation (193) to Equation (194) and the previous figure, the author assigns value for $\widehat{GF}_x(i, j, k)$ and $\widehat{GF}_y(i, j, k)$ in the FDTD programming as

$$\widehat{GF}_x(i, j, k) \begin{cases} = \frac{2}{\ln\left(\frac{\Delta x}{r_0}\right)} \leftrightarrow \left(i = m, j = n, k \in \left[o - \frac{(\Delta l - 1)}{2} : o + \frac{(\Delta l - 1)}{2} \right] \right) \\ = \frac{2}{\ln\left(\frac{\Delta x}{r_0}\right)} \leftrightarrow \left(i = m \pm 1, j = n, k \in \left[o - \frac{(\Delta l - 1)}{2} : o + \frac{(\Delta l - 1)}{2} \right] \right) \\ = 1 \leftrightarrow \text{Otherwise} \end{cases} \quad (195)$$

$$\widehat{GF}_y(i, j, k) \begin{cases} = \frac{2}{\ln\left(\frac{\Delta y}{r_0}\right)} \leftrightarrow \left(i = m, j = n, k \in \left[o - \frac{(\Delta l - 1)}{2} : o + \frac{(\Delta l - 1)}{2} \right] \right) \\ = \frac{2}{\ln\left(\frac{\Delta y}{r_0}\right)} \leftrightarrow \left(i = m, j = n \pm 1, k \in \left[o - \frac{(\Delta l - 1)}{2} : o + \frac{(\Delta l - 1)}{2} \right] \right) \\ = 1 \leftrightarrow \text{Otherwise} \end{cases} \quad (196)$$

If $\Delta x = \Delta y = \Delta z$

$$\widehat{GF}(i, j, k) \begin{cases} = \frac{2}{\ln\left(\frac{\Delta z}{r_0}\right)} \leftrightarrow \left(i = m, j = n, k \in \left[o - \frac{(\Delta l - 1)}{2} : o + \frac{(\Delta l - 1)}{2} \right] \right) \\ = \frac{2}{\ln\left(\frac{\Delta z}{r_0}\right)} \leftrightarrow \left(i = m \pm 1, j = n \pm 1, k \in \left[o - \frac{(\Delta l - 1)}{2} : o + \frac{(\Delta l - 1)}{2} \right] \right) \\ = 1 \leftrightarrow \text{Otherwise} \end{cases} \quad (197)$$

The two general forms

$$GF(i, j, k) = \begin{cases} \frac{\Delta z_0}{\Delta z} \in (0, 1] \leftrightarrow (i = m, j = n, k = o) \\ = 1 \leftrightarrow \text{Otherwise} \end{cases}$$

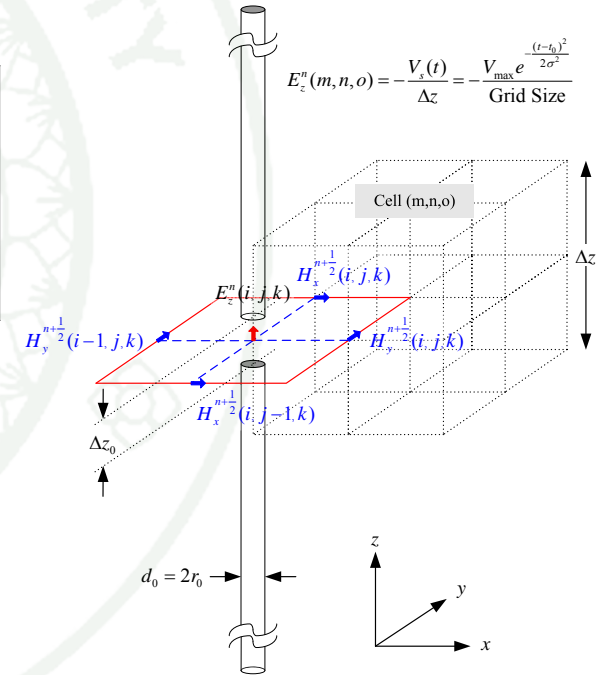
If $\frac{\Delta z_0}{\Delta z} = 1$ then these general forms present the infinitesimal gap model

$$\widehat{GF}_x(i, j, k) = \begin{cases} \frac{2}{\ln\left(\frac{\Delta x}{r_0}\right)} \leftrightarrow \left(i = m, j = n, k \in \left[o - \frac{(\Delta l - 1)}{2} : o + \frac{(\Delta l - 1)}{2} \right]\right) \\ \frac{2}{\ln\left(\frac{\Delta x}{r_0}\right)} \leftrightarrow \left(i = m \pm 1, j = n, k \in \left[o - \frac{(\Delta l - 1)}{2} : o + \frac{(\Delta l - 1)}{2} \right]\right) \\ = 1 \leftrightarrow \text{Otherwise} \end{cases}$$

$$\widehat{GF}_y(i, j, k) = \begin{cases} \frac{2}{\ln\left(\frac{\Delta y}{r_0}\right)} \leftrightarrow \left(i = m, j = n, k \in \left[o - \frac{(\Delta l - 1)}{2} : o + \frac{(\Delta l - 1)}{2} \right]\right) \\ \frac{2}{\ln\left(\frac{\Delta y}{r_0}\right)} \leftrightarrow \left(i = m, j = n \pm 1, k \in \left[o - \frac{(\Delta l - 1)}{2} : o + \frac{(\Delta l - 1)}{2} \right]\right) \\ = 1 \leftrightarrow \text{Otherwise} \end{cases}$$

$$H_y^{n+\frac{1}{2}}(i, j, k) = H_y^{n-\frac{1}{2}}(i, j, k) - \left(\frac{\Delta t}{\mu}\right) \left[\begin{aligned} & \left(\frac{E_x^n(i, j, k+1) - E_x^n(i, j, k)}{\Delta z} \right) \\ & \left(\frac{GF(i+1, j, k) \cdot \widehat{GF}_x(i+1, j, k) \cdot E_z^n(i+1, j, k) - GF(i, j, k) \cdot \widehat{GF}_x(i, j, k) \cdot E_z^n(i, j, k)}{\Delta x} \right) \end{aligned} \right]$$

$$H_x^{n+\frac{1}{2}}(i, j, k) = H_x^{n-\frac{1}{2}}(i, j, k) - \left(\frac{\Delta t}{\mu}\right) \left[\begin{aligned} & \left(\frac{GF(i, j+1, k) \cdot \widehat{GF}_y(i, j+1, k) \cdot E_z^n(i, j+1, k) - GF(i, j, k) \cdot \widehat{GF}_y(i, j, k) \cdot E_z^n(i, j, k)}{\Delta y} \right) \\ & \left(\frac{E_y^n(i, j, k+1) - E_y^n(i, j, k)}{\Delta z} \right) \end{aligned} \right]$$



$$E_z^n(m, n, o) = -\frac{V_s(t)}{\Delta z} = -\frac{V_{\max}}{\text{Grid Size}} e^{-\frac{(t-t_0)^2}{2\sigma^2}}$$

Figure 124 The two general forms of the dipole feeding gap.

Equation (193) and Equation (194) are the generalization of feeding gap models for dipole antenna. In addition, the one-cell gap model, the infinitesimal gap model and the finite gap model are generalized. It is apparent that if $\frac{\Delta z_0}{\Delta z} = 1$ then these equations are equal to the equations of infinitesimal gap model. Especially, it is easy to implement to the smart algorithm, Equation (161) to Equation (167).

1.5 The Electromagnetic Cycle (EM-Cycle)

The smart algorithm, from Equation (161) to Equation (167), is the best algorithm to analyze the electromagnetic problems. However, it is hard to understand. To put it more simply, the author proposed the Electromagnetic Cycle (EM-Cycle) corresponding to the smart algorithm. The Electromagnetic Cycle is as the following figure

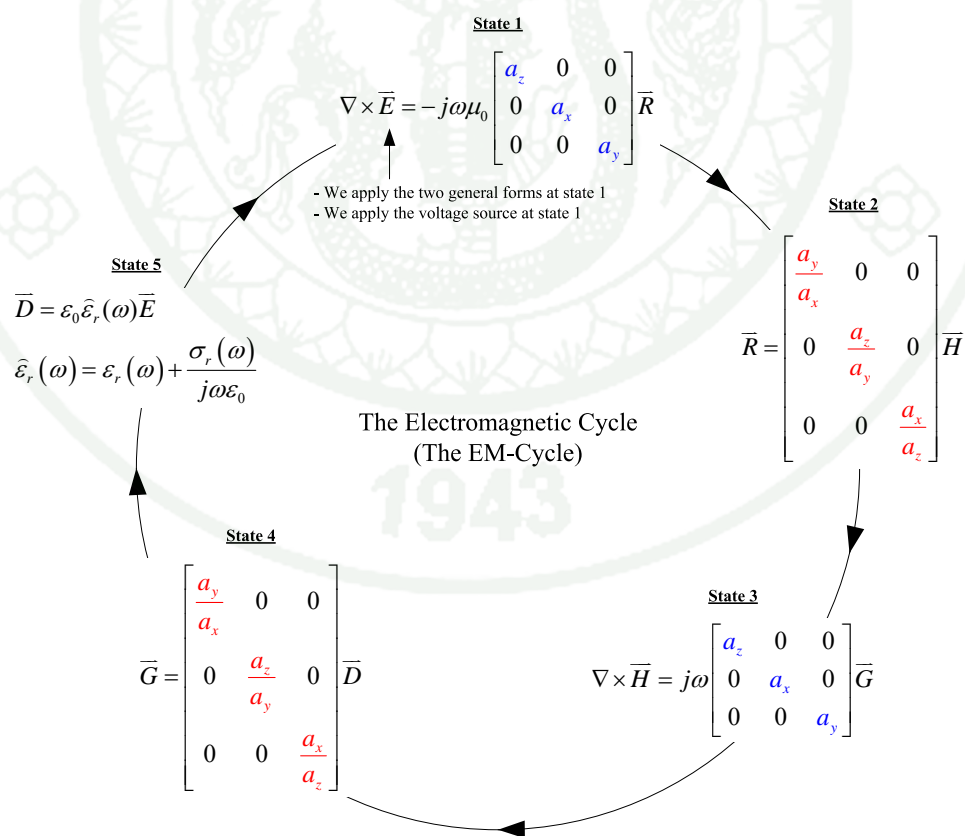


Figure 125 The Electromagnetic Cycle (EM-Cycle).

1.6 The simulated dipole feeding gap model

This research uses the Gaussian pulse to excite the one-cell gap, the infinitesimal gap and the finite gap. Its results, input impedance and return loss, will be compared to MoM. Geometry for this model is drawn as the following figure

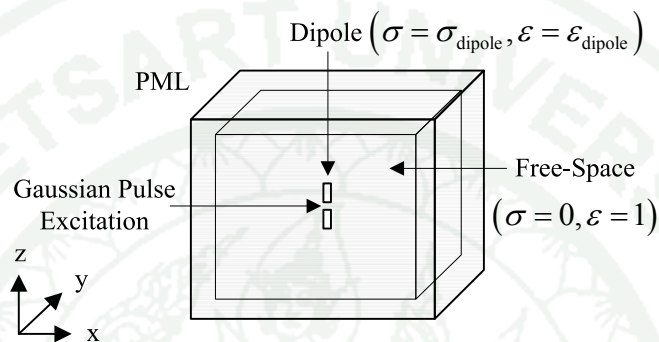


Figure 126 Geometry for the simulated dipole feeding gap.

2. The Reduced Domain

Sometime, we need to truncate the model. Then, this research proposes the reduced domain which is the computational domain truncated by 40 %. The results will be compared to the reference model, Figure 91.

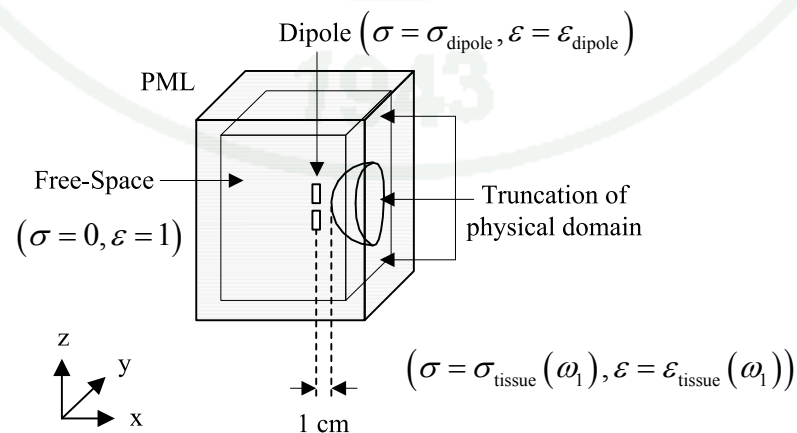


Figure 127 Geometry for the reduced domain.

3. The FDTD Simulation of a Mobile Phone Operating near a Metal Wall

This research proposes the model of the FDTD simulation of a mobile phone operating near a Metal Wall (Appendix Figure A4). Also, geometry for this model is drawn as the following figure

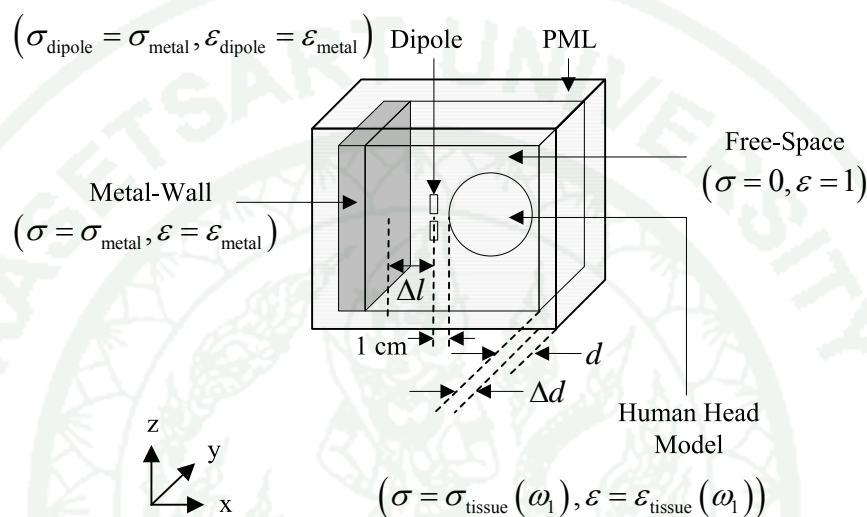


Figure 128 Geometry for the FDTD simulation of a mobile phone operating near a Metal Wall.

Source: Homsup and Jariyanorawiss (2006); Homsup *et al.* (2008b, 2009a); Jariyanorawiss and Homsup (2006); Jariyanorawiss *et al.* (2009)

The simulated physical domain is containing a dipole antenna, an artificial human head and a Metal Wall. A Metal Wall which can reflect waves has a thickness of about 1 cm. Also, a Metal Wall is located at a various distances, Δl , (0-20 cm) away from a dipole. In addition, the dipole is fixed at 1 cm away from the artificial human head. In brief, the results of this model (SAR 1-g, SAR 10-g and P_{avg}) will be compared to the results from the reference model, Figure 91.

RESULTS AND DISCUSSION

Results

In this research, the simulations were computed in the Research Center of Applied Electromagnetic (RECAPE) laboratory and were divided into three parts which consisted of the verification of FDTD programming, the simulation of a reduced computational domain and the simulation of a mobile phone operating near a Metal Wall. In conclusion, the readers please follow the diagram in Appendix Figure A5.

1. The Verification of the FDTD Programming

1.1 The excitation for comparison of the electromagnetic field (E_{Total}) simulated by the FDTD programming

The feeding signal is the Gaussian excitation as well as Equation (170).

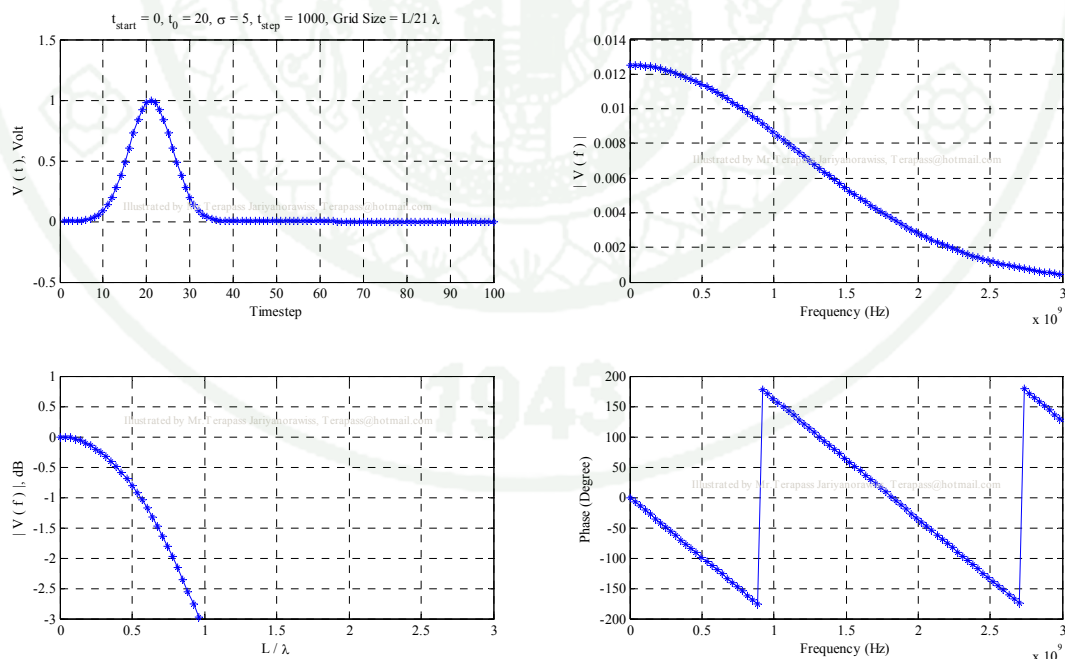


Figure 129 Sample of the feeding signal for the one-cell gap model, the infinitesimal

gap model and the finite gap model, $\frac{l}{\Delta} = 21$.

1.2 Comparison of the electromagnetic field (E_{Total} , dB) simulated by the FDTD programming between xy-plane and xz-plane

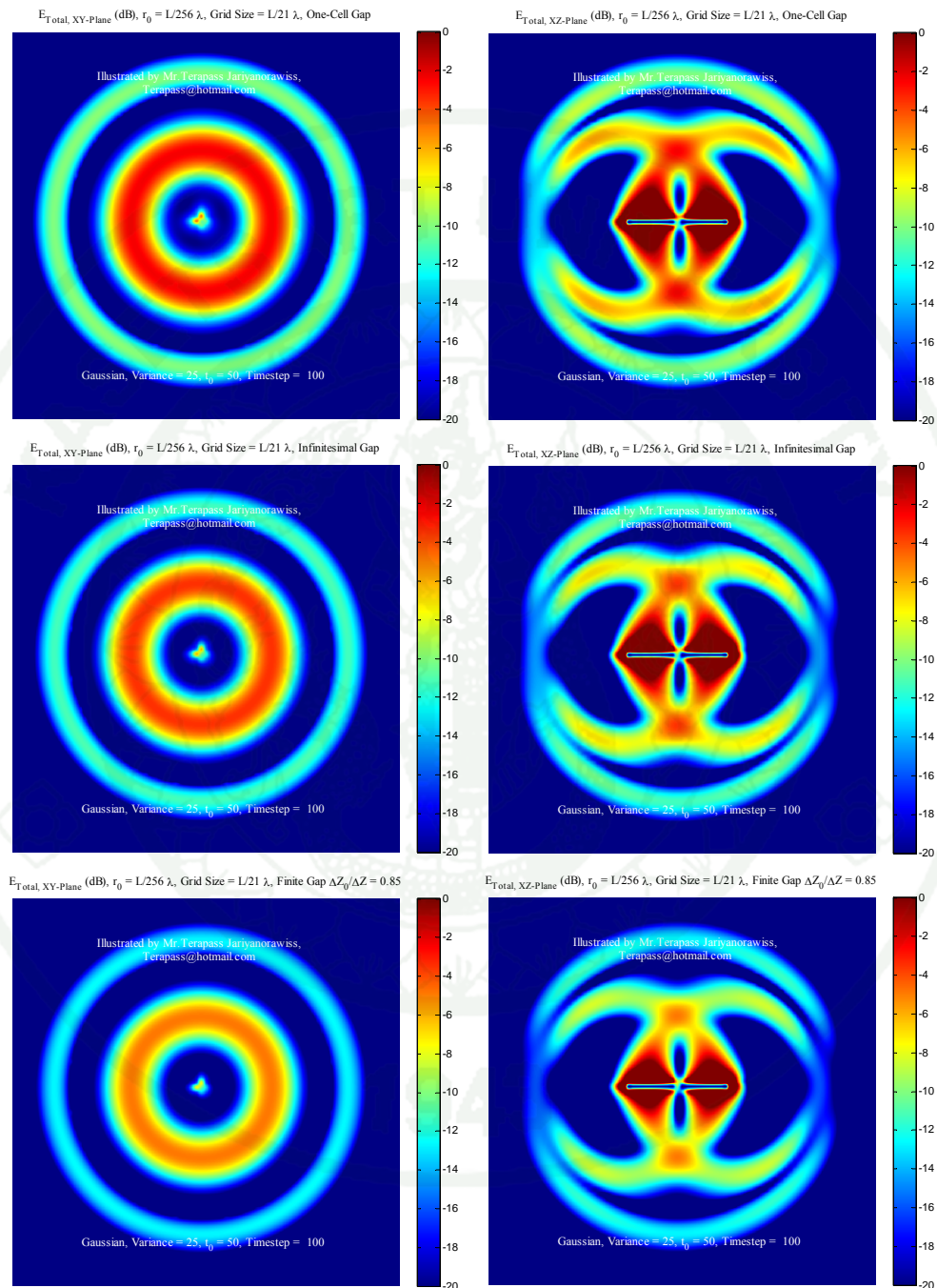


Figure 130 Comparison of the electromagnetic field (E_{Total} , dB) simulated by the one-cell gap model, the infinitesimal gap model and the finite gap model $\frac{\Delta z_0}{\Delta z} = 0.85$, respectively, at timestep = 100.

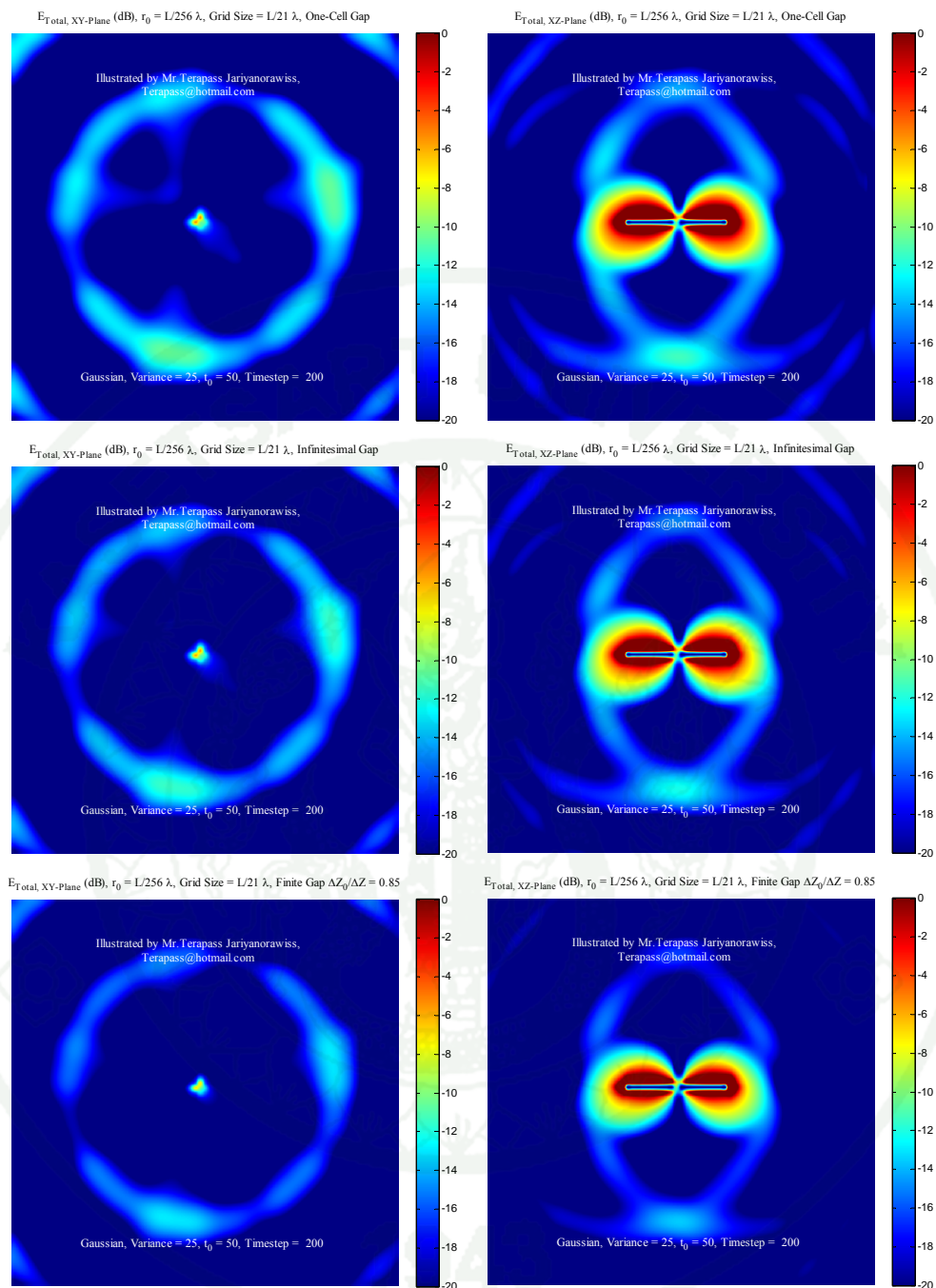


Figure 131 Comparison of the electromagnetic field (E_{Total} , dB) simulated by the one-cell gap model, the infinitesimal gap model and the finite gap model $\frac{\Delta z_0}{\Delta z} = 0.85$, respectively, at timestep = 200.

1.3 The excitation for comparison of the input impedance simulated by the FDTD programming

The feeding signal is the Gaussian excitation as well as Equation (170).

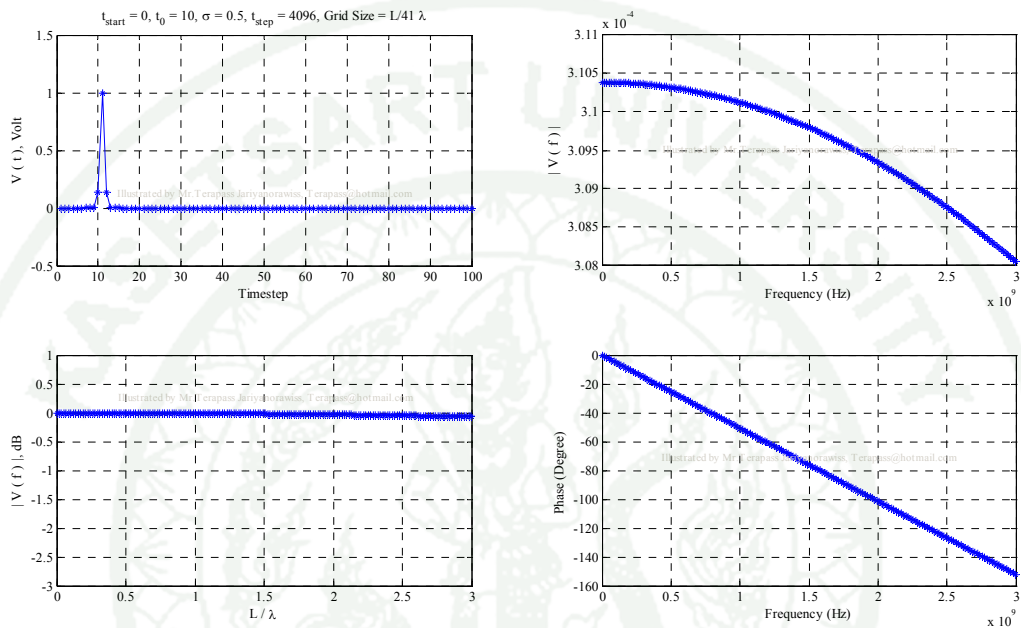


Figure 132 Sample of the feeding signal for the one-cell gap model, the infinitesimal gap model and the finite gap model, $\frac{l}{\Delta} = 41$, Timestep = 4096.

The feeding signal is the Gaussian excitation as well as Equation (170). There are slightly different,

$$\frac{l}{\Delta} = 21, \text{ Timestep} = 2048, \text{ Domain} = 70 \times 70 \times 70$$

$$\frac{l}{\Delta} = 41, \text{ Timestep} = 4096, \text{ Domain} = 100 \times 100 \times 100$$

$$\frac{l}{\Delta} = 61, \text{ Timestep} = 4096, \text{ Domain} = 150 \times 150 \times 150$$

Sample of the other parameters are as the following table

Table 20 Sample of parameters for simulate feeding-gap of the dipole antenna,

$$\frac{l}{\Delta} = 41.$$

Parameters	Value	Unit
Velocity (c)	3.00E+08	m/s
Frequency (f)	1.00E+09	Hertz
Wavelength (λ)	0.30000	m
Dipole Length (l) / Wavelength (λ)	1.00	-
Dipole Length (l)	0.30	m
Dipole Segment (n)	41	-
Dipole Length (l) / Dipole Segment (n)	0.00732	m
V_{\max}	1	Volts
$\Delta t \leq$	1.40817E-11	s
Timestep	4096	-
t_0	10	-
σ -Gaussian	0.5	-
Domain	100x100x100	-
Grid Size (Δ)	0.00732	m
Feeding-Gap Address	50,50,50	-
PML, Layer	10	-
PML, Degree (m)	3	-
PML, σ -max	30	-

1.4 The input impedance simulated by the commercial software, XFDTD, and the FDTD programming

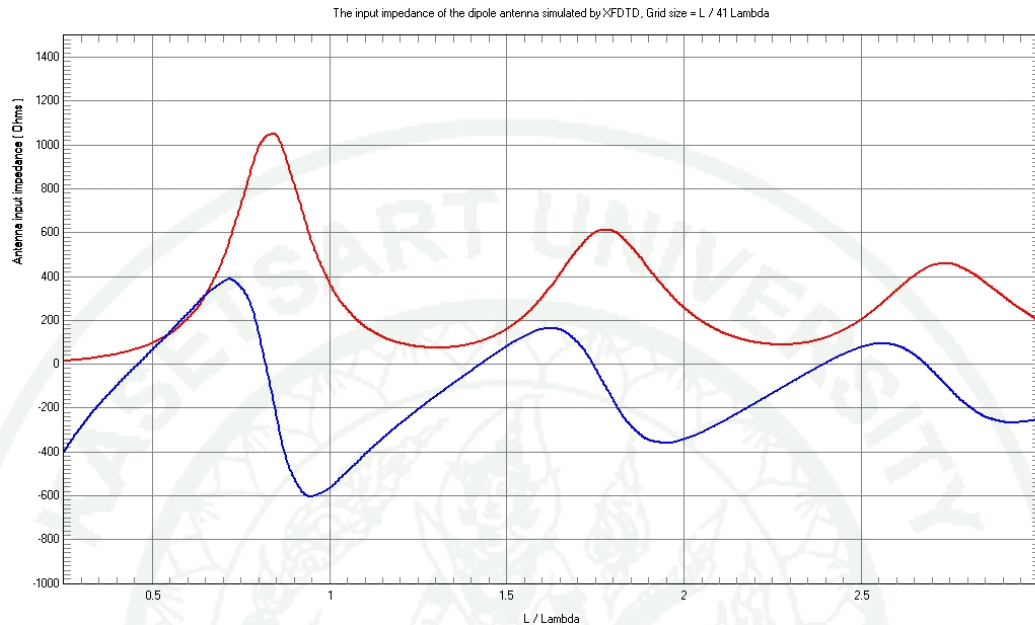


Figure 133 The input impedance simulated by the commercial software, XFDTD.

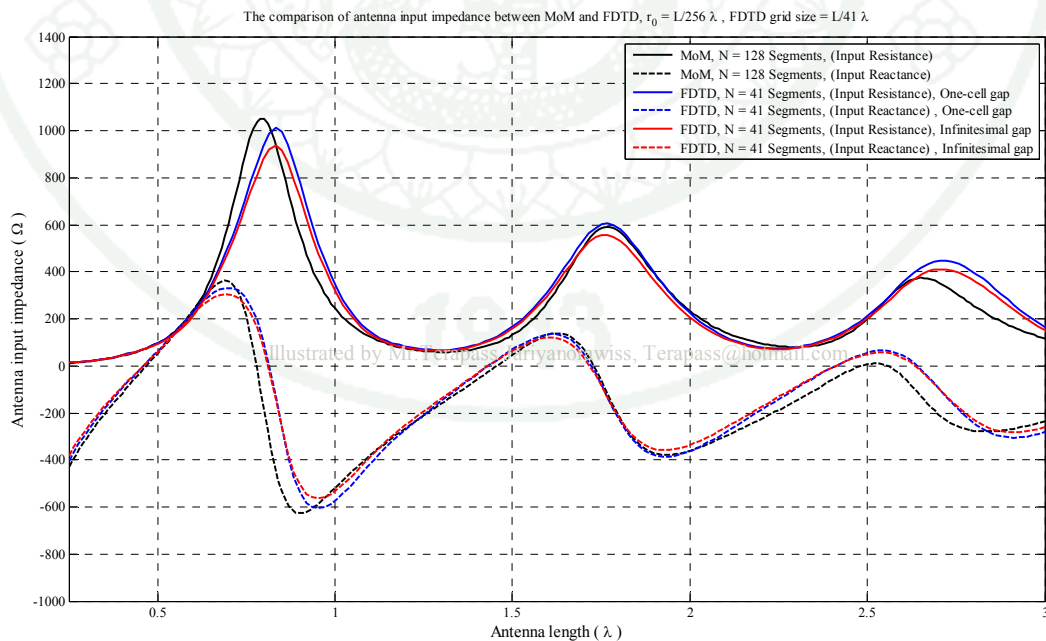


Figure 134 The input impedance simulated by MoM and the FDTD programming.

1.5 The input impedance and the return loss simulated by MoM and the FDTD programming

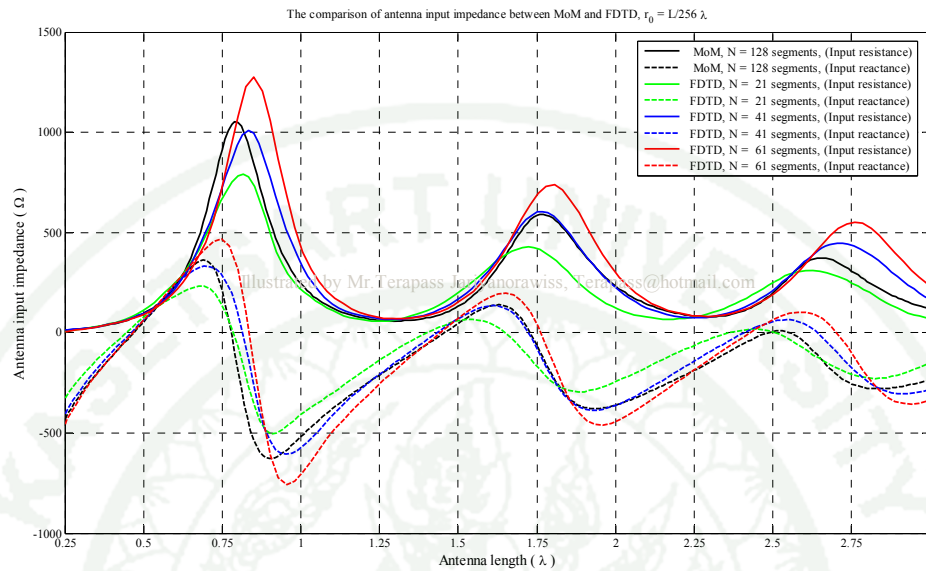


Figure 135 Comparison the input impedance simulated by MoM, $N = 128$, and the one-cell gap model, $l/r_0 = 256$.

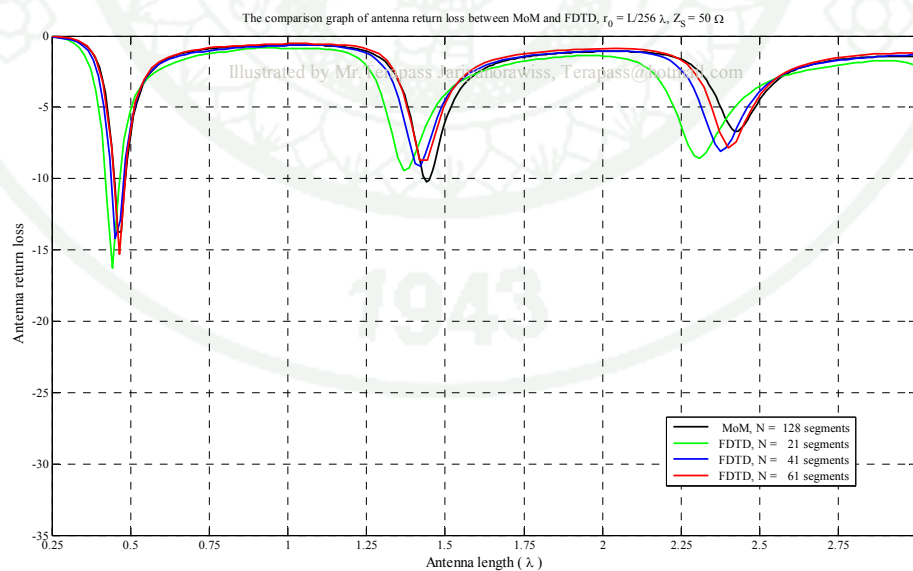


Figure 136 Comparison the return loss simulated by MoM, $N = 128$, and the one-cell gap model, $l/r_0 = 256$, $Z_S = 50 \Omega$.

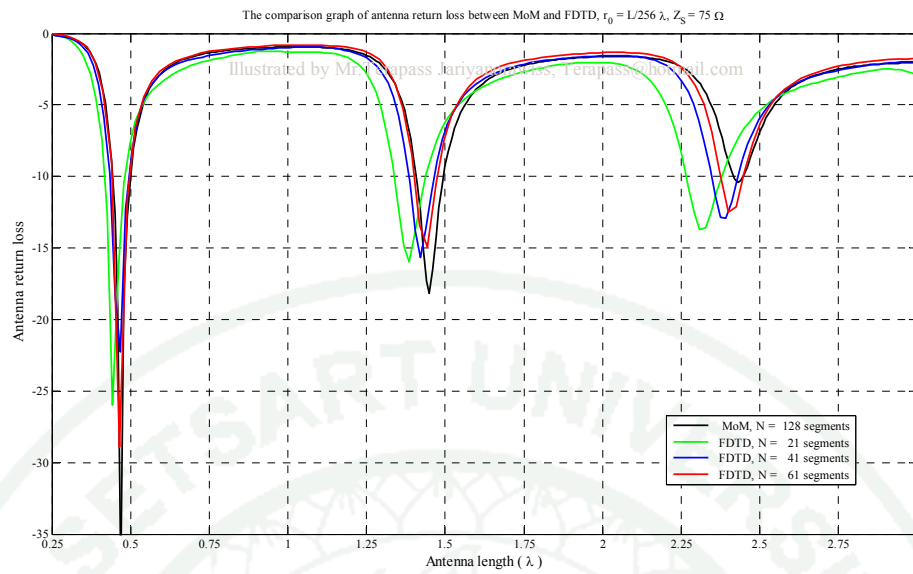


Figure 137 Comparison the return loss simulated by MoM, $N = 128$, and the one-cell gap model, $l / r_0 = 256$, $Z_S = 75 \Omega$.

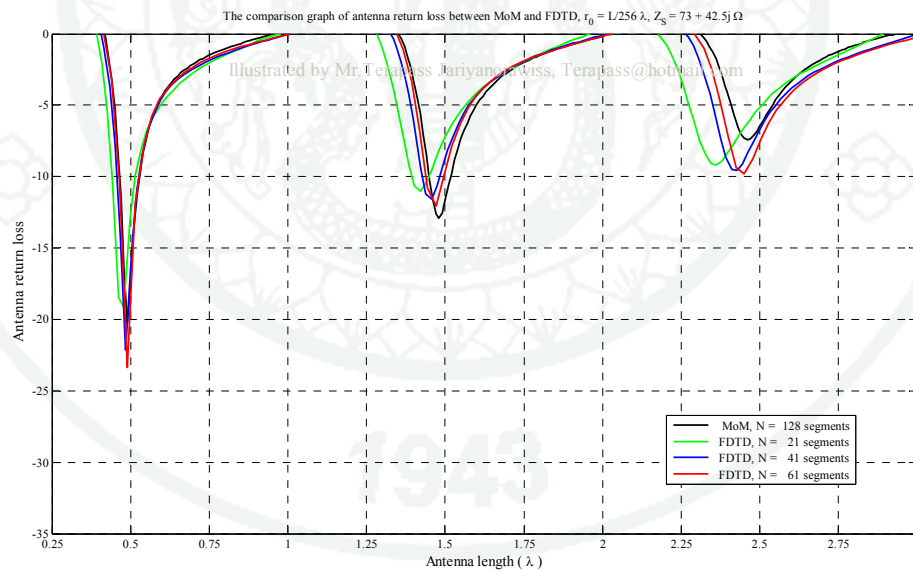


Figure 138 Comparison the return loss simulated by MoM, $N = 128$, and the one-cell gap model, $l / r_0 = 256$, $Z_S = 73 + j42.5 \Omega$.

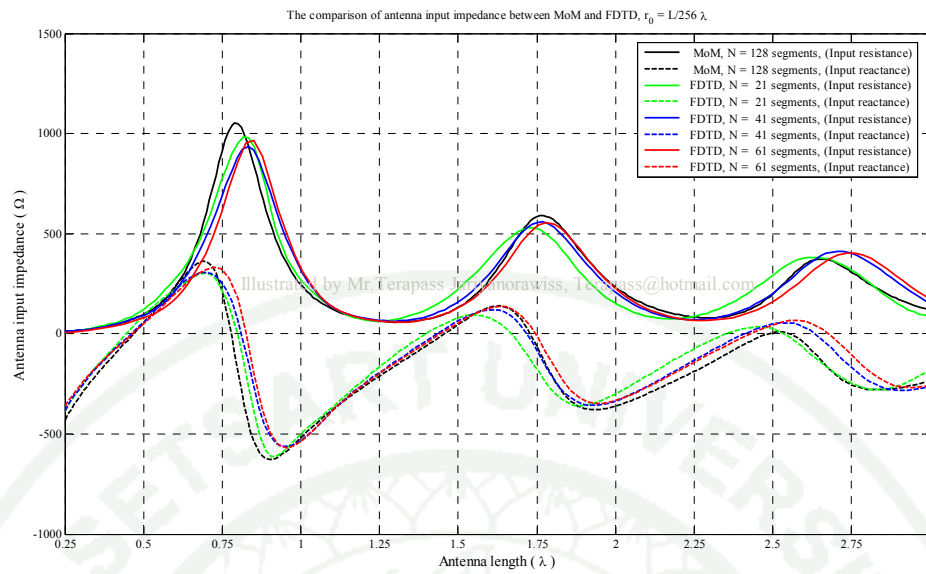


Figure 139 Comparison the input impedance simulated by MoM, $N = 128$, and the infinitesimal gap model, $l / r_0 = 256$.

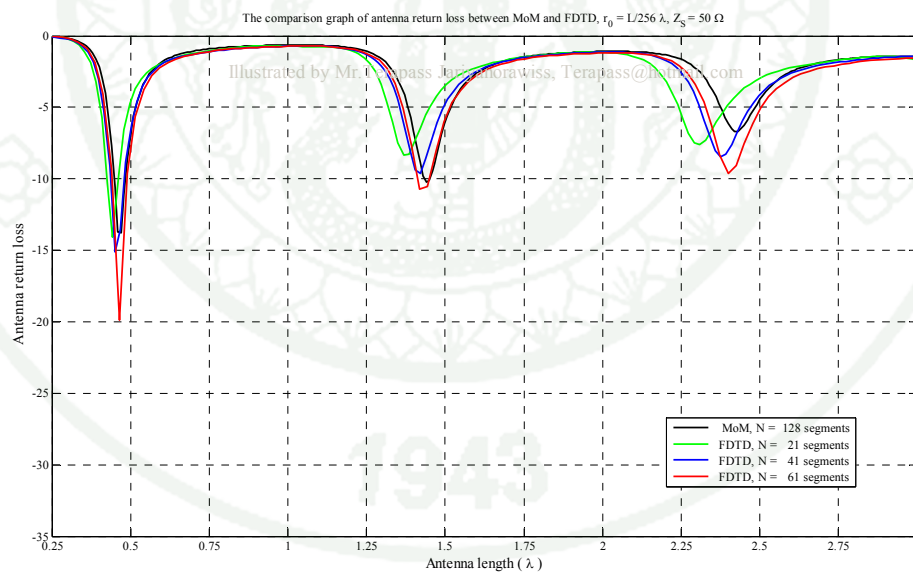


Figure 140 Comparison the return loss simulated by MoM, $N = 128$, and the infinitesimal gap model, $l / r_0 = 256$, $Z_S = 50 \Omega$.

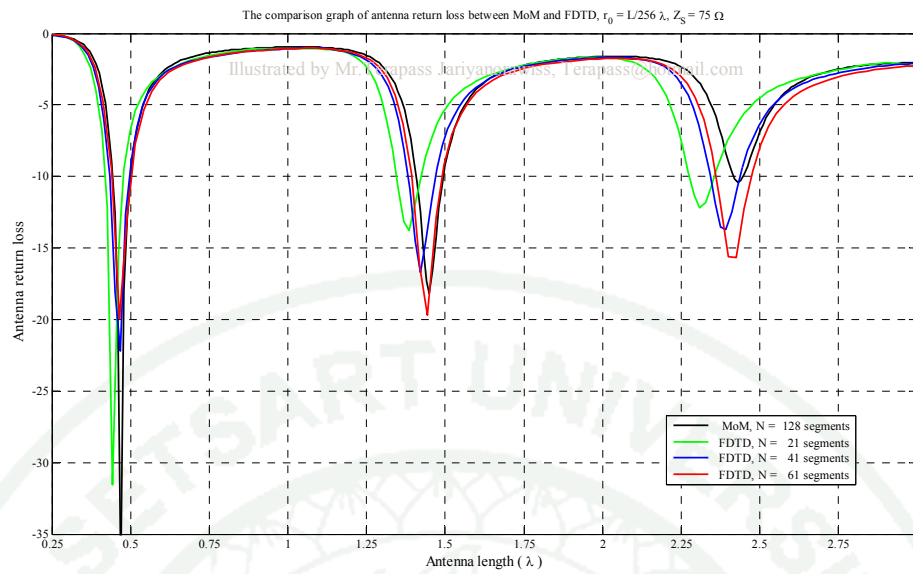


Figure 141 Comparison the return loss simulated by MoM, $N = 128$, and the infinitesimal gap model, $l / r_0 = 256$, $Z_S = 75 \Omega$.

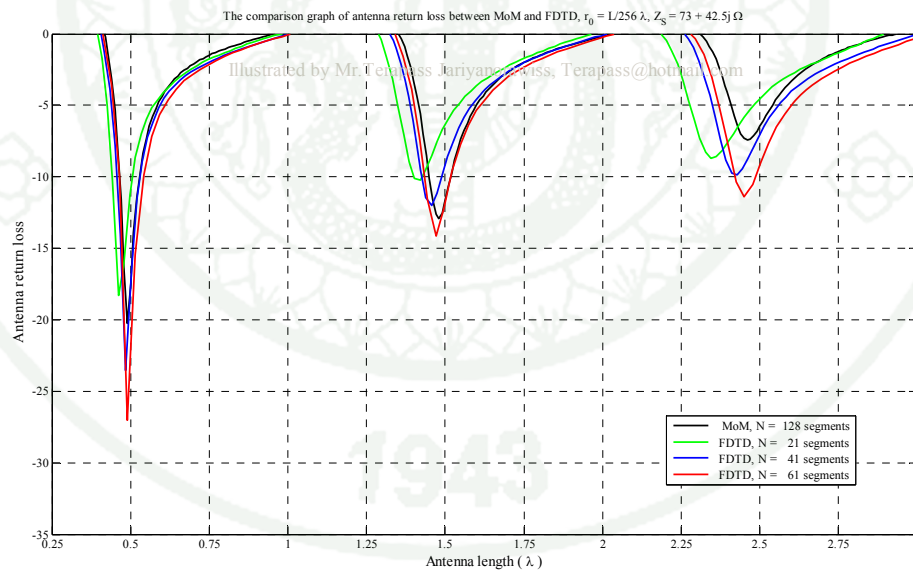


Figure 142 Comparison the return loss simulated by MoM, $N = 128$, and the infinitesimal gap model, $l / r_0 = 256$, $Z_S = 73 + j42.5 \Omega$.

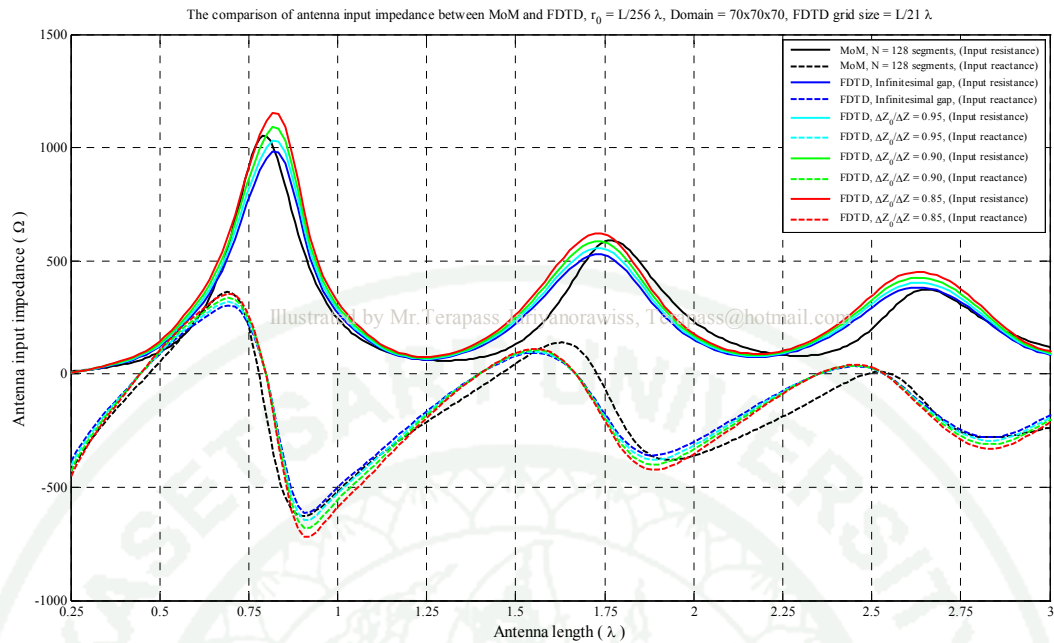


Figure 143 Comparison the input impedance simulated by MoM, $N = 128$, the infinitesimal gap and the finite gap model, $l/r_0 = 256$.

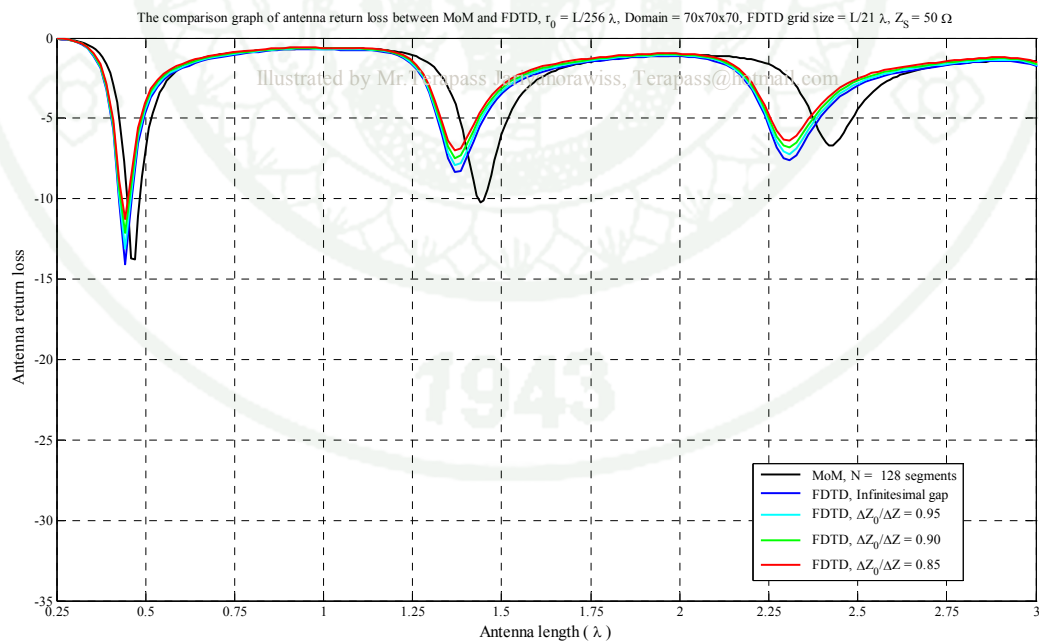


Figure 144 Comparison the return loss simulated by MoM, $N = 128$, the infinitesimal gap and the finite gap model, $l/r_0 = 256$, $Z_S = 50 \Omega$.

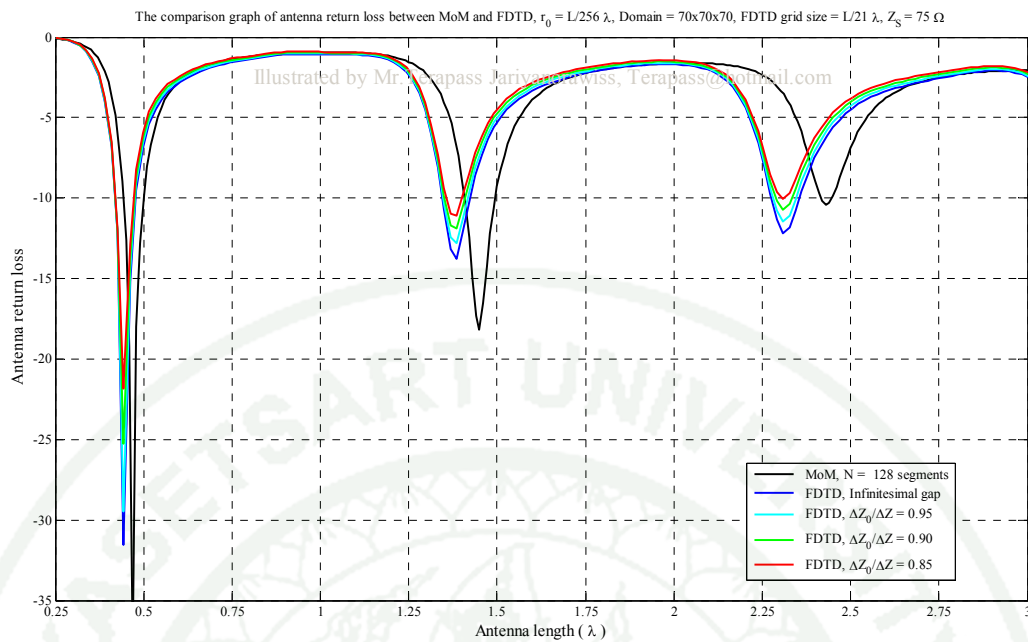


Figure 145 Comparison the return loss simulated by MoM, N = 128, the infinitesimal gap and the finite gap model, $l/r_0 = 256$, $Z_S = 75 \Omega$.

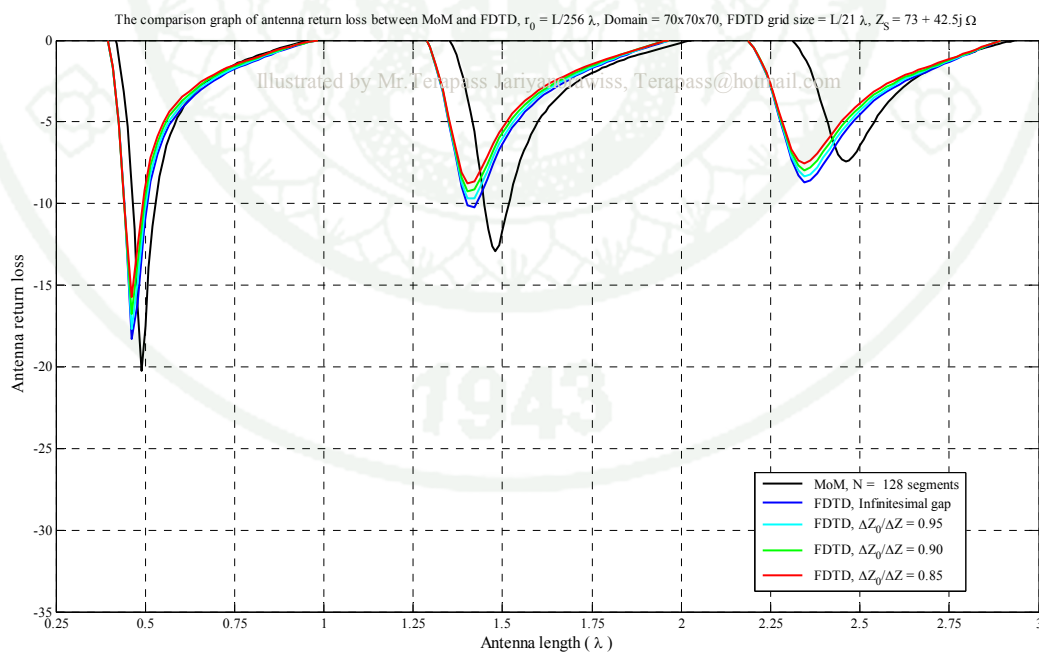


Figure 146 Comparison the return loss simulated by MoM, N = 128, the infinitesimal gap and the finite gap model, $l/r_0 = 256$, $Z_S = 73 + j42.5 \Omega$.

2. The Reduced Domain

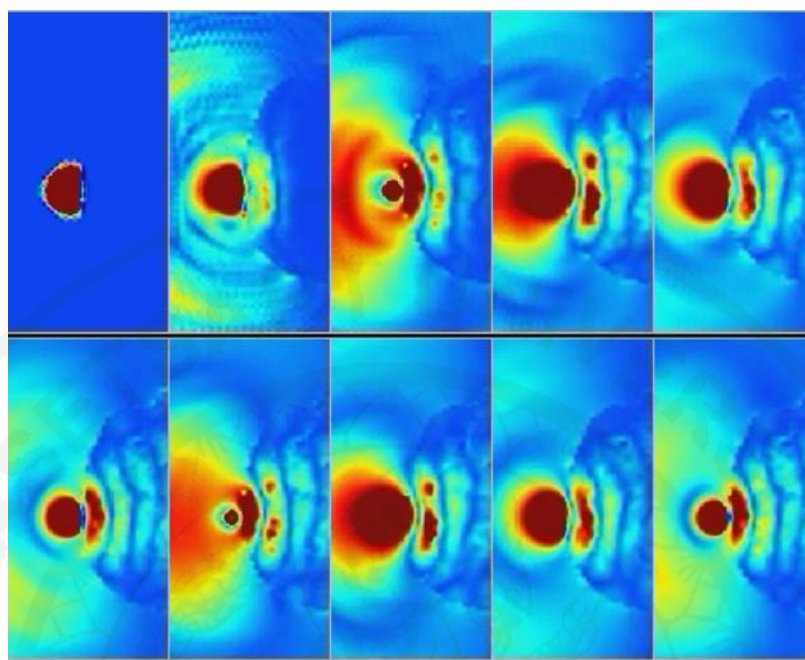


Figure 147 The simulation of a mobile phone located at 1 cm from a human head with a truncated domain and a mobile phone operated at 900 MHz. The simulation start from 0 and end with $1000\Delta t$.

Source: Jariyanorawiss and Homsup (2005b)

Table 21 Comparison of SAR between reference model and compact model at 900 MHz.

Freq = 900 MHz	SAR 1-g (W/kg)			SAR 10-g (W/kg)	Max SAR (W/kg)
	Cell 1	Cell 2	Cell 3		
Reference domain	1.44307	1.12532	0.84079	1.30634	3.9732
40 % Reduced domain	1.44861	1.13991	0.85311	1.31526	3.9934
% Error	0.3839	1.29652	1.46529	0.68282	0.50841

Source: Homsup *et al.* (2009a)

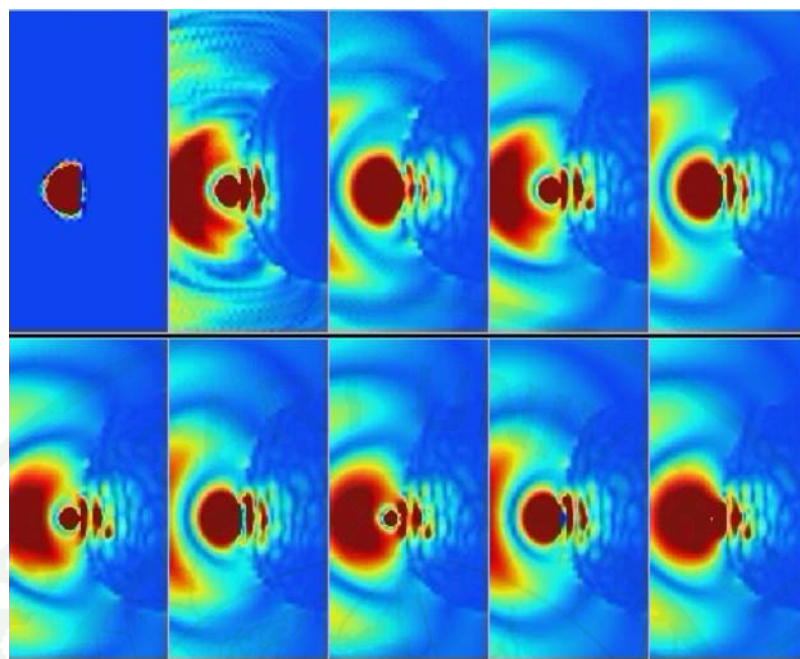


Figure 148 The simulation of a mobile phone located at 1 cm from a human head with a truncated domain and a mobile phone operated at 1.8 GHz. The simulation start from 0 and end with $1000\Delta t$.

Source: Jariyanorawiss and Homsup (2005b)

Table 22 Comparison of SAR between reference model and compact model at 1.8 GHz.

Freq = 1.8 GHz	SAR 1 g (W/kg)			SAR 10 g (W/kg)	Max SAR (W/kg)
	Cell 1	Cell 2	Cell 3		
Reference domain	1.28455	0.92336	1.15199	1.17044	6.9036
40 % Reduced domain	1.28438	0.92363	1.15197	1.17042	6.9015
% Error	0.01323	0.02924	0.00174	0.00171	0.03042

Source: Homsup *et al.* (2009a)

3. The Simulation of a Mobile Phone Operating near a Metal Wall

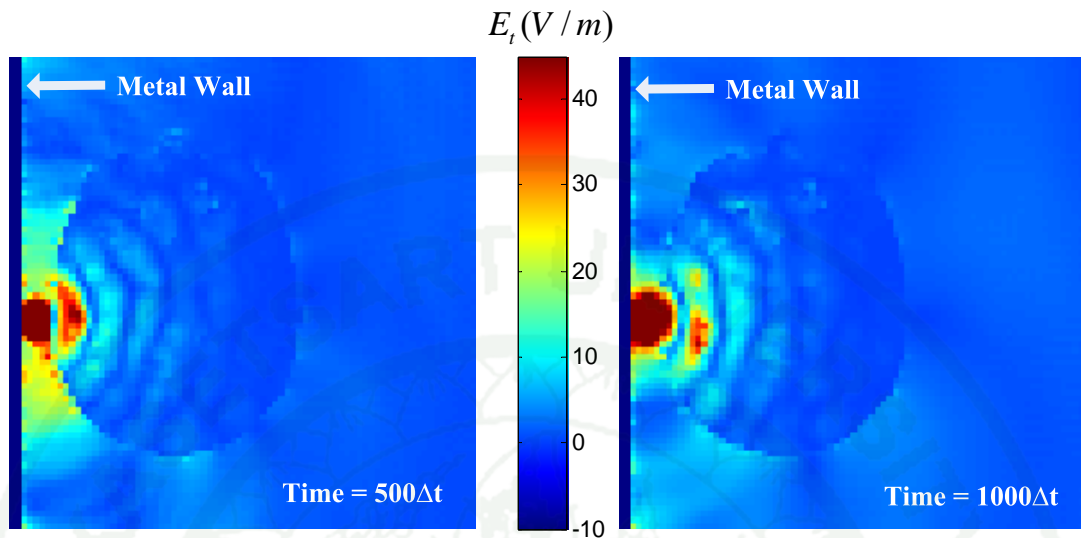


Figure 149 Top view of E_t in the simulated physical domain (Operating frequency = 900 MHz and $\Delta l = 1$ cm).

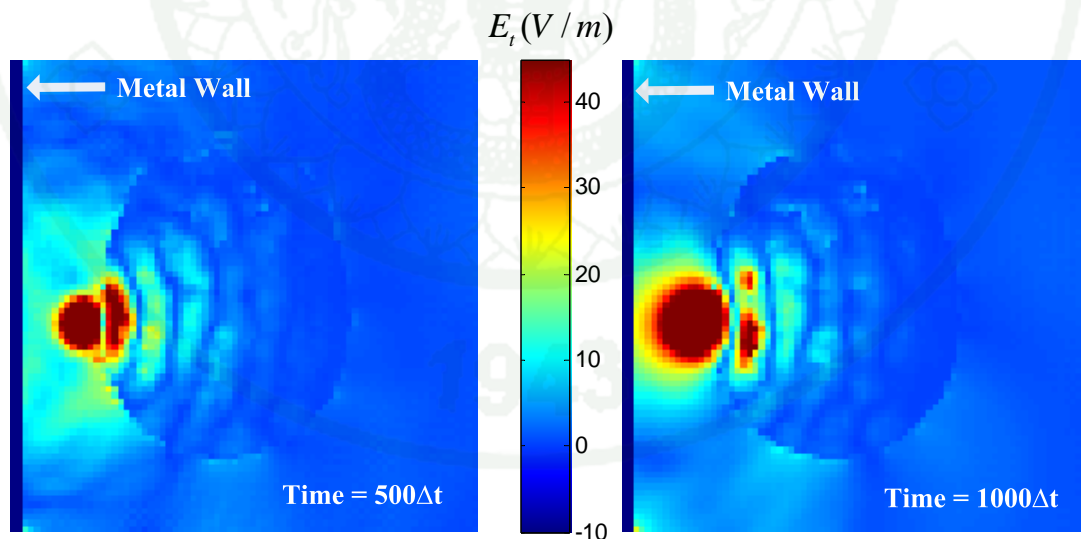


Figure 150 Top view of E_t in the simulated physical domain (Operating frequency = 900 MHz and $\Delta l = 5$ cm).

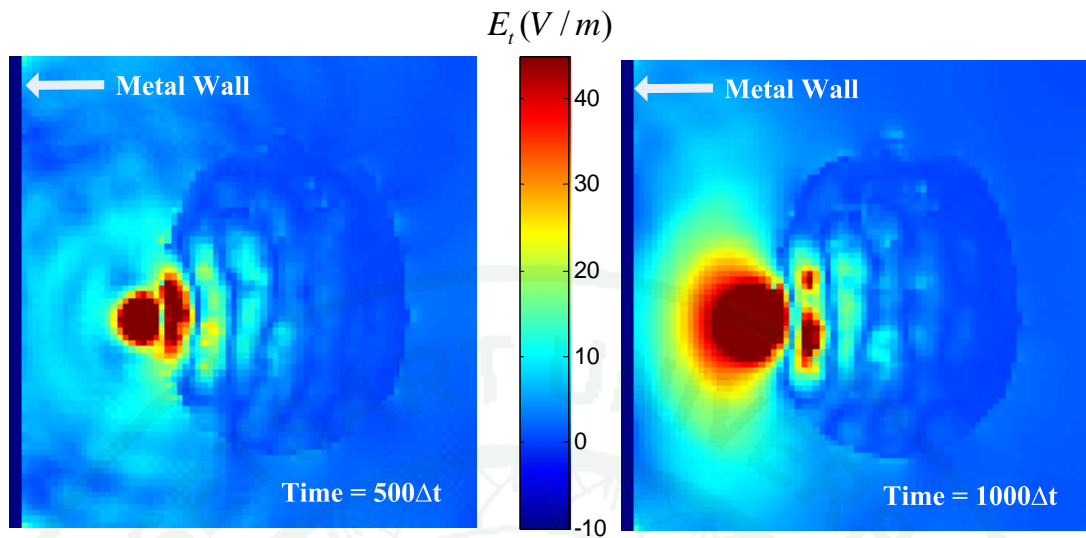


Figure 151 Top view of E_t in the simulated physical domain
(Operating frequency = 900 MHz and $\Delta l = 10$ cm).

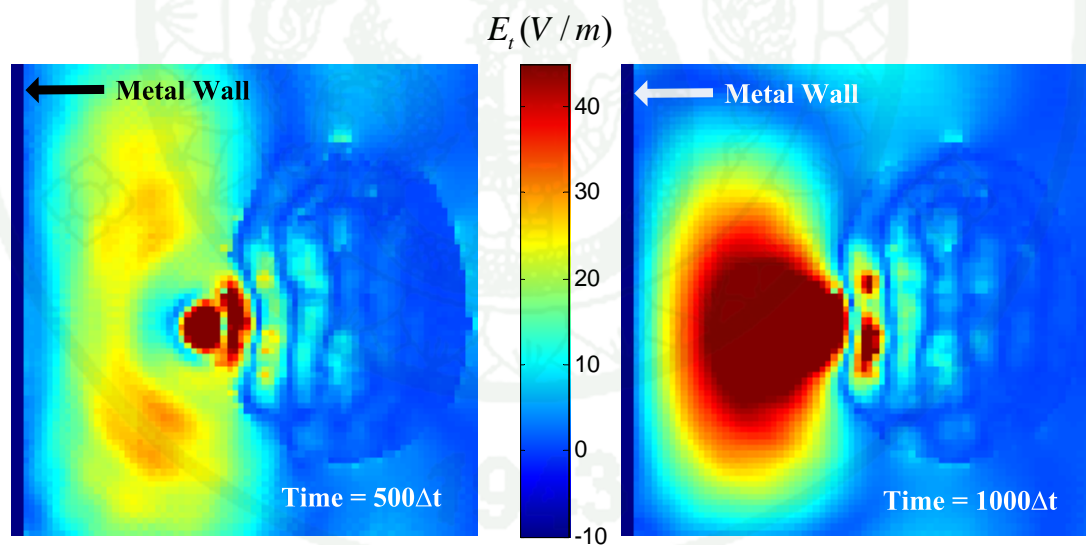


Figure 152 Top view of E_t in the simulated physical domain
(Operating frequency = 900 MHz and $\Delta l = 15$ cm).

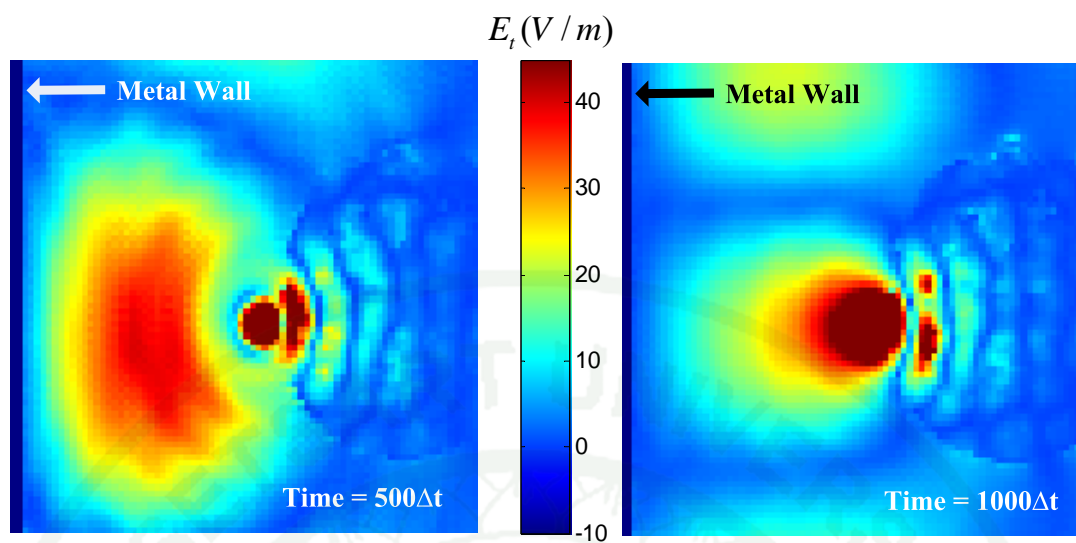


Figure 153 Top view of E_r in the simulated physical domain
(Operating frequency = 900 MHz and $\Delta l = 20$ cm).

Table 23 The comparison table of SAR 1-g, SAR 10-g and the average power absorbed (P_{avg}) by a human head respecting to Δl , frequency = 900 MHz.

Operating Frequency = 900 MHz			
Δl (cm)	SAR 1-g (W/kg)	SAR 10-g (W/kg)	P_{avg} (Watts)
0	0.61379	0.40430	0.02219
1	1.00024	0.87751	0.12693
2	1.27426	1.12381	0.15684
3	1.35583	1.20720	0.17440
4	1.39680	1.25170	0.18601
5	1.41969	1.27754	0.19440
6	1.43345	1.29431	0.20102
7	1.44151	1.30465	0.20668
8	1.44639	1.31209	0.21190
9	1.44840	1.31631	0.21699
10	1.44866	1.31897	0.22221
11	1.44791	1.32053	0.22772
12	1.44671	1.32141	0.23340
13	1.44631	1.32221	0.23872
14	1.44784	1.32325	0.24227
15	1.45177	1.32394	0.24199
16	1.45654	1.32305	-
17	1.45884	1.31903	-
18	1.45761	1.31287	-
19	1.45393	1.30691	-
20	1.44850	1.30131	-

Note 1. Reduced domain at $\Delta l = 16-20$ cm.

2. SAR 1-g, IEEE Standard, = 1.6 W/kg

3. SAR 1-g, Reference model, = 1.44307 W/kg

4. SAR 10-g, Reference model, = 1.30634 W/kg

5. P_{avg} , Reference model, = 0.21486 Watts

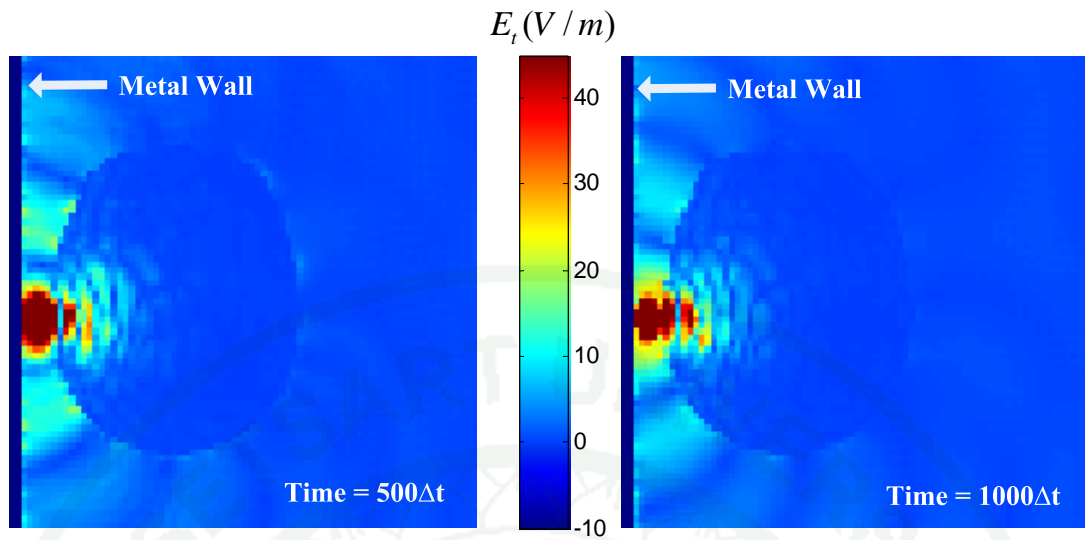


Figure 154 Top view of E_t in the simulated physical domain
(Operating frequency = 1.8 GHz and $\Delta l = 1$ cm).

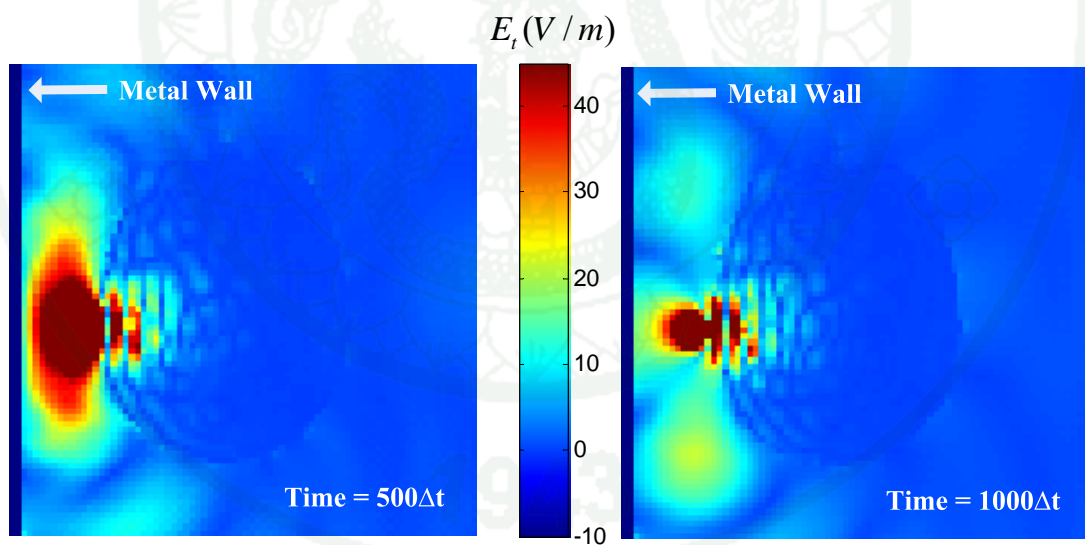


Figure 155 Top view of E_t in the simulated physical domain
(Operating frequency = 1.8 GHz and $\Delta l = 5$ cm).

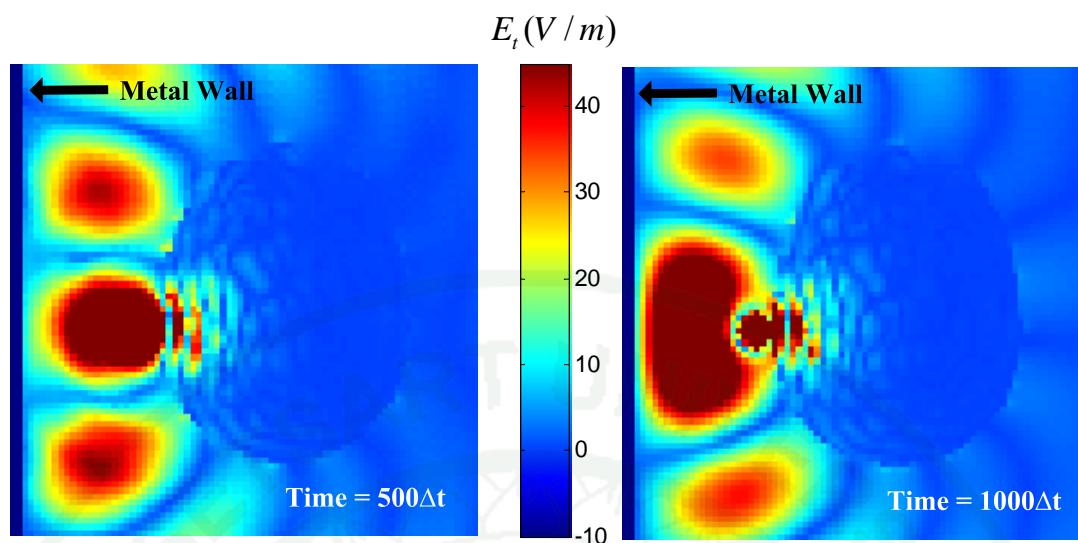


Figure 156 Top view of E_t in the simulated physical domain
(Operating frequency = 1.8 GHz and $\Delta l = 10$ cm).

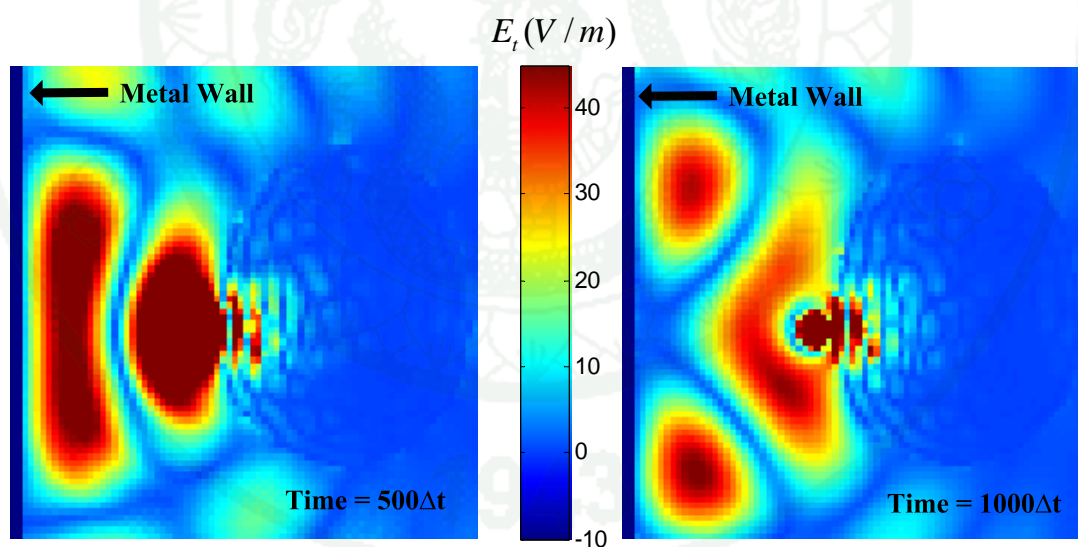


Figure 157 Top view of E_t in the simulated physical domain
(Operating frequency = 1.8 GHz and $\Delta l = 15$ cm).

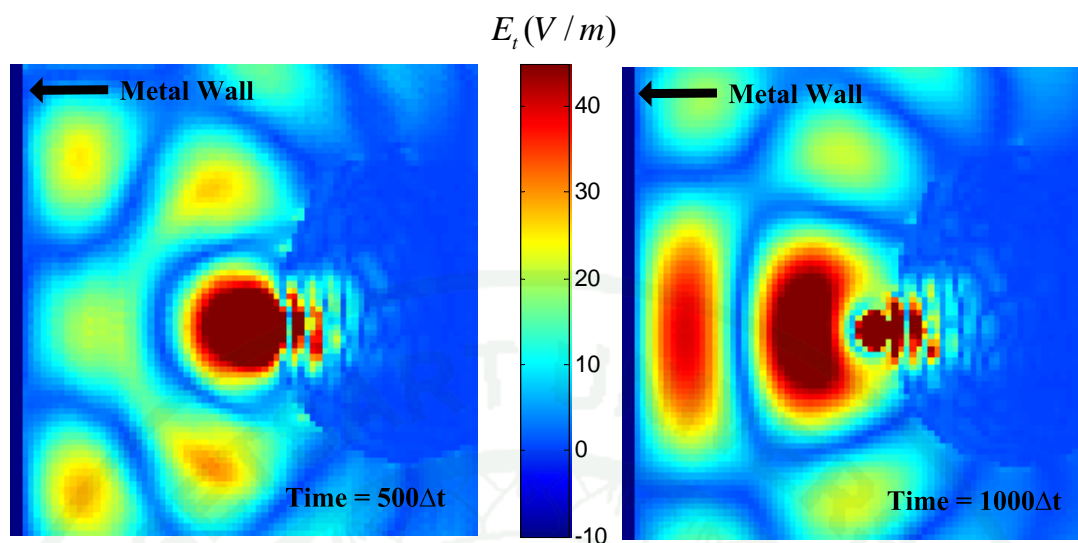


Figure 158 Top view of E_t in the simulated physical domain
(Operating frequency = 1.8 GHz and $\Delta l = 20$ cm).

Table 24 The comparison table of SAR 1-g, SAR 10-g and the average power absorbed (P_{avg}) by a human head respecting to Δl , frequency = 1.8 GHz.

Operating Frequency = 1.8 GHz			
Δl (cm)	SAR 1-g (W/kg)	SAR 10-g (W/kg)	P_{avg} (Watts)
0	0.52972	0.36830	0.02891
1	0.95286	0.84421	0.07804
2	1.19120	1.06668	0.09767
3	1.25438	1.14256	0.10954
4	1.27078	1.17600	0.12071
5	1.26223	1.18656	0.13519
6	1.24755	1.18397	0.15436
7	1.25964	1.17822	0.16393
8	1.28890	1.16948	0.14840
9	1.30374	1.16299	0.12696
10	1.30449	1.16327	0.11538
11	1.29937	1.16838	0.11287
12	1.29120	1.17403	0.11594
13	1.28025	1.17790	0.12300
14	1.26859	1.17782	0.13282
15	1.26832	1.17594	0.14006
16	1.28560	1.17708	-
17	1.30023	1.17841	-
18	1.30320	1.17733	-
19	1.29841	1.17459	-
20	1.28912	1.17211	-

Note 1. Reduced domain at $\Delta l = 16-20$ cm.

2. SAR 1-g, IEEE Standard, = 1.6 W/kg

3. SAR 1-g, Reference model, = 1.28455 W/kg

4. SAR 10-g, Reference model, = 1.17044 W/kg

5. P_{avg} , Reference model, = 0.11773 Watts

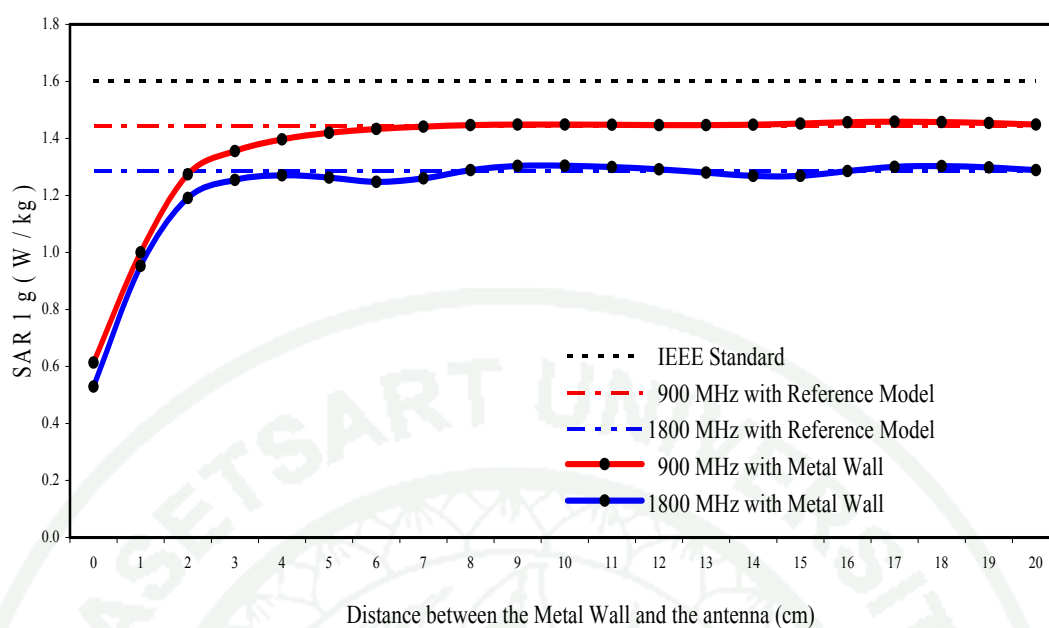


Figure 159 Spatial- average SAR 1-g respecting to the distance between the Metal Wall and the antenna, Δl .

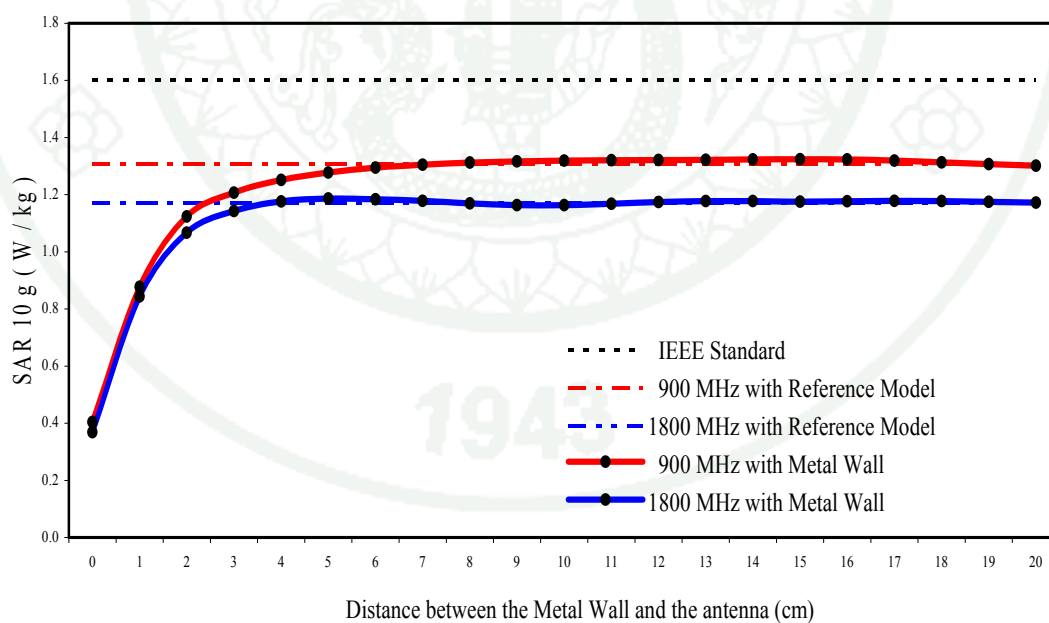


Figure 160 Spatial- average SAR 10-g respecting to the distance between the Metal Wall and the antenna, Δl .

Table 25 The comparison table of the average power absorbed (P_{avg}) by materials in the human head respecting to Δl , frequency = 900 MHz.

Average Power Absorbed (Watts) at 900 MHz (from timestep 900 - 1000)								
Distance (cm)	Materials							
	Human Head	Skin	Bone	Muscle	Fat	Eye	Brain	Blood
0	0.02219	0.01135	0.00118	0.00328	0.00203	1.8E-05	0.00242	0.00221
1	0.12693	0.06850	0.00720	0.01769	0.01165	3.5E-05	0.01268	0.01059
2	0.15684	0.08338	0.00864	0.02127	0.01491	3.8E-05	0.01654	0.01383
3	0.17440	0.09069	0.00939	0.02357	0.01721	3.6E-05	0.01938	0.01613
4	0.18601	0.09531	0.00988	0.02511	0.01877	3.4E-05	0.02132	0.01775
5	0.19440	0.09854	0.01023	0.02626	0.01990	3.2E-05	0.02273	0.01896
6	0.20102	0.10102	0.01052	0.02720	0.02078	3.2E-05	0.02384	0.01995
7	0.20668	0.10309	0.01077	0.02804	0.02152	3.3E-05	0.02477	0.02081
8	0.21190	0.10496	0.01101	0.02886	0.02218	3.6E-05	0.02560	0.02162
9	0.21699	0.10678	0.01125	0.02970	0.02281	4.1E-05	0.02637	0.02240
10	0.22221	0.10866	0.01151	0.03063	0.02342	5.0E-05	0.02710	0.02318
11	0.22772	0.11069	0.01181	0.03166	0.02404	6.2E-05	0.02780	0.02395
12	0.23340	0.11286	0.01213	0.03281	0.02463	8.1E-05	0.02841	0.02467
13	0.23872	0.11501	0.01246	0.03401	0.02514	1.0E-04	0.02883	0.02523
14	0.24227	0.11661	0.01274	0.03503	0.02538	1.3E-04	0.02887	0.02540
15	0.24199	0.11680	0.01283	0.03546	0.02516	1.5E-04	0.02833	0.02497

Table 26 The comparison table of the average power absorbed (P_{avg}) by materials in the human head respecting to Δl , frequency = 1.8 GHz.

Average Power Absorbed (Watts) at 1.8 GHz (from timestep 900 - 1000)								
Distance (cm)	Materials							
	Human Head	Skin	Bone	Muscle	Fat	Eye	Brain	Blood
0	0.02891	0.01346	0.00176	0.00499	0.00266	3.6E-06	0.00265	0.00340
1	0.07804	0.03617	0.00430	0.01296	0.00863	5.1E-06	0.00828	0.00794
2	0.09767	0.04487	0.00527	0.01621	0.01087	4.3E-06	0.01055	0.01016
3	0.10954	0.04964	0.00582	0.01838	0.01224	3.9E-06	0.01206	0.01167
4	0.12071	0.05392	0.00639	0.02067	0.01347	5.8E-06	0.01338	0.01316
5	0.13519	0.05942	0.00723	0.02393	0.01493	2.1E-05	0.01483	0.01507
6	0.15436	0.06699	0.00853	0.02866	0.01669	7.7E-05	0.01628	0.01731
7	0.16393	0.07126	0.00944	0.03171	0.01730	1.6E-04	0.01622	0.01797
8	0.14840	0.06558	0.00870	0.02862	0.01559	1.5E-04	0.01414	0.01574
9	0.12696	0.05718	0.00736	0.02350	0.01353	1.0E-04	0.01224	0.01317
10	0.11538	0.05244	0.00652	0.02045	0.01253	6.0E-05	0.01158	0.01196
11	0.11287	0.05127	0.00623	0.01952	0.01241	3.6E-05	0.01177	0.01184
12	0.11594	0.05232	0.00629	0.01996	0.01282	2.2E-05	0.01240	0.01236
13	0.12300	0.05497	0.00664	0.02143	0.01359	1.5E-05	0.01326	0.01332
14	0.13282	0.05877	0.00723	0.02371	0.01457	2.0E-05	0.01415	0.01455
15	0.14006	0.06171	0.00779	0.02564	0.01520	4.4E-05	0.01446	0.01536

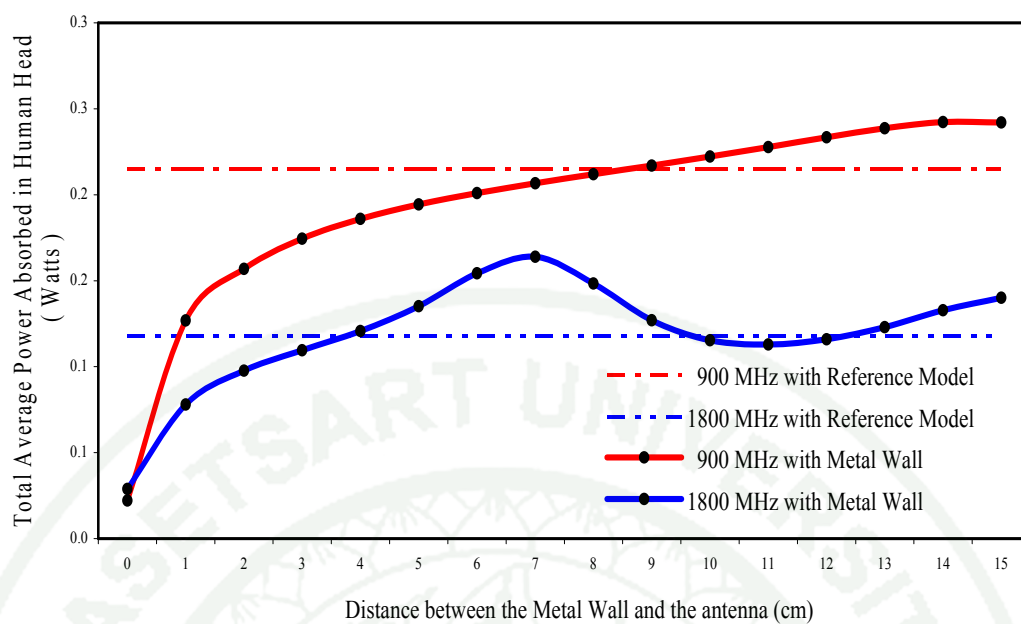


Figure 161 Total average power absorbed in human head respecting to the distance between the Metal Wall and the antenna, Δl .

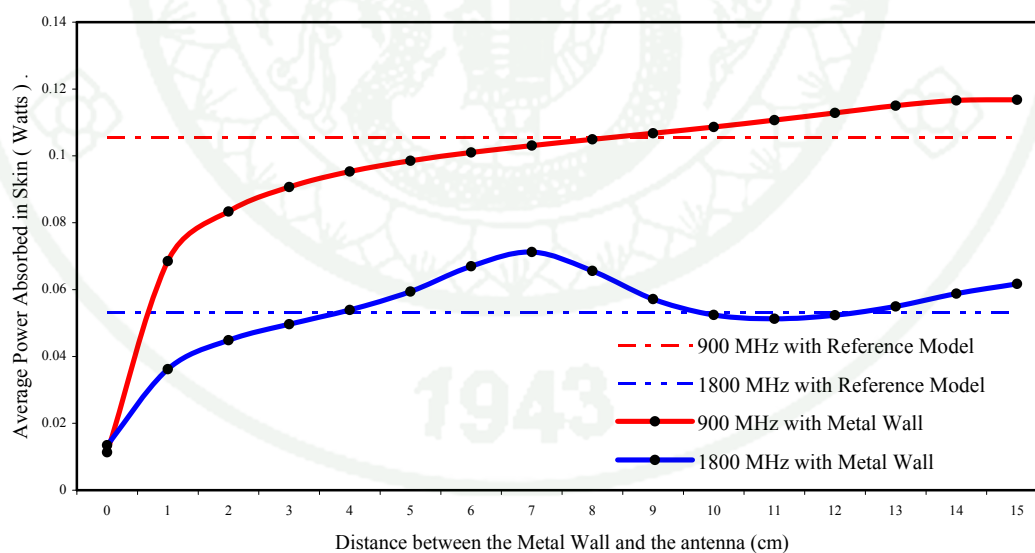


Figure 162 The average power absorbed (P_{avg}) in Skin respecting to the distance between the Metal Wall and the antenna, Δl .

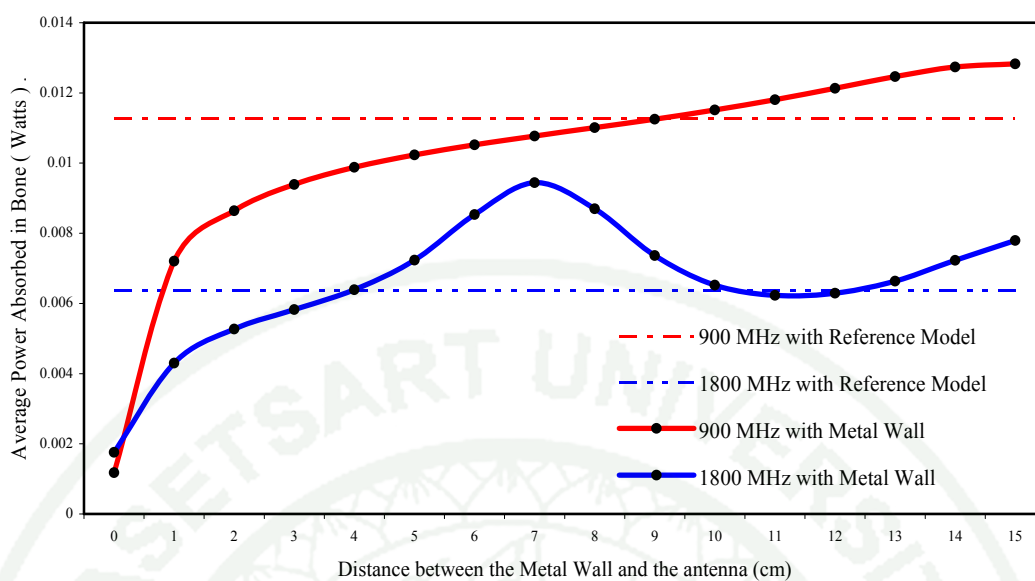


Figure 163 The average power absorbed (P_{avg}) in Bone respecting to the distance between the Metal Wall and the antenna, Δl .

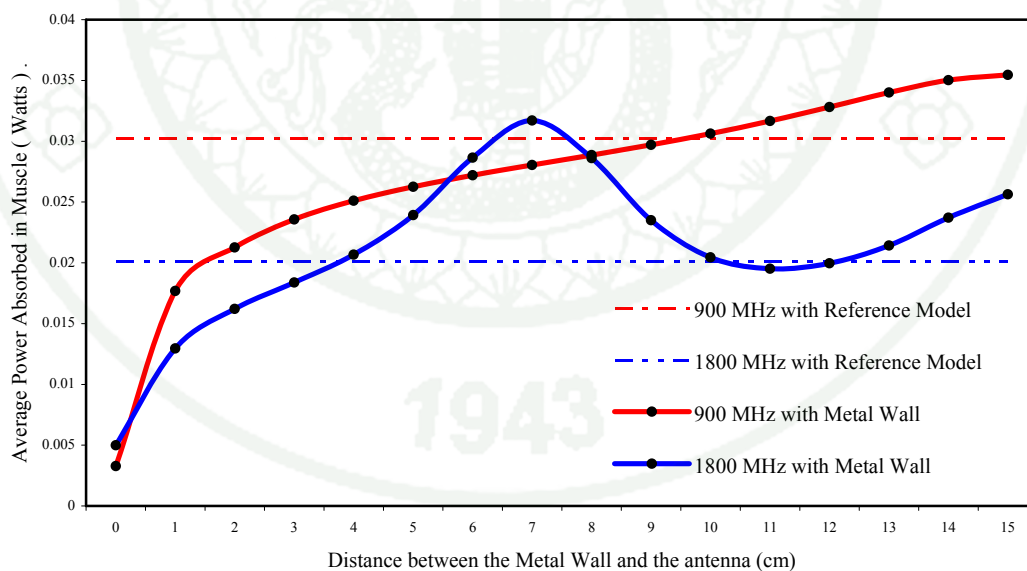


Figure 164 The average power absorbed (P_{avg}) in Muscle respecting to the distance between the Metal Wall and the antenna, Δl .

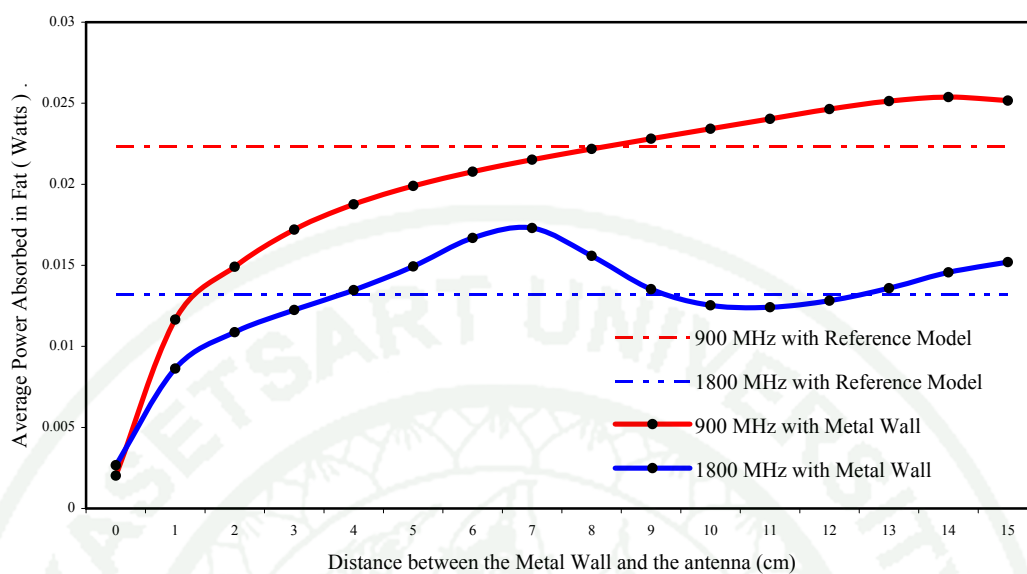


Figure 165 The average power absorbed (P_{avg}) in Fat respecting to the distance between the Metal Wall and the antenna, Δl .

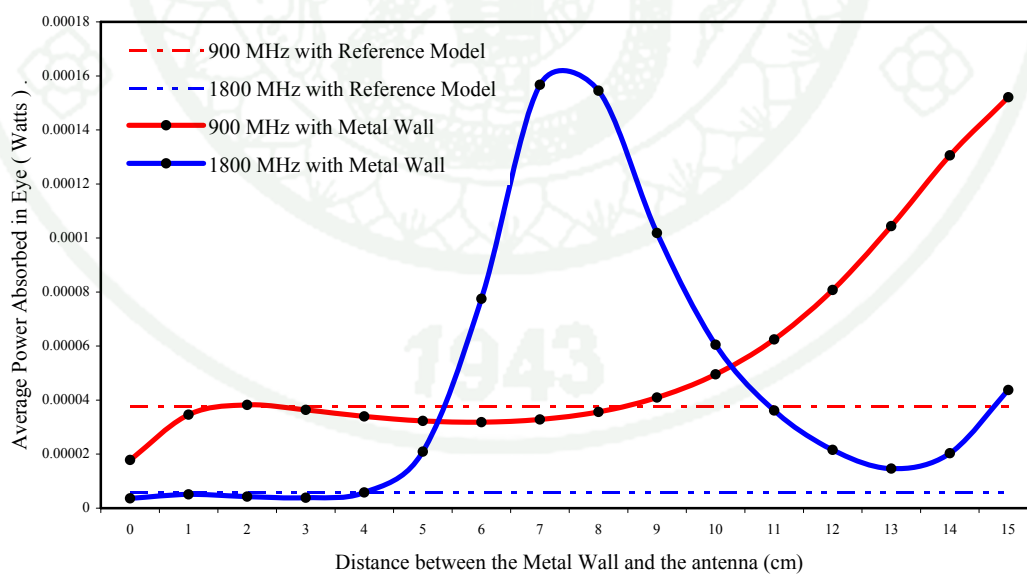


Figure 166 The average power absorbed (P_{avg}) in Eye respecting to the distance between the Metal Wall and the antenna, Δl .

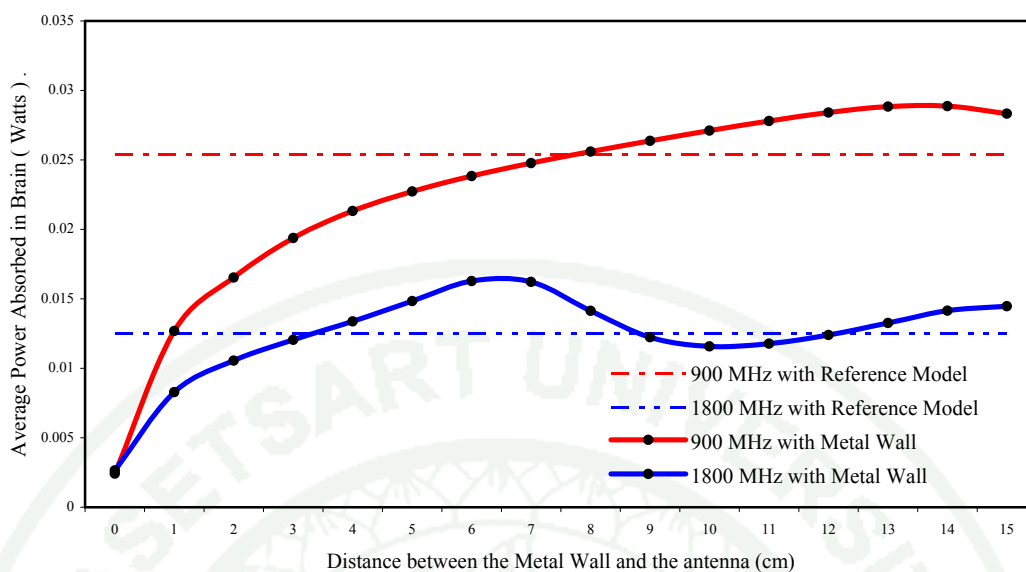


Figure 167 The average power absorbed (P_{avg}) in Brain respecting to the distance between the Metal Wall and the antenna, Δl .

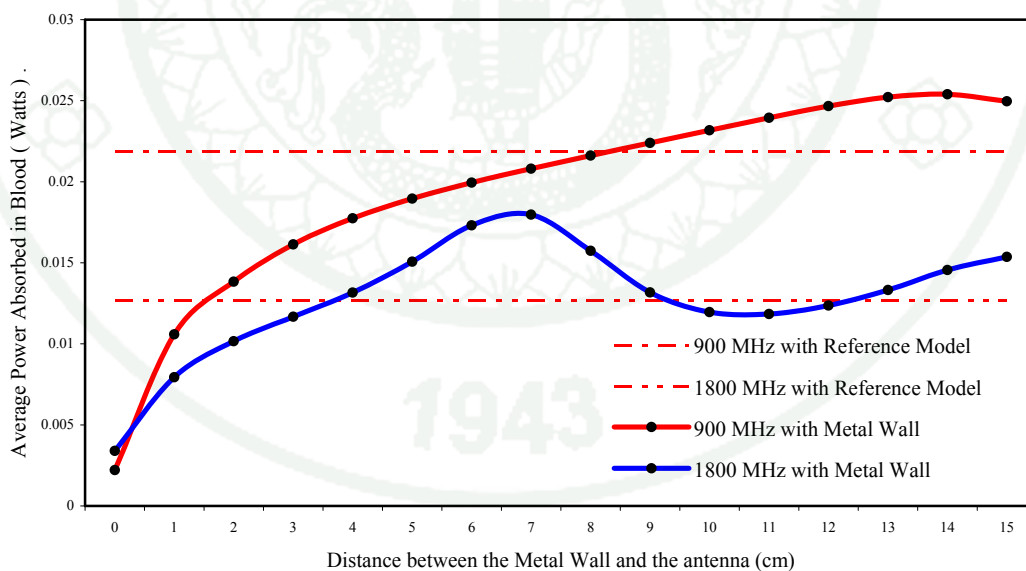


Figure 168 The average power absorbed (P_{avg}) in Blood respecting to the distance between the Metal Wall and the antenna, Δl .

Discussion

In this research, the electromagnetic simulation system was implemented using the FDTD scheme. Simulation results were comparable with result from MoM. With high confident, this FDTD programming could be used to simulate other interaction problems between electromagnetic fields and various materials.

For the simulation of a mobile phone operating near a Metal Wall, we need to truncate the human head at $\Delta l = 16 - 20$ cm because of the limitation of memory, 32-bits CPU. However, we can compute the average power absorbed by the human head in range of $\Delta l = 0 - 15$ cm.

With a distance (Δl) 0 - 5 cm, the values of both SAR decrease dramatically at both frequencies as distance gets smaller. Results from Table 23 and Table 24 show the reduction of the peak spatial-average SAR 1-g and SAR 10-g because of the rule of the reflection, the wave will cancel itself automatically. Also, it shows that the variation of the average SAR at a distance (Δl) longer than 5 cm is comparable to the reference model. Interestingly, the simulations which were operated at 1.8 GHz give both SAR values lower than those operated at 900 MHz.

Correspondingly, the instantaneous power absorbed (P_{avg}) is related to the conductivity ($\sigma_i(\omega)$) of different tissues in human head and determined by integrating the absorbed power density over the volume (V) of the human head model. Also, the instantaneous power absorbed can be related to the RMS of the Electric Field Strength at a point by Equation (182).

As the simulation results, the average power absorbed in the human head will suggest that using a mobile phone which was operated at 1.8 GHz give the average power absorbed lower than those operated at 900 MHz except for the average power absorbed in muscle ($6 < \Delta l < 8$ cm) and eye ($6 < \Delta l < 10$ cm).

CONCLUSION AND RECOMENDATIONS

Conclusion

The FDTD simulations had been applied to the situation where a mobile phone operated close to a Metal Wall at 900 MHz and 1.8 GHz. Results show that maximum value of E_{Total} was observed at the head model surface. In side the head model, the electromagnetic field decays monotonically. Also, SAR 1-g and SAR 10-g ($\Delta l < 20$ cm) do not exceed the ANSI/IEEE standard. Moreover, the average power absorbed in all tissue models with a mobile phone operated at 1.8 GHz has an average power lower than those operated at 900 MHz except for the average power absorbed in muscle ($6 < \Delta l < 8$ cm) and eye ($6 < \Delta l < 10$ cm). In conclusion, using a mobile phone operating near a Metal Wall in some cases can reduce the SAR value.

Recommendations

1. Simulation results show that SAR 1-g and SAR 10-g values could be changed when a mobile phone operating near a metal wall. These results should be studied further to find ways to reduce the SAR occurred in a human head.
2. The FDTD programming with the finite gap is agree well with the practical dipole as the following figure

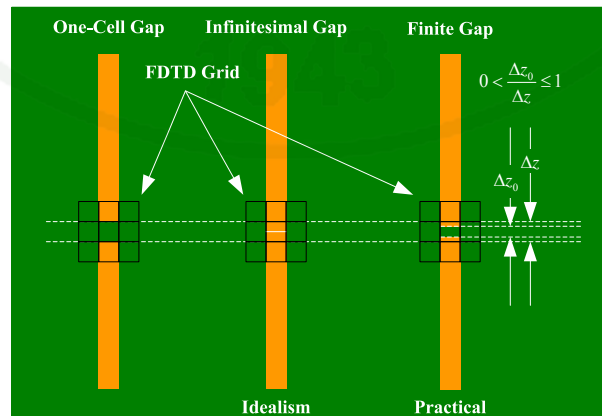


Figure 169 The practical dipole.

The dipole is an omnidirectional antenna which radiates power uniformly in one plane with a directive pattern shape (Donut shaped) in a perpendicular plane, Figure 130 and Figure 131. In brief, the omnidirectional antenna is generally implemented with unmanned systems: Bomb Disposal Robot and Quadrotor (Homsup and Jariyanorawiss, 2007; Homsup *et al.*, 2008a; Homsup *et al.*, 2009b).

3. The FDTD programming was written as the EM-Cycle. Apparently, this smart algorithm is flexible to handle efficiently with any type of materials. In conclusion, The EM-Cycle can be applied to any materials at state 5 in the following figure

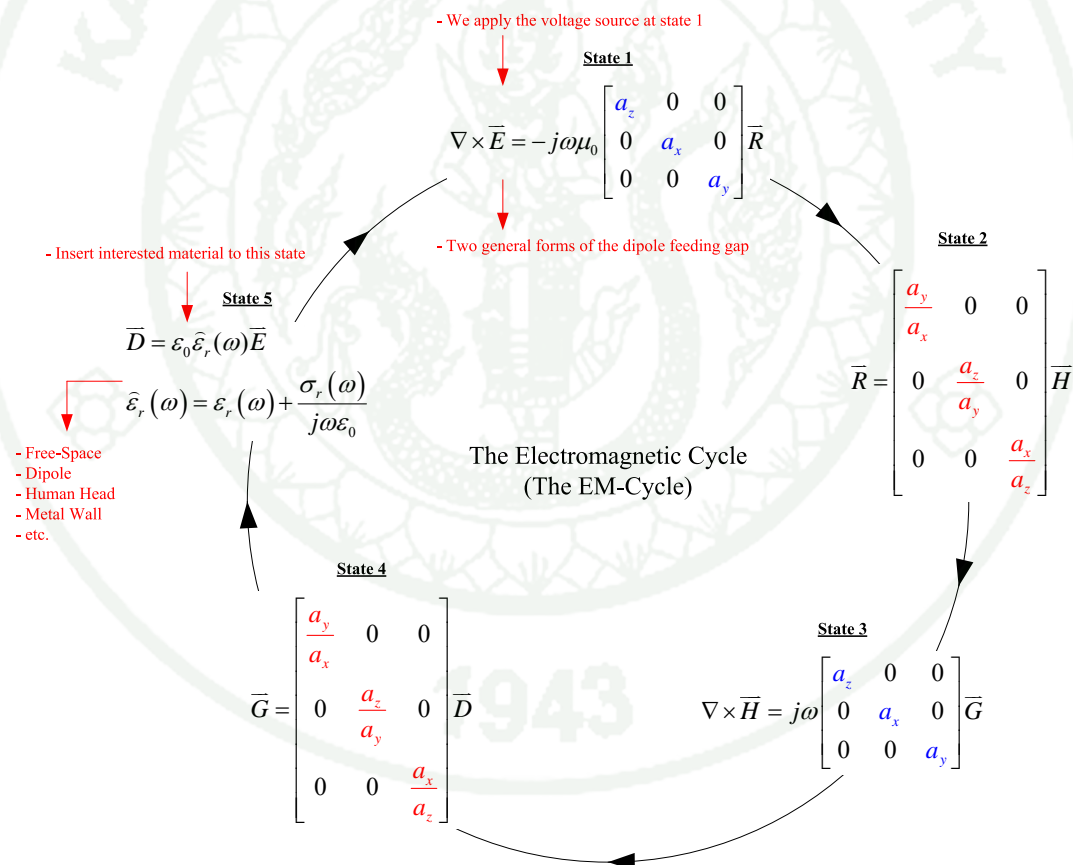


Figure 170 How to insert interested material to the EM-Cycle.

LITERATURE CITED

- Balanis, C.A. 2005. **Antenna Theory Analysis and Design**. 3rd ed. John Wiley & Sons, Inc., Hoboken, New Jersey.
- Berenger, J.P. 1994. A Perfectly Matched Layer for the absorption of electromagnetic waves. **Journal of Computational Physics** 114: 185-200.
- _____. 1996. Three-Dimensional Perfectly Matched Layer for the absorption of electromagnetic waves. **Journal of Computational Physics** 127: 363-379.
- Briggs, W.L., V.E. Henson and S.F. McCormick, 2000. **A Multigrid Tutorial**. 2nd ed. SIAM: Society for Industrial and Applied Mathematics, 3600 University City Science Center, Philadelphia, PA 19104-2688.
- Chapra, S.C. and R.P. Canale. 2002. **Numerical Method for Engineers**. 4th ed. McGraw-Hill Companies, Inc., 1221 Avenue of the Americas, New York, 10020.
- Chew, W.C. and W.H. Weedon. 1994. A 3D Perfectly Matched medium from modified Maxwell's equations with stretched coordinates. **Microwave and Optical Technology Letters** 7 (13): 599-604.
- Collin, R.E. 1985. **Antennas and Radiowave Propagation**. 1st ed. McGraw-Hill, Singapore.
- Elliott, R.S. 2003. **Antenna Theory and Design**. Revised ed. John Wiley & Sons, Inc., United States of America.
- Federal Communications Commission. 1998. **Information on Human Exposure to Radiofrequency Fields from Cellular and PCS Radio Transmitter**. Federal Communications Commission, 445 12th Street, SW Washington, DC 20554. January 1998.

- Fikioris, G. and T.T. Wu. 2001. On the application of numerical methods to Hallen's Equation. **IEEE Transactions on Antennas and Propagation** 49 (3): 383-392.
- Gandhi, O.P., G. Lazzi and C.M. Furse. 1996. Electromagnetic Absorption in the Human Head and Neck for Mobile Telephones at 835 and 1900 MHz. **IEEE Transactions on Microwave Theory and Techniques** 44 (10): 1884-1897.
- Gedney, S.D. 1996a. An anisotropic Perfectly Matched Layer-absorbing medium for the truncation of FDTD lattices. **IEEE Transactions on Antennas and Propagation** 44 (12): 1630-1639.
- _____. 1996b. An anisotropic PML absorbing media for the FDTD simulation of fields in lossy and dispersive media. **Electromagnetics** 16 (4): 339-415.
- Gibson, W.C. 2007. **The Method of Moments in Electromagnetics**. 1st ed. Chapman & Hall/CRC, Taylor & Francis Group, 6000 Broken Sound Parkway NW, Suite 300 Boca Raton, FL 33487-2742.
- Hallen, E. 1938. Theoretical investigations into the transmitting and receiving qualities of antennae. **Nova Acta Regiae Societatis Scientiarum Upsaliensis** 11 (4): 1-44.
- Harrington, R.F. 1993. **Field Computation by Moment Methods**. 1st ed. The Institute of Electrical and Electronics Engineers, Inc., New York.
- Haykin, S. 2001. **Communications Systems**. 4th ed. John Wiley and Sons, Inc., New York.
- Hayt, W.H. 1989. **Engineering Electromagnetics**. 5th ed. McGraw-Hill, Singapore.

Hoffman, J.D. 2001. **Numerical Methods for Engineers and Scientists**. 2nd ed. Marcel Dekker, Inc., 270 Madison Avenue, New York 10016.

Homsup, N., T. Jariyanorawiss and W. Homsup. 2004. Truncation of the head model in cellular phone simulations using a simple PML formulation, pp. 793-796. **In Proceedings of the International Symposium on Communications and Information Technologies 2004 (ISCIT 2004)**. 26-29 October 2004, Sapporo, Japan.

_____, _____ and _____. 2006. FDTD simulation of a mobile phone operating near a Metal Wall, pp. 332-335. **In Proceedings of the International Symposium on Communications and Information Technologies 2006 (ISCIT 2006)**. 18-20 October, 2006, Grand Mercure Fortune Hotel, Bangkok, Thailand.

_____, _____ and W. Homsup. 2008a. A control of a Bomb Disposal Robot using a stereoscopic vision, pp. 293-294. **In Proceedings of the IEEE SoutheastCon 2008**. 3-6 April, 2008, Von Braun Center, Huntsville, Alabama, USA.

_____, _____ and _____. 2008b. FDTD simulation of a mobile phone operating near a Metal Wall, pp. 305-308. **In Proceedings of the IEEE SoutheastCon 2008**. 3-6 April, 2008, Von Braun Center, Huntsville, Alabama, USA.

_____, _____ and _____. 2009a. FDTD simulation of a mobile phone operating near a Metal Wall. **Journal of Computers** 4 (2): 168-175.

_____, _____ and _____. 2010. An improved FDTD model for the feeding gap of a dipole antenna, pp. 475-478. **In Proceedings of the IEEE SoutheastCon 2010 (SoutheastCon)**. 18-21 March, 2010, Charlotte-Concord, North Carolina, USA.

Homsup, W. and T. Jariyanorawiss. 2007. A steering control of a Bomb Disposal Robot to the target using a 3-D vision, pp. 102-105. *In Proceedings of the 21st Conference of Mechanical Engineering Network of Thailand (ME NETT)*. 17-19 October, 2007, Jomtien Beach Hotel, Pattaya City, Chon Buri, Thailand.

_____, _____, R. Ramanjite and S. Buddee. 2009b. Quadrotor. *RTAFA Journal of Science and Technology* 5 (5): 94-99.

Jariyanorawiss, T. 2004. **Implementation of an Electromagnetic Perfectly Matched Layer (PML) in a Head Model using Finite Difference Time Domain (FDTD)**. M.S. Thesis, Kasetsart University.

_____ and N. Homsup. 2005a. Implementation of an electromagnetic Perfectly Matched Layer in head model using FDTD, pp. 718-721. *In Proceedings of the 2005 Electrical Engineering / Electronics, Computer, Telecommunications, and Information Technology (ECTI) International Conference*. 12-13 May 2005, Asia Pattaya Beach Hotel, Pattaya City, Chonburi, Thailand.

_____ and _____. 2005b. Implementation of FDTD scheme using PML for truncation of the head model in cellular phone simulations, pp. 623-626. *In Proceedings of the International Symposium on Communications and Information Technologies 2005 (ISCIT 2005)*. 12-14 October 2005, Fragrant Hotel, Beijing, China.

_____ and _____. 2006. Power comparison between a mobile phone operated at 1.8 GHz and 900 MHz near a Metal Wall, pp. 336-339. *In Proceedings of the International Symposium on Communications and Information Technologies 2006 (ISCIT 2006)*. 18-20 October, 2006, Grand Mercure Fortune Hotel, Bangkok, Thailand.

_____, _____ and W. Homsup. 2009. Unsplit-Field FDTD simulation of a mobile phone operating near a Metal Wall, pp. 364-368.

In Proceedings of the World Congress on Computer Science and Information Engineering 2009 (CSIE 2009). 31-2 April, 2009, Wilshire Grand, Los Angeles, USA.

Johnson, S.G. 2010. **Note on Perfectly Matched Layers (PMLs)**. Available Source: <http://math.mit.edu/~stevenj/18.369/>, March 29, 2010.

Katz, D.S., E.T. Thiele and A. Taflove, 1994. Validation and extension to three dimensions of the Berenger PML absorbing boundary condition for FD-TD meshes. **IEEE Microwave and Guided Wave Letters** 4 (8): 268-270.

Keith, A.J. and J.A. Becker. 2010. **The Whole Brain Atlas**. Available Source: <http://www.med.harvard.edu/AANLIB/home.html>, April 04, 2010.

King, R.W.P. 1953. An alternative method of solving Hallen's Integral Equation and its application to antennas near resonance. **Journal of Applied Physics** 24 (2): 140-147.

_____. 1956. **The Theory of Linear Antennas**. Harvard University Press, Cambridge, Massachusetts.

_____. 1959. Linear arrays: currents, impedances, and fields, I*. **IRE Transactions on Antennas and Propagation** 7: 440-457.

_____. 1967. The linear antenna—Eighty years of progress, pp. 2-16. *In Proceedings of the IEEE*. January 1967.

_____ and C.W. Harrison. 1943. The distribution of current along a symmetrical center-driven antenna, pp. 548-567. *In Proceedings of the I.R.E.* October 1943.

- Kouveliotis, N.K., P.T. Trakadas and C.N. Capsalis. 2002. Investigation of a dipole antenna performance and SAR distribution induced in a human head model, pp. 813-819. *In Proceedings of the International Workshop on Biological Effects of Electromagnetic Fields 2*. 2002.
- Kuhiran, W., T. Jariyanorawiss, M. Polpasee and N. Homsup. 2004. Solving for the current distribution using Gauss-Seidel iteration and Multigrid method, pp. 390-392. *In Proceedings of the First Electrical Engineering / Electronics, Computer, Telecommunications, and Information Technology (ECTI) Annual Conference*. 13-14 May 2004, Amari Orchid Resort, Pattaya City, Chonburi, Thailand.
- Kunz K.S. and R.J. Luebbers. 1993. **The Finite Difference Time Domain Method for Electromagnetics**. 1st ed. CRC-Press LLC, 2000 N.W., Corporate Blvd., Boca Raton, Florida 33431.
- Kwon, Y.W. and H. Bang. 1996. **The Finite Element Method using Matlab**. 1st ed. CRC-Press LLC, 2000 N.W., Corporate Blvd., Boca Raton, Florida 33431.
- Lan, K., K.K. Mei and Y.W. Liu. 1999. Extension of the Mei method and its applications on thin wire antennas, pp. 203-219. *In Progress in Electromagnetics Research 21*. 1999.
- Lee, F.K.W. 2003. **Modeling of Electromagnetic Wave Propagation in Printed Circuit Board and Related Structures**. Ph.D. Thesis, Multimedia University.
- Ling, L., L. Ronglin, X. Suming and N. Guangzheng, 2002. A New Generalized Perfectly Matched Layer for terminating 3-D lossy media. **IEEE Transactions on Magnetics** 38 (2): 713-716.
- Mei, K.K. 1965. On the integral equations of thin wire antennas. **IEEE Transactions on Antennas and Propagation** 1: 374-378.

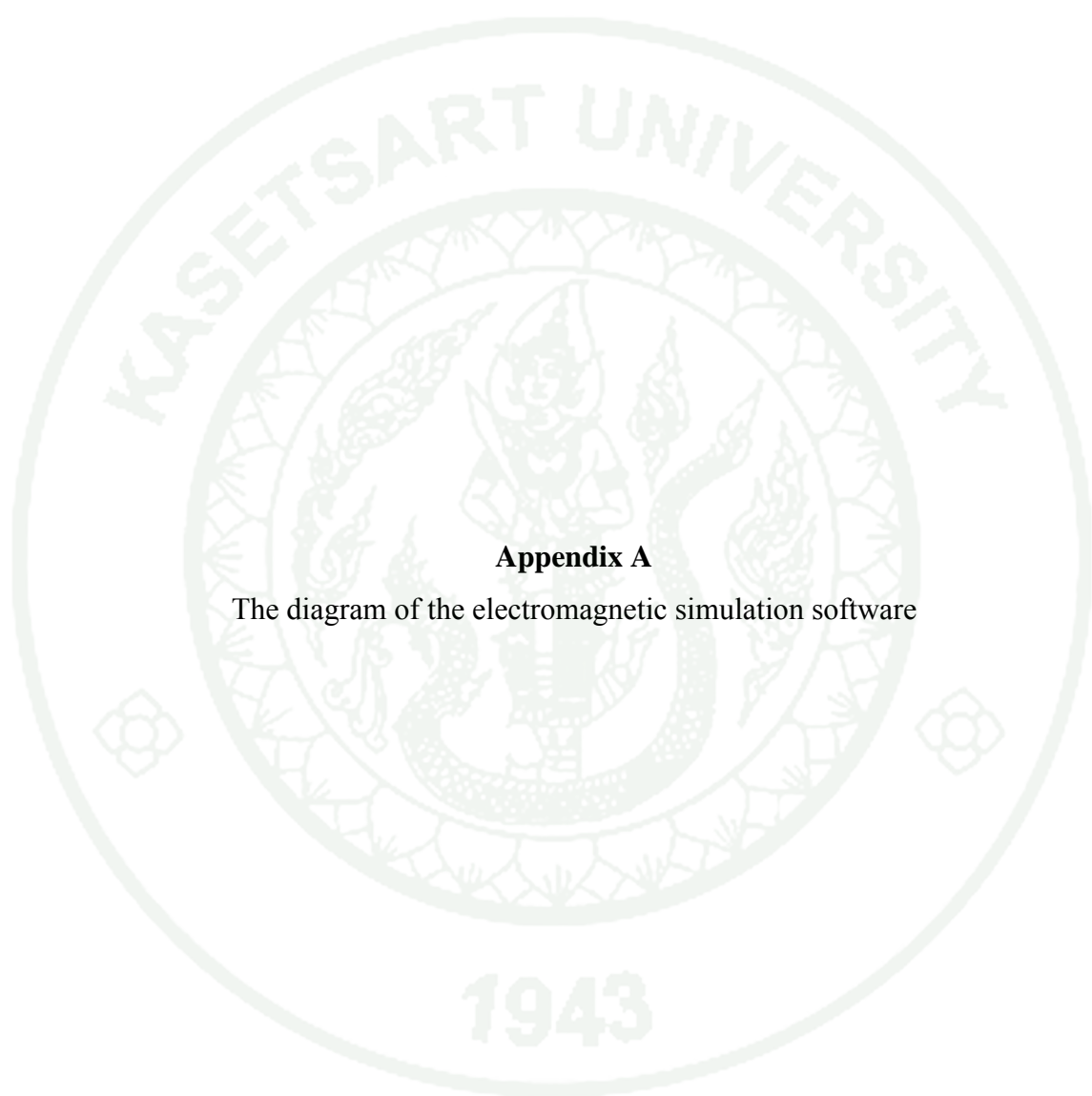
- Neff, H.P. 1987. **Basic Electromagnetic Fields**. 2nd ed. Harper & Row Publishers, New York.
- Orfanidis, S.J. 2008. **Electromagnetic Waves and Antennas**. Available Source: <http://www.ece.rutgers.edu/~orfanidi/ewa/>, January 20, 2010.
- Pan, G.W. 2003. **Wavelets in Electromagnetics and Device Modeling**. 1st ed. John Wiley & Sons, Inc., Hoboken, New Jersey.
- Poljak, D. 2007. **Advanced Modeling in Computational Electromagnetic Compatibility**. 1st ed. John Wiley & Sons, Inc., Hoboken, New Jersey.
- Pozar, D.M. 1998. **Microwave Engineering**. 2nd ed., John Wiley and Sons, Inc., New York.
- Rappaport, C.M. 1995. Perfectly Matched absorbing boundary conditions based on anisotropic lossy mapping of space. **IEEE Microwave and Guided Wave Letters** 5 (3): 90-92.
- Raida, Z. 2001. **Multimedia textbook of electromagnetic waves and microwave technique**. Available Source: <http://www.urel.feec.vutbr.cz/~raida/>, January 09, 2010.
- Sacks, Z.S. 1995. A Perfectly Matched anisotropic absorber for use as an absorbing boundary condition. **IEEE Transactions on Antennas and Propagation** 43 (12): 1460-1463.
- Sadiku, M.N.O. 2001. **Numerical Techniques in Electromagnetics**. 2nd ed. CRC-Press LLC, 2000 N.W., Corporate Blvd., Boca Raton, Florida 33431.
- Stutzman, W.L. and G.A. Thiele. 1998. **Antenna Theory and Design**. 2nd ed. John Wiley & Sons, Inc., 605 Third Avenue, New York.

- Taflove, A. 1995. **Computational Electrodynamics The Finite-Difference Time-Domain Method**. 1st ed. Artech House, Inc., 685 Canton Street Norwood, MA 02062.
- The Institute of Electrical and Electronics Engineers. 2002. **IEEE Recommended Practice for Measurements and Computations of Radio Frequency Electromagnetic Fields with Respect to Human Exposure to such Fields, 100 kHz-300 GHz**. IEEE Std C95.3TM-2002. The Institute of Electrical and Electronics Engineers (IEEE) Inc., New York, USA.
- The Institute of Electrical and Electronics Engineers. 2003. **IEEE Recommended Practice for Determining the Peak Spatial-Average Specific Absorption Rate (SAR) in the Human Head from Wireless Communications Devices: Measurement Techniques**. IEEE Std 1528TM-2003. The Institute of Electrical and Electronics Engineers (IEEE) Inc., New York, USA.
- Watanabe S. and M. Taki. 1998. An improved FDTD model for the feeding gap of a thin-wire antenna. **IEEE Microwave and Guided Wave Letters** 8 (4): 152-154.
- Wesseling, P. 1992. **An Introduction to Multigrid Methods**. 1st ed. John Wiley & Sons, Ltd., Baffins, Lane, Chichester, West Sussex PO19 1UD, England.
- Yahya, R.S. 2010. **Real Time Simulation of the Interaction of Electromagnetic Waves with a Human Head**. Available Source: <http://www.ee.olemiss.edu/atef/head/headpresentation/>, April 04, 2010.
- Yee, K.S. 1966. Numerical solution of initial boundary value problems involving Maxwell's equations in isotropic media. **IEEE Transactions on Antennas and Propagation** 14 (3): 302-307.

- Young, N. 1988. **An Introduction to Hilbert space**. 1st ed. Press Syndicate of the University of Cambridge, The Pitt Building, Trumpington Street, Cambridge CB2 1RP 32 East 57th Street, New York 10022, USA, 10 Stamford Road, Oakleigh, Melbourne 3166, Australia.
- Zhao, L. and A.C. Candgellaris. 1996a. A general approach for the development of Unsplit-Field Time-Domain implementations of Perfectly Matched Layers for FDTD grid truncation. **IEEE Microwave and Guided Wave Letters** 6 (5): 209 - 211.
- _____ and _____. 1996b. GT-PML: Generalized Theory of Perfectly Matched Layers and its application to the reflectionless truncation of Finite-Difference Time-Domain grids. **IEEE Transactions on Microwave theory and techniques** 44 (12): 2555 - 2563.
- Zhu, Y. 2006. **Multigrid Finite Element Methods for Electromagnetic Field Modeling**. 1st ed. John Wiley & Sons, Inc., Hoboken, New Jersey.

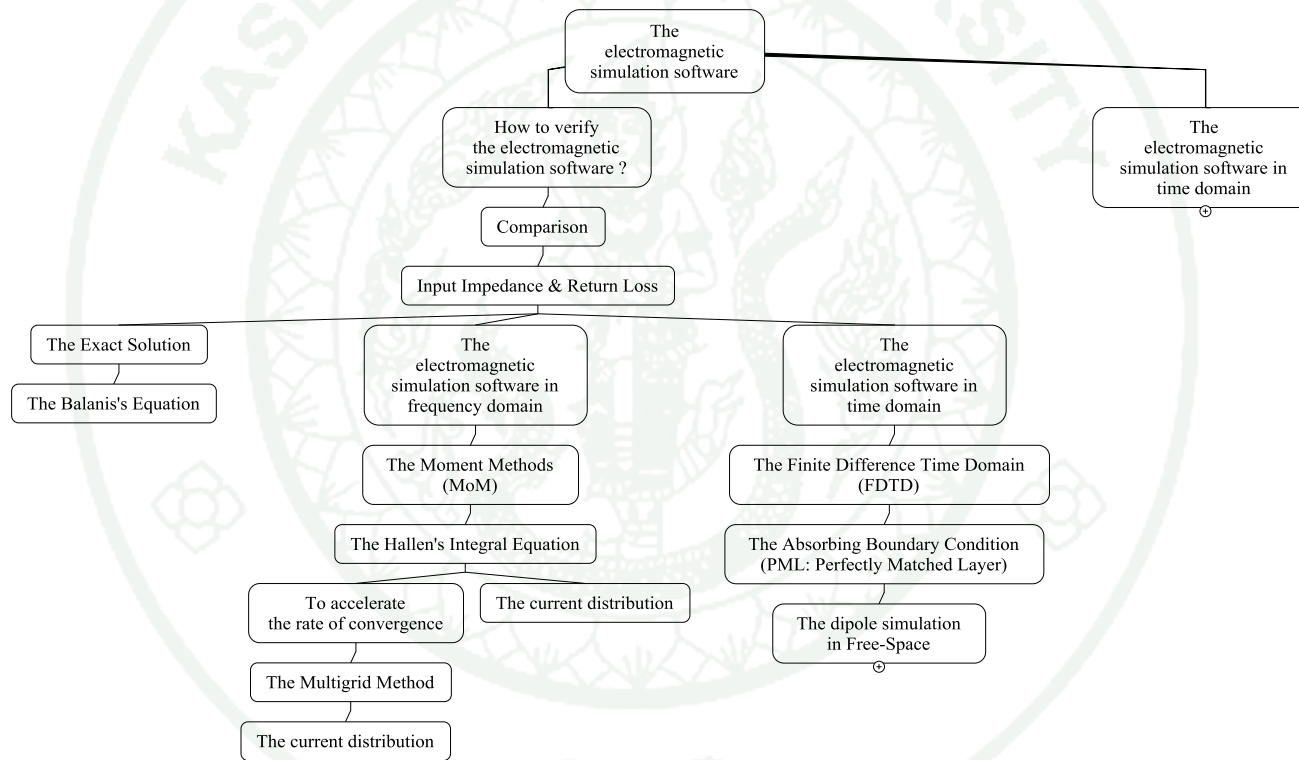


APPENDIX

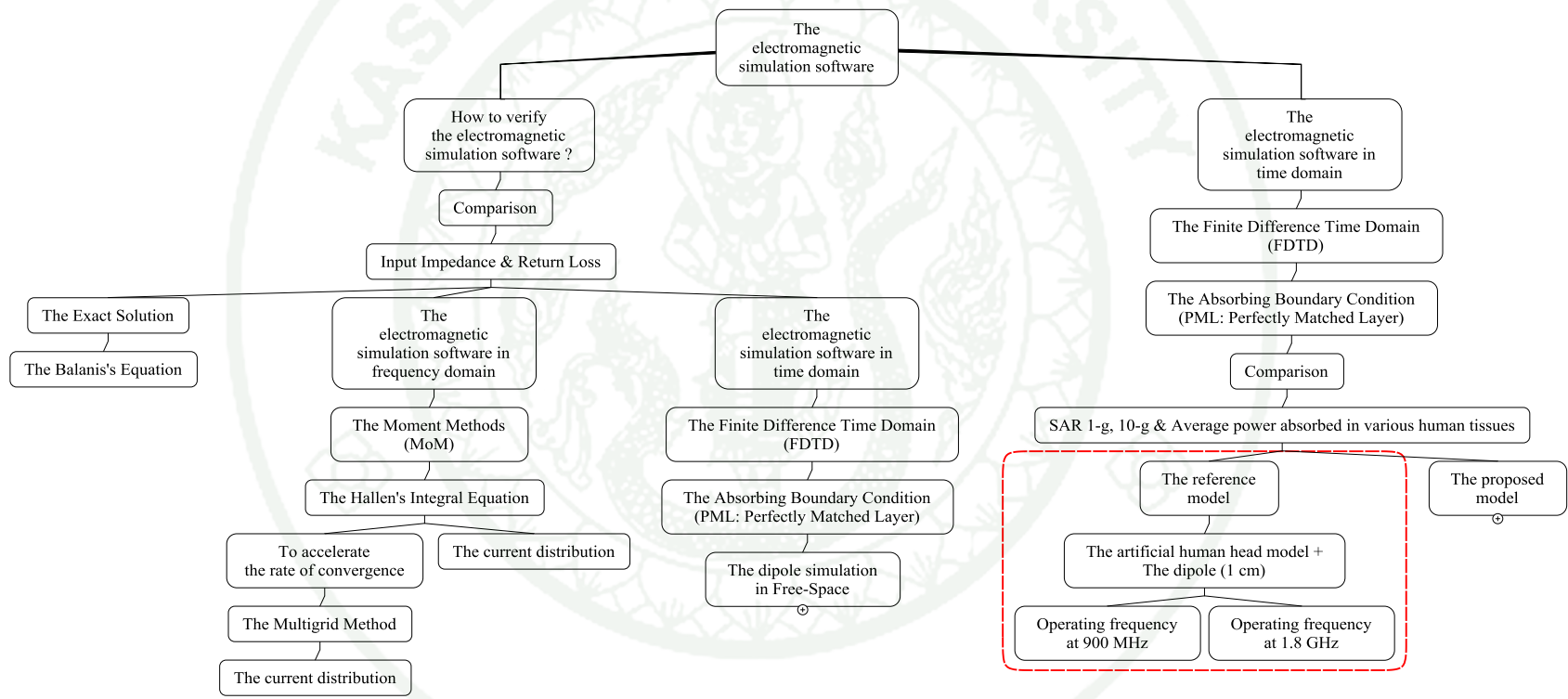


Appendix A

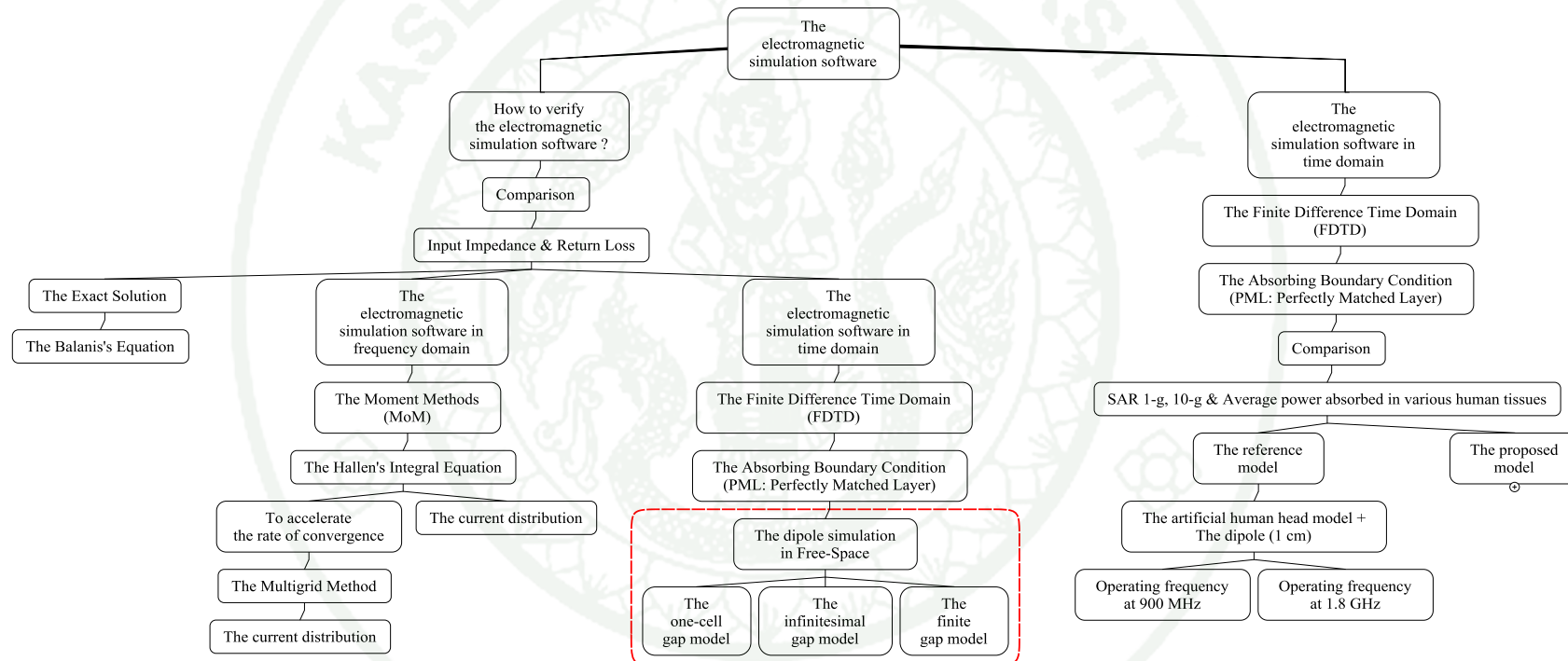
The diagram of the electromagnetic simulation software



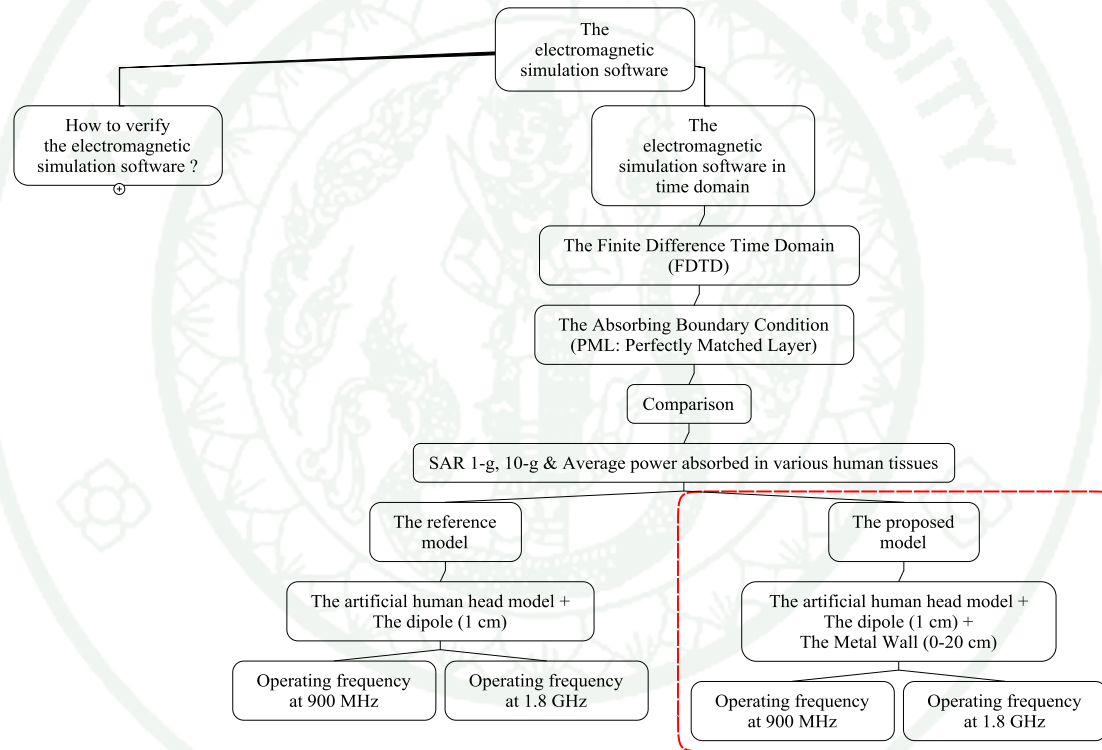
Appendix Figure A1 The diagram of how to verify the electromagnetic simulation software.



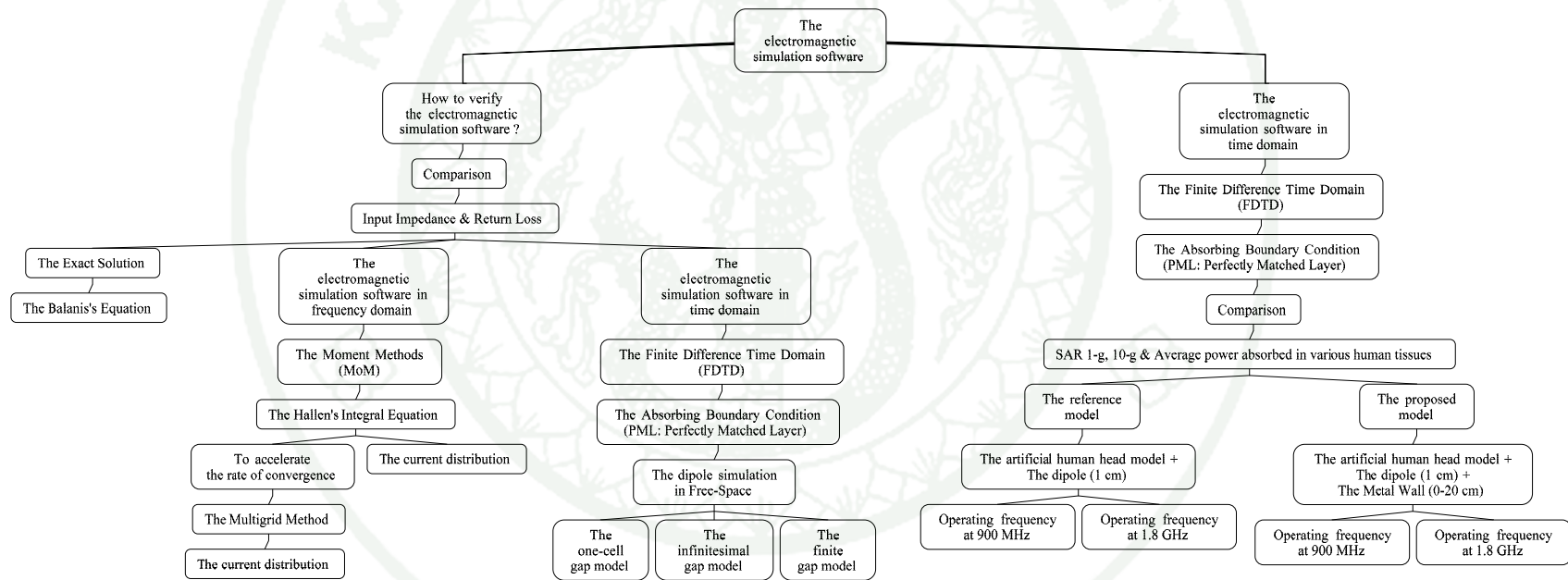
Appendix Figure A2 The diagram of the reference model.



Appendix Figure A3 The diagram of the dipole feeding gap model.



Appendix Figure A4 The diagram of the proposed model.



Appendix Figure A5 The diagram of the electromagnetic simulation software.

CURRICULUM VITAE



NAME : Mr. Terapass Jariyanorawiss

EDUCATION	: YEAR	INSTITUTE	DEGREE/DIPLOMA
	2002	Kasetsart University	B.Eng. (Electrical)
	2004	Kasetsart University	M.Eng. (Electrical)

SCHOLARSHIP :

- 2002 Research Scholarship, National Research Council of Thailand
– **Study the Effect of Using Mobile Telephone and Hands-Free on Driving Performance**
- 2002-2003 Teaching Assistant Scholarship, Electrical Engineering, Kasetsart University, Thailand
– **Electromagnetic Fields & Wave I**
– **Microwave Engineering**
– **Antenna Engineering**
- 2004-2005 Teaching Assistant Scholarship, Graduate School, Kasetsart University, Thailand
– **Numerical Analysis for Electrical Engineers**
- 2006 Research Scholarship, National Research Council of Thailand
– **Research and Development for Bomb Disposal Robot I**
- 2007 Research Scholarship, National Research Council of Thailand
– **Research and Development for Bomb Disposal Robot II**

- 2008 Research Scholarship, National Research Council of Thailand
 – **Research and Development for Autonomous Paramotor for Surveillance and a Bomb Disposal Robot Transport**
- 2009 Research Scholarship, National Research Council of Thailand
 – **Design and Development of Vertical Takeoff and Landing Air Vehicle**
- 2010 Research Scholarship, National Research Council of Thailand
 – **Design and Development of Coaxial Helicopter for Explosive Searching Mission in the Southern Part of Thailand**

INTERNATIONAL PUBLICATIONS :

- Homsup, N., T. Jariyanorawiss and W. Homsup. 2004. Truncation of the head model in cellular phone simulations using a simple PML formulation, pp. 793-796. *In Proceedings of the International Symposium on Communications and Information Technologies 2004 (ISCIT 2004)*. 26-29 October 2004, Sapporo, Japan.
- _____ and _____. 2006. FDTD simulation of a mobile phone operating near a Metal Wall, pp. 332-335. *In Proceedings of the International Symposium on Communications and Information Technologies 2006 (ISCIT 2006)*. 18-20 October, 2006, Grand Mercure Fortune Hotel, Bangkok, Thailand.
- Homsup, N., T. Jariyanorawiss and W. Homsup. 2008. A control of a Bomb Disposal Robot using a stereoscopic vision, pp. 293-294. *In Proceedings of the IEEE SoutheastCon 2008*. 3-6 April, 2008, Von Braun Center, Huntsville, Alabama, USA.
- _____, _____ and _____. 2008. FDTD simulation of a mobile phone operating near a Metal Wall, pp. 305-308. *In Proceedings of the IEEE SoutheastCon 2008*. 3-6 April, 2008, Von Braun Center, Huntsville, Alabama, USA.

_____, _____ and _____. 2009. FDTD simulation of a mobile phone operating near a Metal Wall. **Journal of Computers** 4 (2): 168-175.

_____, _____ and _____. 2010. An improved FDTD model for the feeding gap of a dipole antenna, pp. 475-478. *In Proceedings of the IEEE SoutheastCon 2010 (SoutheastCon)*. 18-21 March, 2010, Charlotte-Concord, North Carolina, USA.

Jariyanorawiss, T. 2004. **Implementation of an Electromagnetic Perfectly Matched Layer (PML) in a Head Model using Finite Difference Time Domain (FDTD)**. M.S. Thesis, Kasetsart University.

_____ and N. Homsup. 2005a. Implementation of an electromagnetic Perfectly Matched Layer in head model using FDTD, pp. 718-721. *In Proceedings of the 2005 Electrical Engineering / Electronics, Computer, Telecommunications, and Information Technology (ECTI) International Conference*. 12-13 May 2005, Asia Pattaya Beach Hotel, Pattaya City, Chonburi, Thailand.

_____ and _____. 2005b. Implementation of FDTD scheme using PML for truncation of the head model in cellular phone simulations, pp. 623-626. *In Proceedings of the International Symposium on Communications and Information Technologies 2005 (ISCIT 2005)*. 12-14 October 2005, Fragrant Hotel, Beijing, China.

_____ and _____. 2006. Power comparison between a mobile phone operated at 1.8 GHz and 900 MHz near a Metal Wall, pp. 336-339. *In Proceedings of the International Symposium on Communications and Information Technologies 2006 (ISCIT 2006)*. 18-20 October, 2006, Grand Mercure Fortune Hotel, Bangkok, Thailand.

_____, _____ and W. Homsup. 2009. Unsplit-Field FDTD simulation of a mobile phone operating near a Metal Wall, pp. 364-368.

In Proceedings of the World Congress on Computer Science and Information Engineering 2009 (CSIE 2009). 31-2 April, 2009, Wilshire Grand, Los Angeles, USA.

Kuhiran, W., T. Jariyanorawiss, M. Polpasee and N. Homsup. 2004. Solving for the current distribution using Gauss-Seidel iteration and Multigrid method, pp. 390-392. ***In Proceedings of the First Electrical Engineering / Electronics, Computer, Telecommunications, and Information Technology (ECTI) Annual Conference***. 13-14 May 2004, Amari Orchid Resort, Pattaya City, Chonburi, Thailand.

THAILAND PUBLICATIONS :

Homsup, N. and T. Jariyanorawiss. 2003. A driving simulator for studying effects of using mobile telephone and hand-free on driving performance, pp. 540-543. ***In Proceedings of the 26th Electrical Engineering Conference***. 6-7 November, 2003, Golden Sand Hotel, Hat Cha-Am, Phetchaburi, Thailand.

Homsup, W. and T. Jariyanorawiss. 2007. A steering control of a Bomb Disposal Robot to the target using a 3-D vision, pp. 102-105. ***In Proceedings of the 21st Conference of Mechanical Engineering Network of Thailand (ME NETT)***. 17-19 October, 2007, Jomtien Beach Hotel, Pattaya City, Chon Buri, Thailand.

_____, _____, R. Ramanjite and S. Buddee. 2009. Quadrotor. ***RTAFA Journal of Science and Technology*** 5 (5): 94-99.